



Catechol chemistry for biosensor manufacturing: synthesis and electro-crosslinking of gold nanoparticles/enzymes

Rémy Savin

► To cite this version:

Rémy Savin. Catechol chemistry for biosensor manufacturing: synthesis and electro-crosslinking of gold nanoparticles/enzymes. Chemical Physics [physics.chem-ph]. Université de Strasbourg, 2022. English. NNT : 2022STRAE008 . tel-04213531

HAL Id: tel-04213531

<https://theses.hal.science/tel-04213531>

Submitted on 21 Sep 2023

HAL is a multi-disciplinary open access archive for the deposit and dissemination of scientific research documents, whether they are published or not. The documents may come from teaching and research institutions in France or abroad, or from public or private research centers.

L'archive ouverte pluridisciplinaire **HAL**, est destinée au dépôt et à la diffusion de documents scientifiques de niveau recherche, publiés ou non, émanant des établissements d'enseignement et de recherche français ou étrangers, des laboratoires publics ou privés.

ÉCOLE DOCTORALE DE PHYSIQUE et CHIMIE-PHYSIQUE

Institut Charles Sadron CNRS-UPR22

THÈSE présentée par :

Rémy SAVIN

soutenue le: **28 mars 2022**

pour obtenir le grade de : **Docteur de l'université de Strasbourg**

Discipline: Chimie – Physique

**La chimie des catéchols pour le
développement de biocapteurs : Synthèse et
électro-réticulation de nanoparticules d'or
fonctionnalisées par des enzymes**

THÈSE dirigée par :

Mme BOULMEDAIS Fouzia

Directrice de Recherche, CNRS

RAPPORTEURS :

Mme MARCHI Valérie

Directrice de Recherche, CNRS

M. LAKARD Boris

Professeur, Université de Bourgogne Franche-Comté

AUTRES MEMBRES DU JURY :

M. PICHON Benoît

Professeur, Université de Strasbourg

Acknowledgements

Je remercie en premier lieu le jury : Valérie Marchi, Boris Lakard et Benoît Pichon pour la revue attentive de cette thèse à laquelle j'ai consacré trois années de travail. Merci également à toi, lecteur, pour l'intérêt que tu y portes en espérant que tu y trouveras une lecture agréable. Ce sujet m'a beaucoup apporté dans les domaines de l'électrochimie et de la bioélectronique et c'est avec plaisir que je partage ici les réponses à mes propres questions et le travail expérimental que j'ai réalisé sur les bioélectrodes.

J'en profite pour exprimer ici mon immense gratitude envers ma directrice de thèse Fouzia Boulmedais. Je ne peux faire ici la liste de toute ses qualités humaines alors je m'en tiendrais à ces mots : Merci Fouzia pour la confiance et l'autonomie que tu m'as accordée durant ces trois années. Merci pour ta patience, ta disponibilité et parfois même ton intransigeance qui m'a permis de me recentrer sur les objectifs « essentiels ». Ce manuscrit est le fruit de mon travail mais également du tien, cela va sans dire.

Je remercie également ma conjointe Elsa Potoudis pour son soutien au quotidien, et en particulier lors des moments difficiles. Merci de me suivre dans mes passions et mes projets les plus saugrenus. Merci pour ce temps que tu m'as permis de gagner sur les périodes de travail acharné. Ma gratitude s'adresse de la même manière à l'ensemble de ma famille qui m'a soutenu tout au long de mon parcours malgré des situations parfois compliquées.

Je remercie toute l'équipe PECMAT avec laquelle j'ai passé des moments mémorables. Je ne peux tous les citer mais merci à ces personnes qui ont rendues cette thèse si plaisante au quotidien. Je remercie plus globalement les personnes de l'ICS pour leur accueil et leur support, notamment le personnel des plateformes de caractérisation et microscopie. Je suis également reconnaissant envers Christian Njel du KIT à Karlsruhe pour les analyses XPS de même qu'envers Anne Hébraud, Sergey Pronkin, Stéphanie Ferry, Housseinou Ba, Jean-Mario Nhut et Guy Schlatter de l'ICPEES pour la collaboration sur les membranes conductrices.

J'exprime également ma reconnaissance envers l'école doctorale ED182 et l'Université de Strasbourg pour avoir retenu mon profil et m'avoir financé sur ce projet.

Enfin j'adresse mes derniers mots de remerciement à toutes les personnes qui s'engagent pour rendre la science intègre et accessible à tous. Merci à Alexandra Elbakyan pour m'avoir questionné sur une conception de la science qui ne me serait jamais venu à l'esprit autrement.

Acknowledgements

Résumé de thèse en français (French summary)

General Introduction

Chapter 1 – Bibliographic Review

I. Enzymatic bioelectrodes	6
I.1 Bioelectrodes and their applications	6
I.1.1 Electrochemical biosensors	7
I.1.2 Enzymatic biofuel cells	9
I.1.3 Self-powered enzymatic biosensors	10
I.1.4 Enzymatic logic gates.....	12
I.1.5 Smart electro-driven drug release coupled biosensors	13
I.2 Electrochemical biosensor generations	16
I.2.1 Redox-enzyme based biosensors.....	16
I.2.2 Non-redox enzyme-based biosensors	18
II. Mechanisms of the electron transfer towards the electrode.....	21
II.1 Mediated electron transfer biocatalysis.....	22
II.2 Immobilized mediated electron transfer biocatalysis.....	23
II.3 Choice of the mediator	25
II.4 Direct electron transfer biocatalysis	27
II.5 DET and commercial enzymes	33
II.6 Glucose oxidase and horseradish peroxidase biosensors	34
III. Electro-triggered enzyme immobilization.....	38
III.1 Enzyme immobilization principles.....	38
III.1.1 Non-covalent adsorption and physical entrapment	38
III.1.2 Covalent attachment and cross-linking	39
III.1.3 Bio-conjugation immobilization	41
III.2 Electro-triggered immobilization strategies	42
III.2.1 Manual vs electro-triggered strategies	42
III.2.2 Electrodeposition of physically entrapped enzymes	43
III.2.3 Electrodeposition of covalently linked enzymes.....	48
III.3 Electrodeposition mechanisms	52
IV. References	55

Chapter 2 – Material and methods

I. Material and sample Preparation	85
I.1 Polyphenols	85
I.1.1 Commercial catechol and gallol molecules	85
I.1.2 Chemical properties of polyphenols	86
I.1.3 Polyphenol/enzyme interaction	88
I.2 Enzymes	89
I.2.1 Glucose oxidase (GOx)	89
I.2.2 Horseradish peroxidase (HRP)	90
I.3 Redox mediators	92
I.3.1 Ferrocene molecules	92
I.3.2 Others redox molecules	92
I.4 Nanoparticle synthesis	93
I.5 Polyurethane/graphene membrane preparation	94
II. Instrumentation	95
II.1 Electrochemical and quartz microbalance	95
II.1.1 The EC apparatus coupled with quartz crystal microbalance	95
II.1.2 The EC apparatus for gold interdigitated microelectrodes	97
II.1.3 The EC set-up for membrane testing	97
II.2 Spectroscopic apparatus	98
II.2.1 UV-Vis spectrophotometer	98
II.2.2 Dynamic light scattering	100
II.2.3 X-ray photoelectron spectroscopy	102
II.3 Electron Microscopy	102
II.3.1 Scanning electron microscopy	103
II.3.2 Transmission electron microscopy	105
III. Methods	106
III.1 Polyphenol and AuNPs Characterization	106
III.1.1 Gallol moieties quantification	106
III.1.2 Nanoparticles size	108
III.1.3 Nanoparticles concentration	109
III.2 Enzyme characterization	110

III.2.1	Enzyme and cofactor concentration	110
III.2.2	Enzyme size and glycosylation state	111
III.2.3	Enzyme activity with colorimetric test.....	111
III.2.4	Accessible lysine/cysteine residues.....	112
III.3	Enzyme/nanoparticles complexes	114
III.3.1	Estimation of the theoretical monolayer ratio	114
III.3.2	Aggregation/flocculation Test.....	115
III.3.3	Bradford test.....	115
III.3.4	Activity test	116
III.4	Electrodeposition and thin film characterizations	117
III.4.1	Preliminary electrochemical requirement	117
III.4.2	Estimation of the electroactive surface area.....	118
III.4.3	Preparation of electrodeposition solution.....	118
III.4.4	Deposit mass and electrodeposition efficiency	119
III.4.5	Morphology	120
III.4.6	XPS chemical analysis	120
III.5	Biosensor properties	120
III.5.1	Characterization of the biocatalytic current	120
III.5.2	Sensitivity, limit of detection, response time and interferents	121
III.5.3	Stability with time, tween-20 test and bending	122
III.5.4	Kinetics of michaelian enzymes.....	123
IV.	References	124

Chapter 3 – Mussel-inspired electro-crosslinking of Tannic Acid Capped Gold Nanoparticles and Enzymes for Biosensing Applications

Abstract	131
I. Introduction	131
II. TA@AuNPs synthesis and characterisation	134
III. GOx/TA@AuNPs complexes characterization.....	135
IV. Electrodeposition of GOx/TA@AuNPs coatings.....	137
V. XPS analysis of GOx/TA@AuNPs coatings.....	140
VI. GOx/TA@AuNPs coating biosensing properties	144

VII. Versatility of the process.....	150
Conclusion.....	152
References	152

Chapter 4 – Optimization of electro-crosslinked enzyme/tannic acid nanoparticles as nanohybrid biosensors

Abstract.....	158
Introduction	158
I. Nanoparticles Synthesis and characterization.....	160
II. Gold Nanoparticles Electrodeposited Coatings.....	162
III. Sensitivity optimization of enzyme/NPs coatings	164
IV. Enzyme/NPs bioconjugate characterization	169
Conclusion.....	173
References	174

Chapter 5 – Toward Smart Wound Dressings Based On Graphenized Polyurethane Membranes

I. Context of acute and chronic wounds	179
I.1 The wound healing process	179
I.2 Acute and chronic wounds	180
I.3 Simple biomarkers of the wound status	181
I.3.1 Hydrogen peroxide.....	181
I.3.2 pH value	182
I.3.3 Uric acid	183
I.3.4 Glucose.....	184
I.3.5 Summary on the studied biomarkers	184
II. Development of a smart wound dressing	185
II.1 Characterization of PU-FLG membrane	185
II.2 Development of IMET glucose H ₂ O ₂ biosensors.....	188
II.3 Development of the pH sensor	192
Conclusions	194
References	195

General conclusion

Summary

Glossary and abbreviations

AN – Aspergillus Niger	NP7 – 7 nm AuNPs
AuNPs – Gold nanoparticles	NP11 – 11 nm AuNPs
BFC – Biofuel cells	NP30 – 30 nm AuNPs
CNT – Carbon nanotubes	OCP – Open circuit potential
CV – Cyclic voltammetry	Ox – Oxidized state
DET – Direct electron transfer	PANI – Polyaniline
DLS – Dynamic light scattering	PEDOT – Poly(3,4-ethylenedioxythiophene)
EC – Electrochemistry	pH – Potential of hydrogen
FAD – Flavin adenine dinucleotide	pI – Isoelectric point
Enz – Enzyme	PSS – Polystyrene sulfonate
FcOH – Ferrocene methanol	Ppy – Polypyrrole
FcB(OH)₂ – Ferrocene boronic acid	PU – Polyurethane
FLG – Few layers graphene	Q – Quinone (oxidized state)
GA – Gallic Acid	QCM – Quartz crystal microbalance
H₂Q – Hydroquinone (reduced form)	Red – Reduced state
H₂O₂ – Hydrogen peroxide	SEM – Scanning electron microscopy
HRP – Horseradish Peroxidase	SWCNTs – Single-walled carbon nanotubes
i.e – Id Est (that is)	TA – Tannic Acid
IET – Internal electron transfer	TA@AuNPs – Tannic acid capped gold nanoparticles
IMET – Immobilized mediated electron transfer	TEM – Transmission electron microscopy
MET – Mediated electron transfer	XPS – X-ray photoelectron spectroscopy
MWCNT – Multi-walled carbon nanotubes	
NP – Nanoparticle	

Résumé en Français
(French summary)

I. Introduction

I.1 Contexte du projet

Dans le diagnostic médical et la surveillance de l'environnement, les biocapteurs enzymatiques sont en plein essor en raison des perspectives de miniaturisation et d'automatisation permettant leur utilisation en routine en temps réel et *in-situ*. Les bio-batteries et bio-puces, souvent basées sur des réactions enzymatiques, sont également des domaines de recherche très prometteurs avec l'alimentation électrique de dispositifs bio-implantés¹ et la découverte de nouveaux médicaments/biomarqueurs². Dans ces trois domaines de recherche, le processus critique concerne la fabrication des bio-électrodes où l'immobilisation d'enzymes doit être correctement contrôlée afin de limiter la dénaturation de l'enzyme et d'assurer une stabilité du dispositif à long terme.

Il y a une dizaine d'années, un procédé bio-inspiré basé sur la chimie des catéchols a été développé permettant de produire avec des revêtements polymériques sur tous types de surface.³ Notre équipe a par la suite contribué au développement d'un procédé d'électro-réticulation à base de catéchols.^{4,5} En procédant ainsi, un contrôle spatial et temporel du dépôt est obtenu ce qui permet par exemple de fonctionnaliser des microélectrodes avec des macromolécules d'intérêts. Un premier biocapteur à glucose a été ainsi développé en 2018 en utilisant l'oxydation par électrochimie, d'une molécule biscatéchol en bisquinone.⁵ La molécule de bisquinone réagit de manière covalente avec l'enzyme, la glucose oxydase (GOx), permettant son immobilisation sur l'électrode du biocapteur. Ce procédé bio-inspiré a permis (i) d'immobiliser en une étape l'enzyme, sans la modifier au préalable, (ii) d'obtenir une immobilisation covalente et (iii) de fonctionnaliser spécifiquement des micro-électrodes (Tableau 1).

Tableau 1: Bilan sur le premier dispositif développé en 2018⁵

Avantages	Limites actuelles
Procédé en une étape	Sensibilité/limite de détection insuffisante (de l'ordre de 1 mM)
Contrôle spatial de la fonctionnalisation	Temps de réponse (> 10min)
Réticulation de l'enzyme	Utilisation d'une molécule bis-catéchol synthétisée au laboratoire
Pas de modification préalable de l'enzyme	Nécessité d'utiliser des médiateurs libres en solution pour le transfert d'électrons

Cependant, le système développé présente des limites dans le contexte des bio-électrodes. La nécessité d'utiliser un médiateur, transporteur d'électrons, libre en solution ainsi que des limites de détection insuffisantes pour des applications spécifiques sont les principaux inconvénients du procédé développé.

Dans le contexte, mon projet de thèse a ainsi consisté en l'amélioration du procédé bio-inspiré de fonctionnalisation d'électrode par des enzymes avec deux objectifs prioritaires. Dans un premier temps, nous avons voulu améliorer la sensibilité du biocapteur et atteindre une limite de détection de l'ordre du micro-molaire. En effet, la plupart des analytes présent dans les fluides biologiques ont des concentrations très inférieure à 1 mM.⁶ Dans un deuxième temps, l'objectif consistait à obtenir un transfert électronique de l'enzyme vers l'électrode sans l'aide de médiateurs libres en solution. En effet, le médiateur libre en solution va se retrouver 'dilué' dans un circuit ouvert tel que la circulation sanguine entraînant une diminution de la sensibilité du biocapteur avec le temps. Le but a été de développer des biocapteurs de 2.5^e génération, utilisant un médiateur immobilisé dans le revêtement. Les biocapteurs de 3^e génération n'ont pas été envisagés ici étant donné qu'un tel transfert d'électron sans médiateur se révèle impossible pour l'immense majorité des enzymes. Ce point est discuté dans le chapitre II de cette thèse.

I.2 Objectifs du projet

Après avoir réalisé une revue de la littérature, nous avons décidé d'élargir le procédé d'électro-réticulation aux assemblages enzymes/nanoparticules d'or (AuNPs) en utilisant la chimie des catéchols (Figure 1.a). La présence d'AuNPs a permis d'augmenter la surface électro-active de l'électrode et donc à priori la sensibilité du biocapteur. La synthèse colloïdale des AuNPs a été réalisée par réaction spontanée d'un sel d'or avec de l'acide tannique, molécule naturelle et abondante porteuse de groupements gallols. Les gallols ont des propriétés chimiques similaires aux catéchols. Ainsi, les groupements gallols, présent en surface des nanoparticules, ont été oxydés par électrochimie afin de réagir avec les amines primaires des enzymes (lysines) en formant des bases de Schiff et des adduits de Michael (Figure 1.b).

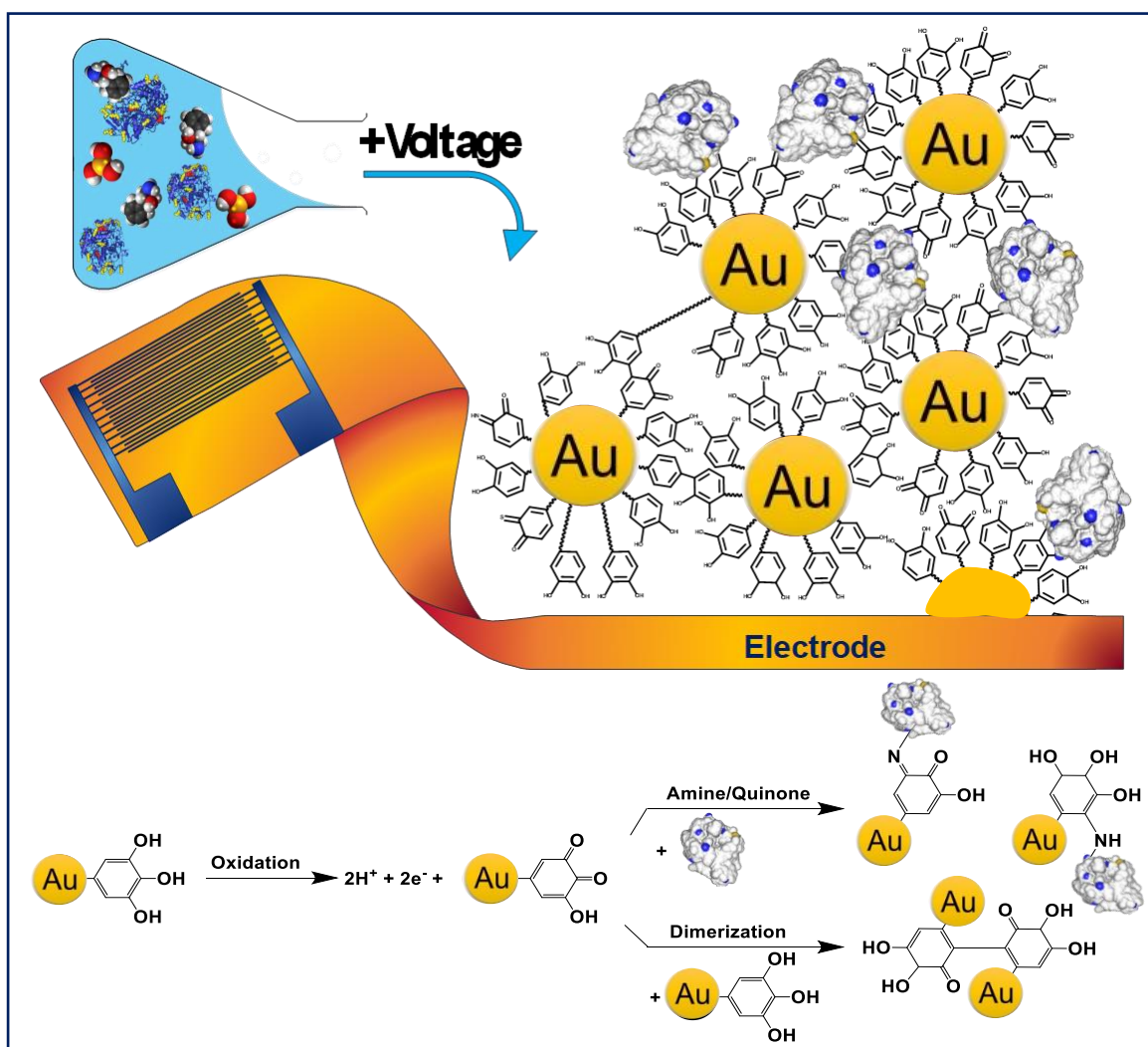


Figure 1 : (a) Représentation schématique du revêtement enzymes/nanoparticules d'or obtenu par électrodéposition. (b) Principe d'électro-réticulation des enzymes avec les nanoparticules ou des nanoparticules entre elles

II. Résumé des résultats obtenus

Lors de la première année, nous avons souhaité remplacer le biscatéchol synthétisé au laboratoire par une alternative commerciale. Ce biscatechol nécessite trois étapes de synthèse et présente des problèmes de solubilité. Comme alternative, nous avons principalement utilisé l'acide tannique (TA), un composé bio-sourcé et peu onéreux (~10 centimes d'euro par gramme). Ce composé possède des fonctions gallols qui ont la même réactivité que les fonctions catéchols. D'autres polyphénols tels que l'acide gallique, l'acide rosmarinique, l'acide nordihydroguaiarétique et la dopamine ont également été testés. L'acide tannique a donné les résultats les plus prometteurs et sont discutés dans cette thèse. Le système GOx/TA@AuNPs a été choisi comme système modèle afin de comparer nos résultats à ceux obtenus précédemment dans l'équipe. De plus, la détermination du taux de glucose présente un intérêt médical et industriel majeur (près de 10% de la population mondiale souffre de diabète et 7 millions en meurent chaque année).⁷ La figure 2 résume l'analyse séquentielle qui a été menée au cours de ces trois années.

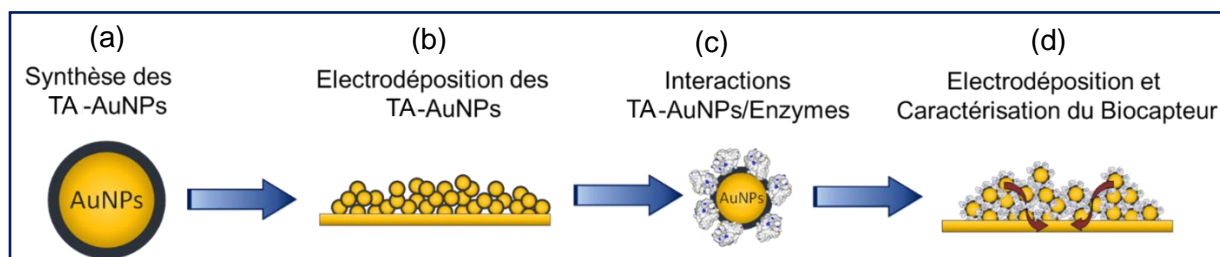


Figure 2: Analyse séquentielle du système GOx/TA@AuNPs/Médiateur/Electrode

II.1 Synthèse des nanoparticules

Bien qu'une synthèse *in-situ* des nanoparticules soit envisageable, l'ensemble des travaux s'est centré sur l'utilisation de TA@AuNPs synthétisées *ex-situ* (Figure 2.a) puis mélangées avec la GOx (Figure 2.c). La synthèse des nanoparticules se base sur la réduction d'un sel d'or Au(III) par l'acide tannique qui joue également le rôle de ligand anionique pour la stabilisation des solutions colloïdales (Figure 3.a). Certaines publications ont montré que les interactions GOx/nanoparticules changeaient avec le rayon de courbure des NPs^{8,9}. Nous avons ainsi synthétisé et étudié différentes tailles de TA@AuNPs comprises entre 4 et 40 nm. Lors de la synthèse colloïdale, les concentrations, pH, vitesse d'addition, force ionique ont été ajustées

afin d'obtenir différentes tailles de nanoparticules. Les nanoparticules NP12 avaient une taille centrée autour de 10-12 nm et un écart-type de 2 nm (Figure 3.b-c).

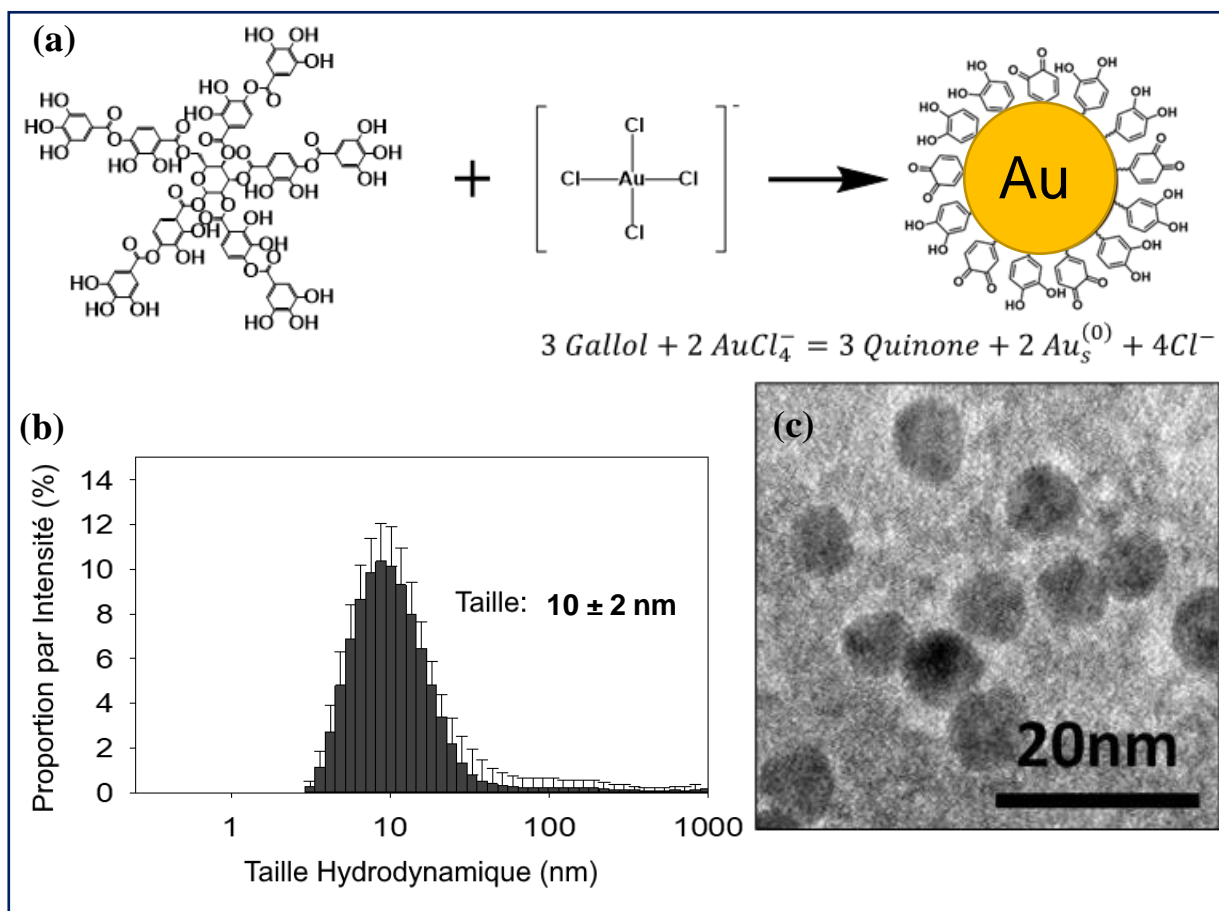


Figure 3: (a) Synthèse des nanoparticules TA@AuNPs. (b) Analyse en diffusion de la lumière de la répartition en taille des nanoparticules de 12 nm et (c) image de microscopie électronique en transmission de mêmes nanoparticules.

II.2 Electrodéposition des nanoparticules seules

L'électro-réticulation des nanoparticules seules a été réalisée en utilisant la réaction des gallols avec les gallols oxydés (Figure 1.b). Cette étude avait pour objectif de démontrer la faisabilité d'un dépôt électro-contrôlé avec l'acide tannique. Le ferrocène methanol (FcOH) a été utilisé comme médiateur avec les systèmes TA/FcOH et TA@AuNPs/FcOH pour mettre en évidence une réaction de type réaction électrochimique catalysé par le ferrocène. Dans ce procédé, le FcOH, oxydé à chaque cycle de volta-ampérométrie cyclique, diffuse et réagit ensuite avec les gallols des nanoparticules dans une certaine couche limite à proximité de l'électrode. Cette

réaction induit un électro-dépôt des TA@AuNPs (autour de $5 \mu\text{g}\cdot\text{h}^{-1}$) et différentes tailles peuvent être déposées (7, 10 et 40 nm). La figure 4.b montre le dépôt obtenu pour des nanoparticules de 10 nm au microscope électronique à balayage (MEB). Ces films sont denses et constitués d'un nombre limité de couches de nanoparticules. Les résultats pour les autres 1 tailles sont dans le chapitre IV de cette thèse.

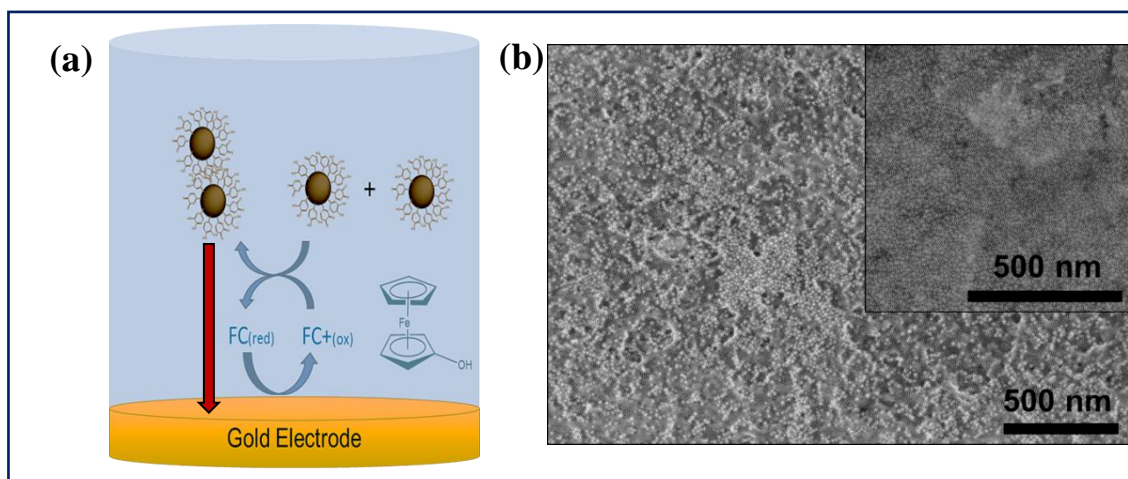


Figure 4 : Electrodeposition des nanoparticules seules. (a) Principe de l'électro-réticulation des TA@AuNPs utilisant le FcOH comme médiateur électrochimique. (b) Image de microscopie électronique à balayage de TA@AuNPs électro-réticulées.

II.3 Interactions enzymes/nanoparticules

Une fois l'électro-réticulation des TA@AuNPs validée, nous avons d'abord étudié les interactions TA@AuNPs avec la glucose oxydase (GOx) et la peroxidase (HRP). En effet, les polyphénols en solution sont connus pour altérer l'activité des enzymes en complexant/réagissant fortement avec elles.¹⁰ Cette inhibition est soit causée par une dénaturation de l'enzyme, soit due à une inaccessibilité du substrat au site catalytique de l'enzyme (couche imperméable).¹¹ C'est d'ailleurs la raison pour laquelle la chimie des polyphénols n'est pas beaucoup exploitée dans le domaine des biocapteurs enzymatiques mais qu'une petite communauté s'y intéresse en tant que médicament plus ou moins ciblé de protéines impliquées dans des cancers¹² ou des infections virales¹³. Nous avons montré que l'inhibition des enzymes était limitée lorsque l'acide tannique se retrouvait uniquement immobilisé en surface des nanoparticules (nanoparticules lavées). Dans le cas de la HRP, les enzymes immobilisées en surface des TA@AuNPs sont 100% actives quel que soit le ratio enzyme/nanoparticules (Figure 5.a).

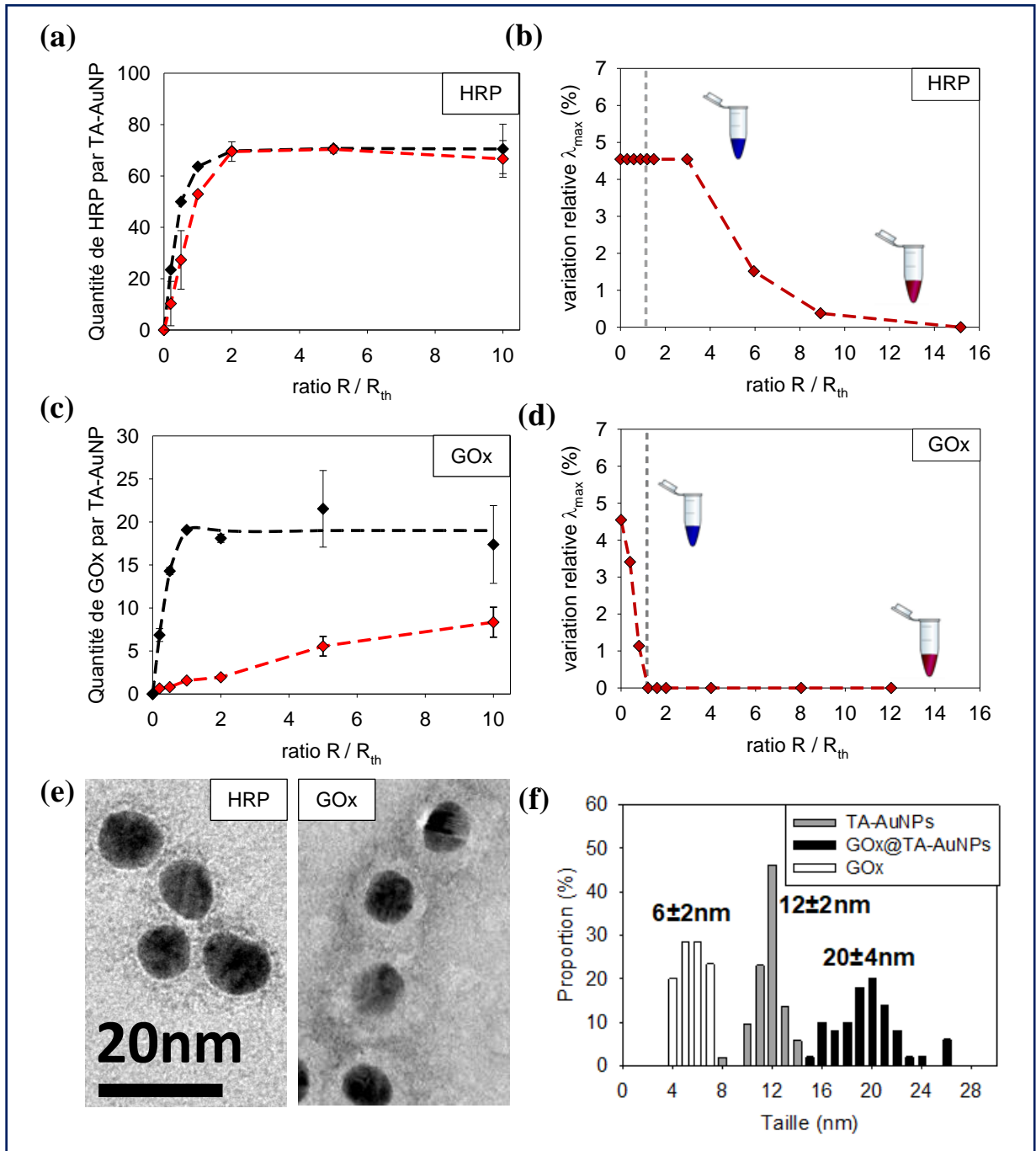


Figure 5: Caractérisation des complexes enzymes/TA@AuNPs, avec les nanoparticules de 12 nm. Test de floculation des HRP/TA@AuNPs (a) et des GOx/TA@AuNPs (c) à différents ratios dans une solution fortement saline à 1 M NaCl. Quantité d'enzyme (courbe noire) et test d'activité (courbe rouge) des complexes HRP/TA@AuNPs (b) et GOx/TA@AuNPs (d). (e) Images de microscopie électronique en transmission des HRP/TA@AuNPs et GOx/TA@AuNPs en présence d'acétate d'uranyle comme agent de contraste. (f) Analyse de la dispersité en taille du système GOx/TA@AuNPs obtenue sur les images de microscopie électronique en transmission.

Dans le cas de la GOx, l'inhibition causée par l'adsorption des enzymes à la surface des TA@AuNPs est entre 90 et 65%, diminuant fortement lorsque le ratio enzyme/TA@AuNPs en solution augmente (Figure 5.c). Cela suggère qu'à forte concentration d'enzyme, une organisation différente de la GOx autour des nanoparticules est obtenue.¹⁴ En utilisant les NP12, le ratio maximal d'enzymes adsorbées sur les TA@AuNPs est de 20 pour la GOx et de 70 pour la HRP. Cela correspond à environ une fois et deux fois le ratio théorique d'une monocouche pour la GOx et la HRP, respectivement. Dans le cas de la HRP, un ratio enzyme/TA@AuNPs, correspondant à 14 fois la monocouche théorique, est nécessaire pour empêcher la floculation des NPs. Cela suggère que la couche enzymatique est extrêmement fine ou incomplète. Cette analyse est confirmée par les images de microscopie électronique en transmission. L'acétate d'uranyle, agent de contraste utilisé, n'a pas permis d'observer la couche de HRP alors qu'il confirme la présence d'une monocouche de GOx (~ 6 nm) sur les TA@AuNPs (Figure 5.e-f).

II.4 Electro-réticulation des complexes enzymes/TA@AuNPs

L'électro-réticulation du mélange GOx/TA@AuNPs/FcOH a ensuite été réalisée à un potentiel fixe de 0.7 V (vs Ag/AgCl) sur des électrodes d'or. L'importance de chacun des composants a été vérifiée. Ainsi, les masses déposées du système GOx/TA@AuNPs/FcOH étaient plus élevées en comparaison des systèmes TA@AuNPs/FcOH et TA@AuNPs/GOx (Figure 6.a). Différents paramètres ont ensuite été optimisés tels que le temps et le pH du mélange ou encore la concentration des trois composés. Cette optimisation a été réalisée en cherchant à accroître la sensibilité du revêtement obtenu. Les films construits à faible pH ($\text{pH} < 6$) ne permettaient pas d'obtenir un film robuste, à $\text{pH} > 8.5$ le film devenait très robuste mais la sensibilité chutait drastiquement (données non présentées ici). Par la suite, toutes les expériences ont été réalisées au pH natif du mélange autour de 7. Pour la durée d'application du potentiel électrique, une déposition de 10 minutes conduit à une sensibilité inférieure en comparaison à 30 minutes. Au-delà de 30 minutes, les sensibilités étaient similaires. Nous avons donc fixé un temps de dépôt d'une heure pour tous les échantillons. Le mélange optimisé comprenait $\sim 2 \mu\text{M}$ de TA@AuNPs d'une taille de 10-12 nm, $\sim 5 \mu\text{M}$ GOx, 5 mM FcOH et 50 mM NaCl et donnait une vitesse de dépôt en masse autour de $10\text{-}15 \mu\text{g}\cdot\text{h}^{-1}$. Les images de microscopie électronique en transmission des dépôts confirment la formation d'un film homogène d'enzymes/TA@AuNPs (Figure 6.b). Des films robustes ont été obtenus avec aucune perte enzymatique au cours du temps de

stockage ou en présence de surfactant. De plus, les dépôts enzymes/nanoparticules ont été obtenus avec un excellent contrôle spatial sur des microélectrodes de 10 μm de large. La figure 6.c illustre la co-localisation des nanoparticules observées en champ clair avec la GOx-Rhod, enzyme covalamment marquée à la rhodamine B (sonde fluorescente).

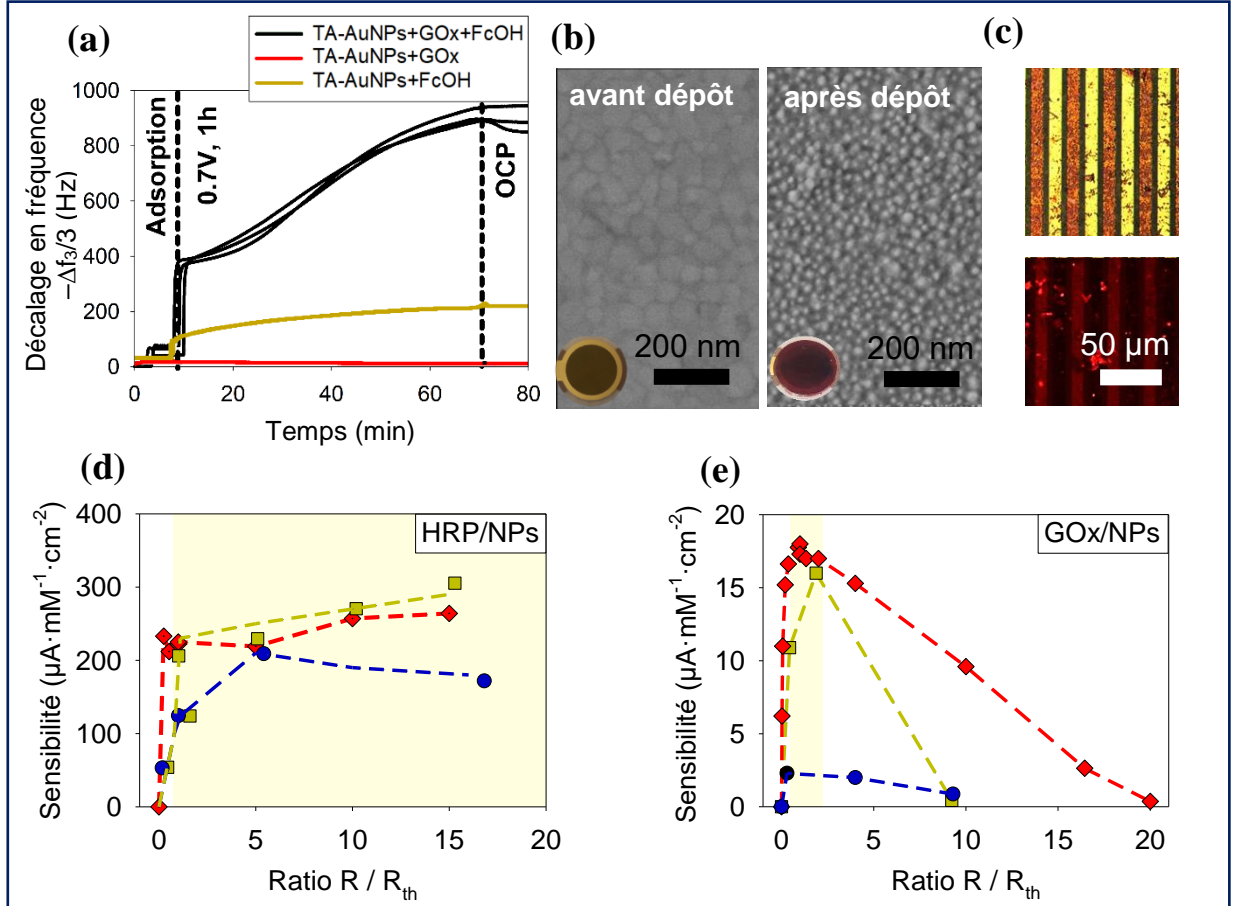


Figure 6: Electro-réticulation des complexes enzymes/nanoparticules. (a) Evolution de la fréquence de résonance, mesurée par QCM, en fonction du temps des mélanges GOx/TA@AuNPs/FcOH (3 courbes noires), TA@AuNPs/FcOH (courbe jaune) et GOx/TA@AuNPs (courbe rouge). (b) Images de microscopie électronique à balayage du cristal de QCM avant (gauche) et après électro-réticulation du mélange GOx/TA@AuNPs/FcOH (droite). (c) Images en microscopie optique en champ clair (haut) et en fluorescence (bas) après électro-réticulation du mélange GOx-Rhod/TA@AuNPs/FcOH sur des électrodes interdigitées de largeur 10 μm . Evolution de la sensibilité des revêtements obtenus pour la GOx (d) et la HRP (e) en fonction du ratio enzyme/nanoparticules et pour différentes tailles de nanoparticules : 7 nm (jaune), 11 nm (rouge) et 40 nm (bleu).

Le ratio enzyme/nanoparticules a un impact important sur la sensibilité du biocapteur obtenu. Dans le cas de la HRP, une augmentation de la sensibilité est observée lorsque la quantité d'enzyme augmente dans la solution électrodéposée jusqu'à atteindre un plateau à partir du ratio théorique d'une monocouche (Figure 6.d). Une légère augmentation est observée au-delà de ce ratio pour les nanoparticules les plus petites (7 et 11 nm). Dans le cas de la GOx, une augmentation de la sensibilité est également observée jusqu'au ratio théorique de la monocouche (R_{th}) mais diminue drastiquement au-delà. Une concentration trop faible en enzyme limite l'activité globale du film (nanoparticules faiblement couvertes) et un ratio GOx/TA@AuNPs trop important limite l'électroréticulation à cause d'une couronne d'enzyme trop dense empêchant l'activation des catéchols ou leur accessibilité. Cette observation est corroborée par une plus faible masse déposée pour les GOx/TA@AuNPs à des valeurs élevées en ratio enzyme/nanoparticules. Cette baisse de sensibilité est confortée par les images de microscopie électronique en transmission (figure 5.e). Concernant la GOx, la taille des NPs joue un rôle déterminant. La sensibilité avec la GOx est meilleure pour les petites nanoparticules et un optimum est observé pour les NPs de 10-12 nm (Figure 6.d). Pour les NPs 30 et 40 nm, une chute drastique de cette sensibilité est observée ce qui n'est pas le cas pour la HRP.

En électrodéposant la solution au ratio théorique enzyme/nanoparticules d'une monocouche, les biocapteurs à glucose ont une sensibilité 25 fois supérieures aux films sans TA@AuNPs et une limite de détection 50 fois inférieure au système développé avec le biscatéchol en 2018.⁵ Ces biocapteurs ont montré une réponse stable même après 14 jours d'opération à température ambiante et une gamme de linéarité intéressante pour des mesures dans différents fluides biologiques (sang, urine...).

II.5 Extension du procédé sur électrode souple et immobilisation simultanée du médiateur utilisé.

Les difficultés liées à la sensibilité étant maintenant résolues par l'utilisation de nanoparticules, nous avons ensuite cherché à résoudre deux autres problèmes majeurs pour une application in-situ: l'utilisation de médiateurs libres en solution ainsi que l'utilisation d'électrodes rigides. Dans le cadre du projet BioSensDress, nous souhaitons développer des pansements souples capables de mesurer des biomarqueurs d'intérêts dans le liquide des plaies chroniques. Une

électrode souple permet d'épouser la forme de la plaie et de s'adapter aux mouvements du patient. Nous avons ainsi utilisé comme électrode de travail des membranes de polyuréthane électrospinnées recouvertes par quelques couches de graphènes, développées par Anne Hébraud, Jean-Mario Nhut (ICPEES) et Housseinou Ba (BlackLeaf©).

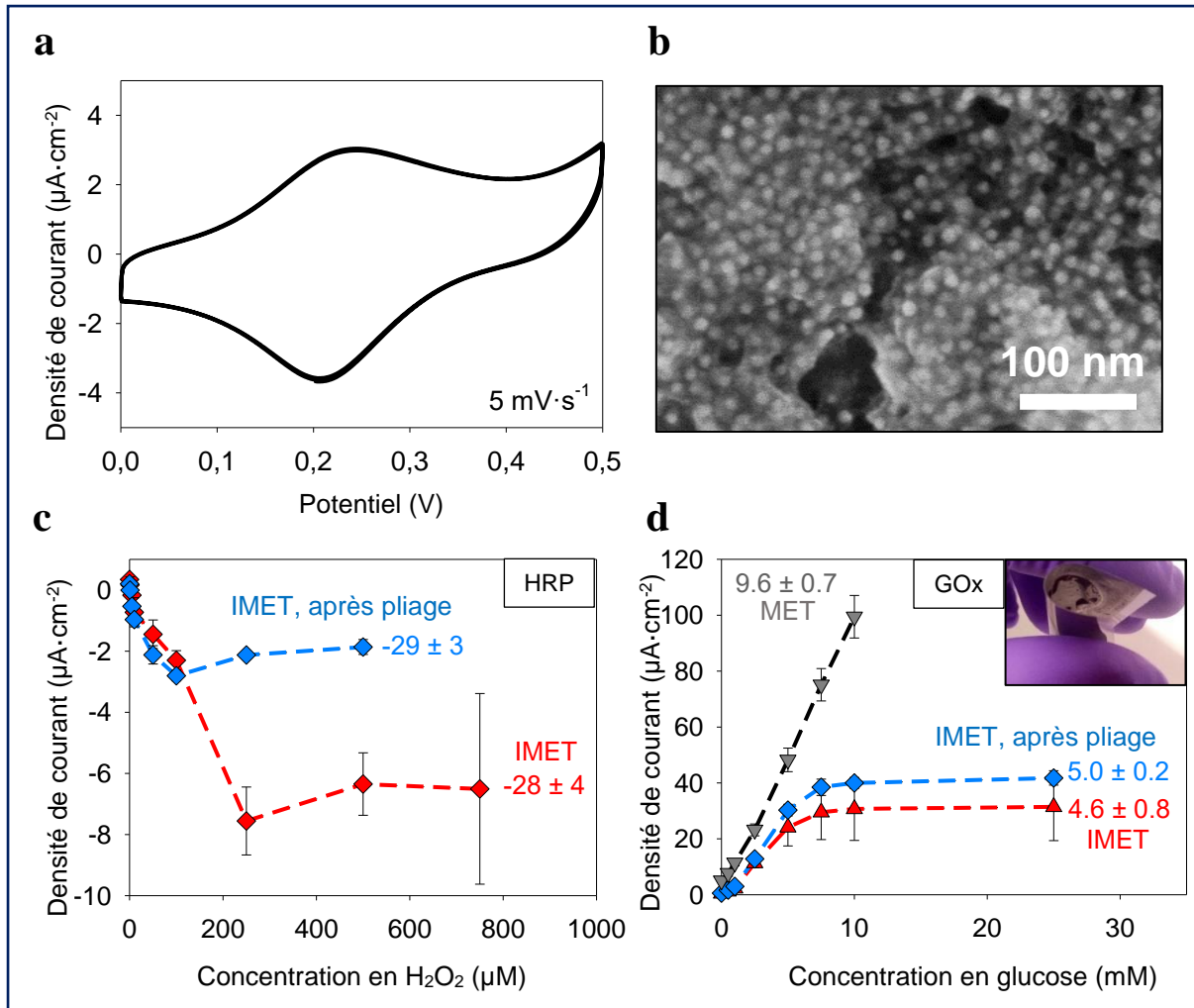


Figure 7: Electroréticulation des complexes enzymes/nanoparticules sur des membranes de polyurethane électrospinnées recouvertes de graphènes (PU-FLG) avec immobilisation du ferrocène. (a) Observation des pics redox du ferrocene immobilisé utilisés pour la détection du glucose ou du peroxyde d'hydrogène. (b) Image de microscopie électronique à balayage d'un revêtement GOx/TA@AuNPs électrodéposé sur membrane PU-FLG. Sensibilité des films obtenus pour HRP/TA@AuNPs (c) et GOx/TA@AuNPs (d) avant et après une série de 100 flexions de la membrane.

Ces membranes se sont révélées hautement conductrices avec une capacité intéressante de rétention du ferrocène par simple adsorption sur la couche de graphène. Après élimination du ferrocène non adsorbé, les pics redox du ferrocène sont clairement visibles (Figure 7.a) avec $1.4 \pm 0.2 \text{ nmol}\cdot\text{cm}^{-2}$ de ferrocène immobilisé. Des morphologies similaires à celles obtenues sur les électrodes d'or rigides ont été observées pour les revêtements HRP ou GOx/TA@AuNPs sur PU-FLG (Figure 7.b). L'influence du pliage sur la sensibilité au glucose ou au H_2O_2 a été quantifiée pour les deux revêtements (Figure 7.c-d). La sensibilité diminue légèrement avec la déformation de la membrane. Des problèmes de stabilité dans le temps ont néanmoins été observés avec une perte drastique du ferrocène adsorbé après trois jours. La sensibilité obtenue avec le médiateur immobilisé est environ deux fois plus faible qu'avec le médiateur libre en solution. Cette baisse reste très raisonnable comparativement à la faible concentration en médiateur adsorbé. La gamme de linéarité obtenue est satisfaisante pour la détection du glucose et H_2O_2 à leurs concentrations typiques dans une plaie et l'analyse de l'état d'une plaie (infection, inflammation, guérison...) peut ainsi être évalué.

II.6 Limites et perspectives

En l'état, des améliorations sur l'immobilisation du ferrocène doivent encore être réalisés. Une immobilisation covalente sur un graphène activé ou une adsorption plus forte en utilisant du biphenylferrocene sont à envisager. Plusieurs applications pourront ensuite être abordées :

- (1) Le diagnostic médical et la compréhension spatio-temporelle de processus biologiques via la détection d'analytes d'intérêts. Les systèmes envisagés sont la détection des infections bactériennes (acide urique en immobilisant l'uricase) et la compréhension de maladies neuro-biologiques (acétylcholine en immobilisant une couple choline esterase/acétylcholine esterase).
- (2) La recherche automatisée de nouveaux médicaments/biomarqueurs (recherche d'inhibiteurs de l'acétylcholine estérase pour le développement de médicaments contre l'Alzheimer).
- (3) La production d'électricité avec les biopiles enzymatiques, à base de glucose oxydase, pour des applications in vivo de faible puissance (neurostimulateurs, implants cochléaires,...).

III. Valorisation des travaux

III.1 Publications scientifiques

Un premier article concernant le principe d'électro-réticulation sur les biocapteurs à glucose basé sur les complexes GOx/TA-AuNPs a été publié en open-access chez Materials Advances (Savin R et al. Mater. Adv. 2022, 3, 2222). Sur ce premier travail, présenté dans le Chapitre III, l'accent a été porté sur la faisabilité du procédé d'électroréticulation. Ce procédé a permis de déposer de façon localisée et contrôlée des nanoparticules en associations avec des enzymes. En plus du contrôle spatio-temporel lors du dépôt des complexes enzymes/nanoparticules, les avantages de cette méthode sont : (i) un procédé en une seule étape sans modification préalable des enzymes, (ii) un dépôt robuste qui présente une haute réponse enzymatique stable pour au moins deux semaines à température ambiante et (iii) une versatilité qui permet d'adapter le processus à un large panel d'enzymes. Un second papier a été soumis chez Molecules (MDPI) pour leur numéro spécial consacré à la conception et à la nano-organisation des matériaux fonctionnels (Advances in Nanomaterials Design and Nanoarchitectonics of Functional Materials). Cet article prolonge les travaux publiés précédemment et permet une comparaison détaillée entre deux biocapteurs d'intérêts : le biocapteur à glucose avec les revêtements GOx/TA@AuNPs et le biocapteur à peroxyde d'hydrogène avec les revêtements HRP/TA@AuNPs. Une optimisation systématique de ces deux revêtements a été proposée en regardant l'influence de la taille des nanoparticules d'or ainsi que du ratio enzymes/nanoparticules. La compréhension de ces mécanismes constitue le cœur de ce second papier dont les résultats sont détaillés dans le chapitre IV. Un troisième papier est envisagé suite à la collaboration avec l'ICPEES sur des pansements intelligents (collaboration avec Dr Anne Hebraud, Dr Sergey Pronkin, Housseinou Ba et Jean-Mario Nhut).

III.2 Communications orales

Avec le contexte sanitaire, une seule communication orale a été effectuée concernant ces travaux. Cette présentation en anglais s'est tenue à Nice au congrès scientifique: « Nature Inspires Creativity Engineers » centré sur les matériaux bio-inspirés et bio-sourcés. La présentation était intitulée « Electro-cross-linking of enzymes/gold nanoparticles based polyphenols: a mussel-inspired tool for enzymatic biosensors manufacturing » et portait sur les travaux du Chapitre III de cette thèse.

IV. À propos des formations

IV.1 Formations Scientifiques

Intitulé	Code Amethis	Nombre d'heures	Date de validation
Introduction to Numerical Simulations and High Performance Computing: From Materials Science to Biochemistry	ST-ED182-FHC-4	12 h 1 module	janvier 2019
ED182 - Surfactant Self-Assembly in Bulk and at Interfaces	ST-ED182-FHC-8	16 h 1 module	mai 2019
ED182 -Near Field Probes for the Nanosciences	ST-ED182-FHC-8	14 h 1 module	mai 2019
Web conference : Physics-Biology interface	Hors Catalogue	1 h 30	2020

IV.2 Formations Transversales

Intitulé	Code Amethis	Nombre d'heures	Date de validation
Congrès Matériaux	Hors Catalogue	2 x 4 h	novembre 2018
A.17. Propriété Industrielle : protégé par le brevet	ST-COL-MR-18	3 h	novembre 2018
A.18. Propriété intellectuelle : quels droits visés ? Quel titulaire ? Comment et pourquoi protéger ? Comment valoriser ?	ST-COL-MR-19	3 h	novembre 2018
D.7. Formation 1er Secours PSC1	ST-COL-AFT-7	8 h	janvier 2019
C.10. Création d'entreprise, comment élaborer un business plan ?	ST-COL-PP-9	18 h	janvier 2019
A.1. Charte de déontologie des métiers de la Recherche	ST-COL-MR-1	3 h	mai 2019
MOOC "Intégrité scientifique dans les métiers de la recherche	ST-COL-MR-45	10 h	juillet 2019

D1 – Concevoir et animer son enseignement par classe inversée	Hors Catalogue IDIP (B04 Cycle D)	3 h 30	novembre 2020
D2 – Initier une pédagogie par projet	Hors Catalogue IDIP (B04 Cycle D)	3 h 30	novembre 2020
D5 – Organiser et accompagner le travail en groupe	Hors Catalogue IDIP (B04 Cycle D)	3 h 30	novembre 2020
F1 – Favoriser le développement des compétences transversales par les étudiants	Hors Catalogue IDIP (B06 Cycle F)	3 h 30	novembre 2020
H1 – Noter avec pertinence et équité les travaux des étudiants	Hors Catalogue IDIP (B08 Cycle H)	3 h 30	novembre 2020
J2 – Evaluer les compétences des étudiants	Hors Catalogue IDIP (B10 Cycle J)	3 h 30	décembre 2020
A.27. Partenaires Scientifiques pour la classe (PSC/ASTEP)	Hors Catalogue	36 h	juillet 2021
Fête de la Science	Hors Catalogue	8 h	Octobre 2021
Ouvrir un Blog Scientifique	Hors Catalogue URFIST	3 h 30	Novembre 2021
	Total	> 100 h	-

V. Références

- (1) Davis, F.; Higson, P. J. Biofuel Cells — Recent Advances and Applications. **2007**, 22, 1224–1235.
- (2) Bodovitz, S.; Joos, T.; Bachmann, J. Protein Biochips: The Calm before the Storm. *Drug Discovery Today*. **2005**, 10 (4) 283–287.
- (3) Lee, H.; Dellatore, S. M.; Miller, W. M.; Messersmith, P. B. Mussel-Inspired Surface Chemistry for Multifunctional Coatings. *Science* (80-.). **2007**, 318 (5849), 426–430.
- (4) Maerten, C.; Jierry, L.; Schaaf, P.; Boulmedais, F. Review of Electrochemically Triggered Macromolecular Film Buildup Processes and Their Biomedical Applications. *ACS Appl. Mater. Inter.* **2017**, 9 (34), 28117–28138.
- (5) El-Maiss, J.; Cuccarese, M.; Lupattelli, P.; Chiumminto, L.; Funicello, M.; Schaaf, P.; Boulmedais, F. Mussel-Inspired Electro-Cross-Linking of Enzymes for the Development of Biosensors. *ACS Appl. Mater. Inter.* **2018**, 10 (22), 18574–18584.
- (6) Fasman, G. D. *Handbook of Biochemistry and Molecular Biology*; Francis, T. &, Ed.; Abingdon-on-Thames (United Kingdom), **2019**.
- (7) Diabetes around the world in 2021 <https://diabetesatlas.org/> (accessed 2022 -01 -28).
- (8) Seehuber, A.; Dahint, R. Conformation and Activity of Glucose Oxidase on Homogeneously Coated and Nanostructured Surfaces. *J. Phys. Chem. B* **2013**, 117 (26), 6980-6989.
- (9) Malel, E.; Mandler, D. Direct Electron Transfer between Glucose Oxidase and Gold Nanoparticles; When Size Matters. *ChemElectroChem* **2019**, 6 (1), 147–154.
- (10) Hagerman, A. E. Fifty Years of Polyphenol-Protein Complexes. In *Recent Advances in Polyphenol Research*; **2012**.
- (11) Mole, S.; Waterman, P. G. Tannic Acid and Proteolytic Enzymes: Enzyme Inhibition or Substrate Deprivation? *Phytochemistry* **1986**, 26, 99–102.
- (12) Tanimura, S.; Kadomoto, R.; Tanaka, T.; Zhang, Y. J.; Kouno, I.; Kohno, M. Suppression of Tumor Cell Invasiveness by Hydrolyzable Tannins (Plant Polyphenols) via the Inhibition of Matrix Metalloproteinase-2/-9 Activity. *Biochem. Biophys. Res. Commun.* **2005**, 330 (4), 1306–1313.
- (13) Chen, C. N.; Lin, C. P. C.; Huang, K. K.; Chen, W. C.; Hsieh, H. P.; Liang, P. H.; Hsu, J. T. A. Inhibition of SARS-CoV 3C-like Protease Activity by Theaflavin-3,3'- Digallate (TF3). *Evidence-based Complement. Altern. Med.* **2005**, 2 (2), 209–215.

- (14) Wang, Y.; Jonkute, R.; Lindmark, H.; Keighron, J. D.; Cans, A.-S. Molecular Crowding and a Minimal Footprint at a Gold Nanoparticle Support Stabilize Glucose Oxidase and Boost Its Activity. *Langmuir* **2019**, *36*, 37–46.

General introduction

Electrochemistry is the typical science field that deals with the relationship between electrical currents and chemical reactions. Two main categories are generally described: galvanic and electrolytic processes. In a galvanic process, a chemical reaction spontaneously happens and generates an electrical current that is collected by the cell. On the contrary in an electrolytic cell, a current source triggers electrochemical reactions. In both cases, capacitive changes (charges accumulation/depletion) and electron exchanges (redox reactions) take place at the interface between a media (liquid/solid/gas) and a working electrode as further detailed in Chapter I & II. In the following manuscript, an electrode will be defined as a solid material able to conduct the electric current whose function is either to apply an electrical signal to the environment (through a generator) or to collect it from the electrochemical reaction (collector). Electrochemical galvanic cells allow producing electricity with battery-like and fuel cells devices or screen the surrounding environment of the electrode to retrieve valuable information about the physicochemical state of the medium (sensors). It is also one of the most powerful bioanalytical tools to study how electrons flow in the biological living systems (enzymatic respiratory and photosynthetic chains¹). Electrochemical electrolytic cells are of industrial interest to produce purified materials such as aluminium², exfoliated graphene³, chlorine/hydroxide/bleach/H₂/O₂/H₂O₂ (chloralkali⁴ and water electrolysis processes), adiponitrile⁵ in nylon production, or aldehyde/alcohol/carboxylic acid from CO₂ valorization⁶ among others chemicals. All these electro-generated species can either be used as a fuel, a sanitizer, or a synthesis reagent. Electrolytic cells are also used to electroplate/electro-engrave thin coatings onto electrodes with specific surface properties, such as corrosion passivation⁷ (polymeric paints and oxide layers) or with a micro-scale morphology for hydrophobicity⁸, electrocatalysis^{9,10}, entrapment¹¹, and optical^{12,13,14} properties.

Bioelectronics is another wide and very promising topic defined thirty years ago¹⁵ as the use of biological materials and bio-inspired architectures for the development of information processing systems, sensors and actuators, and molecular manufacturing with a bottom-up approach (self-assembly). The junction between bioelectronics and electrochemistry, i.e. the enzyme based coating, will be the restricted research area explored in this thesis. Around 150,000 proteins are currently known among which 17-20% are oxido-reductases enzymes (PDB website¹⁶). The lecturer could have a look at Roche Metabolic Pathways¹⁷ to be

convinced how redox enzymes cascades are predominant in biological life. Based on this statement and the fact that redox enzymes are particularly well suited for electron-exchange with bioelectronics devices, redox enzymes will be mainly discussed. Independently of the applications, the electrode coatings based on biomolecules tend to become more and more complex to achieve electrical wiring, specificity and efficiency. Indeed to reach high reactivity and large active surface area, different components are commonly used such as metallic nanoparticles, conducting polymers, carbon based materials (graphite, graphene, etc...) and many others materials (porous electrode, metal oxide frameworks, etc...). However, the multiplicity of the components in the overall mixture make it very difficult to analyze.

With the development of a new electrodeposition method, my host team designed an enzymatic biosensor based on the mussel-inspired electro-cross-linking of enzymes using a catechol-based organic cross-linkers. The electric signal imposed on the working electrode allowed the electro-oxidation of catechol into quinone followed by its cross-linking with the enzymes. The sensitivity of the developed biosensor was similar to the ones obtained by drop-casting using glutaraldehyde.¹⁸

My thesis aimed to improve the sensitivity of the enzymatic biosensor obtained by mussel-inspired electro-crosslinking using natural polyphenol. The strategy was based on the use of tannic acid to synthesize gold nanoparticles and use them as cross-linker. Two transversal issues encountered for all bioelectrochemical devices have been tackled: **(1)** how to efficiently deposit enzymes onto small electrodes to design micro-sensors or lab-on-a-chip devices and **(2)** how to reach the greatest spatial organization of the different components in order to achieve the optimal electrocatalytic properties. The latter often embedded behind the term “nanoarchitectonics” in the literature is of critical importance as the electrical wiring of redox enzymes and electrode is not trivial.^{19,20}

The Ph.D. manuscript is divided into five chapters. **Chapter I** details the emerging opportunities in bioelectronics. An extensive but non-exhaustive list of concerned devices is described such as biosensor, biofuel cell, lab-on-a-chip, enzymatic logic gate and biocatalytic support for industrial purposes. **Chapter II** gathers the information on the materials and methods used during the Ph.D.

Chapter III deals with the development of a nanohybrid enzymatic biosensor using glucose oxidase (GOx), 12 nm tannic acid capped gold nanoparticles (TA@AuNPs), and ferrocene methanol (FcOH), as a mediator. The electro-cross-linking of TA@AuNPs/GOx has been proven to obtain an efficient and robust nanohybrid biosensor. The electrocatalytic current

was evaluated upon glucose addition and proven to be suitable for diabetic applications. The process was extended to TA@AuNPs/HRP.

Chapter IV make the critical optimization of TA@AuNPs/GOx and TA@AuNPs/HRP coatings using different enzymes/AuNPs ratio as well as AuNPs size. Differences and similitudes between these two systems enhanced us to draw general guidelines for the electro-triggered deposition of enzyme/nanoparticles complexes.

Chapter V presents the preliminary study of a future smart wound dressing. In collaboration with Anne Hébraud (ICPEES, Strasbourg), the TA@AuNPs/enzyme coating was electrodeposited on a polyurethane membrane, obtained by electrospinning and functionalized by few-layers graphene, (PU-FLG). The major benefit of this new electrode is its flexibility that enhances the development of tissue-like biosensors. To extend the versatility of this new platform for health care application, a pH sensor, a H₂O₂ and a GOx biosensor were developed on the PU-FLG membrane using the mussel-inspired electro-crosslinking process. The influences of the bending and chemical interferences have been evaluated. This type of device will be of crucial importance for the fabrication of multifactorial intelligent dressings in the near future.

The manuscript ends with conclusions and gives some outlooks of the Ph.D work.

Chapter 1

Bibliographic Review

Chapter 1 – Table of Contents

I. Enzymatic bioelectrodes	6
I.1 Bioelectrodes and their applications	6
I.1.1 Electrochemical biosensors	7
I.1.2 Enzymatic biofuel cells	9
I.1.3 Self-powered enzymatic biosensors	10
I.1.4 Enzymatic logic gates.....	12
I.1.5 Smart electro-driven drug release coupled biosensors	13
I.2 Electrochemical biosensor generations	16
I.2.1 Redox-enzyme based biosensors.....	16
I.2.2 Non-redox enzyme-based biosensors	18
II. Mechanisms of the electron transfer towards the electrode.....	21
II.1 Mediated electron transfer biocatalysis.....	22
II.2 Immobilized mediated electron transfer biocatalysis.....	23
II.3 Choice of the mediator	25
II.4 Direct electron transfer biocatalysis	27
II.5 DET and commercial enzymes.....	33
II.6 Glucose oxidase and horseradish peroxidase biosensors	34
III. Electro-triggered enzyme immobilization.....	38
III.1 Enzyme immobilization principles.....	38
III.1.1 Non-covalent adsorption and physical entrapment	38
III.1.2 Covalent attachment and cross-linking	39
III.1.3 Bio-conjugation immobilization	41
III.2 Electro-triggered immobilization strategies	42
III.2.1 Manual vs electro-triggered strategies	42
III.2.2 Electrodeposition of physically entrapped enzymes	43
III.2.3 Electrodeposition of covalently linked enzymes.....	48
III.3 Electrodeposition mechanisms	52
IV. References	55

I. Enzymatic bioelectrodes

I.1 Bioelectrodes and their applications

A bioelectrode is a conducting material that is designed to be at the interface between biological living systems and electronic devices (Figure 1.1).¹ It can either be active by inducing physiochemical changes through electrical signal generation (emitter) or passive by simply monitoring its biological environment (collector). This distinction is somewhere in between the receptor/generator convention in electricity and the galvanic/electrolytic difference as defined in the general introduction.

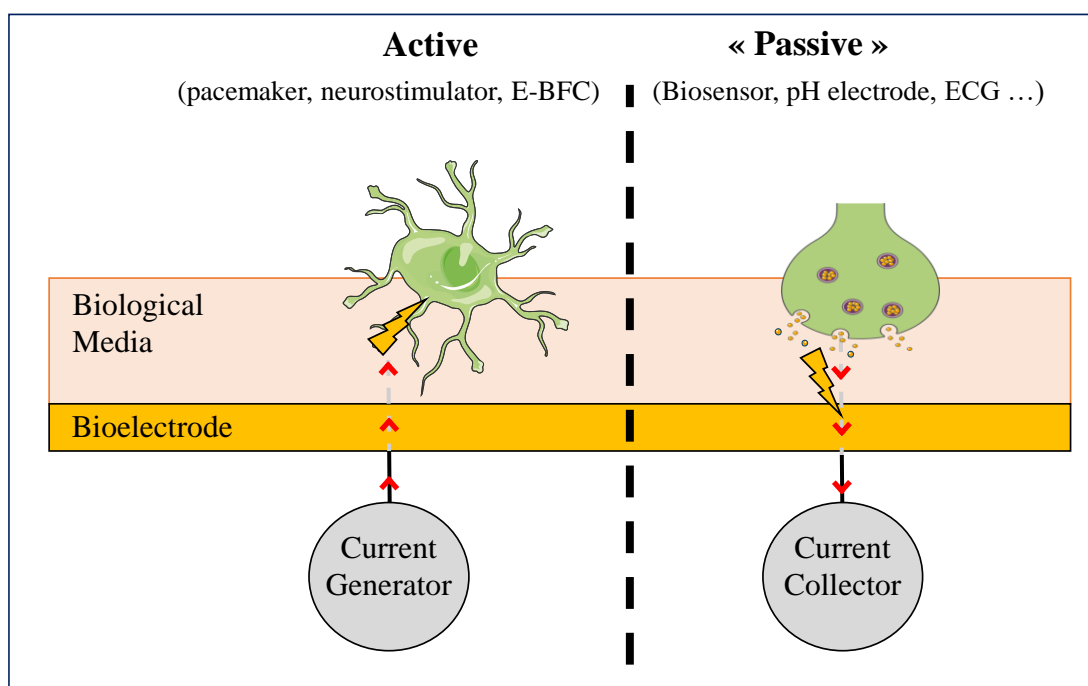


Figure 1.1: Illustration of active and passive bioelectrodes as defined by their interaction with their bioenvironment

The main application of active bioelectrode is the stimulation of tissues in the management of health troubles. Pacemaker² being the oldest example of an active bioelectrode, new applications emerged such as for neurological disorders. For example, hypothalamus electrostimulation was found beneficial for patients suffering from Alzheimer, Parkinson diseases and addictions.³ Bioelectrode is also an emerging tool for skin and bone regeneration since cell migration and proliferation are greatly enhanced by external electrical stimulation.⁴ Also, advances in micro-electromechanical active devices is also promising for electro controlled drug delivery.⁵ Most of these proactive systems can be fueled by a specific type of

bioelectrode called biofuel cell. On the contrary, passive bioelectrodes collect specific signals arising from the surroundings and convert them into electrical interpretable signals. This category gathers all biosensors in its largest definition such as electrocardiograph electrodes that record ionic conduction change, pH electrodes and the wide variety of biochemical sensors that detect many kinds of biomolecules.

1.1.1 Electrochemical biosensors

An electrochemical biosensor is a passive bioelectrode designed to detect a specific analyte in its surrounding. It integrates biological material (enzymes, antibodies, cells...) as recognizing agent and use an electrochemical transducer⁶. Some nanomaterials/organic or inorganic molecules can be incorporated inside the sensitive layer to immobilize the biological material or enhance its communication. Together the electrode and the biosensing layer can be named biosensors (Figure 1.2).

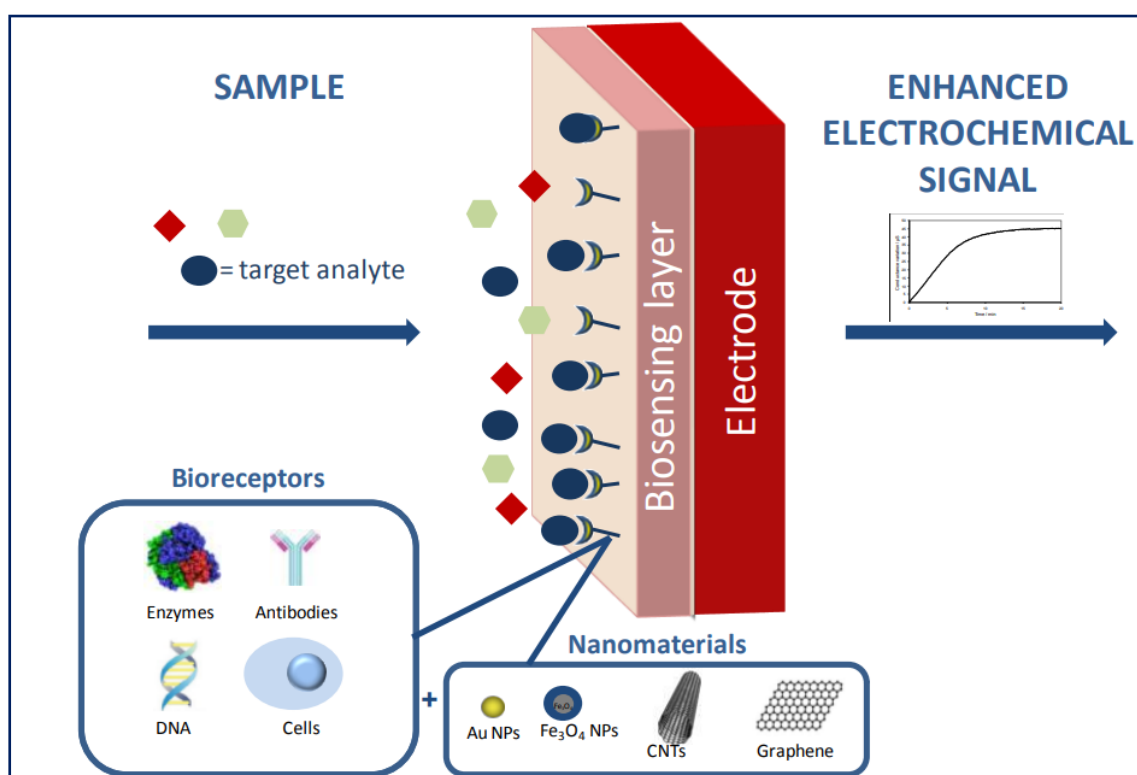


Figure 1.2: Schematic representation of an electrochemical biosensor, according to [2]

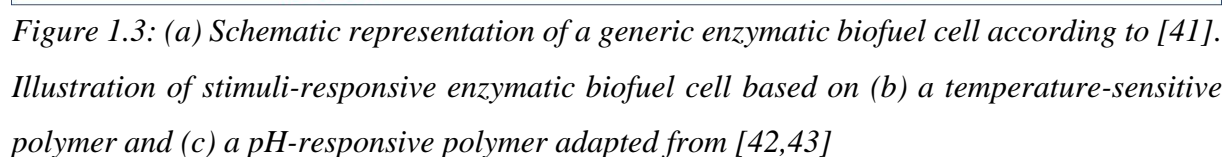
The domains of medicine and the agro-alimentary industry could directly benefit from advances in electrochemical biosensors. Few others, such as bioterrorism or spatial research, could also benefit from this technology⁷. The market is estimated at 33 bn.\$ in 2027⁸ (12 bn.\$ in 2015⁹). The following but not exhaustive list details some possibilities reported in the

literature with a focus on electrochemical biosensors, the most promising ones in terms of miniaturization and real-time monitoring.

By now, health is the most appealing and fruitful field for electrochemical biosensors. The first commercially available biosensor was for diabetics with the monitoring of glucose blood level, being still an expanding market due to the increase of patients and the need for adequate/non-invasive solutions. The monitoring of urea and creatinin¹⁰ is useful to control the efficiency of dialysis or to detect kidneys dysfunctions, which could lead to digestive and neurological issues⁶. The monitoring of cholesterol has been exploited for the detection of hypertension and heart attack¹¹. Almost all neurocognitive diseases are caused by or affect an enzyme (acetylcholine esterase)¹². Parkinson, Alzheimer or dementia treatments have thus taken the advantage of enzymatic biosensors to develop new drugs. Cancer biomarkers (alpha-fetoprotein, many antigens); autoimmune (glycopeptides)¹³ or infectious diseases¹⁴ can be detected with electrochemical biosensors. AIDS (anti-human CD4)¹⁵, Hepatitis B (DNA)¹⁶, urinary infection (anti lactoferrin)¹⁷, influenza (anti hemagglutinin)¹⁸, coronavirus (DNA)¹⁹ are just a few examples of viruses that can be detected with electrochemical biosensors.

In the agro-alimentary industry, many bacteria, viruses¹⁴, toxins or allergens could lead to some risks for humans or others species. Efficient tools to manage these risks coming from a bio-organism or chemical release are needed. The increase of publications on this topic witnesses the rise of interest in this technology. *E. Coli*, known for serious gastro-intestinal issues, can be detected by the measurement of impedance (antibody)²⁰. Acrylamide, a compound caused by food heating, is reported as a carcinogenic substance by the World Health Organization and can be detected using biosensors (haemoglobin adduct)²¹. Enzymatic biosensors were used to determine Bisphenol A concentration in beverages (tyrosinase)^{22–25} and organophosphorus pesticides (acetylcholine esterase)^{26–32} that were widely used in agronomy and cause several neurologic troubles. Their use is a good way to control the correct application of European Standard and also to detect unsung health concerns. The freshness of food (meat, fish and fruits)^{33,34} can be monitored using enzymes such as xanthine oxidase or alcohol dehydrogenase immobilized onto the 'on package' indicator. Devices for real-time quantification of lactose based on β -galactosidase and galactose oxidase provide an interesting way to control the food for people suffering from lactose intolerance^{35,36}. Some sentinel shellfish-coupled biosensors (mussel, oysters) have been developed mainly motivated for agro-alimentary seafood safety. These species are known to accumulate from water heavy metal and sea toxins such as okadaic acid. Protein phosphatases were found to be inhibited by these contaminants and the use of

The first purpose of biofuel cells is to provide electricity through biological redox reactions theoretically as long as the fuel is provided on the same model as a classical fuel cell. The difference lies in the fuel that is used and the nature of the electrode. Enzymatic biofuel cell uses biologically available fuel in body fluids, such as glucose, cholesterol, ethanol and oxygen⁴⁰ (Figure 1.3.a).



These devices are considered to be a ‘greener’ source of energy (largely available in food/drinks). Also, it could be implanted *in-vivo* and work in physiological fluids without additional energetic input. Enzymatic biofuel cells could supply low-power artificial devices and possibly remove the need for further reoperation. Interesting progress has been made on biofuel cells to obtain a switch between a passive and an active mode upon external stimulus. The ON/OFF activation is implemented to produce electricity on demand when a specific external condition is fulfilled and to stop it when it is not required. This can be of great interest for biomedical applications.⁴⁴ Interfacial resistance change through $\text{Cu}^{2+}/\text{Cu}^0$ reduction⁴⁵ or Fe^{II} -cytochrome attraction/repulsion⁴⁶ has been successfully used as a voltage trigger. Temperature⁴² and pH⁴³ switch have also been explored as illustrated in Figure 1.3 using glucose oxidase (GOx) at the bioanode and laccase at the biocathode. The temperature-sensitive fuel cell was designed with a poly(N-isopropylacrylamide) as a low critical solution temperature (LCST) coating polymer (Figure 1.3.b). Below the critical temperature ($\sim 33^\circ\text{C}$), the polymer is soluble leading to a swollen GOx-entrapped polymer film where a redox mediator can easily transport electrons from the catalytic site to the electrode (ON state). When the temperature is higher than 33°C , the composite film is shrunk (insoluble polymer) and the electrical wiring is no longer ensured. By switching below and above the phase transition temperature (45°C to 20°C), a repeatable change by a factor 6 of the power output density was obtained⁴². The pH switching biofuel cell was achieved with a pH-responsive block copolymer of poly(4-vinylpyridine) and polystyrene (Figure 1.3.c). Pyridine moieties of this polymer are protonated below its pK_a (~ 4.8) and enhance enzyme/electrode communication through negatively charged redox mediators (ON state). When the pH increases above the pK_a of the polymer, pyridine moieties become positively charged and repulsion with negatively charged mediators prevent the electrical communication (OFF state). By switching pH from 4.5 to 7, the power out density was divided by ten⁴². It has to be noted that enzymes are intrinsically temperature and pH-sensitives. Glucose catalytic activity is nearly constant on pH 4-7 and 20 - 45°C ⁴⁷ ranges. On the contrary, laccase activity strongly varies on these ranges⁴⁸ so the ON/OFF switch is probably not only due to the stimuli-responsive polymers but also to the enzyme intrinsic properties.

1.1.3 Self-powered enzymatic biosensors

Biofuel cells can also be coupled to a biosensor leading to self-powered electrochemical biosensors^{49,50}. Introduced in 2001⁵¹, the concept is to choose the enzyme for bioanode or

biocathode depending on the analyte one wants to detect. Therefore, the change in current at open-circuit voltage is proportional to the concentration of this analyte. For instance, a biofuel cell built with glucose dehydrogenase at the anode will be sensitive to the glucose concentration (Figure 1.4.a). These biosensors can somehow be used for an *in-situ* continuous monitoring of the analyte as long as they can supply a wireless transmitter. Few examples of self-powered emitting biosensors for health applications (glucose⁵², urinary⁵³) and environment (non-enzymatic water monitoring for plants⁵⁴) can be found in the literature. As the electrocatalytic current is often not sufficient to fuel a radio transmitter, most strategies are based on the use of a capacitor⁵²⁻⁵⁵, able to discharge a sufficient value of energy. This system was employed to develop a self-powered biosensor with a crosslinked composite of glucose dehydrogenase and a carbon ink at the anode and a crosslinked bilirubin oxidase (BOD)/ platinum-carbon ink at the cathode (Figure 1.4.a). As the rapidity of the energy charge is directly dependent on the substrate concentration, the frequency of emission is directly proportional to the fuel concentration and shift from 0 Hz to 0.25 Hz when the glucose concentration is increased from 0 to 6 mM (Figure 1.4.b). This frequency shift can further be interpreted via an adequate radioreceptor.

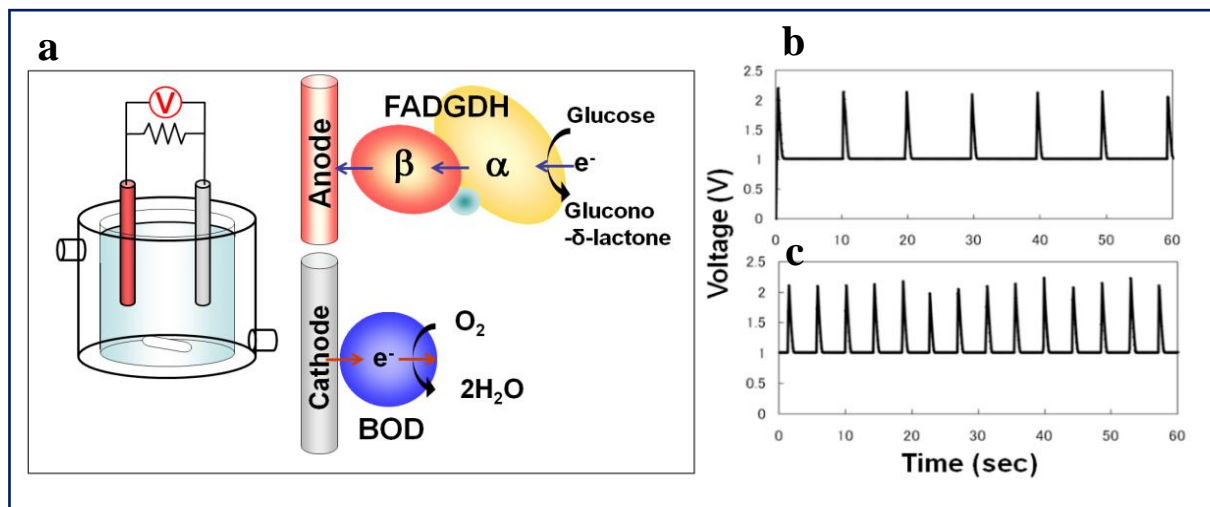


Figure 1.4: (a) Illustration of a glucose self-powered biosensor using flavin adenine dinucleotide-dependent glucose dehydrogenase (FADGDH) and bilirubin oxidase (BOD). The device is coupled with a capacitor-emitter circuit. The capacitor discharge toward the radioemitter at various periodic times depending on the glucose concentration: (b) 1.7 mM and (c) 6.6 mM. The frequency of the discharge and therefore of the emitted signal is directly proportional to the glucose concentration. The figure is adapted from [52].

1.1.4 Enzymatic logic gates

In 2010-2012, few researchers came to the idea that the enzymatic reactions may act as logic gates^{56,57} with the substrate as an input and the product as a boolean output (imperfect ON/OFF state). Several enzymes require two substrates or a cosubstrate (ion, prosthetic group) to be catalytically active. The simplest example is a single enzymatic reaction as illustrated by horseradish peroxidase (HRP) (Figure 1.5.a). If one restricts this enzyme activity to the peroxidase-like activity⁵⁸, a full catalytic cycle (enzyme regeneration) is performed only if the hydrogen peroxide and a co-substrate like a tetramethylbenzidine are present. When HRP is electrically wired to an electrode, a current is collected only if both species are simultaneously present thus the HRP bioelectrode act as a AND logic gate.

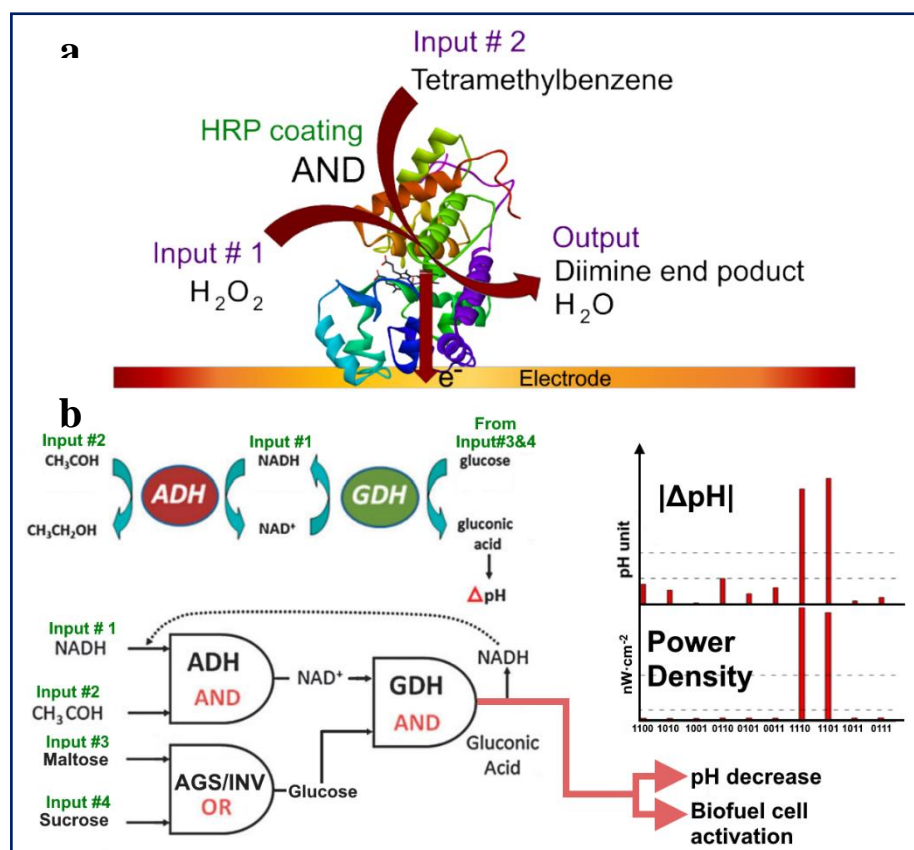


Figure 1.5: (a) Illustration of a simple AND enzymatic logic gate based on horseradish peroxidase (HRP). (b) Illustration of several AND enzymatic gates with alcohol dehydrogenase (ADH), glucose dehydrogenase (GDH), amyloglucosidase (AGS) and invertase (INV). This cascade reaction was used to trigger a pH decrease by gluconic acid production that further switches on a glucose biofuel cell via a pH-responsive pyridine polymer coating. Figure (b) is adapted from [56,59]

Another simple logic gate called OR can be made by two enzymes such as amyloglucosidase and invertase that produces the same output⁵⁹ – glucose in this specific case. More complex mathematical operations (NAND, XOR) have been settled with enzymatic logic gates^{56,60,61} by coupling several cascades of enzyme reactions. These logic gates being the underlying principle behind computer and microelectronics, the scientist dream could be pushed to the full replacement of microcontrollers into biocomputation with enzymatic Boolean logic gates. In practice, every biosensor and few biofuel cells are coupled to a microcontroller to interpret and return the adequate response (actuator). This sense-act device⁶² can be condensed to a simple enzymatic boolean gate that sense the presence of a specific analyte in its environment and switch to a proactive state (act depending on its environment). For example, figure 1.5.b illustrates recent progress about pH-responsive biofuel cells coupled with enzymatic logic gates. In this system, an osmium- poly(4-vinylpyridine) pH-responsive polymer was used to immobilize laccase. Others enzymes (glucose oxidase, glucose dehydrogenase and alcohol dehydrogenase) were freely diffusing inside the biofuel cell compartment. Using this logic gate combination, the presence of NAD^+/NADH , ethanol and glucose lead to the formation of gluconic acid that acidifies locally the solution similarly to glucose oxidase. The concentration of 0.5 mM NAD^+ , 10 mM ethanol and in-situ produced glucose from 100 mM maltose / 300 mM sucrose led to a pH drop from 6.5 to 4.5.⁵⁹ As already described in section I.1.3, pyridine-based polymers switch towards a swollen state at $\text{pH} < \text{pKa} \sim 4.8$ enhancing electrode-enzyme communication. Thus the produced pH decrease is sufficient to turn on the biofuel cell made by the freely diffusing glucose oxidase and the immobilized laccase as active biocathode.

I.1.5 Smart electro-driven drug release coupled biosensors

Conventional oral drug delivery suffers from two disadvantages: the protein/peptide-based drug cannot cross the intestinal epithelium and can be digested by proteases present in the stomach⁶³ before reaching their target and the pharmacokinetic profile is not properly controlled. Usually, the release profile, concentration vs time, presents an overshoot above the limit of the drug toxicity followed by a fast decrease below the therapeutic range^{64,65}. Thus, a limited efficiency for long-time drug treatment is observed unless new ingestions are done at short intervals. To greatly improve the medication, reservoirs based on polymeric matrix, micelles, or liposomes were developed to get an adequate diffusion-controlled drug profile. Implantable contraceptive patches are working on a similar principle. However, some drug delivery requires a more

irregular profile and a system able to adapt their response to fluctuations on a minute/hour scale. For instance, glucose concentration is known to rapidly increase after a meal.⁶⁶ To control hyperglycemia, the insulin (diabetic medication) has to vary in the course of the day based on the patient's activity. Stimuli-responsive molecules to pH, temperature, glucose and ionic strength have been used to switch on and off the drug delivery⁶⁷. However, electro-triggered techniques look even more attractive for precise remote control of drug release. Electro-responsive gels^{68–75} can be loaded with drugs and release an adequate amount of drugs by swelling due to conformational change or gel erosion.⁷⁶ Erosion electro-induced gels are often based on weak hydrogen bonding polyelectrolytes that can be reversed by pH change. Poly(ethyloxazoline) and poly(methacrylic acid) form supramolecular complexes that have been used to entrap 0.5% weight insulin.⁷⁷ Upon + 5 mA current, hydroxyl ions are produced by water electrolysis and the local pH increase above the critical value of 5.4 for which hydrogen bonds are disrupted and polymer and drugs are released together. This process enhanced to release of insulin at a rate of $0.1 \text{ mg} \cdot \text{h}^{-1}$ and 70% of the total insulin was released after approximately 10 hours compared to 4% after three days in the absence of potential.⁷⁷ On the contrary to electro-erosion gels, electro-swelling gels are often cross-linked to prevent their release simultaneously to the drug. A crosslinked poly(methacrylic acid) film⁷⁸ sensitive to pH has been used to entrap 0.09 moles of insulin per dm^{-3} of gel. Electro-release was carried out by application of $3.3 \text{ V} \cdot \text{cm}^{-1}$ and about 20% of the total entrapped insulin can be released within the hour. Also, no leakage of insulin in the absence of potential was observed. A release profile that illustrates the good reactivity and repeatability of the gel upon ON/OFF voltage switching was obtained. Another family of electro-swelling films is based on conductive polymers like polyaniline⁷⁴ or polythiophene.⁷⁰ In these films, voltage induces permeability change that allows drug diffusion.

The coupling of this electro-responsive drug-tank electrode with self-powered biosensors is extremely promising. Sense-act-treat bioelectrodes⁶² that can analyze the body fluid and release the adequate drug to treat the metabolic disorder in real-time can be developed. By a thoughtful choice of the logical gate, the feedback loop usually performed by a microcontroller can be implemented within the enzymatic bioelectrode. To the best of my knowledge, a single electrochemical sense-act-treat device has been reported in the literature for lactate sensing and abdominal trauma curation⁶². The sensor was based on a glassy carbon electrode functionalized with carbon nanotube and meldola blue (immobilized mediator). With the concomitant presence

of two inputs (1,1 state) – namely lactate dehydrogenase (LDH) and its substrate lactic acid – a substantial increase of the open circuit potential and current density were observed at the electrode (Figure 1.6.a). This shift was not observed in the presence of LDH or lactic acid alone (0,1 and 1,0 states) showing that the bioelectrode is acting as a boolean and logic gate (Figure 1.6.b). Acetaminophen (paracetamol) was entrapped within a conductive film of poly(3,4-ethylenedioxythiophene) at the cathode. The release was self-triggered with the current arising from the NAD^+ mediated lactate/LDH reaction having an average value of $\sim 40 \mu\text{A}\cdot\text{cm}^{-2}$ after 60 min. 20 mM laccase, 20 mM NAD^+ and $10 \text{ U}\cdot\text{mL}^{-1}$ LDH was used as the ‘abnormal concentration’ to trigger the electro-release of acetaminophen (Figure 1.6.c). Acetaminophen has been quantified by oxidation at 0.4V although the release kinetic, as well as the PEDOT acetaminophen reservoir capability, could not be retrieved from this study.⁶²

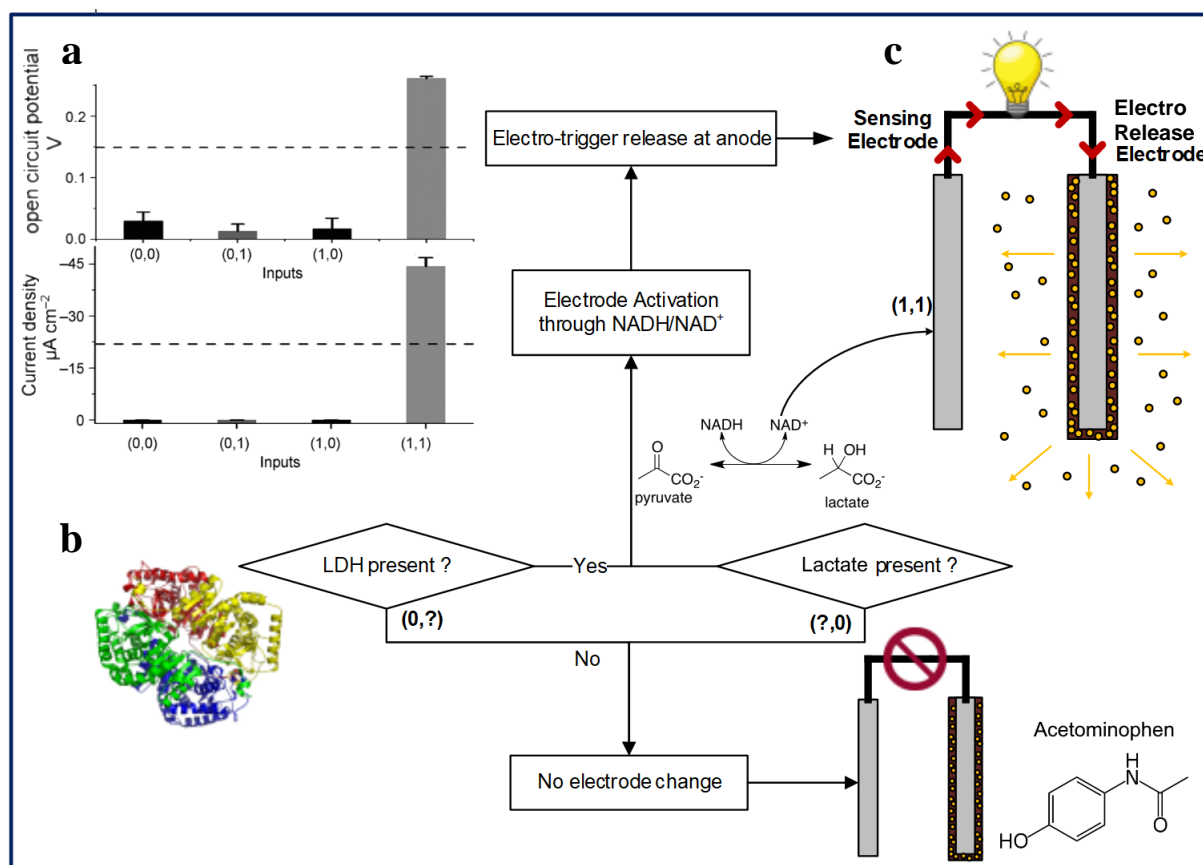


Figure 1.6: (a) Illustration of the obtained power density between anode and cathode depending on input combination, (b) Illustration of a simple and enzymatic logic gate depending on homogeneous lactate/LDH inputs at anode coupled with an electro-driven of acetaminophen from acetaminophen entrapped in PEDOT coating onto the cathode. The figure is adapted from reference [62]

1.2 Electrochemical biosensor generations

In the following, we will focus on enzymatic bioelectrodes and in particular enzymatic biosensors. The different generations that will be defined can be found for other types of bioelectrodes such as biofuel cells and enzymatic logic gates.

1.2.1 Redox-enzyme based biosensors

Glucose oxidase based biosensors will be taken as the main example to describe the various detection strategies developed for redox enzyme-based biosensors. The first biosensor has been introduced by Clark and Lyons in 1962⁷⁹ using oxygen as a mediator (*i.e.* electron carrier). Using an oxygen electrode, a decrease in the measured oxygen concentration was proportional to the glucose concentration. Oxygen depletion was however a bad option due to its variability in the biological matrix. Later in 1975, the first commercial glucose biosensor was based on the amperometric detection of hydrogen peroxide, reported as a first-generation glucose biosensor. The H_2O_2 reduction (-0.5 V vs Ag/AgCl) or oxidation ($+0.7\text{ V}$ vs Ag/AgCl) was measured at the electrode (Figure 1.7), as reported in the following equation with the analyte written in red and the mediator in blue:

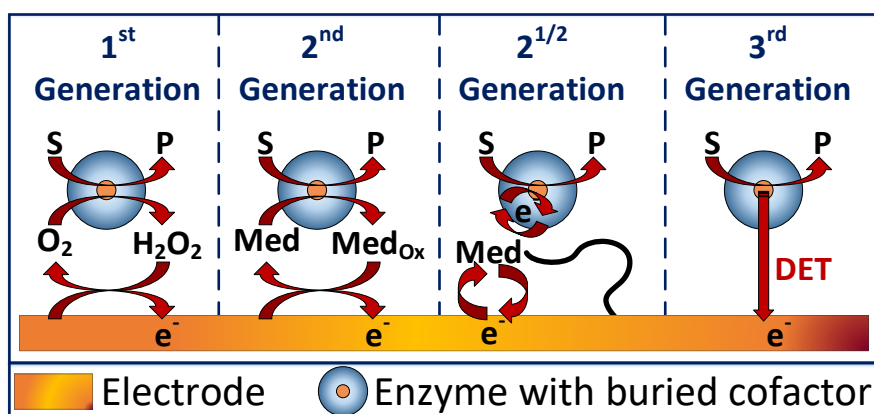
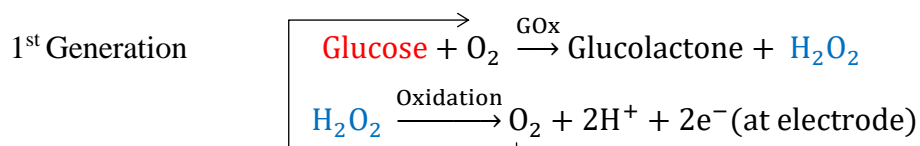
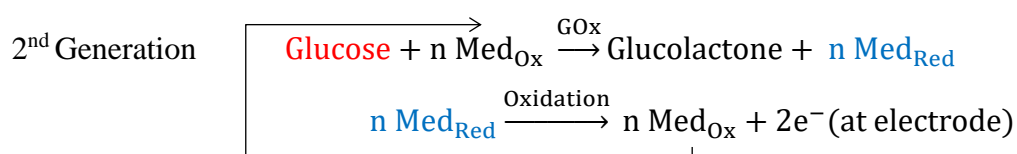


Figure 1.7: Representation of the successive generations of bioelectrode

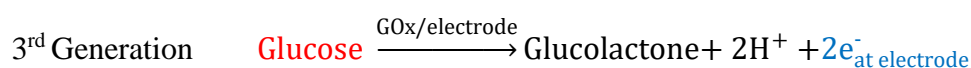
However, a very high potential was used which also induces the oxidation of several interferents present in the biological medium (ascorbic acid, uric acid, salicylic acid, H_2O_2 , NAD^+ ...). To prevent the influence of the interferents, the second generation biosensors were developed

based on the use of mediators in the analyte solution (Figure 1.7). To limit the kinetic competition between the dissolved oxygen and this mediator, redox species with good electron transfer and good diffusion properties in both redox states were selected. Also, the redox potential of the mediator was chosen as close as possible to the enzyme cofactor potential to reduce as much as possible the voltage window for interferents. Thus for oxidase enzymes, an ideal mediator has a cofactor as follow: $E_{\text{cofactor}} < E_{\text{mediator}} < E_{\text{interferents}} < E_{H_2O_2}$. This order is reversed for the reductase enzyme and this discussion is extended in I.4.3. Ferrocene, quinone, osmium, Prussian blue, or ruthenium are often used as glucose oxidase mediators. The electron transfer is described in the following equation with the analyte written in red and the mediator in blue:



Biosensors based on immobilized mediators are of $2^{1/2}$ generation (Figure 1.7). For sake of simplicity, this transfer process will further be denoted as IMET for Immobilized Mediated Electron Transfer. The electrical signal is here provided by an electron exchange cascade from the enzyme's catalytic site towards the electrode. IMET transfer is relying on the electron/counter charge hopping between successive mediators and is assumed to be triggered by the electrode potential. The drawbacks are similar between MET and IMET biosensors. However, a consequent benefit is added here as the immobilization of the mediator prevent its leakage with time. As mediator no longer has to be added along with analyte, *in-situ* analysis underflow are enhanced. A catechol-chitosan redox capacitor film has been proved to connect electrochemically glucose dehydrogenase and electrode.^{80,81} Enzyme catalytic cycle was connected to the electrode via the charge/discharge of the redox film acting as an intermediate collector/emitter to screen/induce biochemical changes.

An alternative called third-generation biosensors were then developed to obtain a direct transfer of the electrons from the enzymes towards the electrode (Figure 1.7). By definition, the direct electron transfer (DET) does not use further redox mediators and electrons are directly hopping from the buried cofactor to the electrode/conductive material as depicted in the following equation, with the analyte written in red and the mediator in blue:

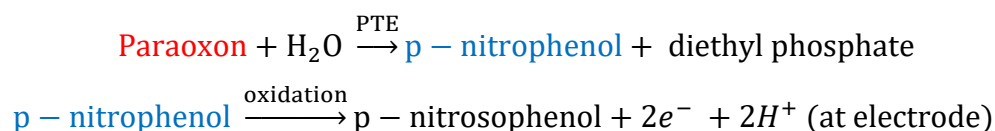


The influence of interference molecules should be limited in this case. It has to be noted that glucose oxidase based biosensors where the electric signal cannot be seen in oxygen-free glucose solution cannot be considered to be based on DET since O₂ can behave as a competing mediator⁸².

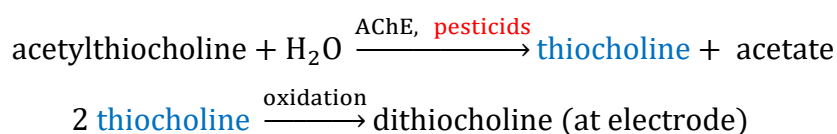
1.2.2 Non-redox enzyme-based biosensors

As reported previously, approximately 80% of all proteins are not redox-active. Three strategies have been developed to obtain non-redox enzyme-based biosensors.

Non-redox enzyme able to produce an electroactive product. Some enzymes may lead to a redox-active product that will act as a diffusing mediator. In this case, the detection strategy is similar to a 2nd generation electrode. Phosphotriesterase (PTE) is an enzyme able to catalyze the hydrolysis of organophosphorus in the presence of water (Lewis base) and zinc cation helping to make the phosphorus centre more electrophilic.⁸³ This enzyme presents no redox-active cofactor but its end-product (p-nitrophenol) can be further oxidized into p-nitrosophenol.^{84–86} This strategy has been employed to develop biosensors for chemical warfare nerve agent and pesticides detection such as paraoxon as depicted in the following equation, with the analyte written in red and the mediator in blue:

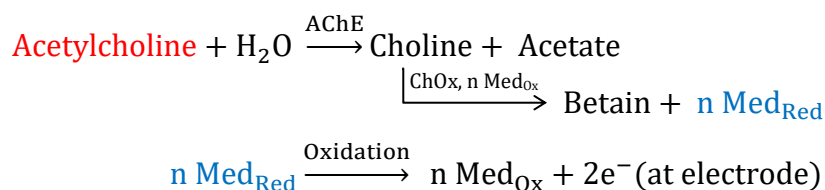


Another substrate than the natural substrate of the enzyme can also be used to produce a redox-active product. This strategy is very interesting for “activation/inhibition sensors”. These devices use a constant substrate concentration and sense the enzyme activity modulation in the presence of competitive inhibitors or activators. Few biosensors of organophosphorus pesticides^{27,32,87} were developed based on the irreversible inhibition of acetylcholine esterase (AChE) in their presence. Acetylthiocholine is used instead of the natural substrate (acetylcholine) and is catalytically transformed into thiocholine, able to be oxidized at the electrode as depicted in the following equation, with the analyte written in red and the mediator in blue:



Upon addition of pesticides, the overall AChE catalytic rate decreases with increasing concentration leading to a decrease in electrochemical signal. However, inhibition biosensors need to be complemented by extensive laboratory analysis as a myriad of chemicals can cause inhibition (lack of selectivity). In Alzheimer's disease, the availability of acetylcholine is reduced for neurotransmission. Thus, almost every medication for Alzheimer to improve cognitive functions are based on the reversible inhibition of AChE to limit the acetylcholine elimination pathway.^{88,89} Few AChE based biosensors were developed to evaluate potential new therapeutics for Alzheimer's disease.^{90,91}

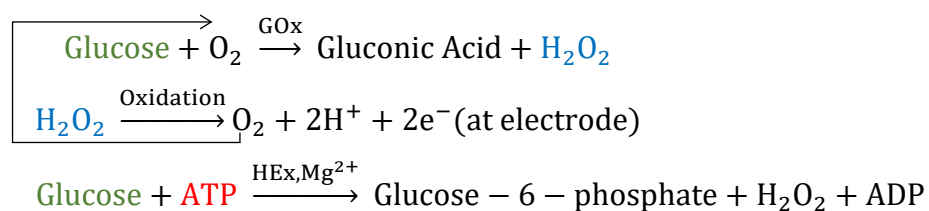
Bi-enzymatic system based on cascade reactions. The non-redox active enzyme can be immobilized with a redox-active one to produce through a cascade reaction an electroactive product. Thus, AChE can be associated with choline oxidase (ChOx) which is a redox-active cofactor (FAD) that can further exchange electrons with O₂ or any mediator as depicted in the following equation, with the analyte written in red and the mediator in blue:



In the case of AChE, this strategy enhance to use of the natural substrate of the enzyme. A microelectrode with a great time and spatial resolution was developed with AChE and ChOx to record acetylcholine release events from a vesicle using this strategy.⁹² Cascade reactions are also routinely employed in electrochemistry to coupled oxidase enzymes with horseradish peroxidase (HRP).

Bi-enzymatic system based on competitive reactions. The non-redox active enzyme can be immobilized with a redox-active one which is a competitor toward the consumption of the analyte (substrate). These competitive enzymatic reactions were used to quantify the concentration of Adenosine-5'-triphosphate (ATP) in biological fluids⁹³. ATP is known to be the "currency molecule" of energy transfer in almost all intracellular energy processes and all living beings. Even if ATP is redox-active, its direct oxidation onto electrode is obtained at too high potentials (1.3 V vs Ag/AgCl)⁹⁴ to avoid the oxidation interferences. Some innovative devices use an indirect way based on two competitive enzymatic reactions using hexokinase

(HEx) and GOx as depicted in the following equations, with the analyte written in red, the mediator in blue and the shared substrate in green:



In the presence of glucose, the GOx-catalyzed reaction induces a current corresponding to the oxidation of H_2O_2 at the electrode. In the presence of ATP and Mg^{2+} (the cofactor of HEx) with glucose, the HEx-catalyzed reaction becomes competitive in glucose consumption leading to a decrease of the current intensity proportional to the ATP concentration.

II. Mechanisms of the electron transfer towards the electrode

The different mechanisms of detection will be presented depending on the diffusion limitations and the type of electron transfer. The first and second-generation biosensors are based on mediated electron transfer (MET) and the 2.5th generation biosensor on immobilized MET (IMET). The 3rd generation biosensors are based on direct electron transfer (DET). Details about analytical solutions and the characterization of kinetic parameters can be found in works from M. Saveant^{95–99}, P.N. Bartlett^{100–102}, K. Kano^{103,104} and Lo Gorton^{105,106} teams. Characterization of the electron transfer is often performed by cyclic voltammetry (intensity vs electric potential). This electrochemical method is called cyclic because the applied potential is swept linearly from high (E_f) to low values (E_i) and vice versa (Figure 1.8.a). In the absence of a redox event, a capacitive current is observed caused by the charge/discharge of the interfacial layer (absorbing/desorption of electrolyte ions). If some redox molecules can exchange electrons with the electrode surface, the current increases with the formation of peaks when the diffusion limitation occurs (Figure 1.8.b). The potential scan rate v ($V \cdot s^{-1}$) is often a critical parameter as it controls the time during which the electrode is held at a given potential. Therefore, it rules the quantity of oxidized/reduced molecules produced. The cyclic voltammetry also helps study the kinetic rate (via the scan rate) and the energy activation (linked to the potential) of redox reactions.

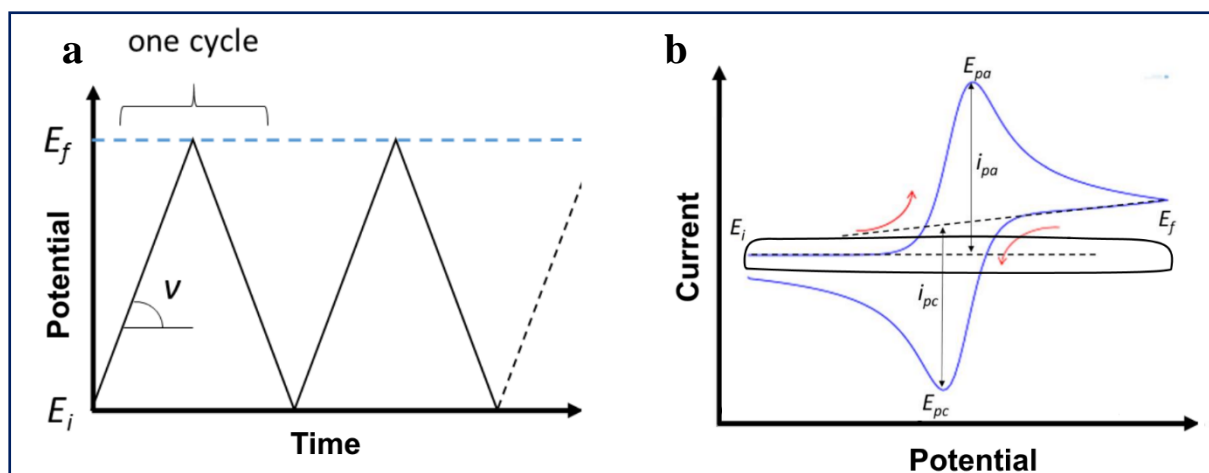
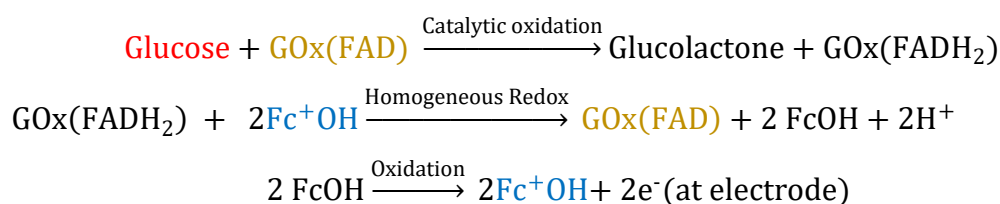


Figure 1.8: (a) Illustration of the linear potential change with time. (b) cyclic voltammogram shows the capacitive current (black curve) along with a reversible probe (blue curve). Anodic and cathodic peak are characterized by their potential (E_{pa} , E_{pc}) and their current (i_{pa} , i_{pc}).

Figure is adapted from [288]

II.1 Mediated electron transfer biocatalysis

In the case of MET, a freely diffusing homogeneous co-substrate (*i.e.* mediator) is used. Two typical examples of enzyme monolayer/free mediator systems were extensively studied HRP/[Os(bpy)₂pyCl]^{2+/+} and GOx/FcOH.^{95,97,107} A "ping-pong" mechanism^{99,108} between substrate/enzyme and enzyme/mediator is observed with symmetry of the different redox reactions (Figure 1.9.a). In the following example, the GOx cofactor named Flavin adenine dinucleotide (FAD) is regenerated by ferrocenium methanol reduction (Fc⁺OH) and ferrocenium is regenerated by oxidation at the electrode. GOx oxidized state named GOx(FAD) is written in yellow in the following equation.



The typical response of a mediated biocatalytic system is illustrated in Figure 1.9.b. In the absence of the enzyme-substrate, the shape of the voltammogram of the FcOH mediator is a typical two waves oxidation/reduction, ruled by the following Randles–Ševčík equation:

$$i_p = 26900nAC\sqrt{nvD} \text{ with } \begin{cases} i_p: \text{current maximum (A)} \\ n: \text{number of exchanged electron} \\ A: \text{electrode area (cm}^2\text{)} \\ C: \text{Med concentration (mol}\cdot\text{cm}^{-3}\text{)} \\ v: \text{the scan rate (V}\cdot\text{s}^{-1}\text{)} \\ D: \text{Med diffusion coefficient (cm}^2\cdot\text{s}^{-1}\text{)} \end{cases} \quad (\text{Equation 1.1})$$

Above the saturating concentration of the substrate (glucose), the kinetic is controlled by the enzymatic reaction leading to an S-shaped response with a complete disappearance of the reduction peak of FcOH and overexpression of its oxidation peak (red curve, Figure 1.9.b). The analytical solution of this situation, *i.e.* no diffusion limitation of the substrate and the mediator, has been described by Saveant *et al.*⁹⁹

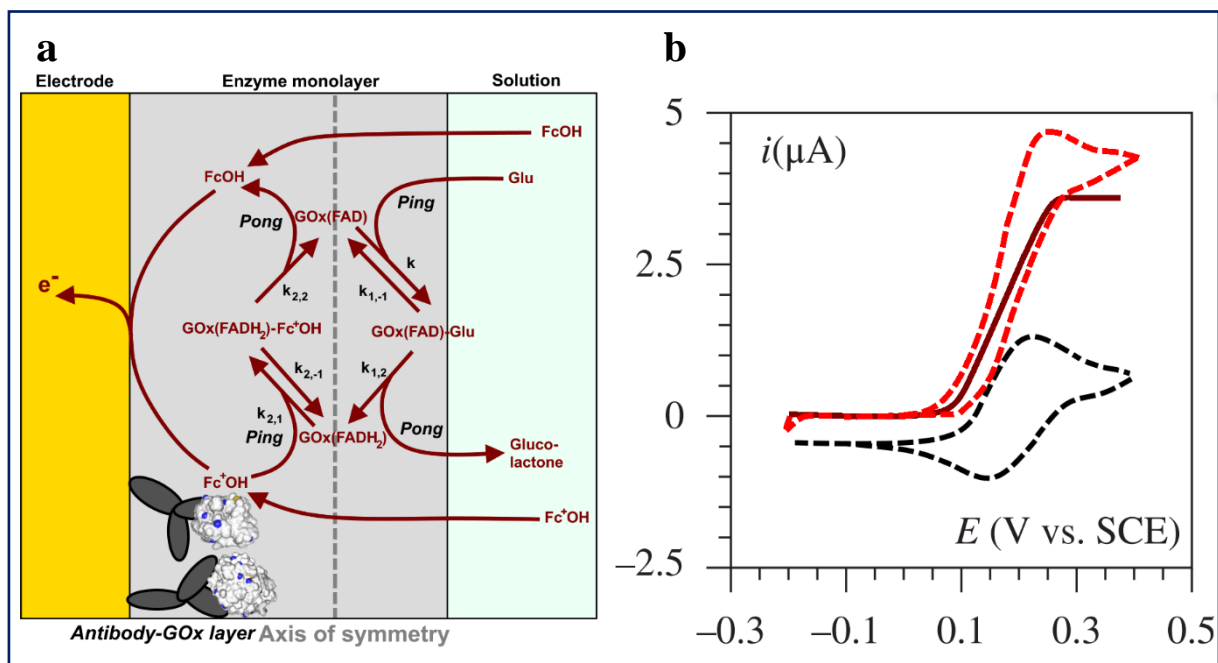


Figure 1.9: (a) Illustration of the mediated ping-pong pathway between the glucose substrate (Glu), the flavin adenine dependent-glucose oxidase $\text{GOx}(\text{FAD})$ and the ferrocene methanol mediator (Fc^+OH). Monolayer enzymatic film was prepared from anti-rabbit IgG-antigen interaction with antibody-functionalized GOx . (b) Illustration of the electrocatalytic current without (red line) and with background subtraction (dashed red line) as compared to the ferrocene response in absence of glucose. Cyclic voltammogram was retrieved at $40 \text{ mV}\cdot\text{s}^{-1}$ with a GOx coverage of $2.6 \cdot 10^{-12} \text{ mol}\cdot\text{cm}^{-2}$ in the presence of 100 mM glucose and 0.1 mM ferrocene methanol (Fc^+OH) at pH8 in 100 mM phosphate buffer. The figure was adapted from [99].

II.2 Immobilized mediated electron transfer biocatalysis

In the case of IMET based biosensors, the mediator is linked to the enzyme or crosslinked in the deposited matrix encapsulating the enzyme. Saveant *et al.* studied two IMET based biosensors: antigen- GOx /antibody- Fc^+OH ¹⁰⁹ and avidin- GOx /biotin- Fc^+OH ⁹⁸ systems (Figure 1.10.a). On the contrary to MET based biosensors, the mediator concentration can be a limiting factor for IMET systems. Indeed in the first case, the concentrations are typically between 0.1 and 5 mM whereas the surfacic concentration in the IMET electrode can be as low as 10^{-9} to $10^{-12} \text{ M}\cdot\text{cm}^{-2}$.¹¹⁰ Two IMET cases are often described in the literature depending on the film thickness. For the thin film, i.e. enzyme monolayer, the immobilized mediator exchanges

diffusion with rapid electron exchange Figure 1.10.b).^{112,113} An apparent “electron” diffusion coefficient is therefore defined and composed of mediator diffusion, and (2) electron hopping. If electron hopping is the main mechanism, a percolation concentration is often observed. Below this value, only electrons from the nearest redox centres are collected. Above the threshold, almost all redox sites are electrically linked to the electrode.¹¹⁴ In all cases, in the presence of the enzyme-substrate, an S-shaped signal centred on $E_{1/2}$ is observed with the overexpression of one of the redox branches and the disappearance of the other one. This means that one of the redox forms has an approximatively zero concentration and the other one is constantly regenerated by the enzymatic catalysis (Figure 1.10.c).

II.3 Choice of the mediator

The choice of the mediator is of crucial importance to enhance an electron flow in MET and IMET bioelectrodes. The adequate mediator has to be chosen among a list of the most common redox probes,^{115–117} depending on the following parameters: (i) its redox potential in comparison to the one of the enzyme cofactor (Figure 1.11). Metalocomplexes¹¹⁸ and quinone¹¹⁹ mediators present a tunable potential depending on the group covalently link to the redox moieties; (ii) its solubility of both forms (MET requirement); (iii) the number of electrons involved in the redox process; (iv) its reversibility (i.e: peak-to-peak-separation) and electrochemical rate constant and (v) its reactive functions toward interaction with others materials (IMET requirement).

The enzyme cofactor is a small molecule/or cluster buried inside the enzyme and responsible for its redox activity. Five redox cofactors are predominant: nicotinic, flavinic, quinonic coenzymes, cytochrome (heme) and metallic clusters. They are also called co-enzymes or ‘prosthetic groups’ when they are covalently bound to the enzyme. As highlighted before, the predominant parameter of choice is the potential of the mediator compared to that of the enzyme cofactor. The enzyme-substrate is often at a lower or equal redox potential than the cofactor to enhance electron flow. If the values of the potentials are too far from each other, the reaction will be irreversible. This tackling issue of electron flow is often seen in biological systems (Krebs cycle, respiratory chain) as well as in biofuel cell technology with the complete oxidation of glucose¹²⁰, glycerol¹²¹ or citric acid¹²². It is similar between cofactors and mediators. An oxidized mediator will spontaneously oxidize the reduced form of an enzyme if it has a higher redox potential than the cofactor ($\Delta G^\circ = -nFE^\circ < 0$).

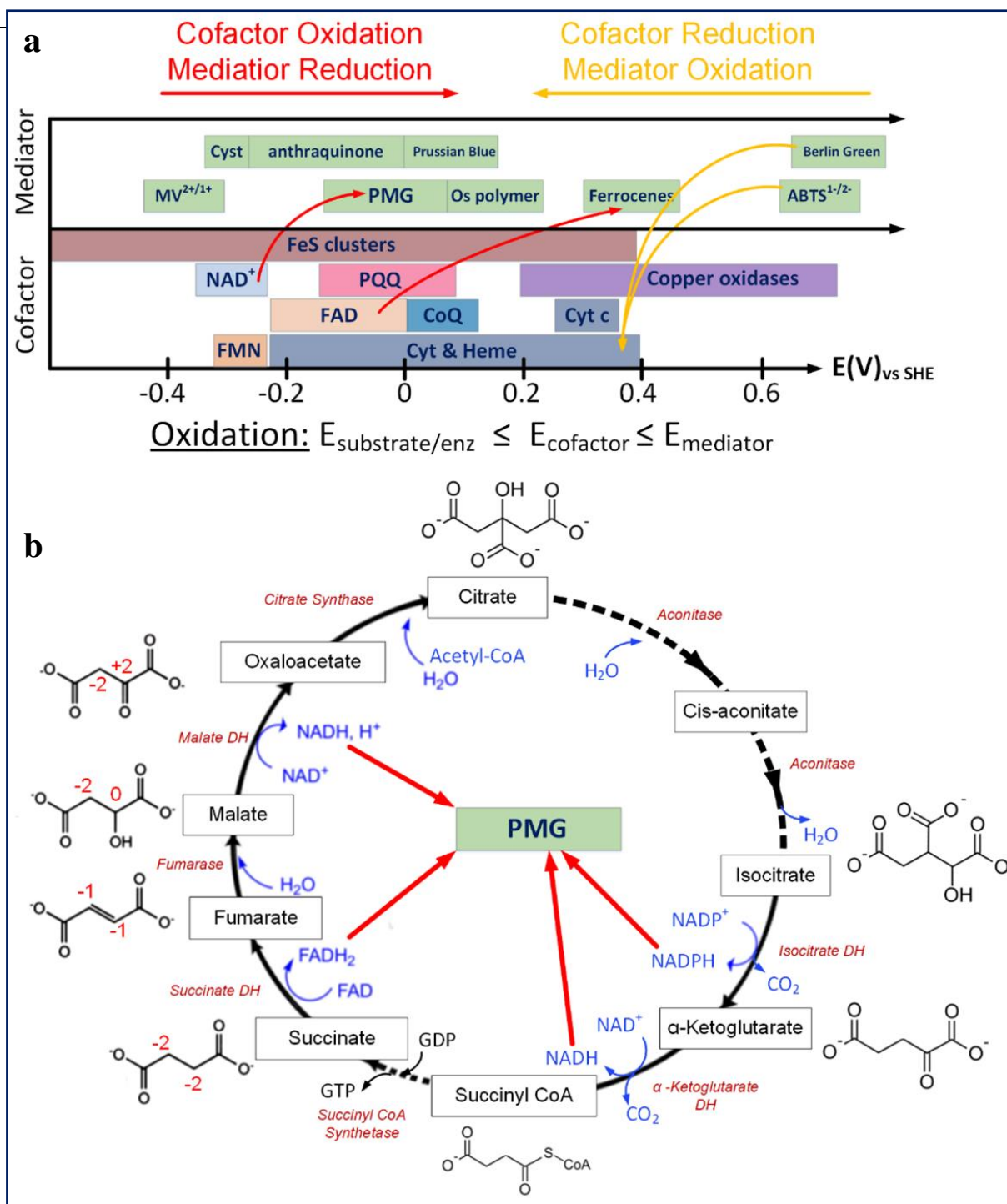


Figure 1.11: (a) Illustration of the electron flow between the cofactor and mediator. Range means that these typical redox probes have a tuned redox potential depending on their environment (pH, chemical function). $E_{\text{substrate/enzyme}}$ means that the substrate/enzyme complex may have a significantly lower redox potential than substrate alone. (b) Illustration of the Krebs citric cycle used to prepare a multi-enzyme biofuel cells with a poly(methylene green) film as electron collector [122].

The case of poly(methylene green) (PMG) is a nice illustration of this phenomenon (Figure 1.12.b).¹²³ In the Krebs cycle, NAD^+ is reduced into NADH by several enzymes. The use of a polymeric coating of PMG having a formal potential around 0 V¹²² is efficient to oxidize back NADH into NAD^+ (Figure 1.11.b). The symmetric case is observed for an enzyme with an oxidized cofactor that has to be regenerated after the catalytic reaction. In this case, a redox mediator with a lower standard potential than the cofactor has to be chosen. Most cofactor standard redox potentials vary with the pH¹²⁴ due to the proton-coupled exchange. Thus, the mediator has to be chosen taking into account the cofactor environment and the operating pH condition. Information about the main cofactors can be found in these references.^{115,125–127}

II.4 Direct electron transfer biocatalysis

In the case of the DET process, no mediators are used and the electrons are directly hopping from the cofactor to the electrode. The field that studies direct electron transfer kinetic of adsorbed/cross-linked enzymes is often referred to as protein film voltammetry in the literature.¹²⁸ Three rates are taken into account: the substrate mass transport toward the electrode, the substrate/enzyme rate at the electrocatalytic site and the electron exchange rate between the cofactor and the electrode. Bollela *et al.*¹²⁹ have studied the DET of an adsorbed fructose dehydrogenase (FDH) onto single-walled carbon nanotubes/anthracene. Kizling *et al.*¹³⁰ have studied a similar adsorbed system onto multi-walled carbon nanotubes (MWCNTs)/glassy carbon electrodes (Figure 1.12.a). The cyclic voltammogram is similar to a typical “adsorbed” mediator ($E_{\text{pa}} = E_{\text{pc}}$) having a peak potential equal to the enzyme cofactor potential (Figure 1.12.b). The rate of the electron transfer is ruled by A. Marcus theory^{131,132} (section I.5.2). Figure 1.12b highlights the fact that the typical faradaic current based on the electron exchange between the cofactor and the electrode is often extremely low compared to the capacitive current. When the enzyme-substrate is present, a significant increase of one of the redox peaks is observed similarly to MET and IMET bioelectrodes (Figure 1.12.c).

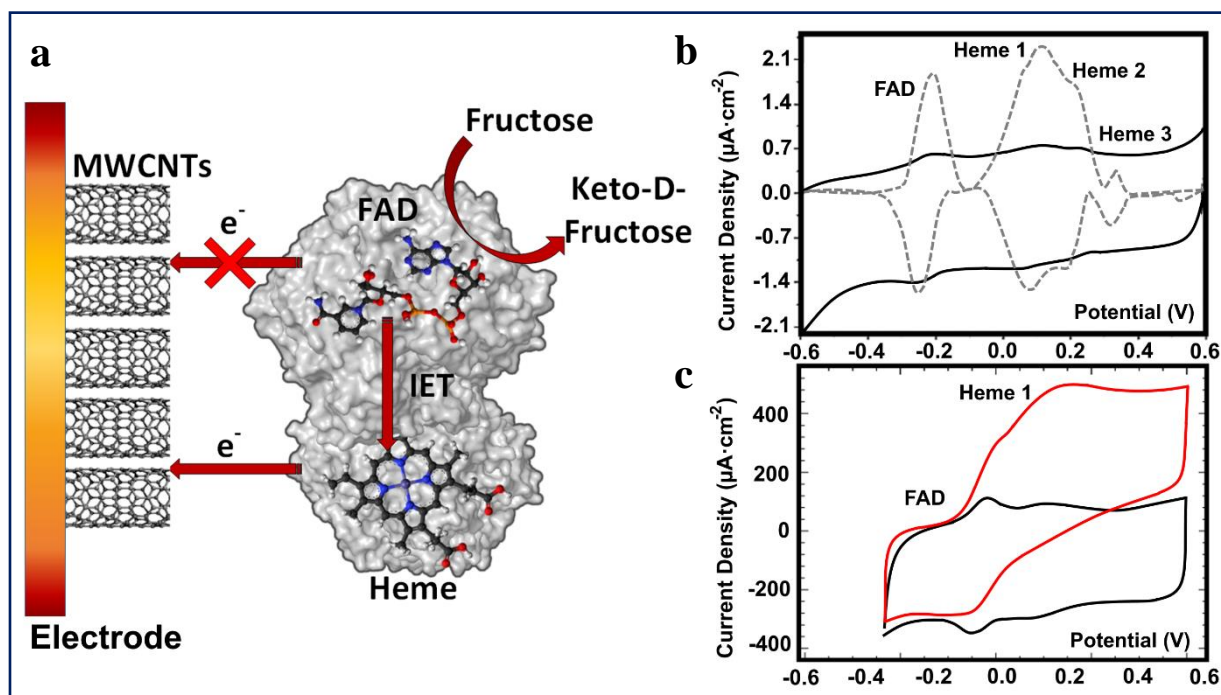


Figure 1.12: (a) Illustration of a fructose direct electron transfer biosensor with an internal electron transfer (IET) between FAD and heme redox site. Fructose dehydrogenase was adsorbed onto multi-walled carbon nanotubes (MWCNTs). (b) Cyclic voltammogram at $1 \text{ mV} \cdot \text{s}^{-1}$ of the FDH in the absence of fructose in buffer solution at pH 5.5 adapted from [130]. (c) Illustration of the direct electrocatalytic current observed for FDH in the presence of 10 mM fructose. Cyclic voltammogram was retrieved at $10 \text{ mV} \cdot \text{s}^{-1}$ in 0.05 M acetate buffer pH 4.5. Figure 1.13.c is adapted from [129]

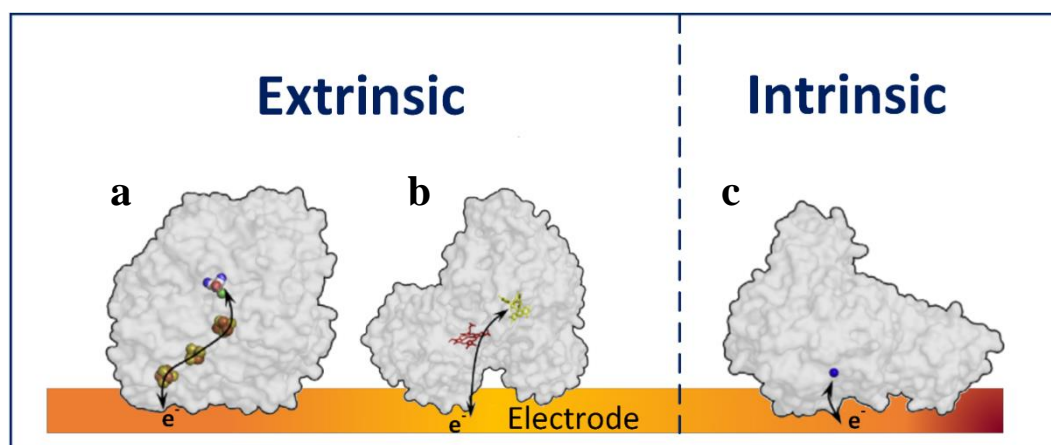


Figure 1.13: Illustration of extrinsic and intrinsic enzymes adapted from [133]. (a) [Ni-Fe] hydrogenase extrinsic enzyme with several metallic clusters. (b) Cellobiose hydrogenase is a representative of the extrinsic enzyme with an IET between FAD and heme. (c) Galactose

oxidase as a representative of the intrinsic enzymes with a single Cu cofactor close to the surface [134]

Table 1.1: Non-exhaustive list of enzymes able to undergo DET from miscellaneous sources. Abbreviations are the following: Aldehyde (Ald), ethanol (EtOH), flavin adenine dinucleotide (FAD), fructose dehydrogenase (FDH), fructose (Fru), glucose (Glu), glucolactone (Glu_{ox}), glucose dehydrogenase (GDH), pyrroloquinoline quinone (PQQ)

	Enzyme	DET process	Cofactor Potential (V vs Ag/AgCl)	Substrate Reaction	Ref
Metallo Enzymes	Horseradish Peroxidase (40 kDa)	Fe ³⁺ /Fe ²⁺ (heme)	-0.34 0.	H ₂ O ₂ + 2H ⁺ + 2e ⁻ = 2H ₂ O	[135,136]
	Laccase (60-70 kDa)	MCO (Multiple Cu centres) with T1 Cu centre	~ 0.6	O ₂ + 4H ⁺ + 4e ⁻ = 2H ₂ O	[137,138]
	Bilirubin Oxidase (60 kDa)	MCO (Multiple Cu centres) with T1 Cu centre	~0.4	O ₂ + 4H ⁺ + 4e ⁻ = 2H ₂ O	[139]
	Nitrate Reductase (~100 kDa)	Prokaryotic: 1x heme, 4x [4Fe-4S], 1x [3Fe-4S] clusters + Mo ^{5+/4+} Eukaryotic: FAD, heme	[4Fe-4S]: -0.16	NO ₃ ⁻ + 2H ⁺ + 2e ⁻ = NO ₂ ⁻ + H ₂ O	[140]
	Hydrogenase (40-200 kDa)	Cluster of [NiFe] or [FeFe] deeply buried + FeS clusters	[NiFe]: -0.29 FeS: -0.34	H ₂ = 2H ⁺ + 2e ⁻	[141,142]
	Glucose Dehydrogenase (80-130 kDa)	from bacterial origin FAD -> [3Fe-4S] cluster -> multi heme c -> electrode	Heme 1: -0.237 Heme 2: -0.155 Heme 3: -0.085	Glu = Glu _{ox} + 2H ⁺ + 2e ⁻	[143]
	Fumarate Reductase (120 kDa)	FAD + FeS clusters	[2Fe-2S]: -0.24 [3Fe4S]: -0.27 FAD: -0.25	Fumarate + 2H ⁺ + 2e ⁻ = Succinate	[144, 145]
	Cellobiose Dehydrogenase (80-100 kDa)	FAD -> heme linked by a flexible peptide	Heme: -0.04 to -0.08	Ose = Ose _{ox} + 2H ⁺ + 2e ⁻	[102,146]
	FAD-Fructose Dehydrogenase (~140 kDa)	FAD toward heme	Heme c1: -0.002 Heme c3: 0.15	Fru = Fru _{ox} + 2H ⁺ + 2e ⁻	[129, 130]
	PQQ dependent Dehydrogenase typeII/III (80-140 kDa)	from PQQ to at least 1 heme (Ca ²⁺ or strontium cations are required to bind PQQ cofactor) Alcohol-DH: active subunit 1PQQ + 1heme c and a third subunit with 3 heme c centres Commercial PQQ-Glucose-DH: cannot perform DET	FDH heme: -0.097 Alcohol-DH: 0.00 GDH heme: -0.08	Fru = Fru _{ox} + 2H ⁺ + 2e ⁻ EtOH = Ald + 2H ⁺ + 2e ⁻ Glu = Glu _{ox} + 2H ⁺ + 2e ⁻	[147] [148] [149]
Others	Glucose Oxidase (~140-160 kDa)	Probable for deglycosylated GOx	FAD -0.35	Glu = Glu _{ox} + 2H ⁺ + 2e ⁻	[150,151]

In practice, only a few natural enzymes can undergo the DET through their surface. This section aims to discuss the required conditions to ensure it and the limitations. Guo and Hill¹⁵² have distinguished two types of redox-active enzymes. The intrinsic enzymes present one single cofactor deeply buried inside its structure. The extrinsic enzymes have several interconnected redox sites (Figure 1.13). According to the literature, the DET is only obtained for proteins having internal electron transfer reducing the gap between the internal cofactor and the enzyme surface small intrinsic proteins with an exposed cofactor^{117,128,153,154} (Table 1.1).

Distance between the enzyme's cofactor and the outside surface is important for the DET because quantum mechanics rules the occurrence of electron hopping. Marcus theory described mathematically internal electron transfer for proteins system as well as heterogeneous electron transfer from enzyme to the electrode.^{131,132} The rate of electron hopping (k_{DET}) is exponentially decreasing with the distance d which imply fetching electron as close as possible to the buried cofactor according to the Marcus theory¹³¹ (Equation 1.3). Page and al.¹⁵⁵ showed that weak DET may occur up to 2-2.5 nm with efficiency only in the range from 0.6 to 1.4 nm, meaning that the DET rate is higher than the catalytic rate of the enzyme (Figure 1.14). Since the DET should not be a rate-limiting step for sensitive biosensors and highly efficient biofuel cells, 1.4 nm can be kept as the critical value. This observation is in good agreement with intrinsic HRP (Table 1.1) that has a heme to surface distance around 2 nm¹⁵⁶ and can only undergo weak DET. Since most of the enzyme monomers are bigger than 30-40 kDa, we can reasonably assume that intrinsic enzymes will not be able to undergo the DET process. Very low scan rate (1-5 mV·s⁻¹) and high substrate concentration are used in practice¹²⁸ for intrinsic and extrinsic enzymes since the DET process remains quite unfavourable. Figure 1.14 shows that the electron hopping rate increases when the free Gibbs energy is swept from +0.25V to -0.5 V. As ΔG° is in close relationship with the electrode potential ($\Delta G^\circ = -nFE^\circ$), a practical way to increase DET efficiency is to apply overpotentials. However, with high overpotentials, interferences from other redox reactions such as water electrolysis will not be negligible.

$$k_{DET} \propto e^{-\beta(d-d_0)} e^{\left[\frac{-(\Delta G^0 + \lambda)^2}{4RT\lambda} \right]} \left\{ \begin{array}{l} k_{DET}: \text{the direct electron transfer rate} \\ \beta: \text{the attenuation factor } (\sim 10 \text{ nm}^{-1}) \\ d: \text{the current electron donor-acceptor distance} \\ d_0: \text{the Van der Waals minimum distance} \\ \Delta G^0: \text{the reaction free Gibbs energy} \\ \lambda: \text{the reorganization energy} \end{array} \right. \quad (\text{Equation 1.3})$$

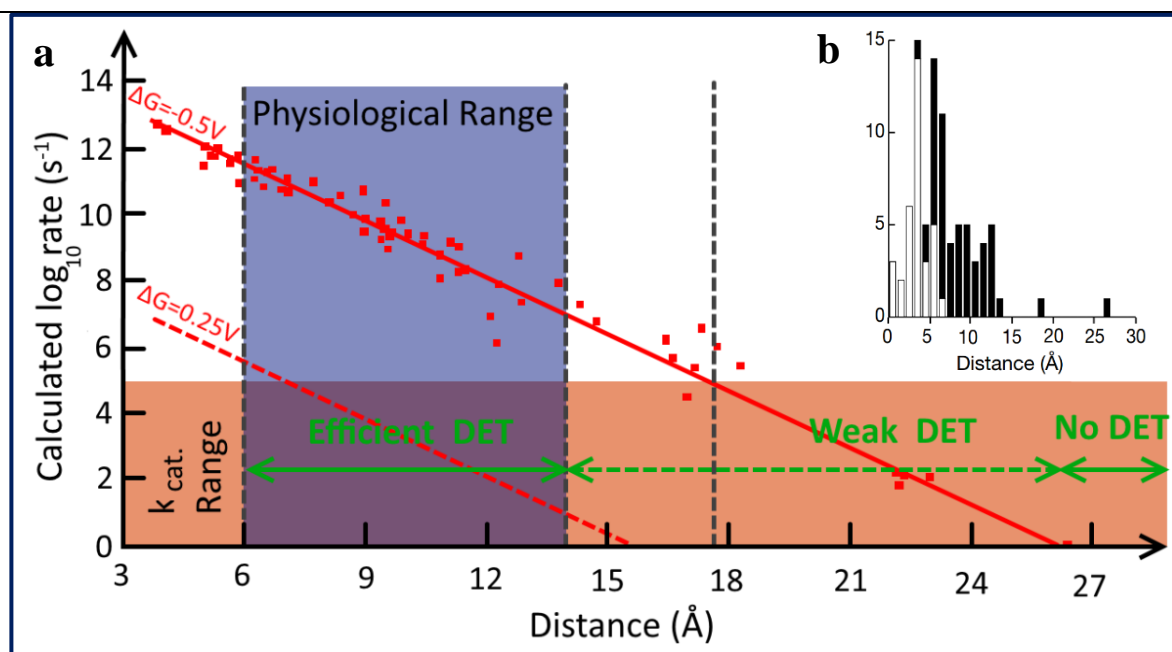


Figure 1.14: (a) Calculated direct electron transfer rate using a model derived from Marcus theory assuming an attenuation factor β of 14 nm^{-1} and a nuclear coordinate energy reorganization of 1 eV . The intersection of the areas marked in orange and blue gives the practical working conditions for efficient DET transfer. (b) Histogram of the tunneling distance for 31 redox proteins that are known to undergo long-range electron hopping (internal electron transfer). Figure is adapted from [155]

Glycosylated enzymes present a carbohydrate shell on their surfaces covalently bonds to the peptide chains of the protein. It concerns $\sim 50\%$ of the enzymes affecting their chemical, thermal and pH stability. Depending on the degree of glycosylation (structure and length of the chains), it can completely change the surface charge and the distance between the buried cofactor and the outer surface. Thus, the efficiency of the electron transfer is modified as well the hydrophilicity and the surface chemical reactivity of the enzyme. The following table gathers information about glycosylation (Table 2). To enhance the electron transfer, the enzymes can be deglycosylated. An efficient deglycosylation of GOx can be performed by its incubation with two enzymes, α -mannosidase and endoglycosidase H in 100 mM phosphate buffer pH5.1 at 37°C for 72h. This procedure successfully remove glycans at N-glycosylation sites.¹⁵¹ the DET transfer was obtained for this deglycosylated GOx allowing the direct electrooxidation of glucose on a glassy electrode with O_2 -independent measurements. Based on the previous procedure, deglycosylation of enzymes is however long, expensive and requires several steps of purifications.

Table 1.2: Mass and diameter changes of enzymes in the glycosylated form compared to the non-glycosylated one

Enzyme	Mass of the glycosylated enzyme	Mass without glycosylation	Mass change diameter increase
GOx- Penicillium Amagasakiense	150-160 kDa	130-133 kDa ¹⁵⁷	10 - 15% + 0.4 nm ¹⁵⁷
GOx- Aspergillus Niger (AN)	160 kDa	138 kDa ¹⁵¹	16-25% ¹⁵¹ + 0.65 nm ¹⁵¹
HRP-C	44 kDa	34.8 kDa ¹⁵⁸	21.8% ¹⁵⁹

The orientation of immobilized enzymes is rarely controlled. However, it appears to be an important parameter to shorten the distance between the buried cofactor and the electrode surface (Figure 1.15). X-ray structural study of enzymes allows to determine the position of the buried cofactor and thus find a strategy to adsorb the enzyme in the most favourable orientation towards the electrode surface. In the case of extrinsic enzymes, an improvement of the DET can be obtained when the heme linker¹⁰² or the [Fe-S] cluster¹⁶⁰ is correctly oriented toward the electrode surface. Orientation also matters for intrinsic enzymes as the buried cofactor is not equidistant with the whole surface.

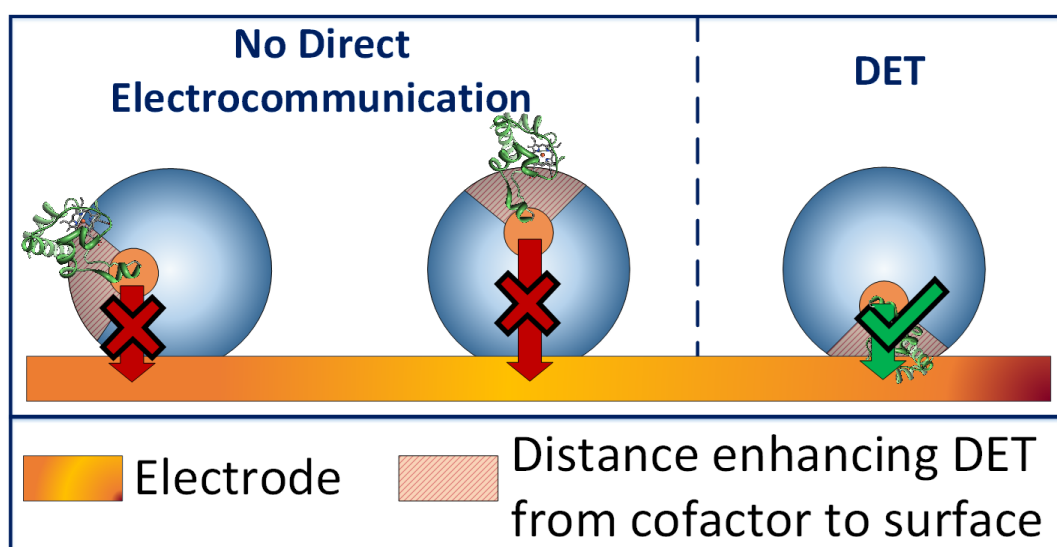


Figure 1.15: Illustration of DET transfer for the extrinsic cellobiose dehydrogenase having a cytochrome *c* domain (heme) that can directly communicate with electrode only if the adsorption orientation is correctly controlled according to [102]

The genetic modification of extrinsic enzymes by cysteine residues allows to control their adsorption on the surface of the electrode, through thiol chemistry and achieve the DET towards the electrode. This sequence modification implies the use of complex biological techniques such as recombinant protein expression in bacteria.¹⁶¹ This technique requires: (1) the recuperation of the DNA sequence that codes for the wild-type enzyme, (2) the insertion of the desired mutation (3) the insertion of these modified DNA fragments into a plasmid vector further injected in a bacteria, (4) the bacteria cell culture to express a large number of recombinant enzymes and (5) several purification steps to isolate the mutant protein. Although these genetically modified enzymes are attractive and greatly improve the DET, the process is expensive and time-consuming which limit its application including in applied research.

II.5 DET and commercial enzymes

In summary without modification, all intrinsic enzymes are limited to MET/IMET processes. However many studies report a DET process for large intrinsic enzymes and especially with glucose oxidase.^{162–165} These studies are using commercial enzymes without further purifications. It has been noted that commercial enzymes are usually heavily-glycosylated and can contain free cofactors.¹⁶⁶ Therefore, the GOx redox peaks observed between -0.45 and -0.2 V^{166,162} can also arise from the free unbound cofactors probably entrapped within the matrix. If so, this system should rather be described as a MET system. To cautiously validate the type of electron transfer, commercial enzymes have first to be properly characterized before their immobilization. The following paragraph presents the different techniques that can be used for this purpose, as reported by Bartlett and coworkers¹⁶⁶ and Milton and coworkers.¹⁶⁷

Usually, commercial lyophilized enzymes could contain many additives (buffer salts, EDTA, albumin, detergents, glutamate, gluconate, glycine,...). After the dissolution of the powder, the real enzyme concentration can be measured using the absorbance of some amino acids at 280 nm or by carrying a Bradford or Biuret complexation test with UV-Vis spectroscopy. The cofactor concentration can be also determined at its specific absorbance (FAD at 452 nm). The molar ratio of enzyme/cofactor can be determined and compared to the theoretical values to ensure that the quantity of free cofactor is negligible (2 moles of FAD per mole of GOx).

To get a rough estimation of its glycosylation state, the hydrodynamic size of the enzyme can be measured by diffusion light scattering and compared to the theoretical value of the X-ray model that can be retrieved from the Protein DataBase.

The activity of the enzyme can be double-checked using an adequate colourimetric test. The oxidation and reductions peaks of the enzyme can be measured by electrochemistry using cyclic voltammetry. The position of the redox peaks is expected to be close to those of the free cofactor, with a possible slight shift due to the bounded state of the cofactor and the applied stress on the enzyme when covalently linked. For the DET process, their presence must be validated in the absence of the enzyme-substrate. In the presence of the substrate, the biocatalytic signal should be observed in the absence and presence of O₂. Otherwise, it means the signal is mediated by O₂. To remove the O₂ contribution, the solution of the substrate can be flushed with argon or nitrogen. The enzyme selectivity can be tested using others substrates and should also be sensitive to activation/inhibition effects such as temperature, pH or divalent cations.

II.6 Glucose oxidase and horseradish peroxidase biosensors

In the following, we have focused our attention on two massively studied enzymes, GOx and HRP that were chosen as model systems during the Ph.D. GOx is an enzyme of industrial interest for the development of glucometer for diabetics as well as biofuel cells for powered-demanding *in vitro* application (neurostimulators, artificial kidneys, pacemakers...). HRP allows the development of an H₂O₂ biosensor. H₂O₂ is a by-product of many redox reactions suspected to be a signalling agent in tumors¹⁶⁸ and wound¹⁶⁹ tissues (phagocytosis). It is also involved in oxidative stress processes.¹⁷⁰

Several pioneering articles have highlighted and cautiously documented how DET transfer with native GOx is a myth^{82,166,171,172}. Since these papers, additional proofs¹⁷³ that others FAD-dependent enzymes such as Choline Oxidase, Alcohol Oxidase, D-Amino Oxidase and Pyranose Oxidase cannot undergo DET transfer were published. HRP can perform DET toward the electrode with however a low catalytic current due to a low concentration of DET-linked enzymes and with a slow kinetic rate by a factor 5 to 10³ compared to MET.^{102,130,174} Considering all these limitations and the extreme difficulty to generalize DET, most of the recent studies deal with the development of new manufacturing techniques for IMET bioelectrodes.

Efficient and reliable biosensors have to fulfil different requirements: an adequate sensitivity range, a good reproducibility of the measurement, a good stability upon storage for commercial use. The measurement of the biosensor is based on a calibration curve presenting a linear range, where the measurement electrochemical signal is proportional to the concentration of the analyte. To be pertinent, this linear range must cover the range in the concentration found in biological fluids. Valuable information can be found in some handbooks gathering information on the normal concentration range of different biomolecules present in biological fluids (blood, serum, urine)^{175–177}. Another important factor, often underestimated, is the response time of the biosensor. Biomolecules have a certain half-life time *in vivo* and thus the response time is a critical parameter when they are monitored in real-time.¹⁷⁸ When the millisecond scale is reached, neurotransmitters (GABA/glutamate^{179,180}, acetylcholine⁹² or catecholamines,...) biosensors provide valuable information about neurodiseases or neuronal communication process (exocytosis).

Table 1.3: Requirements to get an adequate glucose biosensor in a common biological medium and illustrative glucose biosensors characteristics found in the literature from a 2010-2022 period review. Intrinsic GOx-DET biosensor was not considered in this review. The red values are the characteristics of the glucose biosensor developed in our team in 2018 via an electro-crosslinking process and the blue values correspond to an emerging strategy for glucose sensing using cellobiose dehydrogenase (CDH).

Characteristics	Requirements ¹⁸¹	MET (GOx ^{182,183})	DET (GDH ¹⁸⁴ /CDH ¹⁸⁵)
Linear Range (mM)	Blood: 2-10 Wound fluid: 1-2 Urine: 0.5-6 Ocular Fluid: 0.1-5 Sweat: 0.05-1 Saliva: 0.001-0.3	5·10 ⁻³ -13.1 1-12.5	3-30 0.1-30
Limit of detection (μM)	Lower Limit ~ $\frac{2}{2}$	1 600	3140 50
Sensitivity (μA.cm ⁻² .mM ⁻¹)	Blood: > 2 Ocular Fluid: ~ 10 Saliva: ~ 1000	65.8 0.66	1.33 222
Response time (s)	< 60	1-2 300	seconds —
Storage Stability (days)	> 30	20 —	43 —
Reproducibility (deviation)	< 1%	3.9% —	<10% —

It has to be noted that the required sensitivity is dependent on the type of electrode and the type of electrochemical method that is used. Nanoelectrodes for instance have a greater signal to noise ratio due to the drastic diminution of background charging effects. Therefore it enhances to easily determine nano to pico-amperes with almost no transport/diffusion effect.¹⁸⁶ Pulse and square-wave voltammetry methods drastically reduce background capacitive currents and sensitivity as low as 10^{-8}M can be achieved compared to the typical 10^{-6}M range with classic electrochemical methods.¹⁸⁷ The response time is not a critical parameter for commercial diabetic application as long as the patient can read the results in an acceptable time period. Similarly, stability is estimated to make life practical for a future patient. Price and ease of installation are other more important parameters. Table 1.3 also gathers the characteristics of promising GOx and HRP biosensors retrieved from the literature according to recent reviews.^{188–191} The MET biosensors¹⁸² are using adsorbed GOx onto ZnO nanospheres/Nafion film. The high adsorption capability of this film (high surface area and high isoelectric point) achieved the highest glucose sensitivity for the physiological glucose range. The DET-glucose dehydrogenase (GDH) example¹⁸⁴ was made by a simple GDH adsorption on a gold electrode. This study used a recombinant GDH where the FAD subunit is conserved and the subunit containing the heme is removed. The latter was found to be ineffective (acting as an insulant) in the direct electron transfer between FAD and electrode. The DET example¹⁸⁵ using cellobiose dehydrogenase as enzyme and single-walled carbon nanotubes showed that the sensitivity was increased about 30% when the nanotubes are used. This highlights the interest of conductive carbon material to virtually extend the electrode surface in three dimensions.

Regarding HRP based biosensors^{188,189,192}, the requirements are also gathered in Table 1.4. High sensitivity has to be obtained due to the micro molar range in physiological medium and the fast elimination of H_2O_2 in normal condition. Several MET, IMET and DET sensors can be found in the literature. The mediated electron transfer sensor with the highest sensitivity for the 0 - 1mM H_2O_2 range was designed using the glutaraldehyde cross-linking of HRP and gold nanoparticles in polyanilines fibers and hydroquinone as diffusing mediator.¹⁹³ Despite a wide variability depending on the architecture, IMET and DET HRP sensors had lower sensitivities. For example, the sensitivity of HRP/gold nanoparticles layer-by layer film was found to be 8 times lower when the mediator toluidine blue was immobilized.¹⁹⁴ The DET was obtained by linking covalently HRP onto gold nanoparticle, through a cysteine linker, but the overall sensitivity was 100 times lower than the best MET sensor.¹⁹⁵ Another DET biosensor based on

HRP with a reduced linear range from 0.19 to 1.9 μM was found to be 2700 times more sensitive than the previous DET sensor.¹⁹⁶ This film was based on entrapped HRP in poly(N-isopropylacrylamide-co-3-methacryloxy-propyltrimethoxysilane). The enzyme and the polymer were mixed in N,N-dimethylformamide/ water solution and dropcasted onto the electrode so it is possible that this high sensitivity is due to the use of an organic solvent. Indeed, it is known than some hydrophilic organic solvent have the capability to stimulate HRP activity and even enhance DET in some case.^{197–199} It has also to be noted that others less selective hemoproteins were used such as cytochrome C and myoglobin and enhance to achieve higher sensitivity probably due to an easier heme accessibility.

Table 1.4: Requirements for HRP biosensor in common biological medium and illustrative HRP biosensors characteristics found in the literature from a 2010-2022 period review. The classification was done depending on the electron transfer was adopted.

Characteristics	Requirements	MET ¹⁹³	IMET ¹⁹⁴	DET ^{195,196}
Linear Range (mM)	Wound: 0.1-1 ¹⁶⁹ Blood: 0-3.5·10 ⁻² ²⁰⁰ Urine: 0.005-0.1 ²⁰⁰ Ocular Fluid: up to 0.1 ²⁰⁰	0.01-2	1.5·10 ⁻⁴ -8.8	Full range: 8·10 ⁻³ -3 Low range: 1.9·10 ⁻⁴ - 1.9·10 ⁻³
Limit of detection (μM)	$\sim \frac{\text{Lower Limit}}{2}$	1.6	0.07	2 0.05
Sensitivity ($\mu\text{A}\cdot\text{cm}^{-2}\cdot\text{mM}^{-1}$)	Wound: > 10 Blood/Urine: > 100	Est. 280	Est. 34	Est. 0.23 620
Response time (s)	< 1	Est. < 5	3	5 2.5
Storage stability (days)	> 30	30	30	80 15
Reproducibility (deviation)	<1%	3.2%	3.9%* (* repetability)	4.6 % 4.6 %

III. Electro-triggered enzyme immobilization

A bioelectrode requires stable and reproducible immobilization of biomolecules on the electrode surface in order to keep as long as possible its biological activity – *i.e* the biosensor sensitivity or the biofuel cell power. Also, the immobilization method should not drastically decrease the protein activity as compared to its homogeneous activity in order to get the most active coating. The following part of this chapter will review the different enzyme immobilization principles and the different electro-triggered methods developed so far. Finally, the specific case of enzyme/nanoparticle interaction will be discussed in regard of bioelectrode manufacturing. Indeed, nanoparticles are often used in association with enzyme to boost their biocatalytic activity.

III.1 Enzyme immobilization principles

Traditionally, four methods are used for enzyme immobilization, namely (1) non-covalent adsorption and deposition, (2) physical entrapment, (3) covalent attachment/cross-linking, and (4) bio-conjugation, involving weak or covalent bonds.

III.1.1 Non-covalent adsorption and physical entrapment

Non-covalent methods of protein immobilization involve either electrostatic interactions with charged surfaces or adsorption onto hydrophobic surfaces. In general, physical bonding is comparatively weak and is hardly able to keep the enzyme fixed to the carrier under industrial conditions. The physical entrapment of enzymes requires the synthesis of the polymeric network in the presence of the enzyme. As uncoated gold and glass surface²⁰¹ are negatively charged, the electrostatic adsorption has been widely used to adsorb enzymes onto charged nanoparticles and electrodes. As most amino acids are charged, enzymes intrinsically have a global charge. When the pH is below its isoelectric point, the enzyme is positively charged and negatively charged above. In practice, most redox enzymes have a negative charge in physiological condition at pH 7.4. To adsorb negatively charged enzymes, a positively charged polymer is used as anchoring layer. By alternate deposition of polycation and enzyme, the layer-by-layer method was used to develop enzyme based coatings acting as biosensors^{202–204}. Hydrophobic and π - π interactions can also be used to adsorb enzymes as they exhibit some hydrophobic side chains at their surface. Their interactions with carbon material (graphene²⁰⁵, carbon nanotube,²⁰⁶ graphite) is therefore mainly of hydrophobic nature.

The physical entrapment requires the synthesis of a polymeric network in the presence of the enzyme. Electrophoretic deposition, electrodeposition of chitosan through solubility change, electrodeposition through ionic activation and electropolymerization are all based on physical entrapment or electrostatic interactions. These processes will be described in section III.2.2.

III.1.2 Covalent attachment and cross-linking

For more stable attachment, the formation of covalent bonds is required, and these are generally formed through surface electrode functionalization and further reaction with functional groups present on the protein surface (Figure 1.16). The covalent attachment and cross-linking of enzymes involved the use of a bifunctional reagent and can require the chemical modification of the enzymes. Several chemical methods have been used in the literature¹³³.

With thiols mono/bifunctional linkers, dense enzymes coatings were easily prepared onto gold electrode through the creation of covalent Au-S and S-S cysteine bonds²⁰⁷. This strategy is extensively used in the field of Self Assembled Monolayers (SAM). The deposition procedure typically requires sequential dipping in the thiol linker and then in the protein solution (overnight) to enhance a significant adsorption of enzymes. These coatings however suffer from several disadvantages: Au-S bond energy is only 170 kJ·mol⁻¹ and long-term stability is often bad since this bond also tend to oxidize into sulfonate and sulfonate bonds that are even weaker²⁰⁸.

The diazonium based chemistry is pretty interesting because diazonium grafting can be electrochemically triggered through a reduction/adsorption process. Thus, protein or nanoparticles bearing diazonium moieties can be electroaddressed directly onto a metal or carbon electrode by application of a typical reductive potential of -0.1 to 0.2 V vs Ag/AgCl²⁰⁹. This covalent bond chemistry is often reported to be stronger than thiol chemistry since a C-C bond is probably formed with the carbon electrode.²⁰⁸

Aldehyde/amine condensation is largely used for the cross-linking of enzymes by glutaraldehyde.²¹⁰

To use the click chemistry azide-alkyne cycloaddition, the enzymes have to be functionalized by azide or alkyne functions at their surface, using a diazo transfer like imidazole-1-sulfonyl azide.^{211,212} The diazonium strategy is often used to introduce alkyne functions using ethynylaniline derivatives.²¹³

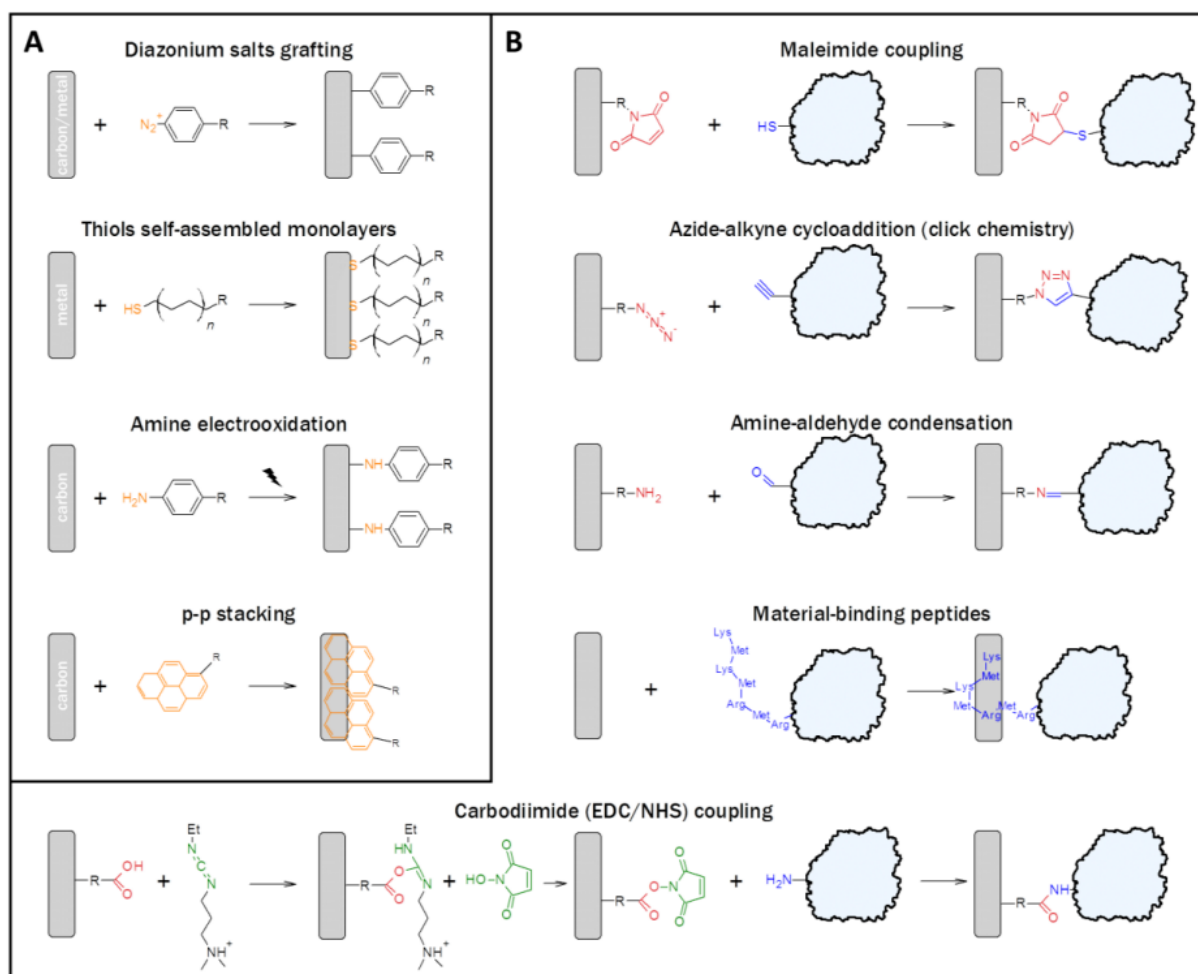


Figure 1.16: Chemical coupling reaction to immobilize proteins onto electrode. (a) chemical function to functionalize carbon electrode and (b) further strategies to bound protein to these reactive groups, adapted from [133].

The Michael addition is another commonly used strategy to immobilize enzyme that are bearing thiols moieties (i.e. reduced cysteine residues). This strategy has been used to immobilize enzyme with maleimide crosslinker²¹⁴.

Carbodiimide chemistry, using N-hydroxysuccinimide, has been successfully used to immobilize bilirubin oxidase (BOD)¹⁰⁰, GOx²¹⁵ and glutamic deshydrogenase (GluD). This method is extensively used to modify protein by fluorescent probe, redox probe as well as antibody.

III.1.3 Bio-conjugation immobilization

Over the years, a number of protein–protein and protein–small molecule binding interactions have been harnessed for immobilization. The most well-known genetically encoded affinity tag is the polyhistidine tag. The polyhistidine tag can chelate metal ions as well Nitrilotriacetic acid (NTA). Thus, NTA/ Ni^{2+} /histidine²¹⁶ is a very promising immobilization strategy for histidine containing proteins^{217,218}. NTA/ Cu^{2+} /biotin²¹⁹ is another similar strategy that requires the chemical modification of protein to graft biotin terminated functions. The coupling reaction between the enzyme and the electrode can also be through biotin/avidin^{98,220} and antigen/antibody¹⁰⁹ affinities. The phosphonate/phosphate²²¹ and adamantine/ β -cyclodextrin²²² can also be used to anchor DNA and GOx, respectively (Figure 1.17).

The affinity coupling reaction enhances the orientation of the enzyme onto the electrode for DET purpose. However, the enzymes remain weakly linked and could desorb under specific conditions (temperature, cations...).

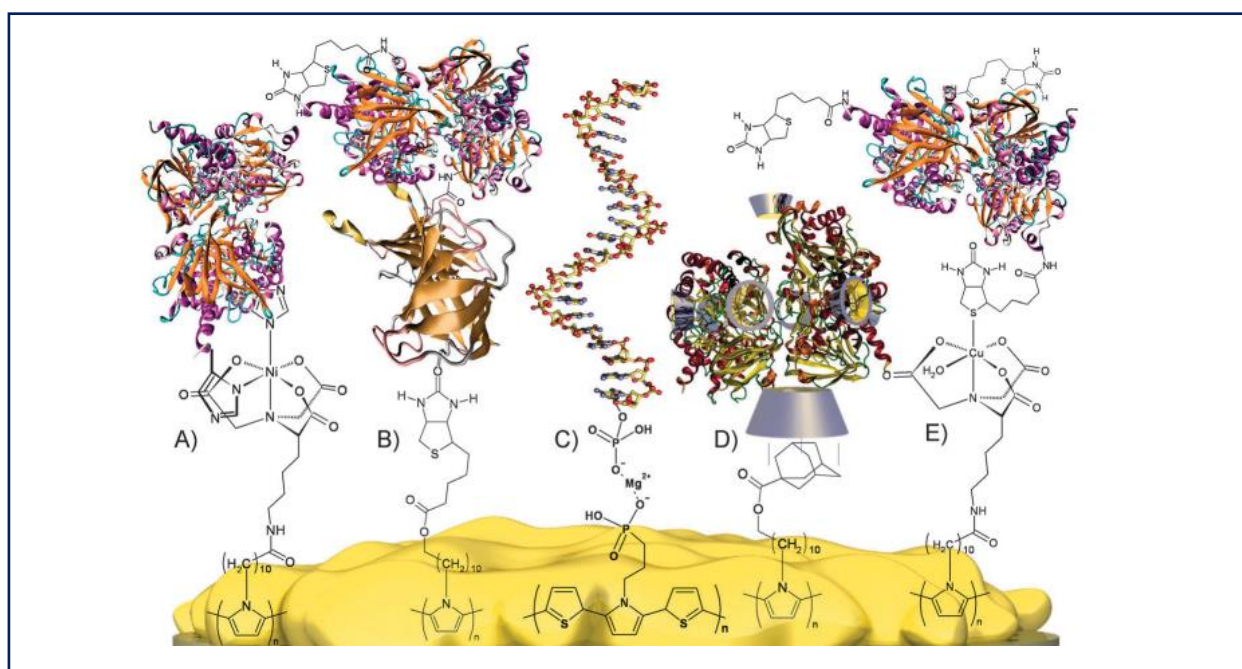


Figure 1.17: Affinity coupling system for protein immobilization according to [223]. (a) nitrilotriacetic acid/ Ni^{2+} /histidine, (b) biotin/avidin, (c) phosphonate/ Mg^{2+} /phosphate, (d) adamantine/ β -cyclodextrin and (e) nitrilotriacetic acid/ Cu^{2+} /biotin

III.2 Electro-triggered immobilization strategies

III.2.1 Manual vs electro-triggered strategies

Most bioelectrodes developed in the literature are based on the drop-casting method, due to its simplicity.^{224,225} Proteins, nanoparticles, organic molecules such as polymers or cross-linkers are blended and a drop of this mixture is deposited onto the electrode followed by a drying step (using heat, air or N₂ gas). Inkjet coating^{226,227} is also a famous technique because of its ease of implementation for large scale industrialization. Dip coating²²⁸, spin coating²²⁹ and spray/sputtering^{230,231} processes are also used to a lesser extent. All these techniques can lead sometimes to inhomogeneous deposition due to the surface tension (coffee-ring effect in dropcasting²²⁴, meniscus in dip coating²³²...) (Figure 1.18).

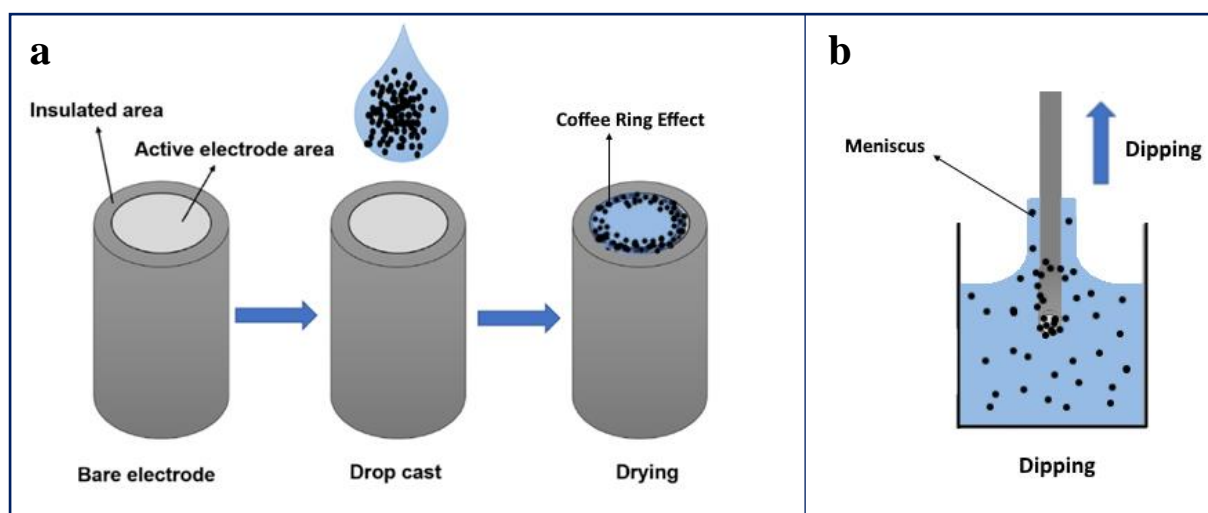


Figure 1.18: (a) Dropcasting manufacturing method adapted from [224] and (b) dip coating method

The electro-triggered enzyme immobilization methods can also face edge effects but they present several advantages, such as the spatio-temporal control of the deposition. Indeed, the use of a current or potential to induce the deposition ensures an effective control of the deposited thickness and its spatial location. This render possible the functionalization of one microelectrode out of an array, which is not possible with the previous techniques without using microfluidics. Also, electro-triggered methods may arrange under a specific pattern onto the electrode enhancing a better control of the deposit properties²³³ extending nanoarchitectonics and self-assembly to this electrolocalized deposit. Two main strategies can be distinguished: the electrochemical deposition (ECD) and the electrophoretic deposition (EPD). The ECD is based on a physico-chemical change of the solution, such as pH, composition by

electrogeneration of new species, etc...by application of the electric signal. The electro-triggered methods, reported in the literature, that have been used to immobilize enzymes according to their state in the obtained coatings will be presented: (i) physical entrapment and (ii) covalent linkage into a polymer matrix.

III.2.2 Electrodeposition of physically entrapped enzymes

III.2.2.1 Electrophoretic deposition of enzymes

Ammam and Fransaer^{36,234–246} have provided an abundant and valuable literature about EPD. The EPD is based on the diffusion of the charged enzymes toward the oppositely charged electrode under the application of a high electrical field (1-500 V) in water at low ionic strength or in organic solvent. The distance between the electrodes is rather small (mm/cm) to achieve high electrical field and pulsed signal are often chosen to prevent solvent electrolysis (bubbles) and achieve a smooth deposition^{238,247}. For EPD, many parameters can be optimized like applied current/potential (potential, time, alternating frequency,...)²⁴⁸. Thick depositions can be obtained with an adequate duration and applied potential.

To be deposited, a particle (enzyme) has to move up to the vicinity of the electrode and secondly being deposited. Hamaker²⁴⁹ has developed a simple kinetic model to explain the mobility part depending on the concentration of particles, their charge and the electrical field. When a potential field is applied, the double-layer envelope surrounding a particle is distorted to become thicker behind and thinner ahead (Figure 1.19.b). The migration of charged ions with the same charge as the particle will eventually withdraw some counter ions and make the double layer even thinner. The deposition is however not well understood but the most reported argument is that particles are neutralized because of the production of H^+ close to the electrode (water electrolysis) that lead to a charge neutralization. The coagulation/deposition of two particles is also often proposed as the deposition mechanism. Indeed, the double-layer envelope distortion can enhance particle to become close enough to induce particle coagulation via Van der Waals attractive forces.

GOx^{241,236,240}, β -galactosidase³⁶, laccase²⁴⁴ and catalase²⁴⁴ have been successfully deposited with EPD for biosensing or a biofuel cells. Several materials of different nature, such as polypyrrole and carbon nanotubes²³⁴, can be co-deposited as long as they have the same charge.

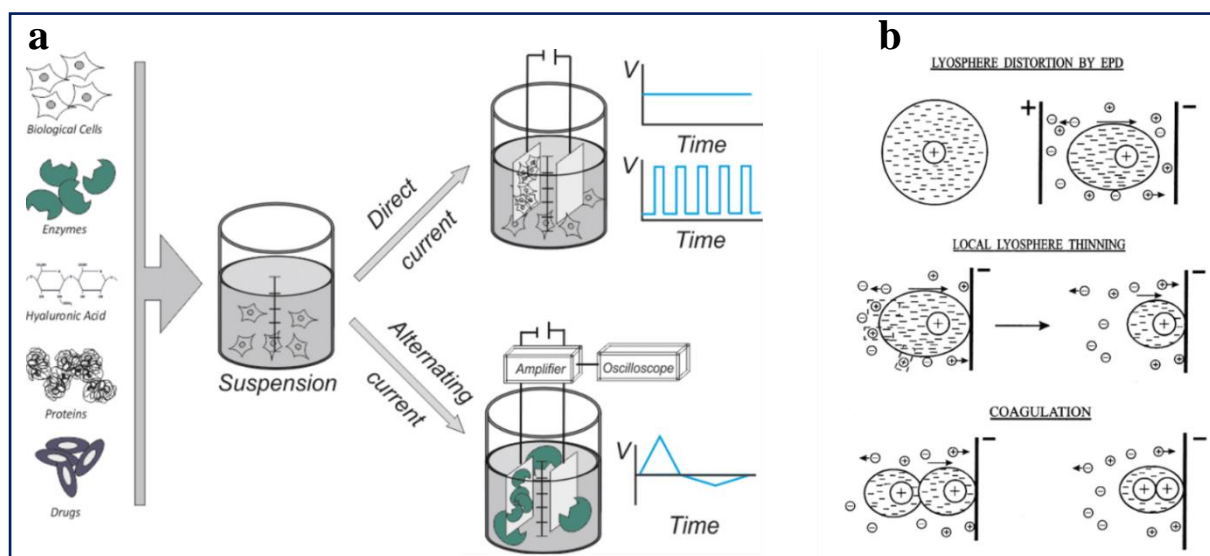


Figure 1.19: (a) Illustration of the versatility of electrophoretic deposition (EPD) under the application of alternating field according to [248] and supposition of the deposition mechanism through three steps: double layer distortion, particle migration and deposition following the distortion with Van der Waals attraction according to [250]

III.2.2.2 Electrodeposition through solubility change

The electrodeposition of the enzymes can be obtained through the solubility change of the polymer present in solution. This process is based on the creation of a H^+ or HO^- gradient at the electrode surface. Polyelectrolytes are soluble when they are charged and turned to insoluble precipitates upon the loss of the charges. To achieve their electrodeposition, a pH change of the solution can be obtained through H^+ production or consumption²⁵¹. This process has been used to “electropaint” in car industry. The electrodeposition of cathodic paints, i.e. polycations soluble at acidic pH, is based on their deprotonation at basic pH and anodic paints, using polyanions soluble at basic pH and insoluble at acidic pH. This pH change can be achieved by water electrolysis or proton-coupled redox molecules like hydroquinone. To achieve an efficient electrodeposition process through solubility change, a balance between pH-dependent group and hydrophobic side chain has to be found. Indeed, if the polymer backbone is too

hydrophilic (too many charges) its precipitation will be difficult as it requires strong pH change. On the exact contrary, if the polymer admits low charge density, it will become too hydrophobic and impossible to dissolve in water prior to deposition.²⁵² A positively charged polysaccharide, named chitosan, was found to be a good compromise and has been successfully electrodeposited by Payne and coworkers²⁵³. By application of a cathodic potential, the pH at the electrode reached a value above the pK_a of chitosan (pH > 6.3) leading to the formation of a hydrogel (Figure 1.20.c). Chitosan was largely used to entrap enzymes²⁵⁴ such as GOx^{255–259} or HRP²⁶⁰. Co-entrapment of conductive materials such as gold nanoparticles²⁶⁰ or graphite²⁵⁵ were also done with chitosan. Similar co-entrapment was proposed with alginate precipitation and HRP²⁶¹.

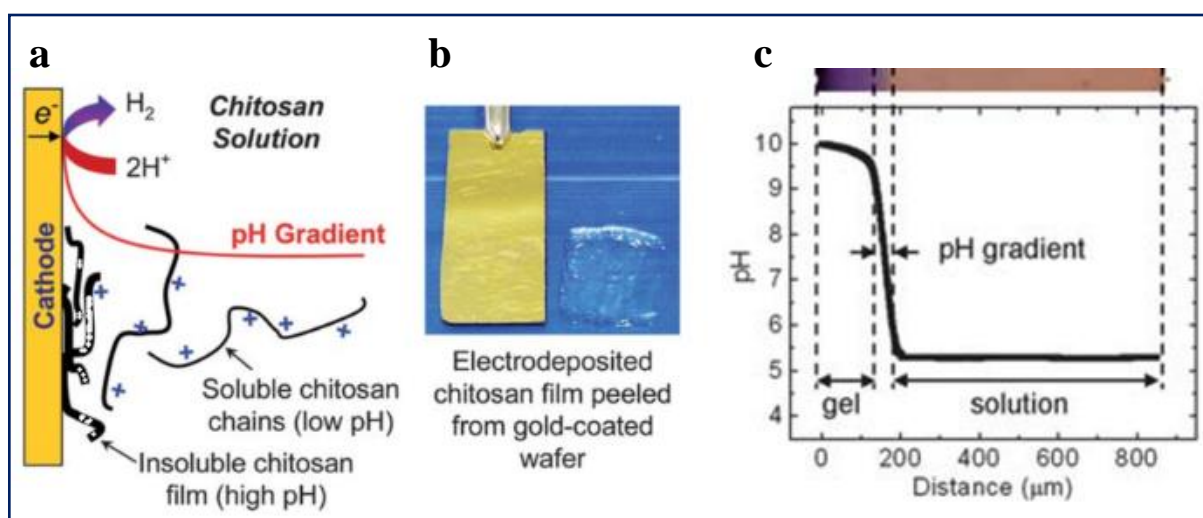


Figure 1.20: (a) Illustration of chitosan electrodeposition, (b) Picture of the obtained film according to [253] and (c) quantification of the electrodeposition pH using pH colorimetric indicator probe according to [251].

III.2.2.3 Electrodeposition through ionic activation

The electrodeposition relying on an ionic activation leads to the formation of a gel or film based on coordinate or ionic bonds. A typical example is the alginate gel formed by the presence of divalent cations, such as calcium ions, which ionically crosslink its carboxylate groups. The self-assembly of alginate gels containing GOx can be obtained by ionic activation from an electrode surface using the electrolysis of water.²⁶² Using a mixture solution of alginate, GOx, and insoluble calcium carbonate (CaCO₃) microparticles, the electrogenerated protons partially dissolve CaCO₃ releasing free calcium ions which interact with alginate to form a gel on the

surface of the electrode (Figure 1.21). Anodization was performed at 100 μA and the entrapped GOx was fully active. Fe(III)/alginate films have been also successfully prepared by Fe(II) oxidation at 0.4 V for the entrapment of BSA and GOx.²⁶³ This system has been efficiently used for the electro-release of BSA as a model protein therapeutic agent²⁶³. Fe(III)-TA coatings were electrodeposited in the same manner²⁶⁴ but was not used to immobilize enzymes.

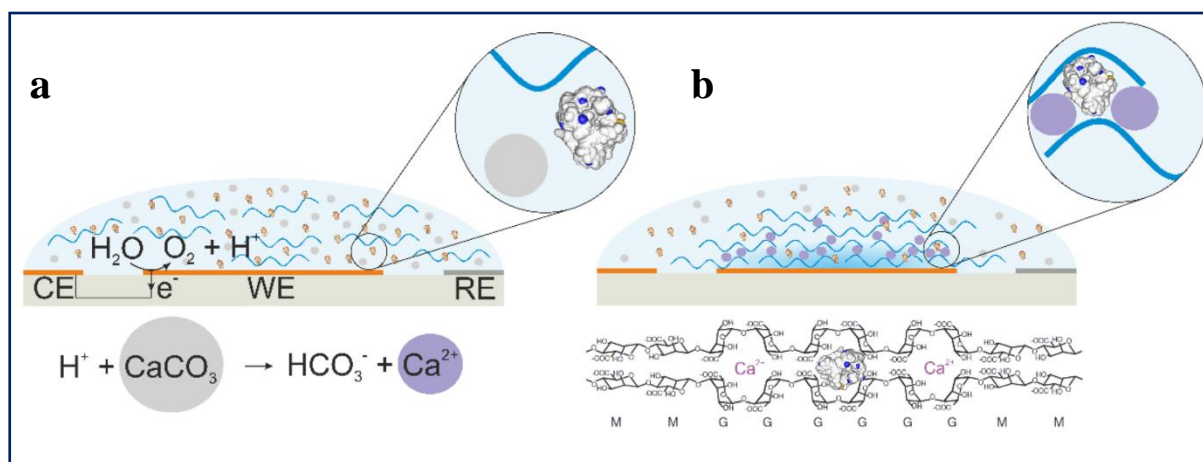


Figure 1.21: (a) Illustration of the calcium cation release via local acidification (water electrolysis) and (b) the released Ca^{2+} react with block G of alginate monomers and lead to the formation of an hydrogel that entrap glucose oxidase according to [262]

III.2.2.4 Electrodeposition through electrostatic interactions

In 2015, our team introduced a new way to electrotrigger the assembly of oppositely charged polyelectrolytes in a one pot manner (Figure 1.22).²⁶⁵ For this purpose, a charge shifting polyanion, poly(allylamine dimethylmaleic acid) (PAHd), was synthesized by modification of PAH with dimethylmaleic functions. PAHd, negatively charged at basic pH, was hydrolyzed into positively charged PAH at the application of an anodic current (above 40 μA) thanks to production of H^+ , through electrooxidation of hydroquinone. In the presence of alkaline phosphatase (AP) negatively charged, PAH/AP complexes were electrodeposited leading to an enzymatically active film. This method was proved to be used for the specific functionalization of micro-electrodes.

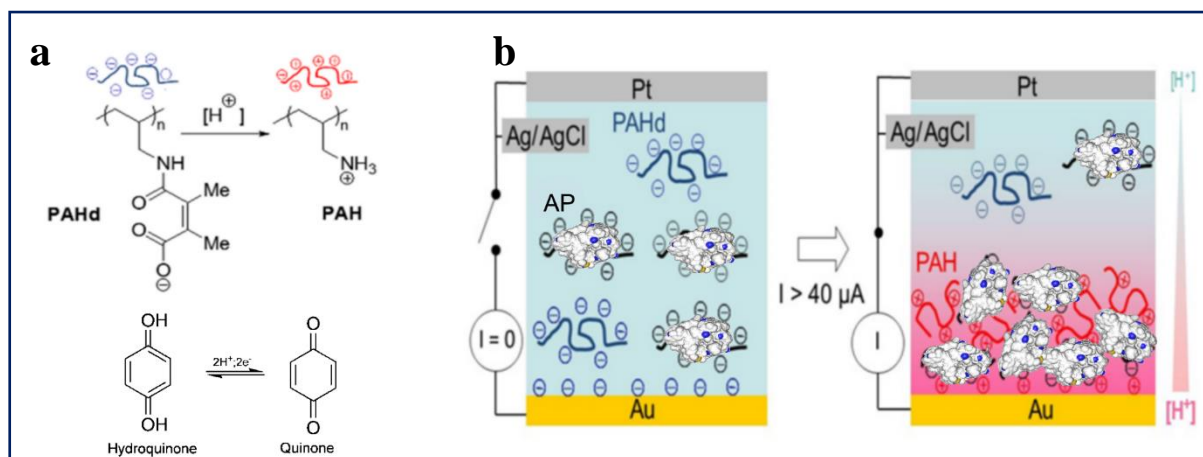


Figure 1.22: (a) Illustration of the poly(allylamine dimethylmaleic acid) (PAHd) hydrolysis at acidic pH via the electrogeneration of $[H]^+$ with hydroquinone oxidation at electrode, (b) illustration of the ON-OFF deposition by turning PAHd charge to induce electrostatic interactions according to [265]

III.2.2.5 Electropolymerization

Electropolymerization provides a major route for the synthesis of polymers to entrap enzymes. Electrochemical polymerization is generally performed in highly conductive electrolyte (0.1 - 0.5 M of salt) to prevent migration of chemicals and at relatively low potentials (0.7 - 1.2 V). It is based on the electrochemical oxidation of monomers, creating reactive radicals which polymerize and generate an insoluble polymer film. This electro-driven mechanism is an extent of the electro-dimerization⁹⁹ process. This kind of reaction is limited to monomers that can undergo an oxidation to form a radical. The process can lead to the deposition of non-conductive or conductive polymers. The deposition of non-conductive polymers generally give few nanometers film with a poor kinetic rate because only molecule in the close vicinity of the electrode can react with the electron²⁶⁶ and once the coating is done, most monomers cannot diffuse anymore inside the film. They are electrodeposited from phenol²⁶⁷, catechol, thiol²⁶⁸, amine²⁶⁹. In most case, bi/multifunctional monomers are required to enhance the deposition otherwise only dimers would be formed. Ticker coatings are obtained by electrodeposition of conducting polymers, allowing the electron hopping through the film. In this case, the main monomers used are pyrrole, aniline, thiophene or indole derivatives^{270,271,272}. Some of them can switch to a non-conductive state if undoped. For instance, a polyaniline film requires acidic environment (presence of H^+) or the presence of cations to act as a conducting polymer.²⁷³

Polypyrrole and polyaniline (Figure 1.23) have been used for GOx^{274,275}, HRP²⁷⁶ immobilization in biosensors or biofuel cells applications. The chemical polymerization of polypyrrole²⁷⁷ or PEDOT²⁷⁸ followed by the dropcasting or dipping of the solution are still widely used compared to the electropolymerization technique.

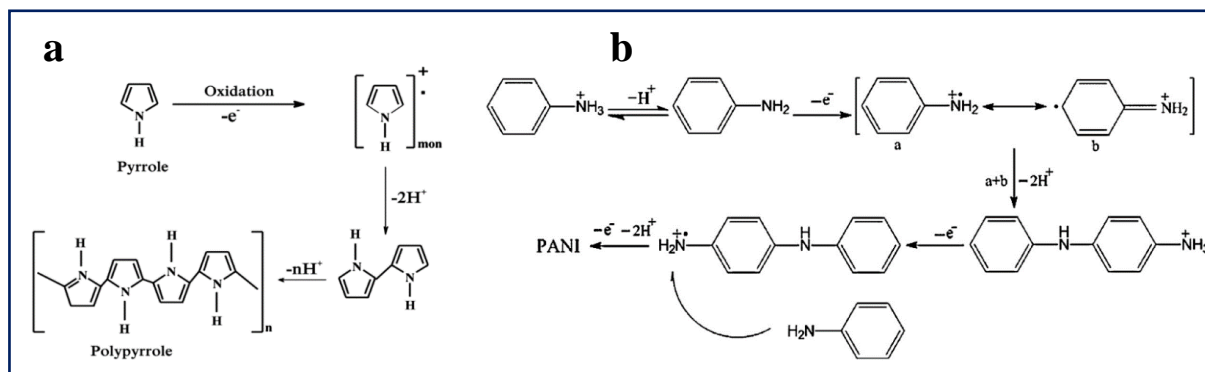


Figure 1.23: (a) Scheme for polypyrrole electropolymerization according to [279] and (b) polyaniline (PANI) electropolymerization according to [280]

III.2.3 Electrodeposition of covalently linked enzymes

This part of the chapter will describe the different methods to electrodeposit polymers and to crosslink concomitantly the enzymes to the matrix. All the previous strategies, based on the physical entrapment of enzymes, can be coupled to a crosslinking process. To this aim, the associated compound, monomer or polymer, should react chemically with the enzyme. This could be obtained in two manners: (i) the compound bearing reactive functions reacts with the chemical functions of the enzymes in the mixture solution or (ii) the electrochemical signal induces the production of a chemical compound inducing the crosslinking.

III.2.3.1 Using unmodified enzymes and reactive polymers

The electropolymerization of thiophene monomers bearing an epoxide group has been used to electrodeposit polythiophene and graft unmodified HRP²⁸¹ (Figure 1.24.a). Epoxy functions are pretty versatile to obtain covalent bonding of many nucleophiles including enzymes lysine or cysteine residues bearing primary amine and thiol group respectively.²⁸² The covalent grafting of HRP is caused by the nucleophilic ring opening of epoxide groups, favored at acidic pH. A similar strategy has been used with an epoxide bearing polymer that is electrodeposited through solubility change (pH gradient through water electrolysis).²⁸³ This deposit was stabilized by a pH-sensitive cross-linker that is concomitantly activated in the vicinity of the electrode due to

amine deprotection by triphenylmethyl group departure (Figure 1.24.b). The deprotected bisamine cross-linker can therefore stabilize the electrodeposited film by reaction with epoxy groups. Simultaneously, laccase and GOx enzymes were covalently immobilized inside the electrodeposited film through reaction of lysine residue with the epoxy pendant groups. In addition to this, Pöller *et al.* also functionalized the pH-sensitive polymer with toluidine blue or osmium complexes, both known to be excellent redox mediator for GOx and laccase respectively. Figure 1.24.b depicted the osmium-complexes used to design IMET biosensors.²⁸³

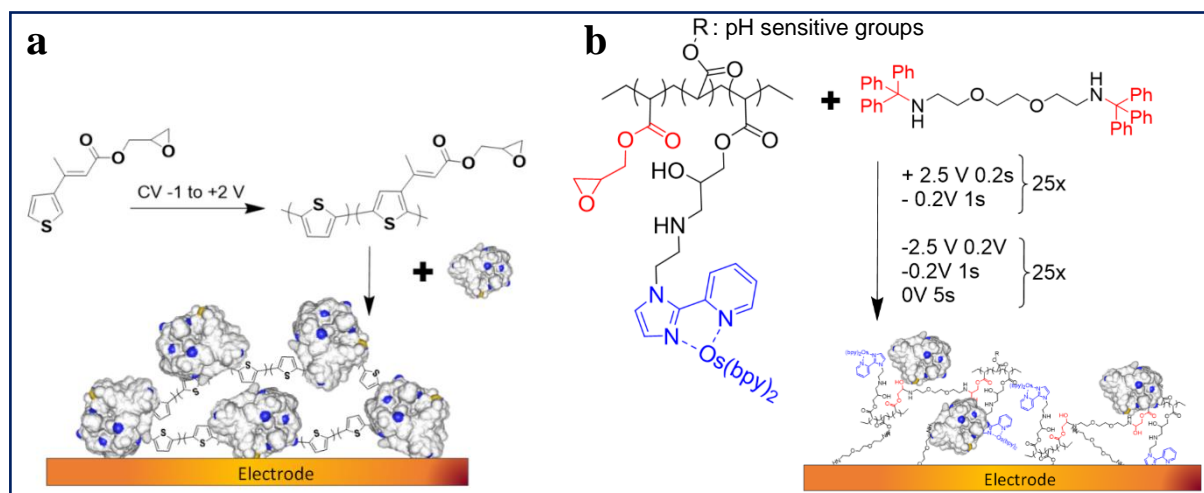


Figure 1.24: Illustration of the electrodeposition of enzyme through covalent bonds (a) a thiophene monomer bearing an epoxide function is electropolymerized and react covalently with HRP via epoxy-lysine grafting [281], (b) a polymer with a pH-dependent solubility bearing epoxide functions is electrodeposited through solubility change. Laccase and GOx are covalently bound to the resulting film via epoxy-lysine grafting. Also, a pH-sensitive triphenylmethylamine crosslinker is deprotected in the vicinity of the electrode and stabilize the film by crosslinking with epoxy. [283]

III.2.3.2 Using enzymes bearing reactive functions

Electro-triggered azide/alkyne cycloaddition can be used to immobilize covalently enzymes but require the preliminary modification of the enzyme with azide or alkyne groups. HRP was covalently electro-immobilized on a surface using this strategy²¹³. To this aim, modified HRP-N₃ was put in contact with a SAM bearing alkyne functions in the presence of CuSO₄. The application of a cathodic potential, between -0.07 and -0.4 V electrogenerate Cu(I) from Cu(II) and catalyze the Huisgen click reaction (Figure 1.25.a).²¹³ Another interesting strategy is to

directly use the enzyme, as a monomer in an electropolymerization process. GOx bearing pyrrole functions was synthesized and electrodeposited in the usual conditions of pyrrole electropolymerization²⁸⁴ (Figure 1.25.b).

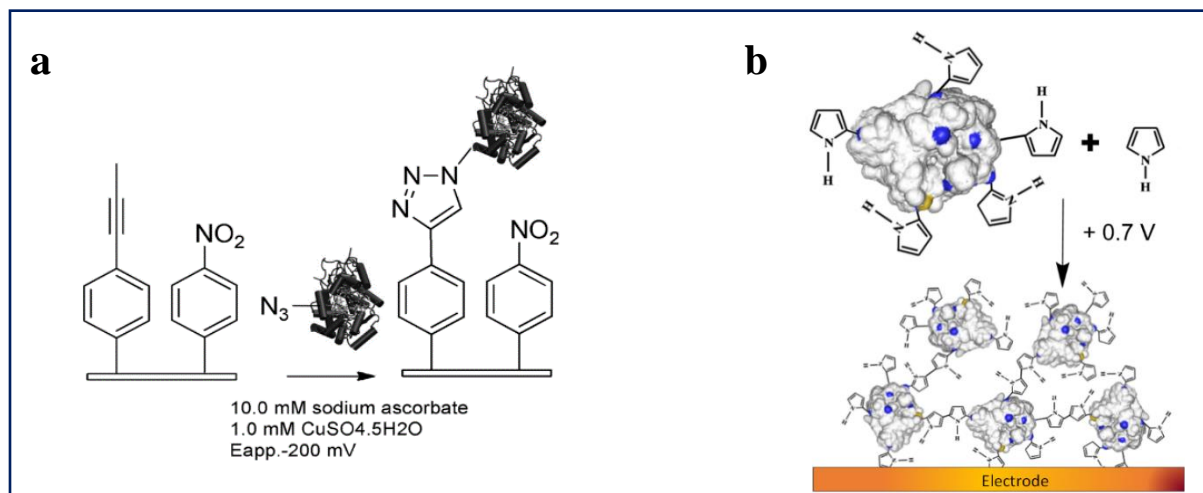


Figure 1.25: (a) a modified HRP bearing azide function react covalently with the SAM through electro-triggered cycloaddition [213]. (b) a modified GOx with pyrrole moieties is electro-dimerized [284]

III.2.3.3 Through in-situ electrogeneration of reactive function

In order to use unmodified enzymes and remove the time-consuming polymer/tether synthesis having the desired pendant group, reactive function able to undergo enzyme crosslinking can be electrogenerated *in-situ* (Figure 1.26). In 2012, Payne and co-workers reported a simple method to combine electrodeposition and enzyme crosslinking without the use of a modified monomer/polymer or modified enzyme. This process was based on the electrogeneration of HOCl/ClO⁻ species with chlor-alkali process (at 0.9 V vs Ag/AgCl or 4 A·m⁻²) in the presence of chitosan, enzyme and NaCl (Figure 1.26.a)²⁸⁵. The reaction between chitosan/enzyme carbohydrates and HOCl/ClO⁻ creates aldehyde moieties that can further react with primary amine. However, this process could induce an irreversible inactivation of the enzyme. In 2018, our team introduced a mussel-inspired electro-crosslinking process of enzymes which also did not require enzyme modification and can be used to functionalize one microelectrode out of an array¹⁸³. The exceptional ability of mussels to adhere on almost any type of surfaces is based on catechol biochemistry (i.e. hydrogen bonds, metal-ligand complexes and covalent bond formation). In particular when oxidized into quinone, catechol moieties react with nucleophilic

groups, such as amines or thiols, through Michael addition and Schiff's base formation. A synthesized homobifunctionalized catechol cross-linker was electro-oxidized to react with amine moieties of GOx by using ferrocene methanol (FcOH) as mediator (Figure 1.26.b). This process allowed to obtain GOx-based biosensor with sensitivities similar to those obtained by drop-casting using glutaraldehyde.

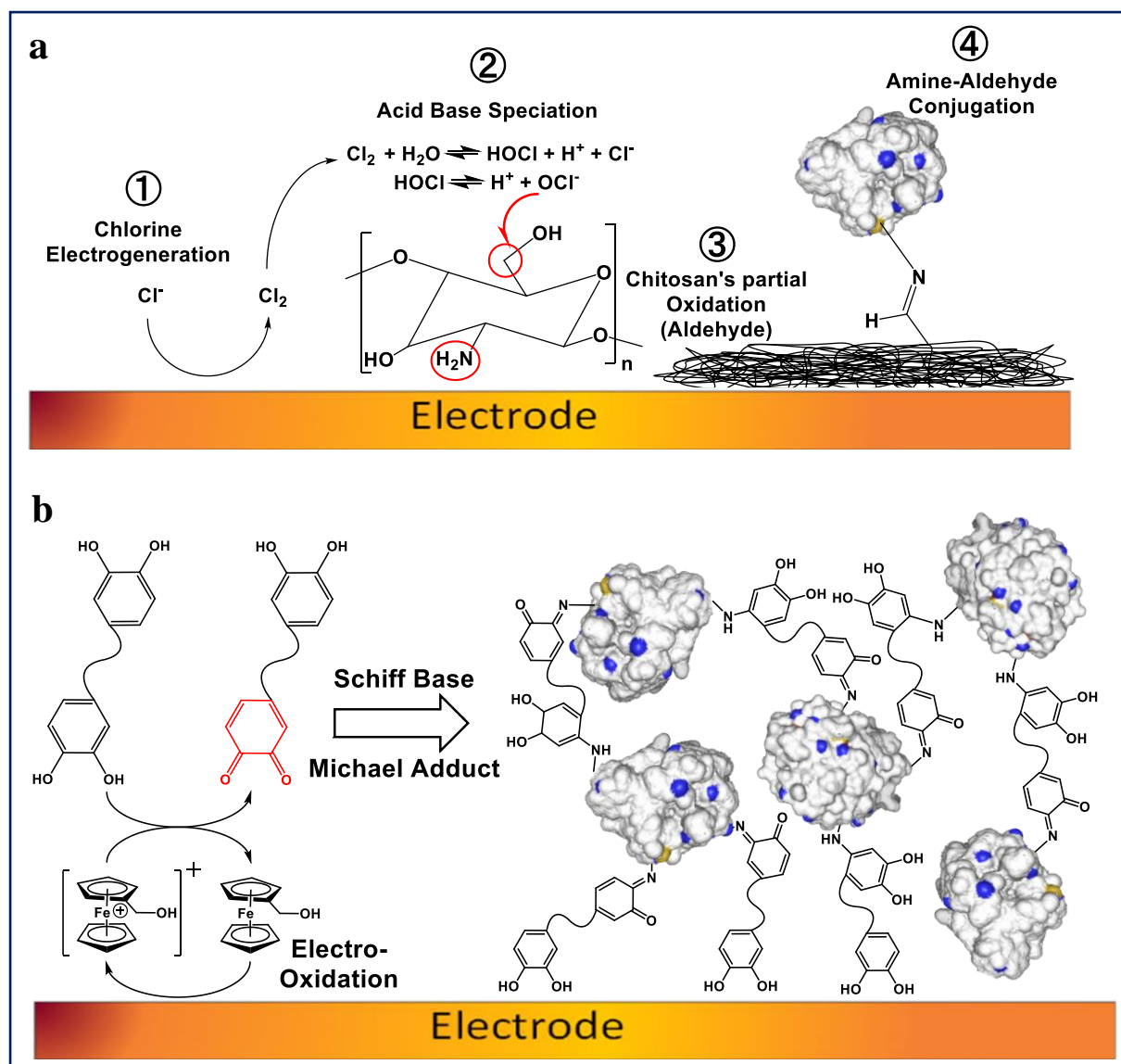


Figure 1.26: Illustration of (a) GOx grafting through HOCl production meanwhile chitosan is electrodeposited at $4 \text{ A}\cdot\text{m}^{-2}$ according to [285], (b) a chitosan catechol grafted film after application of $+0.6 \text{ V}$ and the further cross-linking and (c) the mediated electrooxidation of biscatechol into bisquinone with ferrocene methanol and its further reaction with GOx through amine and lysine functions according to [183].

III.3 Electrodeposition mechanisms

Two main electrodeposition mechanisms can be distinguished depending on the type of electrochemical reaction involved: the direct electrochemical reaction (DEC) and the redox-catalyzed electrochemical reaction (RCEC) as detailed in Figure 1.27. The DEC mechanism involves the direct exchange of electron between the molecule of interest and the electrode leading to the reaction of the molecule in solution through various homogeneous chemical reaction. The DEC mechanism is encountered in the most electrodeposition processes, such as electropolymerization, electrodeposition through ionic activation (Fe(III)/alginate²⁶³, Fe(III)/TA²⁸⁶), the electro-triggered azide/alkyne cycloaddition²⁸⁷ or the electro-crosslinking of biscatechol/PAH²⁶⁴.

RCEC is based on the use of an intermediate Nernstian redox mediator to increase the rate of the homogeneous reaction. In this case, the mediator must have a redox potential below the molecule potential for its oxidation and above for its reduction. Within a thin reaction-diffusion layer, the mediator allows to oxidize or reduce the molecule of interest. This mechanism was employed to increase the deposition rate of a biscatechol/enzyme film¹⁸³. When the deposited film is a poor conductor/insulator, the diffusion of the molecule of interest becomes limited. The oxidation or reduction of the mediator allows to settle a gradient of reactive species close to the electrode. Diffusing towards the film/solution interface, the mediator, smaller than the molecule, exchanges its electron with the molecule in solution leading to a thicker electrodeposited film.

The DEC mechanism is the association of heterogeneous electron transfer 'E' with a follow-up homogeneous chemical reaction 'C' (Table 1.5) which corresponds to the simplest electrolysis process. This homogeneous reaction happens in a reaction-diffusion layer μ whose thickness depends on the diffusion coefficient of the electrogenerated specie and the rate of the follow-up reaction. In the case of a fast electron transfer rate, diffusion/homogeneous reaction of the generated B specie into C is the rate limiting step. To be in pure kinetic solution where analytical solutions are well-known (Table 1.5), one has to study the system with a slow scan rate in cyclic voltammetry compared to the rate of the follow-up 'C' reaction. Follow-up reactions are in practice more complicated such as radical-radical dimerization and radical-substrate polymerization. When a third specie is involved, its concentration has also to be taken into account. Slight difference can be seen on the cyclic voltammetry depending of this follow-up

reaction such as FWMH or peak separation. Description of all these systems can be found in *Elements of Molecular and Biomolecular Electrochemistry*⁹⁹.

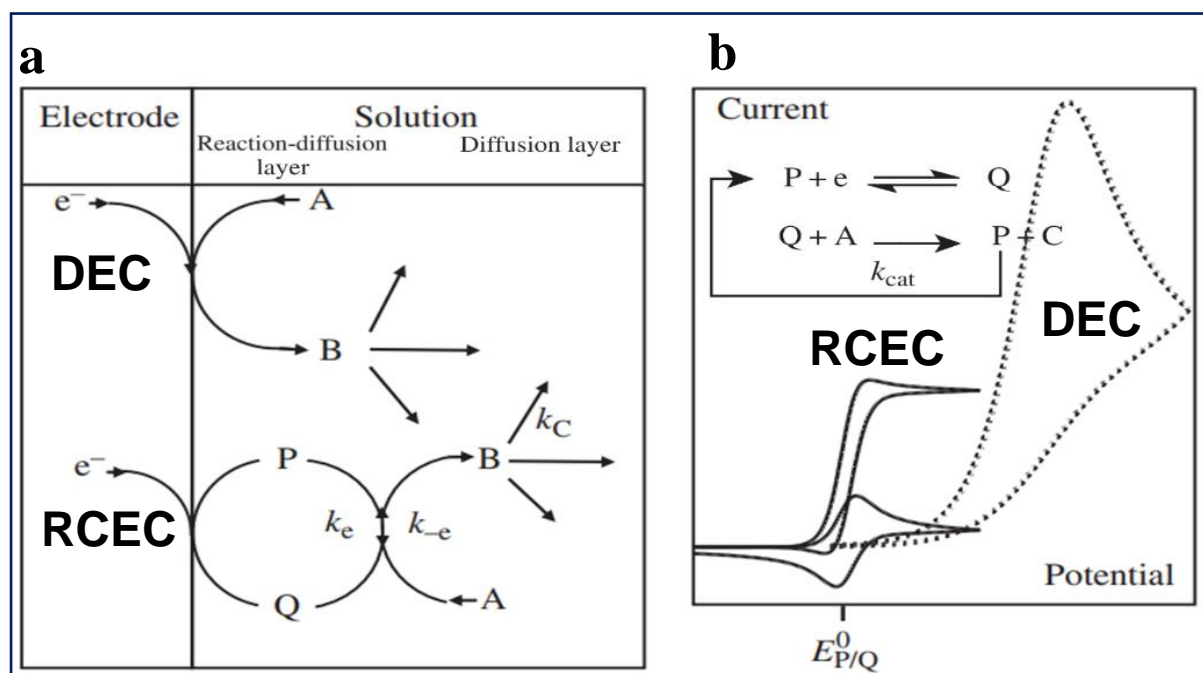


Figure 1.27: (a) Schematic representation of direct electrochemical reaction (DEC) and homogeneously redox catalyzed electrochemical reaction (RCEC). The latter is employing a P/Q redox mediator to catalyze reaction with the molecule of interest (monomer A) within a reaction-diffusion layer. (b) Illustration of cyclic voltammogram for RCEC reaction showing the response of the substrate A alone (dotted curve, DEC reaction), mediator alone ("duck" shape plain curve) and electrocatalytic current in the presence of A and P/Q mediator (S-shaped plain curve, RCEC reaction in pure kinetic condition). Figure is adapted from Saveant *et al.* [99]

RCEC has different working conditions depending on the scan rate, diffusion, mediator and substrate concentrations, reactions rates competitions and reversibility of the follow-up reaction. Compared to DEC, diffusion of the redox mediator and its concentration have to be taken into account in addition to the substrate properties. Two cases have analytical solutions and will be briefly detailed here.

The pure kinetic case is observed when the catalytic consumption of the substrate (A) is negligible. This state has a characteristic S-shape waveform (Figure 1.27.b and Table 1.5). To

reach this condition, large rate constants are required, slow scan rate and also high substrate concentration compared to the mediator concentration.

In the case of low substrate concentration compared to mediator concentration, a substrate-diffusion controlled catalysis is observed. In this case, a classical duck-shape cyclic voltammogram. The only difference with the duck-shape CV of the mediator only is the respective intensities of the redox peak and also a peak full width at half maximum (FWHM) that slightly change.⁹⁹ The complete kinetic analysis of RCEC depending on the different parameters is described in *Elements of Molecular and Biomolecular Electrochemistry*⁹⁹ but will not be detailed here.

Table 1.3: General description of DEC and RCEC mechanisms according to [99]. The follow-up reaction occurs in the characteristic diffusion layer thickness (μ)

Direct electrochemical reaction (DEC)	Homogeneous catalysis of electrochemical reaction (RCEC)
$\text{'E': } A \pm e^- \rightarrow B \quad E^0, \alpha, k_+$ $\text{'C': } B \rightarrow C \quad K=k_+$	$\text{'E': } P \pm e^- \rightleftharpoons Q \quad E^0, \alpha, k_+$ $\text{'C': } Q+A \rightarrow P+B \quad k_{cat}$
$\mu = \sqrt{D_B/k_+}$	$\mu = \sqrt{D_Q/k_{cat}C_A^0}$
Analytical solution for pure kinetic $i_p = 0.496FSC^0\sqrt{D_B}\sqrt{\frac{Fv}{RT}}$	Analytical solution for pure kinetic with no substrate consumption $i = \frac{FSC_{P/Q}^0\sqrt{D_Q}\sqrt{k_{cat}C_A^0}}{1 + \exp[\frac{F}{RT}(E - E_{P/Q}^0)]}$ Analytical solution in case of substrate-diffusion controlled catalytic wave $i_p = 0.609FSC_A^0\sqrt{D_A}\sqrt{\frac{Fv}{RT}}$

IV. References

- (1) Khandpur, R. S. Bioelectrodes: ECG Electrodes. *Compend. Biomed. Instrum.* **2020**, 177–182.
- (2) DiFrancesco, D. Pacemaker Mechanisms in Cardiac Tissue. *Annu. Rev. Physiol.* **2003**, 55, 455–472.
- (3) Lyons, M. K. Deep Brain Stimulation: Current and Future Clinical Applications. *Mayo Clin. Proc.* **2011**, 86 (7), 662–672.
- (4) Kai, H.; Yamauchi, T.; Ogawa, Y.; Tsubota, A.; Magome, T.; Miyake, T.; Yamasaki, K.; Nishizawa, M. Accelerated Wound Healing on Skin by Electrical Stimulation with a Bioelectric Plaster. *Adv. Healthc. Mater.* **2017**, 6 (22), 1700465.
- (5) Villarruel Mendoza, L. A.; Scilletta, N. A.; Bellino, M. G.; Desimone, M. F.; Catalano, P. N. Recent Advances in Micro-Electro-Mechanical Devices for Controlled Drug Release Applications. *Front. Bioeng. Biotechnol.* **2020**, 8, 827.
- (6) Sassolas, A.; Marty, J. Biocapteurs Au Service Du Diagnostic Médical. *Technique de l'Ingénieur*; 2013.
- (7) Dupont, D. Applications Des Biocapteurs : Du Contrôle Des Aliments à La Recherche de Vie Sur Mars. *Techniques de l'Ingénieur*; 2009.
- (8) Pereira da Silva Neves, M. M.; González-García, M. B.; Hernández-Santos, D.; Fanjul-Bolado, P. Future Trends in the Market for Electrochemical Biosensing. *Curr. Opin. Electrochem.* **2018**, 10 (8), 107–111.
- (9) Bahadir, E. B.; Sezgintürk, M. K. Applications of Commercial Biosensors in Clinical, Food, Environmental, and Biothreat/Biowarfare Analyses. *Anal. Biochem.* **2015**, 478 (6), 107–120.
- (10) Sant, W.; Temple-Boyer, P.; E.chanié; Launay, J.; Martinez, A. On-Line Monitoring of Urea Using Enzymatic Field Effect Transistors. *Sensors Actuators, B Chem.* **2011**, 160 (1), 59–64.
- (11) Arya, S. K.; Datta, M.; Malhotra, B. D. Recent Advances in Cholesterol Biosensor. *Biosens. Bioelectron.* **2008**, 23 (7), 1083–1100.
- (12) Pundir, S.; Chauhan, N.; Narang, J.; Pundir, C. S. Amperometric Choline Biosensor Based on Multiwalled Carbon Nanotubes/Zirconium Oxide Nanoparticles Electrodeposited on Glassy Carbon Electrode. *Anal. Biochem.* **2012**, 427 (1), 26–32.

- (13) Real-Fernández, F.; Colson, A.; Bayardon, J.; Nuti, F.; Peroni, E.; Meunier-Prest, R.; Lolli, F.; Chelli, M.; Darcel, C.; Jugé, S.; Papini, A. M. Ferrocenyl Glycopeptides as Electrochemical Probes to Detect Autoantibodies in Multiple Sclerosis Patients' Sera. *Biopolym. - Pept. Sci. Sect.* **2008**, 90 (4), 488–495.
- (14) Khan, M. Z. H.; Hasan, M. R.; Hossain, S. I.; Ahommed, M. S.; Daizy, M. Ultrasensitive Detection of Pathogenic Viruses with Electrochemical Biosensor: State of the Art. *Biosens. Bioelectron.* **2020**, 166, 112–431.
- (15) Mishra, N. N.; Retterer, S.; Zieziulewicz, T. J.; Isaacson, M.; Szarowski, D.; Mousseau, D. E.; Lawrence, D. A.; Turner, J. N. On-Chip Micro-Biosensor for the Detection of Human CD4+ Cells Based on AC Impedance and Optical Analysis. *Biosens. Bioelectron.* **2005**, 21 (5), 696–704.
- (16) Ding, C.; Zhao, F.; Zhang, M.; Zhang, S. Hybridization Biosensor Using 2,9-Dimethyl-1,10-Phenanthroline Cobalt as Electrochemical Indicator for Detection of Hepatitis B Virus DNA. *Bioelectrochemistry* **2008**, 72 (1), 28–33.
- (17) Pan, Y.; Sonn, G. A.; Sin, M. L. Y.; Mach, K. E.; Shih, M. C.; Gau, V.; Wong, P. K.; Liao, J. C. Electrochemical Immunosensor Detection of Urinary Lactoferrin in Clinical Samples for Urinary Tract Infection Diagnosis. *Biosens. Bioelectron.* **2010**, 26 (2), 649–654.
- (18) Kamikawa, T. L.; Mikolajczyk, M. G.; Kennedy, M.; Zhang, P.; Wang, W.; Scott, D. E.; Alocilja, E. C. Nanoparticle-Based Biosensor for the Detection of Emerging Pandemic Influenza Strains. *Biosens. Bioelectron.* **2010**, 26 (4), 1346–1352.
- (19) Chaibun, T.; Puenpa, J.; Ngamdee, T.; Boonapatcharoen, N.; Athamanolap, P.; O'Mullane, A. P.; Vongpunswad, S.; Poovorawan, Y.; Lee, S. Y.; Lertanantawong, B. Rapid Electrochemical Detection of Coronavirus SARS-CoV-2. *Nat. Commun.* **2021**, 12 (1), 1–10.
- (20) Radke, S. M.; Alocilja, E. C. A High Density Microelectrode Array Biosensor for Detection of E. Coli O157:H7. *Biosens. Bioelectron.* **2005**, 20 (8), 1662–1667.
- (21) Stobiecka, A.; Radecka, H.; Radecki, J. Novel Voltammetric Biosensor for Determining Acrylamide in Food Samples. *Biosens. Bioelectron.* **2007**, 22 (9–10), 2165–2170.
- (22) Kochana, J.; Wapiennik, K.; Kozak, J.; Knihnicki, P.; Pollap, A.; Woźniakiewicz, M.; Nowak, J.; Kościelniak, P. Tyrosinase-Based Biosensor for Determination of Bisphenol A in a Flow-Batch System. *Talanta* **2015**, 144, 163–170.

- (23) Zehani, N.; Fortgang, P.; Saddek Lachgar, M.; Baraket, A.; Arab, M.; Dzyadevych, S. V.; Kherrat, R.; Jaffrezic-Renault, N. Highly Sensitive Electrochemical Biosensor for Bisphenol A Detection Based on a Diazonium-Functionalized Boron-Doped Diamond Electrode Modified with a Multi-Walled Carbon Nanotube-Tyrosinase Hybrid Film. *Biosens. Bioelectron.* **2015**, *74*, 830–835.
- (24) Mercante, L. A.; Iwaki, L. E. O.; Scagion, V. P.; Oliveira, O. N.; Mattoso, L. H. C.; Correa, D. S. Electrochemical Detection of Bisphenol A by Tyrosinase Immobilized on Electrospun Nanofibers Decorated with Gold Nanoparticles. *Electrochim. Acta* **2021**, *371*, 137441.
- (25) Wu, L.; Yan, H.; Wang, J.; Liu, G.; Xie, W. Tyrosinase Incorporated with Au-Pt@SiO₂ Nanospheres for Electrochemical Detection of Bisphenol A. *J. Electrochem. Soc.* **2019**, *166* (8), B562–B568.
- (26) Kamtekar, S.; Pande, R.; Marx, K. A.; Kumar, J.; Ayyagari, M. S.; Tripathy, S. K.; Kaplan, D. L. Biosensors for Pesticide Detection Based on Alkaline Phosphatase-Catalyzed Chemiluminescence. *Sens. Actuators B* **1995**, *2*, 191–196.
- (27) Sigolaeva, L. V.; Gladyr, S. Y.; Mergel, O.; Gelissen, A. P. H.; Noyong, M.; Simon, U.; Pergushov, D. V.; Kurochkin, I. N.; Plamper, F. A.; Richtering, W.; Pergushov, D. V.; Kurochkin, I. N.; Plamper, F. A.; Richtering, W. Easy-Preparable Butyrylcholinesterase/Microgel Construct for Facilitated Organophosphate Biosensing. *Anal. Chem.* **2017**, *89* (11), 6091–6098.
- (28) Zhai, C.; Sun, X.; Zhao, W. P.; Gong, Z. L.; Wang, X. Y. Acetylcholinesterase Biosensor Based on Chitosan/Prussian Blue/Multiwall Carbon Nanotubes/Hollow Gold Nanospheres Nanocomposite Film by One-Step Electrodeposition. *Biosens. Bioelectron.* **2013**, *42*, 124–130.
- (29) Du, D.; Ding, J. W.; Cai, J.; Zhang, A. D. One-Step Electrochemically Deposited Interface of Chitosan-Gold Nanoparticles for Acetylcholinesterase Biosensor Design. *J. Electroanal. Chem.* **2007**, *605* (1), 53–60.
- (30) Song, Y. H.; Zhang, M.; Wang, L.; Wan, L. L.; Xiao, X. P.; Ye, S. H.; Wang, J. R. A Novel Biosensor Based on Acetylcholinesterase/Prussian Blue-Chitosan Modified Electrode for Detection of Carbaryl Pesticides. *Electrochim. Acta* **2011**, *56* (21), 7267–7271.
- (31) Pundir, C. S.; Chauhan, N. Acetylcholinesterase Inhibition-Based Biosensors for Pesticide Determination: A Review. *Anal. Biochem.* **2012**, *429* (1), 19–31.

- (32) Jiang, B.; Dong, P.; Zheng, J. A Novel Amperometric Biosensor Based on Covalently Attached Multilayer Assemblies of Gold Nanoparticles , Diazo-Resins and Acetylcholinesterase for the Detection of Organophosphorus Pesticides. *Talanta* **2018**, *183*, 114–121.
- (33) Mustafa, F.; Andreescu, S. Chemical and Biological Sensors for Food-Quality Monitoring and Smart Packaging. *Foods* **2018**, *7* (10), 168.
- (34) Yadav, S. K.; Singh, J.; Agrawal, V. V.; Malhotra, B. D. Nanostructured Nickel Oxide Film for Application to Fish Freshness Biosensor. *Appl. Phys. Lett.* **2012**, *101* (2), 023703.
- (35) Sharma, S. K.; Kumar, A.; Chaudhary, R.; Pundir, S.; Pundir, C. S.; Sehgal, N. Lactose Biosensor Based on Lactase and Galactose Oxidase Immobilized in Polyvinyl Formal. *Artif. Cells, Blood Substitutes, Biotechnol.* **2007**, *35* (4), 421–430.
- (36) Ammam, M.; Fransaer, J. Two-Enzyme Lactose Biosensor Based on Beta-Galactosidase and Glucose Oxidase Deposited by AC-Electrophoresis: Characteristics and Performance for Lactose Determination in Milk. *Sens. Actuators, B* **2010**, *148* (2), 583–589.
- (37) Campàs, M.; Marty, J. L. Enzyme Sensor for the Electrochemical Detection of the Marine Toxin Okadaic Acid. *Anal. Chim. Acta* **2007**, *605* (1), 87–93.
- (38) Hamada-Sato, N.; Minamitani, N.; Inaba, Y.; Nagashima, Y.; Kobayashi, T.; Imada, C.; Watanabe, E. Development of Amperometric Sensor System for , Measurement of Diarrheic Shellfish Poisoning (DSP) Toxin, Okadaic Acid (OA). *Sensors Mater.* **2004**, *16* (2), 99–107.
- (39) Campàs, M.; Prieto-Simón, B.; Marty, J. L. Biosensors to Detect Marine Toxins: Assessing Seafood Safety. *Talanta* **2007**, *72* (3), 884–895.
- (40) Xiao, X.; Xia, H. Q.; Wu, R.; Bai, L.; Yan, L.; Magner, E.; Cosnier, S.; Lojou, E.; Zhu, Z.; Liu, A. Tackling the Challenges of Enzymatic (Bio)Fuel Cells. *Chem. Rev.* **2019**, *119* (16), 9509–9558.
- (41) Rasmussen, M.; Abdellaoui, S.; Minteer, S. D.; Abdellaoui, S.; Minteer, S. D. Enzymatic Biofuel Cells: 30 Years of Critical Advancements. *Biosens. Bioelectron.* **2016**, *76*, 91–102.
- (42) Chen, Y.; Gai, P.; Xue, J.; Zhang, J. R.; Zhu, J. J. An“ON–OFF” Switchable Power Output of Enzymatic Biofuel Cell Controlled by Thermal-Sensitive Polymer. *Biosens. Bioelectron.* **2015**, *74*, 142–149.

- (43) Zang, Y.; Zhu, H.; Xue, H. Design of a Novel “ON-OFF” Switchable Enzymatic Biofuel Cell Based on PH-Sensitive PS-*b*-P4VP Diblock Copolymer. *Electrochim. Acta* **2018**, 259, 676–684.
- (44) Katz, E. Biofuel Cells with Switchable/Tunable Power Output as an Example of Implantable Bioelectronic Devices. *Signal-Switchable Electrochem. Syst.* **2018**, 229–261.
- (45) Katz, E.; Willner, I. A Biofuel Cell with Electrochemically Switchable and Tunable Power Output. *J. Am. Chem. Soc.* **2003**, 125 (22), 6803–6813.
- (46) Pardo-Yissar, V.; Katz, E.; Willner, I.; Kotlyar, A. B.; Sanders, C.; Lill, H. Biomaterial Engineered Electrodes for Bioelectronics. *Faraday Discuss.* **2000**, 116 (0), 119–134.
- (47) Description of enzymes from Toyobo Supplier https://www.toyobo-global.com/seihin/xr/enzyme/enzyme_list/ (accessed 2022 -02 -07).
- (48) Kołodziejczak-Radzimska, A.; Budna, A.; Ciesielczyk, F.; Moszyński, D.; Jesionowski, T. Laccase from *Trametes Versicolor* Supported onto Mesoporous Al₂O₃: Stability Tests and Evaluations of Catalytic Activity. *Process Biochem.* **2020**, 95, 71–80.
- (49) Zhou, M.; Wang, J. Biofuel Cells for Self-Powered Electrochemical Biosensing and Logic Biosensing: A Review. *Electroanalysis* **2012**, 24 (3), 197–209.
- (50) Grattieri, M.; Minter, S. D. Self-Powered Biosensors. *ACS Sensors* **2018**, 3 (1), 44–53.
- (51) Eugenio Katz, †; Andreas F. Bückmann, ‡ and; Itamar Willner*, †. Self-Powered Enzyme-Based Biosensors. *J. Am. Chem. Soc.* **2001**, 123 (43), 10752–10753.
- (52) Hanashi, T.; Yamazaki, T.; Tsugawa, W.; Ikebukuro, K.; Sode, K. BioRadioTransmitter: A Self-Powered Wireless Glucose-Sensing System. *J. Diabetes Sci. Technol.* **2011**, 5 (5), 1030–1035.
- (53) Tanaka, A.; Utsunomiya, F.; Douseki, T. A Wireless Self-Powered Urinary Incontinence Sensor System. In *IEEE Sensors*; 2021; Vol. 5, pp 8–12.
- (54) Tanaka, A.; Ishihara, T.; Utsunomiya, F.; Douseki, T. Wireless Self-Powered Plant Health-Monitoring Sensor System. In *IEEE Sensors*; 2012.
- (55) Hu, Y.; Zhang, Y.; Xu, C.; Lin, L.; Snyder, R. L.; Wang, Z. L. Self-Powered System with Wireless Data Transmission. *Nano Lett.* **2011**, 11 (6), 2572–2577.
- (56) Katz, E.; Privman, V. Enzyme-Based Logic Systems for Information Processing. *Chem. Soc. Rev.* **2010**, 39 (5), 1835–1857.
- (57) Amir, L.; Tam, T. K.; Pita, M.; Meijler, M. M.; Alfonta, L.; Katz, E. Biofuel Cell Controlled by Enzyme Logic Systems. *J. Am. Chem. Soc.* **2009**, 131 (2), 826–832.

- (58) Wu, H.; Liu, Y.; Li, M.; Chong, Y.; Zeng, M.; Lo, Y. M.; Yin, J. J. Size-Dependent Tuning of Horseradish Peroxidase Bioreactivity by Gold Nanoparticles. *Nanoscale* **2015**, 7 (10), 4505–4513.
- (59) Tam, T. K.; Pita, M.; Ornatska, M.; Katz, E. Biofuel Cell Controlled by Enzyme Logic Network — Approaching Physiologically Regulated Devices. *Bioelectrochemistry* **2009**, 76 (1–2), 4–9.
- (60) Baron, R.; Lioubashevski, O.; Katz, E.; Niazov, T.; Willner, I. Two Coupled Enzymes Perform in Parallel the ‘AND’ and ‘InhibAND’ Logic Gate Operations. *Org. Biomol. Chem.* **2006**, 4 (6), 989–991.
- (61) Strack, G.; Pita, M.; Ornatska, M.; Katz, E. Boolean Logic Gates That Use Enzymes as Input Signals. *ChemBioChem* **2008**, 9 (8), 1260–1266.
- (62) Zhou, M.; Zhou, N.; Kuralay, F.; Windmiller, J. R.; Parkhomovsky, S.; Valdés-Ramírez, G.; Katz, E.; Wang, J. A Self-Powered “Sense-Act-Treat” System That Is Based on a Biofuel Cell and Controlled by Boolean Logic. *Angew. Chemie Int. Ed.* **2012**, 51 (11), 2686–2689.
- (63) Carino, G. P.; Mathiowitz, E. Oral Insulin Delivery. *Adv. Drug Deliv. Rev.* **1999**, 35 (2–3), 249–257.
- (64) Ankit, B.; Rathore, R.; Tanwar, Y.; Gupta, S.; IJARPB, G. B.-; 2013, undefined. Oral Sustained Release Dosage Form: An Opportunity to Prolong the Release of Drug. *Citeseer* **2013**, 3 (1), 7–14.
- (65) Mehrotra, N.; Gupta, M.; Kovar, A.; Meibohm, B. The Role of Pharmacokinetics and Pharmacodynamics in Phosphodiesterase-5 Inhibitor Therapy. *Int. J. Impot. Res.* **2007**, 193 **2006**, 19 (3), 253–264.
- (66) Freckmann, G.; Hagenlocher, S.; Baumstark, A.; Jendrike, N.; Gillen, R. C.; Rössner, K.; Haug, C. Continuous Glucose Profiles in Healthy Subjects under Everyday Life Conditions and after Different Meals. *J. diabetes Sci. Technol.* **2007**, 1 (5), 695.
- (67) Patra, J. K.; Das, G.; Fraceto, L. F.; Campos, E. V. R.; Rodriguez-Torres, M. D. P.; Acosta-Torres, L. S.; Diaz-Torres, L. A.; Grillo, R.; Swamy, M. K.; Sharma, S.; Habtemariam, S.; Shin, H. S. Nano Based Drug Delivery Systems: Recent Developments and Future Prospects. *J. Nanobiotechnology* **2018**, 161 **2018**, 16 (1), 1–33.
- (68) Jin, Z.; Harvey, A. M.; Mailloux, S.; Halánek, J.; Bocharova, V.; Twiss, M. R.; Katz, E. Electrochemically Stimulated Release of Lysozyme from an Alginate Matrix Cross-Linked with Iron Cations. *J. Mater. Chem.* **2012**, 22 (37), 19523–19528.

- (69) Gunathilake, T. M. S. U.; Ching, Y. C.; Chuah, C. H.; Hai, N. D.; Nai-Shang, L. Electro-Stimulated Release of Poorly Water-Soluble Drug from Poly(Lactic Acid)/Carboxymethyl Cellulose/ZnO Nanocomposite Film. *Pharm. Res.* **2020**, *37* (9), 1–20.
- (70) Liu, S.; Fu, Y.; Li, G.; Li, L.; Law, H. K. wai; Chen, X.; Yan, F. Conjugated Polymer for Voltage-Controlled Release of Molecules. *Adv. Mater.* **2017**, *29* (35), 1701733.
- (71) Chang, X.; Cheng, Z.; Ren, B.; Dong, R.; Peng, J.; Fu, S.; Tong, Z. Voltage-Responsive Reversible Self-Assembly and Controlled Drug Release of Ferrocene-Containing Polymeric Superamphiphiles. *Soft Matter* **2015**, *11* (38), 7494–7501.
- (72) Zhao, Y.; Tavares, A. C.; Gauthier, M. A. Nano-Engineered Electro-Responsive Drug Delivery Systems. *J. Mater. Chem. B* **2016**, *4* (18), 3019–3030.
- (73) Carayon, I.; Gaubert, A.; Mousli, Y.; Philippe, B. Electro-Responsive Hydrogels: Macromolecular and Supramolecular Approaches in the Biomedical Field. *Biomater. Sci.* **2020**, *8* (20), 5589–5600.
- (74) Paradee, N.; Thanokiang, J.; Sirivat, A. Conductive Poly(2-Ethylaniline) Dextran-Based Hydrogels for Electrically Controlled Diclofenac Release. *Mater. Sci. Eng. C* **2021**, *118*, 111346.
- (75) Sangsuriyong, K.; Paradee, N.; Sirivat, A. Electrically Controlled Release of Anticancer Drug 5-Fluorouracil from Carboxymethyl Cellulose Hydrogels. *Int. J. Biol. Macromol.* **2020**, *165*, 865–873.
- (76) Murdan, S. Electro-Responsive Drug Delivery from Hydrogels. *J. Control. Release* **2003**, *92* (1–2), 1–17.
- (77) Kwon, I. C.; Bae, Y. H.; Kim, S. W. Electrically Erodible Polymer Gel for Controlled Release of Drugs. *Nature* **1991**, *354*, 291–293.
- (78) Sawahata, K.; Hara, M.; Yasunaga, H.; Osada, Y. Electrically Controlled Drug Delivery System Using Polyelectrolyte Gels. *J. Control. Release* **1990**, *14* (3), 253–262.
- (79) Clark Jr., L. C.; Lyons, C. Electrode Systems for Continuous Monitoring in Cardiovascular Surgery. *Ann. N. Y. Acad. Sci.* **1962**, *102*, 29–45.
- (80) Kim, E.; Liu, Y.; Bentley, W. E.; Payne, G. F.; Gregory, F.; Payne, G. F. Redox Capacitor to Establish Bio-Device Redox-Connectivity. *Adv. Funct. Mater.* **2012**, *22* (7), 1409–1416.

- (81) Wu, S.; Kim, E.; Li, J.; Bentley, W. E.; Shi, X. W.; Payne, G. F. Catechol-Based Capacitor for Redox-Linked Bioelectronics. *ACS Appl. Electron. Mater.* **2019**, *1* (8), 1337.
- (82) Wooten, M.; Karra, S.; Zhang, M.; Gorski, W. On the Direct Electron Transfer, Sensing, and Enzyme Activity in the Glucose Oxidase/Carbon Nanotubes System. *Anal. Chem.* **2014**, *86* (1), 752–757.
- (83) Raushel, F. M.; Holden, H. M. Phosphotriesterase: An Enzyme in Search of Its Natural Substrate. *Adv. Enzymol. Relat. Areas Mol. Biol.* **2000**, *74*, 51–93.
- (84) Mohd Razib, M. S.; Latip, W.; Abdul Rashid, J. I.; Knight, V. F.; Wan Yunus, W. M. Z.; Ong, K. K.; Mohd Kasim, N. A.; Mohd Noor, S. A. An Enzyme-Based Biosensor for the Detection of Organophosphate Compounds Using Mutant Phosphotriesterase Immobilized onto Reduced Graphene Oxide. *J. Chem.* **2021**, 2021.
- (85) Ghazizadeh, A. J.; Afkhami, A.; Bagheri, H. Voltammetric Determination of 4-Nitrophenol Using a Glassy Carbon Electrode Modified with a Gold-ZnO-SiO₂ Nanostructure. *Microchim. Acta 2018 1856* **2018**, *185* (6), 1–10.
- (86) Wu, J.; Wang, Q.; Umar, A.; Sun, S.; Huang, L.; Wang, J.; Gao, Y. Highly Sensitive P-Nitrophenol Chemical Sensor Based on Crystalline α -MnO₂ Nanotubes. *New J. Chem.* **2014**, *38* (9), 4420–4426.
- (87) Tang, W.; Wu, J. Amperometric Determination of Organophosphorus Pesticide by Silver Electrode Using an Acetylcholinesterase Inhibition Method. *Anal. Methods* **2014**, *6* (3), 924–929.
- (88) McGleenon, B. M.; Dynan, K. B.; Passmore, A. P. Acetylcholinesterase Inhibitors in Alzheimer's Disease. *Br. J. Clin. Pharmacol.* **1999**, *48* (4), 471.
- (89) Dvir, H.; Silman, I.; Harel, M.; Rosenberry, T. L.; Sussman, J. L. Acetylcholinesterase: From 3D Structure to Function. *Chem. Biol. Interact.* **2010**, *187* (1–3), 10–22.
- (90) Hadd, A. G.; Jacobson, S. C.; Ramsey, J. M. Microfluidic Assays of Acetylcholinesterase Inhibitors. *Anal. Chem.* **1999**, *71* (22), 5206–5212.
- (91) Lenigk, R.; Lam, E.; Lai, A.; Wang, H.; Han, Y.; Carlier, P.; Renneberg, R. Enzyme Biosensor for Studying Therapeutics of Alzheimer's Disease. *Biosens. Bioelectron.* **2000**, *15* (9–10), 541–547.
- (92) Keighron, J. D.; Wigström, J.; Kurczyk, M. E.; Bergman, J.; Wang, Y.; Cans, A. S. Amperometric Detection of Single Vesicle Acetylcholine Release Events from an Artificial Cell. *ACS Chem. Neurosci.* **2015**, *6* (1), 181–188.

- (93) Kueng, A.; Kranz, C.; Mizaikoff, B. Amperometric ATP Biosensor Based on Polymer Entrapped Enzymes. *Biosens. Bioelectron.* **2004**, *19* (10), 1301–1307.
- (94) Xu, Y.; Venton, B. J. Microelectrode Sensing of Adenosine/Adenosine-5'-Triphosphate with Fast-Scan Cyclic Voltammetry. *Electroanalysis* **2010**, *22* (11), 1167–1174.
- (95) Bourdillon, C.; Demaille, C.; Moiroux, J.; Savéant, J. M. From Homogeneous Electroenzymatic Kinetics to Antigen–Antibody Construction and Characterization of Spatially Ordered Catalytic Enzyme Assemblies on Electrodes. *Acc. Chem. Res.* **1996**, *29* (11), 529–535.
- (96) Limoges, B.; Savéant, J. M. Cyclic Voltammetry of Immobilized Redox Enzymes. Interference of Steady-State and Non-Steady-State Michaelis-Menten Kinetics of the Enzyme-Redox Cosubstrate System. *J. Electroanal. Chem.* **2003**, *549*, 61–70.
- (97) Limoges, B.; Savéant, J. M.; Yazidi, D. Quantitative Analysis of Catalysis and Inhibition at Horseradish Peroxidase Monolayers Immobilized on an Electrode Surface. *J. Am. Chem. Soc.* **2003**, *125* (30), 9192–9203.
- (98) Anicet, N.; Anne, A.; Moiroux, J.; Saveant, J. M. Electron Transfer in Organized Assemblies of Biomolecules. Construction and Dynamics of Avidin/Biotin Co-Immobilized Glucose Oxidase/Ferrocene Monolayer Carbon Electrodes [8]. *J. Am. Chem. Soc.* **1998**, *120* (28), 7115–7116.
- (99) Savéant, J.; Costentin, C. *Elements of Molecular and Biomolecular Electrochemistry*, 2nd ed.; Wiley & Sons, Ed.; Hoboken (New Jersey), 2019.
- (100) Al-Lolage, F. A.; Bartlett, P. N.; Gounel, S.; Staigre, P.; Mano, N. Site-Directed Immobilization of Bilirubin Oxidase for Electrocatalytic Oxygen Reduction. *ACS Catal.* **2019**, *9* (3), 2068–2078.
- (101) Bartlett, P. N.; Cooper, J. M. A Review of the Immobilization of Enzymes in Electropolymerized Films. *J. Electroanal. Chem.* **1993**, *362* (1–2), 1–12.
- (102) Meneghello, M.; Al-Lolage, F. A.; Ma, S.; Ludwig, R.; Bartlett, P. N. Studying Direct Electron Transfer by Site-Directed Immobilization of Cellobiose Dehydrogenase. *ChemElectroChem* **2019**, *6* (3), 700–713.
- (103) Ikeda, T.; Kano, K. An Electrochemical Approach to the Studies of Biological Redox Reactions and Their Applications to Biosensors, Bioreactors, and Biofuel Cells. *J. Biosci. Bioeng.* **2001**, *92* (1), 9–18.
- (104) Takagi, K.; Kano, K.; Ikeda, T. Mediated Bioelectrocatalysis Based on NAD-Related Enzymes with Reversible Characteristics 1. *J. Electroanal. Chem.* **1998**, *445*, 211–219.

- (105) Bollella, P.; Gorton, L.; Antiochia, R. Direct Electron Transfer of Dehydrogenases for Development of 3rd Generation Biosensors and Enzymatic Fuel Cells. *Sensors (Switzerland)* **2018**, *18* (5), 1319.
- (106) Ferapontova, E. E.; Shleev, S.; Ruzgas, T.; Stoica, L.; Christenson, A.; Tkac, J.; Yaropolov, A. I.; Gorton, L. Direct Electrochemistry of Proteins and Enzymes. *Perspect. Bioanal.* **2005**, *1*, 517–598.
- (107) Bourdillon, C.; Demaille, C.; Moiroux, J.; Savéant, J. M.; Gueris, J. A Fully Active Monolayer Enzyme Electrode Derivatized by Antigen-Antibody Attachment. *J. Am. Chem. Soc.* **2002**, *115* (26), 12264–12269.
- (108) Battaglini, F.; Calvo, E. J. Enzyme Catalysis at Hydrogel-Modified Electrodes with Soluble Redox Mediator. *J. Chem. Soc. Faraday Trans.* **1994**, *90* (7), 987–995.
- (109) Anicet, N.; Anne, A.; Bourdillon, C.; Demaille, C.; Moiroux, J.; Savéant, J. M. Electrochemical Approach to the Dynamics of Molecular Recognition of Redox Enzyme Sites by Artificial Cosubstrates in Solution and in Integrated Systems. *Faraday Discuss.* **2000**, *116* (0), 269–279.
- (110) Léger, C. *Direct Electrochemistry of Proteins and Enzymes: An Introduction*; 2012.
- (111) Rusling, J. F.; Forster, R. J. Electrochemical Catalysis with Redox Polymer and Polyion–Protein Films. *J. Colloid Interface Sci.* **2003**, *262* (1), 1–15.
- (112) Casado, N.; Hernández, G.; Sardon, H.; Mecerreyes, D. Current Trends in Redox Polymers for Energy and Medicine. *Prog. Polym. Sci.* **2016**, *52*, 107–135.
- (113) Aoki, A.; Heller, A. Electron Diffusion Coefficients in Hydrogels Formed of Cross-Linked Redox Polymers. *J. Phys. Chem.* **2002**, *97* (42), 11014–11019.
- (114) Kaneko, M. Charge Transport in Solid Polymer Matrixes with Redox Centers. *Prog. Polym. Sci.* **2001**, *26* (7), 1101–1137.
- (115) Kano, K. Redox Potentials of Proteins and Other Compounds of Bioelectrochemical Interest in Aqueous Solutions. *Rev. Polarogr.* **2002**, *48*, 29–46.
- (116) Fultz, M. Lou; Durst, R. A. Mediator Compounds for the Electrochemical Study of Biological Redox Systems: A Compilation. *Anal. Chim. Acta* **1982**, *140* (1), 1–18.
- (117) Bollella, P.; Katz, E. Enzyme-Based Biosensors: Tackling Electron Transfer Issues. *Sensors (Basel)*. **2020**, *20* (12), 1–32.
- (118) Waniek, S. D.; Klett, J.; Förster, C.; Heinze, K. Polysubstituted Ferrocenes as Tunable Redox Mediators. *Beilstein J. Org. Chem.* **2018**, *14*, 1004–1015.

- (119) Beheshti, A.; Norouzi, P.; Ganjali, M. R. A Simple and Robust Model for Predicting the Reduction Potential of Quinones Family: Electrophilicity Index Effect. *Int. J. Electrochem. Sci.* **2012**, 7 (5), 4811–4821.
- (120) Xu, S.; Minteer, S. D. Enzymatic Biofuel Cell for Oxidation of Glucose to CO₂. *ACS Catal.* **2011**, 2 (1), 91–94.
- (121) Arechederra, R. L.; Minteer, S. D. Complete Oxidation of Glycerol in an Enzymatic Biofuel Cell. *Fuel Cells* **2009**, 9 (1), 63–69.
- (122) Sokic-Lazic, D.; Minteer, S. D. Citric Acid Cycle Biomimic on a Carbon Electrode. *Biosens. Bioelectron.* **2008**, 24 (4), 939–944.
- (123) Bard, A. J.; Faulkner, L. R. *Electrochemical Methods: Fundamentals and Applications*, 2nd ed.; Wiley & Sons, Ed.; Hoboken (New Jersey), 2001.
- (124) Vogt, S.; Schneider, M.; Schäfer-Eberwein, H.; Nöll, G. Determination of the PH Dependent Redox Potential of Glucose Oxidase by Spectroelectrochemistry. *Anal. Chem.* **2014**, 86 (15), 7530–7535.
- (125) Rucker, R. B.; Chohanadisai, W. Coenzymes and Cofactors. In *Encyclopedia of Food and Health*; Elsevier, Ed.; Amsterdam (Netherlands), 2016; pp 206–224.
- (126) Broderick, J. B. Coenzymes and Cofactors. In *Encyclopedia of Life Sciences*; Sons, W. & Ed.; American Cancer Society: Hoboken (New Jersey), 2001.
- (127) Hosseinzadeh, P.; Lu, Y. Design and Fine-Tuning Redox Potentials of Metalloproteins Involved in Electron Transfer in Bioenergetics. *Biochim. Biophys. Acta - Bioenerg.* **2016**, 1857 (5), 557–581.
- (128) Léger, C.; Bertrand, P. Direct Electrochemistry of Redox Enzymes as a Tool for Mechanistic Studies. *Chem. Rev.* **2008**, 108 (7), 2379–2438.
- (129) Bollella, P.; Hibino, Y.; Kano, K.; Gorton, L.; Antiochia, R. Enhanced Direct Electron Transfer of Fructose Dehydrogenase Rationally Immobilized on a 2-Aminoanthracene Diazonium Cation Grafted Single-Walled Carbon Nanotube Based Electrode. *ACS Catal.* **2018**, 8 (11), 10279–10289.
- (130) Kizling, M.; Bilewicz, R. Fructose Dehydrogenase Electron Transfer Pathway in Bioelectrocatalytic Reactions. *ChemElectroChem* **2018**, 5 (1), 166–174.
- (131) Marcus, R. A.; Sutin, N. Electron Transfers in Chemistry and Biology. *Biochim. Biophys. Acta - Rev. Bioenerg.* **1985**, 811 (3), 265–322.
- (132) Marcus, R. A. On the Theory of Electron-Transfer Reactions. VI. Unified Treatment for Homogeneous and Electrode Reactions. *J. Chem. Phys.* **2004**, 120 (2), 679.

- (133) Mazurenko, I.; Hitaishi, V. P.; Lojou, E. Recent Advances in Surface Chemistry of Electrodes to Promote Direct Enzymatic Bioelectrocatalysis. *Curr. Opin. Electrochem.* **2020**, *19*, 113–121.
- (134) Wayu, M. B.; Pannell, M. J.; Labban, N.; Case, W. S.; Pollock, J. A.; Leopold, M. C. Functionalized Carbon Nanotube Adsorption Interfaces for Electron Transfer Studies of Galactose Oxidase. *Bioelectrochemistry* **2019**, *125*, 116–126.
- (135) Sun, D.; Cai, C.; Li, X.; Xing, W.; Lu, T. Direct Electrochemistry and Bioelectrocatalysis of Horseradish Peroxidase Immobilized on Active Carbon. *J. Electroanal. Chem.* **2004**, *566* (2), 415–421.
- (136) Xu, Y.; Peng, W.; Liu, X.; Li, G. A New Film for the Fabrication of an Unmediated H₂O₂ Biosensor. *Biosens. Bioelectron.* **2004**, *20* (3), 533–537.
- (137) Blanford, C. F.; Foster, C. E.; Heath, R. S.; Armstrong, F. A. Efficient Electrocatalytic Oxygen Reduction by the ‘Blue’ Copper Oxidase, Laccase, Directly Attached to Chemically Modified Carbons. *Faraday Discuss.* **2008**, *140* (0), 319–335.
- (138) Blanford, C. F.; Heath, R. S.; Armstrong, F. A. A Stable Electrode for High-Potential, Electrocatalytic O₂ Reduction Based on Rational Attachment of a Blue Copper Oxidase to a Graphite Surface. *Chem. Commun.* **2007**, No. 17, 1710–1712.
- (139) Tsujimura, S.; Nakagawa, T.; Kano, K.; Ikeda, T. Kinetic Study of Direct Bioelectrocatalysis of Dioxygen Reduction with Bilirubin Oxidase at Carbon Electrodes. *Electrochemistry* **2004**, *72* (6), 437–439.
- (140) Frangioni, B.; Arnoux, P.; Sabaty, M.; Pignol, D.; Bertrand, P.; Guigliarelli, B.; Léger, C. In Rhodobacter Sphaeroides Respiratory Nitrate Reductase, the Kinetics of Substrate Binding Favors Intramolecular Electron Transfer. *J. Am. Chem. Soc.* **2004**, *126* (5), 1328–1329.
- (141) Vincent, K. A.; Belsey, N. A.; Lubitz, W.; Armstrong, F. A. Rapid and Reversible Reactions of [NiFe]-Hydrogenases with Sulfide. *J. Am. Chem. Soc.* **2006**, *128* (23), 7448–7449.
- (142) Léger, C.; Dementin, S.; Bertrand, P.; Rousset, M.; Guigliarelli, B. Inhibition and Aerobic Inactivation Kinetics of Desulfovibrio Fructosovorans NiFe Hydrogenase Studied by Protein Film Voltammetry. *J. Am. Chem. Soc.* **2004**, *126* (38), 12162–12172.
- (143) Okuda-Shimazaki, J.; Yoshida, H.; Sode, K. FAD Dependent Glucose Dehydrogenases – Discovery and Engineering of Representative Glucose Sensing Enzymes -. *Bioelectrochemistry* **2020**, *132*, 107414.

- (144) Iverson, T. M.; Luna-Chavez, C.; Cecchini, G.; Rees, D. C. Structure of the Escherichia Coli Fumarate Reductase Respiratory Complex. *Science* (80-.). **1999**, 284 (5422), 1961–1966.
- (145) Léger, C.; Heffron, K.; Pershad, H. R.; Maklashina, E.; Luna-Chavez, C.; Cecchini, G.; Ackrell, B. A. C.; Armstrong, F. A. Enzyme Electrokinetics: Energetics of Succinate Oxidation by Fumarate Reductase and Succinate Dehydrogenase†. *Biochemistry* **2001**, 40 (37), 11234–11245.
- (146) Lindgren, A.; Larsson, T.; Ruzgas, T.; Gorton, L. Direct Electron Transfer between the Heme of Cellobiose Dehydrogenase and Thiol Modified Gold Electrodes. *J. Electroanal. Chem.* **2000**, 494 (2), 105–113.
- (147) Ikeda, T.; Matsushita, F.; Senda, M. Amperometric Fructose Sensor Based on Direct Bioelectrocatalysis. *Biosens. Bioelectron.* **1991**, 6 (4), 299–304.
- (148) Ikeda, T.; Kobayashi, D.; Matsushita, F.; Sagara, T.; Niki, K. Bioelectrocatalysis at Electrodes Coated with Alcohol Dehydrogenase, a Quinohemoprotein with Heme c Serving as a Built-in Mediator. *J. Electroanal. Chem.* **1993**, 361 (1–2), 221–228.
- (149) Ivnitski, D.; Atanassov, P.; Apblett, C. Direct Bioelectrocatalysis of PQQ-Dependent Glucose Dehydrogenase. *Electroanalysis* **2007**, 19 (15), 1562–1568.
- (150) Demin, S.; Hall, E. A. H. Breaking the Barrier to Fast Electron Transfer. *Bioelectrochemistry* **2009**, 76 (1–2), 19–27.
- (151) Courjean, O.; Gao, F.; Mano, N. Deglycosylation of Glucose Oxidase for Direct and Efficient Glucose Electrooxidation on a Glassy Carbon Electrode. *Angew. Chemie* **2009**, 121 (32), 6011–6013.
- (152) Guo, L.-H.; Allen, H.; Hill, O. Direct Electrochemistry of Proteins and Enzymes. *Adv. Inorg. Chem.* **1991**, 36, 341–375.
- (153) Ghindilis, A. L.; Atanasov, P.; Wilkins, E. Enzyme-Catalyzed Direct Electron Transfer: Fundamentals and Analytical Applications. *Electroanalysis* **1997**, 9 (9), 661–674.
- (154) Wu, Y.; Hu, S. Biosensors Based on Direct Electron Transfer in Redox Proteins. *Microchim. Acta 2007 1591* **2007**, 159 (1), 1–17.
- (155) Page, C. C.; Moser, C. C.; Chen, X.; Dutton, P. L. Natural Engineering Principles of Electron Tunnelling in Biological Oxidation–Reduction. *Nature* **1999**, 402 (6757), 47–52.

- (156) Capone, S.; Pletzenauer, R.; Maresch, D.; Metzger, K.; Altmann, F.; Herwig, C.; Spadiut, O. Glyco-Variant Library of the Versatile Enzyme Horseradish Peroxidase. *Glycobiology* **2014**, *24* (9), 852–863.
- (157) Kalisz, H. M.; Hendle, J.; Schmid, R. D. Structural and Biochemical Properties of Glycosylated and Deglycosylated Glucose Oxidase from *Penicillium Amagasakiense*. *Appl. Microbiol. Biotechnol.* **1997**, *47*, 502–507.
- (158) KG, W. Amino Acid Sequence Studies of Horseradish Peroxidase. Amino and Carboxyl Termini, Cyanogen Bromide and Tryptic Fragments, the Complete Sequence, and Some Structural Characteristics of Horseradish Peroxidase C. *Eur. J. Biochem.* **1979**, *96* (3), 483–502.
- (159) Krainer, F. W.; Glieder, A. An Updated View on Horseradish Peroxidases: Recombinant Production and Biotechnological Applications. *Appl. Microbiol. Biotechnol.* **2015**, *99* (4), 1611.
- (160) Rüdiger, O.; Abad, J. M.; Hatchikian, E. C.; Fernandez, V. M.; De Lacey, A. L. Oriented Immobilization of *Desulfovibrio Gigas* Hydrogenase onto Carbon Electrodes by Covalent Bonds for Nonmediated Oxidation of H₂. *J. Am. Chem. Soc.* **2005**, *127* (46), 16008–16009.
- (161) Langlais, C.; Korn, B. Recombinant Protein Expression in Bacteria. *Encyclopedic Reference of Genomics and Proteomics in Molecular Medicine*; Springer, Berlin, Heidelberg, 2005; pp 1609–1616.
- (162) Liu, S.; Ju, H. Reagentless Glucose Biosensor Based on Direct Electron Transfer of Glucose Oxidase Immobilized on Colloidal Gold Modified Carbon Paste Electrode. *Biosens. Bioelectron.* **2003**, *19*, 177–183.
- (163) Deng, S.; Jian, G.; Lei, J.; Hu, Z.; Ju, H. A Glucose Biosensor Based on Direct Electrochemistry of Glucose Oxidase Immobilized on Nitrogen-Doped Carbon Nanotubes. *Biosens. Bioelectron.* **2009**, *25* (2), 373–377.
- (164) Chen, J.; Zheng, X.; Miao, F.; Zhang, J.; Cui, X.; Zhen, W. Engineering Graphene/Carbon Nanotube Hybrid for Direct Electron Transfer of Glucose Oxidase and Glucose Biosensor. *J. Appl. Electrochem.* **2012**, *42* (10), 875–881.
- (165) Xu, Q.; Gu, S. X.; Jin, L.; Zhou, Y. E.; Yang, Z.; Wang, W.; Hu, X. Graphene/Polyaniline/Gold Nanoparticles Nanocomposite for the Direct Electron Transfer of Glucose Oxidase and Glucose Biosensing. *Sensors Actuators B Chem.* **2014**, *190*, 562–569.

- (166) Bartlett, P. N.; Al-Lolage, F. A. There Is No Evidence to Support Literature Claims of Direct Electron Transfer (DET) for Native Glucose Oxidase (GOx) at Carbon Nanotubes or Graphene. *J. Electroanal. Chem.* **2018**, *819*, 26–37.
- (167) Milton, R. D.; Minteer, S. D. Direct Enzymatic Bioelectrocatalysis: Differentiating between Myth and Reality. *J. R. Soc. Interface* **2017**, *14* (131), 253.
- (168) Lennicke, C.; Rahn, J.; Lichtenfels, R.; Wessjohann, L. A.; Seliger, B. Hydrogen Peroxide – Production, Fate and Role in Redox Signaling of Tumor Cells. *Cell Commun. Signal.* **2015**, *131* **2015**, *13* (1), 1–19.
- (169) Zhu, G.; Wang, Q.; Lu, S.; Niu, Y. Hydrogen Peroxide: A Potential Wound Therapeutic Target? *Med. Princ. Pract.* **2017**, *26* (4), 301.
- (170) Sies, H. Role of Metabolic H₂O₂ Generation: Redox Signaling and Oxidative Stress. *J. Biol. Chem.* **2014**, *289* (13), 8735–8741.
- (171) Goran, J. M.; Mantilla, S. M.; Stevenson, K. J. Influence of Surface Adsorption on the Interfacial Electron Transfer of Flavin Adenine Dinucleotide and Glucose Oxidase at Carbon Nanotube and Nitrogen-Doped Carbon Nanotube Electrodes. *Anal. Chem.* **2013**, *85* (3), 1571–1581.
- (172) Wang, Y.; Yao, Y. Direct Electron Transfer of Glucose Oxidase Promoted by Carbon Nanotubes Is without Value in Certain Mediator-Free Applications. *Microchim. Acta* **2012**, *176* (3–4), 271–277.
- (173) Blazek, T.; Gorski, W. Oxidases, Carbon Nanotubes, and Direct Electron Transfer: A Cautionary Tale. *Biosens. Bioelectron.* **2020**, *163*, 112260.
- (174) Ishida, K.; Orihara, K.; Muguruma, H.; Iwasa, H.; Hiratsuka, A.; Tsuji, K.; Kishimoto, T. Comparison of Direct and Mediated Electron Transfer in Electrodes with Novel Fungal Flavin Adenine Dinucleotide Glucose Dehydrogenase. *Anal. Sci.* **2018**, *34* (7), 783–787.
- (175) Hanin, I.; Massarelli, R.; Costa, E. Acetylcholine Concentrations in Rat Brain: Diurnal Oscillation. *Science* (80-.). **1970**, *170* (3955), 341–342.
- (176) Moulin-Mares, S. R. A.; Zaniqueli, D.; Olios, P. R.; Alvim, R. O.; Bottoni, J. P.; Mill, J. G. Uric Acid Reference Values: Report on 1750 Healthy Brazilian Children and Adolescents. *Pediatr. Res.* **2020**, *89* (7), 1855–1860.
- (177) Robert S., P.; Justin, K. *The Merck Manual of Diagnosis and Therapy*, 19th ed.; Merck Sharp & Dohme Corp, Ed.; Whitehouse Station, NJ, 2011.

- (178) Wang, Y. Creating Ultrafast Biosensors for Neuroscience, Thesis under Supervision of Cans A.S., Chalmers University of Technology, 2019.
- (179) Wang, Y.; Mishra, D.; Bergman, J.; Keighron, J. D.; Skibicka, K. P.; Cans, A. S. Ultrafast Glutamate Biosensor Recordings in Brain Slices Reveal Complex Single Exocytosis Transients. *ACS Chem. Neurosci.* **2019**, *10* (3), 1744–1752.
- (180) Helassa, N.; Dürst, C. D.; Coates, C.; Kerruth, S.; Arif, U.; Schulze, C.; Simon Wiegert, J.; Geeves, M.; Oertner, T. G.; Török, K. Ultrafast Glutamate Sensors Resolve High-Frequency Release at Schaffer Collateral Synapses. *Proc. Natl. Acad. Sci. U. S. A.* **2017**, *115* (21), 5594–5599.
- (181) Du, Y.; Zhang, W.; Wang, M. L. An On-Chip Disposable Salivary Glucose Sensor for Diabetes Control. *J. Diabetes Sci. Technol.* **2016**, *10* (6), 1344–1352.
- (182) Fang, B.; Zhang, C.; Wang, G.; Wang, M.; Ji, Y. A Glucose Oxidase Immobilization Platform for Glucose Biosensor Using ZnO Hollow Nanospheres. *Sensors Actuators B Chem.* **2011**, *155* (1), 304–310.
- (183) El-Maiss, J.; Cuccarese, M.; Lupattelli, P.; Chiummiento, L.; Funicello, M.; Schaaf, P.; Boulmedais, F. Mussel-Inspired Electro-Cross-Linking of Enzymes for the Development of Biosensors. *ACS Appl. Mater. Inter.* **2018**, *10* (22), 18574–18584.
- (184) Lee, H.; Lee, Y. S.; Reginald, S. S.; Baek, S.; Lee, E. M.; Choi, I. G.; Chang, I. S. Biosensing and Electrochemical Properties of Flavin Adenine Dinucleotide (FAD)-Dependent Glucose Dehydrogenase (GDH) Fused to a Gold Binding Peptide. *Biosens. Bioelectron.* **2020**, *165*, 112427.
- (185) Tasca, F.; Zafar, M. N.; Harreither, W.; Nöll, G.; Ludwig, R.; Gorton, L. A Third Generation Glucose Biosensor Based on Cellobiose Dehydrogenase from *Corynascus Thermophilus* and Single-Walled Carbon Nanotubes. *Analyst* **2011**, *136* (10), 2033–2036.
- (186) Wahl, A.; O’Riordan, A. Chapter 6: Nanoelectrodes in Electrochemical Analysis. *RSC Detect. Sci.* **2015**, *2016-January* (6), 205–228.
- (187) Kounaves, S. P. Voltammetric Techniques
<https://www.brown.edu/Departments/Engineering/Courses/En123/Lectures/potentiostat.pdf> (accessed 2022 -02 -05).
- (188) Ali, J.; Najeeb, J.; Asim Ali, M.; Farhan Aslam, M.; Raza, A. Biosensors: Their Fundamentals, Designs, Types and Most Recent Impactful Applications: A Review. *J. Biosens. Bioelectron.* **2017**, *8* (1), 1000235.

- (189) Chen, S.; Yuan, R.; Chai, Y.; Hu, F. Electrochemical Sensing of Hydrogen Peroxide Using Metal Nanoparticles: A Review. *Microchim. Acta* **2013**, *180* (1), 15–32.
- (190) Johnston, L.; Wang, G.; Hu, K.; Qian, C.; Liu, G. Advances in Biosensors for Continuous Glucose Monitoring Towards Wearables. *Front. Bioeng. Biotechnol.* **2021**, *9*, 733810.
- (191) Teymourian, H.; Barfidokht, A.; Wang, J. Electrochemical Glucose Sensors in Diabetes Management: An Updated Review (2010–2020). *Chem. Soc. Rev.* **2020**, *49* (21), 7671–7709.
- (192) Zuccarello, L.; Barbosa, C.; Todorovic, S.; Silveira, C. M. Electrocatalysis by Heme Enzymes—Applications in Biosensing. *Catal. 2021, Vol. 11, Page 218* **2021**, *11* (2), 218.
- (193) Chen, X.; Chen, Z.; Zhu, J.; Xu, C.; Yan, W.; Yao, C. A Novel H₂O₂ Amperometric Biosensor Based on Gold Nanoparticles/Self-Doped Polyaniline Nanofibers. *Bioelectrochemistry* **2011**, *82* (2), 87–94.
- (194) Chen, S.; Yuan, R.; Chai, Y.; Xu, L.; Wang, N.; Li, X.; Zhang, L. Amperometric Hydrogen Peroxide Biosensor Based on the Immobilization of Horseradish Peroxidase (HRP) on the Layer-by-Layer Assembly Films of Gold Colloidal Nanoparticles and Toluidine Blue. *Electroanalysis* **2006**, *18* (5), 471–477.
- (195) Wang, J.; Wang, L.; Di, J.; Tu, Y. Electrodeposition of Gold Nanoparticles on Indium/Tin Oxide Electrode for Fabrication of a Disposable Hydrogen Peroxide Biosensor. *Talanta* **2009**, *77* (4), 1454–1459.
- (196) Sun, Y. X.; Zhang, J. T.; Huang, S. W.; Wang, S. F. Hydrogen Peroxide Biosensor Based on the Bioelectrocatalysis of Horseradish Peroxidase Incorporated in a New Hydrogel Film. *Sensors Actuators B Chem.* **2007**, *124* (2), 494–500.
- (197) Machado, M. F.; Saraiva, J. Inactivation and Reactivation Kinetics of Horseradish Peroxidase in Phosphate Buffer and Buffer–Dimethylformamide Solutions. *J. Mol. Catal. B Enzym.* **2002**, *19–20*, 451–457.
- (198) Batra, R.; Gupta, M. N. Enhancement of Enzyme Activity in Aqueous-Organic Solvent Mixtures. *Biotechnol. Lett.* **1994**, *16* (10), 1059–1064.
- (199) Guo, Y.; Guadalupe, A. R. Direct Electrochemistry of Horseradish Peroxidase Adsorbed on Glassy Carbon Electrode from Organic Solutions. *Chem. Commun.* **1997**, No. 15, 1437–1438.
- (200) Halliwell, B.; Clement, M. V.; Long, L. H. Hydrogen Peroxide in the Human Body. *FEBS Lett.* **2000**, *486* (1), 10–13.

- (201) Behrens, S. H.; Grier, D. G. The Charge of Glass and Silica Surfaces. *J. Chem. Phys.* **2001**, *115* (14), 6716.
- (202) Ai, H.; Jones, S. A.; Lvov, Y. M. Biomedical Applications of Electrostatic Layer-by-Layer Nano-Assembly of Polymers, Enzymes, and Nanoparticles. *Cell Biochem. Biophys.* **2003**, *39* (1), 23–43.
- (203) Forzani, E. S.; López Teijelo, M.; Nart, F.; Calvo, E. J.; Solís, V. M. Effect of the Polycation Nature on the Structure of Layer-by-Layer Electrostatically Self-Assembled Multilayers of Polyphenol Oxidase. *Biomacromolecules* **2003**, *4* (4), 869–879.
- (204) Xing, Q.; Eadula, S. R.; Lvov, Y. M. Cellulose Fiber–Enzyme Composites Fabricated through Layer-by-Layer Nanoassembly. *Biomacromolecules* **2007**, *8* (6), 1987–1991.
- (205) Li, X.; Yin, Z.; Cui, X.; Yang, L. Capillary Electrophoresis-Integrated Immobilized Enzyme Microreactor with Graphene Oxide as Support: Immobilization of Negatively Charged L-Lactate Dehydrogenase via Hydrophobic Interactions. *Electrophoresis* **2020**, *41* (3–4), 175–182.
- (206) Kim, B. C.; Lee, I.; Kwon, S. J.; Wee, Y.; Kwon, K. Y.; Jeon, C.; An, H. J.; Jung, H. T.; Ha, S.; Dordick, J. S.; Kim, J. Fabrication of Enzyme-Based Coatings on Intact Multi-Walled Carbon Nanotubes as Highly Effective Electrodes in Biofuel Cells. *Sci. Reports* **2017**, *7* (1), 1–10.
- (207) Hitaishi, V. P.; Mazurenko, I.; Harb, M.; Clément, R.; Taris, M.; Castano, S.; Duché, D.; Lecomte, S.; Ilbert, M.; De Poulpiquet, A.; Lojou, E. Electrostatic-Driven Activity, Loading, Dynamics, and Stability of a Redox Enzyme on Functionalized-Gold Electrodes for Bioelectrocatalysis. *ACS Catal.* **2018**, *8* (12), 12004–12014.
- (208) Gooding, J. J. Advances in Interfacial Design for Electrochemical Biosensors and Sensors: Aryl Diazonium Salts for Modifying Carbon and Metal Electrodes. *Electroanalysis* **2008**, *20* (6), 573–582.
- (209) Allongue, P.; Delamar, M.; Desbat, B.; Fagebaume, O.; Hitmi, R.; Pinson, J.; Savéant, J. M. Covalent Modification of Carbon Surfaces by Aryl Radicals Generated from the Electrochemical Reduction of Diazonium Salts. *J. Am. Chem. Soc.* **1997**, *119* (1), 201–207.
- (210) Walt, D. R.; Agayn, V. I. The Chemistry of Enzyme and Protein Immobilization with Glutaraldehyde. *TrAC Trends Anal. Chem.* **1994**, *13* (10), 425–430.

- (211) Van Dongen, S. F. M.; Teeuwen, R. L. M.; Nallani, M.; Van Berkel, S. S.; Cornelissen, J. J. L. M.; Nolte, R. J. M.; Van Hest, J. C. M. Single-Step Azide Introduction in Proteins via an Aqueous Diazo Transfer. *Bioconjug. Chem.* **2009**, *20* (1), 20–23.
- (212) Ran, Q.; Peng, R.; Liang, C.; Ye, S.; Xian, Y.; Zhang, W.; Jin, L. Covalent Immobilization of Horseradish Peroxidase via Click Chemistry and Its Direct Electrochemistry. *Talanta* **2011**, *83* (5), 1381–1385.
- (213) Hayat, A.; Marty, J. L.; Radi, A. E. Novel Amperometric Hydrogen Peroxide Biosensor Based on Horseradish Peroxidase Azide Covalently Immobilized on Ethynyl-Modified Screen-Printed Carbon Electrode via Click Chemistry. *Electroanalysis* **2012**, *24* (6), 1446–1452.
- (214) Belbekhouche, S.; Guerrouache, M.; Carbonnier, B. Thiol–Maleimide Michael Addition Click Reaction: A New Route to Surface Modification of Porous Polymeric Monolith. *Macromol. Chem. Phys.* **2016**, *217* (8), 997–1006.
- (215) Huang, Y.; Dong, X.; Shi, Y.; Li, C. M.; Li, L.-J. J.; Chen, P. Nanoelectronic Biosensors Based on CVD Grown Graphene. *Nanoscale* **2010**, *2* (8), 1485.
- (216) Davis, J.; Glidle, A.; G Cass, A. E.; Zhang, J.; Cooper, J. M. Spectroscopic Evaluation of Protein Affinity Binding at Polymeric Biosensor Films Scheme 1. *J. Chem. Soc., Chem. Commun* **1996**, *35* (6), 12.
- (217) Breger, J. C.; Oh, E.; Susumu, K.; Klein, W. P.; Walper, S. A.; Ancona, M. G.; Medintz, I. L. Nanoparticle Size Influences Localized Enzymatic Enhancement - A Case Study with Phosphotriesterase. *Bioconjug. Chem.* **2019**, *30* (7), 2060–2074.
- (218) Lata, J. P.; Gao, L.; Mukai, C.; Cohen, R.; Nelson, J. L.; Anguish, L.; Coonrod, S.; Travis, A. J. Effects of Nanoparticle Size on Multilayer Formation and Kinetics of Tethered Enzymes. *Bioconjug. Chem.* **2015**, *26* (9), 1931–1938.
- (219) Baur, J.; Holzinger, M.; Gondran, C.; Cosnier, S. Immobilization of Biotinylated Biomolecules onto Electropolymerized Poly(Pyrrole-Nitrilotriacetic Acid)–Cu²⁺ Film. *Electrochem. commun.* **2010**, *12* (10), 1287–1290.
- (220) Cosnier, S. Biosensors Based on Immobilization of Biomolecules by Electrogenated Polymer Films. *Appl. Biochem. Biotechnol.* **2000**, *89* (2), 127–138.
- (221) Thompson, L. A.; Kowalik, J.; Josowicz, M.; Janata, J. Label-Free DNA Hybridization Probe Based on a Conducting Polymer. *J. Am. Chem. Soc.* **2002**, *125* (2), 324–325.

- (222) Holzinger, M.; Bouffier, L.; Villalonga, R.; Cosnier, S. Adamantane/ β -Cyclodextrin Affinity Biosensors Based on Single-Walled Carbon Nanotubes. *Biosens. Bioelectron.* **2009**, *24* (5), 1128–1134.
- (223) Cosnier, S.; Holzinger, M. Electrosynthesized Polymers for Biosensing. *Chem. Soc. Rev.* **2011**, *40* (5), 2146–2156.
- (224) Kaliyaraj Selva Kumar, A.; Zhang, Y.; Li, D.; Compton, R. G. A Mini-Review: How Reliable Is the Drop Casting Technique? *Electrochem. commun.* **2020**, *121*, 106867.
- (225) Ahmad, R.; Wolfbeis, O. S.; Hahn, Y. B.; Alshareef, H. N.; Torsi, L.; Salama, K. N. Deposition of Nanomaterials: A Crucial Step in Biosensor Fabrication. *Mater. Today Commun.* **2018**, *17*, 289–321.
- (226) Setti, L.; Fraleoni-Morgera, A.; Mencarelli, I.; Filippini, A.; Ballarin, B.; Di Biase, M. An HRP-Based Amperometric Biosensor Fabricated by Thermal Inkjet Printing. *Sensors Actuators B Chem.* **2007**, *126* (1), 252–257.
- (227) Kassal, P.; Kim, J.; Kumar, R.; De Araujo, W. R.; Steinberg, I. M.; Steinberg, M. D.; Wang, J. Smart Bandage with Wireless Connectivity for Uric Acid Biosensing as an Indicator of Wound Status. *Electrochem. commun.* **2015**, *56*, 6–10.
- (228) Brice, I.; Grundsteins, K.; Atvars, A.; Alnis, J.; Viter, R.; Ramanavicius, A. Whispering Gallery Mode Resonator and Glucose Oxidase Based Glucose Biosensor. *Sensors Actuators B Chem.* **2020**, *318*, 128004.
- (229) Rathinamala, I.; Jeyakumaran, N.; Prithivikumaran, N. Sol-Gel Assisted Spin Coated CdS/PS Electrode Based Glucose Biosensor. *Vacuum* **2019**, *161*, 291–296.
- (230) Naderi Asrami, P.; Aberoomand Azar, P.; Saber Tehrani, M.; Mozaffari, S. A. Glucose Oxidase/Nano-ZnO/Thin Film Deposit FTO as an Innovative Clinical Transducer: A Sensitive Glucose Biosensor. *Front. Chem.* **2020**, *8*, 503.
- (231) Samavat, S.; Lloyd, J.; O'Dea, L.; Zhang, W.; Preedy, E.; Luzio, S.; Teng, K. S. Uniform Sensing Layer of Immiscible Enzyme-Mediator Compounds Developed via a Spray Aerosol Mixing Technique towards Low Cost Minimally Invasive Microneedle Continuous Glucose Monitoring Devices. *Biosens. Bioelectron.* **2018**, *118*, 224–230.
- (232) Javidi, M.; Pope, M. A.; Hrymak, A. N. Investigation on Dip Coating Process by Mathematical Modeling of Non-Newtonian Fluid Coating on Cylindrical Substrate. *Phys. Fluids* **2016**, *28* (6), 063105.

- (233) Rydzek, G.; Ji, Q. M.; Li, M.; Schaaf, P.; Hill, J. P.; Boulmedais, F.; Ariga, K. Electrochemical Nanoarchitectonics and Layer-by-Layer Assembly: From Basics to Future. *Nano Today* **2015**, *10* (2), 138–167.
- (234) Ammam, M.; Fransaer, J. Glucose/O₂ Biofuel Cell Based on Enzymes, Redox Mediators, and Multiple-Walled Carbon Nanotubes Deposited by AC-Electrophoresis Then Stabilized by Electropolymerized Polypyrrole. *Biotechnol. Bioeng.* **2012**, *109* (7), 1601–1609.
- (235) Ammam, M. Electrochemical and Electrophoretic Deposition of Enzymes: Principles, Differences and Application in Miniaturized Biosensor and Biofuel Cell Electrodes. *Biosens. Bioelectron.* **2014**, *58*, 121–131.
- (236) Ammam, M.; Fransaer, J. Glucose Oxidase and 1-Butyl-3-Methylimidazolium Deposited by AC-Electrophoresis on Pt as a Glucose Bioanode for Biofuel Cells. *Electrochim. Acta* **2012**, *81*, 129–137.
- (237) Ammam, M.; Fransaer, J. AC-Electrophoretic Deposition of Metalloenzymes: Catalase as a Case Study for the Sensitive and Selective Detection of H₂O₂. *Sens. Actuators, B* **2011**, *160* (1), 1063–1069.
- (238) Ammam, M. Electrophoretic Deposition under Modulated Electric Fields: A Review. *Rsc Adv.* **2012**, *2* (20), 7633–7646.
- (239) Ammam, M.; Fransaer, J. Effects of AC-Electrolysis on the Enzymatic Activity of Glucose Oxidase. *Electroanalysis* **2011**, *23* (3), 755–763.
- (240) Ammam, M.; Fransaer, J. AC-Electrophoretic Deposition of Glucose Oxidase. *Biosens. Bioelectron.* **2009**, *25* (1), 191–197.
- (241) Ammam, M.; Fransaer, J. Glucose Microbiosensor Based on Glucose Oxidase Immobilized by AC-EPD: Characteristics and Performance in Human Serum and in Blood of Critically Ill Rabbits. *Sens. Actuators, B* **2010**, *145* (1), 46–53.
- (242) Ammam, M.; Fransaer, J. Biosensors and Bioelectronics AC-Electrophoretic Deposition of Glucose Oxidase. **2009**, *25*, 191–197.
- (243) Ammam, M.; Fransaer, J. A Study on Electrodeposition of Glucose Oxidase from Low Conductivity Solutions. *Electrochim. Acta* **2010**, *55* (28), 9125–9131.
- (244) Ammam, M.; Fransaer, J. Combination of Laccase and Catalase in Construction of H₂O₂-O₂ Based Biocathode for Applications in Glucose Biofuel Cells. *Biosens. Bioelectron.* **2013**, *39* (1), 274–281.

- (245) Ammam, M.; Fransaer, J. Micro-Biofuel Cell Powered by Glucose/O₂ Based on Electro-Deposition of Enzyme, Conducting Polymer and Redox Mediators: Preparation, Characterization and Performance in Human Serum. *Biosens. Bioelectron.* **2010**, 25 (6), 1474–1480.
- (246) Ammam, M.; Fransaer, J. Highly Sensitive and Selective Glutamate Microbiosensor Based on Cast Polyurethane/AC-Electrophoresis Deposited Multiwalled Carbon Nanotubes and Then Glutamate Oxidase/Electrosynthesized Polypyrrole/Pt Electrode. *Biosens. Bioelectron.* **2010**, 25 (7), 1597–1602.
- (247) Besra, L.; Uchikoshi, T.; Suzuki, T. S.; Sakka, Y. Experimental Verification of PH Localization Mechanism of Particle Consolidation at the Electrode/Solution Interface and Its Application to Pulsed DC Electrophoretic Deposition (EPD). *J. Eur. Ceram. Soc.* **2010**, 30 (5), 1187–1193.
- (248) Seuss, S.; Boccaccini, A. R. Electrophoretic Deposition of Biological Macromolecules, Drugs, And Cells. *Biomacromolecules* **2013**, 14 (10), 3355–3369.
- (249) Hamaker, H. C. Formation of a Deposit by Electrophoresis. *Trans. Faraday Soc.* **1940**, 35 (0), 279–287.
- (250) Sarkar, P.; Nicholson, P. S. Electrophoretic Deposition (EPD): Mechanisms, Kinetics, and Application to Ceramics. *J. Am. Ceram. Soc.* **1996**, 79 (8), 1987–2002.
- (251) Cheng, Y.; Luo, X. L.; Betz, J.; Buckhout-White, S.; Bekdash, O.; Payne, G. F.; Bentley, W. E.; Rubloff, G. W. In Situ Quantitative Visualization and Characterization of Chitosan Electrodeposition with Paired Sidewall Electrodes. *Soft Matter* **2010**, 6 (14), 3177–3183.
- (252) Guschin, D. A.; Shkil, H.; Schuhmann, W. Electrodeposition Polymers as Immobilization Matrices in Amperometric Biosensors: Improved Polymer Synthesis and Biosensor Fabrication. *Anal. Bioanal. Chem.* **2009**, 395 (6), 1693–1706.
- (253) Liu, Y.; Zhang, B.; Gray, K. M.; Cheng, Y.; Kim, E.; Rubloff, G. W.; Bentley, W. E.; Wang, Q.; Payne, G. F. Electrodeposition of a Weak Polyelectrolyte Hydrogel: Remarkable Effects of Salt on Kinetics, Structure and Properties. *Soft Matter* **2013**, 9 (9), 2703–2710.
- (254) Chen, P. C.; Chen, R. L. C. C.; Cheng, T. J.; Wittstock, G. Localized Deposition of Chitosan as Matrix for Enzyme Immobilization. *Electroanalysis* **2009**, 21 (7), 804–810.

- (255) Yang, S. L.; Lu, Z. Z.; Luo, S. L.; Liu, C. B.; Tang, Y. H. Direct Electrodeposition of a Biocomposite Consisting of Reduced Graphene Oxide, Chitosan and Glucose Oxidase on a Glassy Carbon Electrode for Direct Sensing of Glucose. *Microchim. Acta* **2013**, *180* (1–2), 127–135.
- (256) Song, Y. H.; Liu, H. Y.; Wang, Y.; Wang, L. A Glucose Biosensor Based on Cytochrome c and Glucose Oxidase Co-Entrapped in Chitosan- Gold Nanoparticles Modified Electrode. *Anal. Methods* **2013**, *5* (16), 4165–4171.
- (257) Li, J. J.; Yuan, R.; Chai, Y. Q. Simple Construction of an Enzymatic Glucose Biosensor Based on a Nanocomposite Film Prepared in One Step from Iron Oxide, Gold Nanoparticles, and Chitosan. *Microchim. Acta* **2011**, *173* (3–4), 369–374.
- (258) Du, Y.; Luo, X. L.; Xu, J. J.; Chen, H. Y. A Simple Method to Fabricate a Chitosan-Gold Nanoparticles Film and Its Application in Glucose Biosensor. *Bioelectrochemistry* **2007**, *70* (2), 342–347.
- (259) Meyer, W. L.; Liu, Y.; Shi, X. W.; Yang, X. H.; Bentley, W. E.; Payne, G. F. Chitosan-Coated Wires: Conferring Electrical Properties to Chitosan Fibers. *Biomacromolecules* **2009**, *10* (4), 858–864.
- (260) Tangkuaram, T.; Ponchio, C.; Kangkasomboon, T.; Katikawong, P.; Veerasai, W. Design and Development of a Highly Stable Hydrogen Peroxide Biosensor on Screen Printed Carbon Electrode Based on Horseradish Peroxidase Bound with Gold Nanoparticles in the Matrix of Chitosan. *Biosens. Bioelectron.* **2007**, *22* (9–10), 2071–2078.
- (261) Liu, C. H.; Guo, X. L.; Cui, H. T.; Yuan, R. An Amperometric Biosensor Fabricated from Electro-Co-Deposition of Sodium Alginate and Horseradish Peroxidase. *J. Mol. Catal. B Enzym.* **2009**, *60* (3–4), 151–156.
- (262) Márquez, A.; Jiménez-Jorquera, C.; Domínguez, C.; Muñoz-Berbel, X. Electrodepositable Alginate Membranes for Enzymatic Sensors: An Amperometric Glucose Biosensor for Whole Blood Analysis. *Biosens. Bioelectron.* **2017**, *97*, 136–142.
- (263) Jin, Z. Y.; Guven, G.; Bocharova, V.; Halamek, J.; Tokarev, I.; Minko, S.; Melman, A.; Mandler, D.; Katz, E.; Güven, G.; Bocharova, V.; Halámek, J.; Tokarev, I.; Minko, S.; Melman, A.; Mandler, D.; Katz, E. Electrochemically Controlled Drug-Mimicking Protein Release from Iron-Alginate Thin-Films Associated with an Electrode. *ACS Appl. Mater. Interfaces* **2012**, *4* (1), 466–475.

- (264) Maerten, C.; Garnier, T.; Lupattelli, P.; Chau, N. T. T.; Schaaf, P.; Jierry, L.; Boulmedais, F.; Trang, N.; Chau, T.; Schaaf, P.; Boulmedais, F.; Maerten, C.; Garnier, T.; Lupattelli, P.; Chau, N. T. T.; Schaaf, P.; Jierry, L.; Boulmedais, F. Morphogen Electrochemically Triggered Self-Construction of Polymeric Films Based on Mussel-Inspired Chemistry. *Langmuir* **2015**, *31* (49), 13385–13393.
- (265) Dochter, A.; Garnier, T.; Pardieu, E.; Chau, N. T. T.; Maerten, C.; Senger, B.; Schaaf, P.; Jierry, L.; Boulmedais, F.; Dochter, A.; Garnier, T.; Pardieu, E.; Chau, N. T. T.; Maerten, C.; Senger, B.; Schaaf, P.; Jierry, L.; Boulmedais, F. Film Self-Assembly of Oppositely Charged Macromolecules Triggered by Electrochemistry through a Morphogenic Approach. *Langmuir* **2015**, *31* (37), 10208–10214.
- (266) Gharbi, T.; Herlem, G. *Electrodeposition of Insulating Thin Film Polymers from Aliphatic Monomers as Transducers for Biosensor Applications*; IntechOpen Book: Rijeka (Croatia), 2011.
- (267) Fletcher, S.; Black, V. J. Poly(Bisphenol) Polymers as Passivating Agents for Carbon Electrodes in Ionic Liquids. *J. Phys. Chem. C* **2016**, *120* (15), 8014–8022.
- (268) Lakard, B.; Herlem, G.; Fahys, B. Electrochemical Polymerization of 1,2-Ethanedithiol as a New Way to Synthesize Polyethylenedisulfide. *Polymer (Guildf)*. **2008**, *49* (7), 1743–1747.
- (269) Lakard, B.; Herlem, G.; Fahys, B. Ab Initio Study of the Electrochemical Polymerization Mechanism Leading from DETA to PEI. *J. Mol. Struct. THEOCHEM* **2002**, *593* (1–3), 133–141.
- (270) Waltman, R. J.; Bargon, J. Electrically Conducting Polymers - a Review of the Electropolymerization Reaction, of the Effects of Chemical-Structure on Polymer Film Properties, and of Applications towards Technology. *Can. J. Chem.* **1986**, *64* (1), 76–95.
- (271) Imisides, M. D.; John, R.; Riley, P. J.; Wallace, G. G. The Use of Electropolymerization to Produce New Sensing Surfaces: A Review Emphasizing Electrode Position of Heteroaromatic Compounds. *Electroanalysis* **1991**, *3* (9), 879–889.
- (272) Sadki, S.; Schottland, P.; Brodie, N.; Sabouraud, G. The Mechanisms of Pyrrole Electropolymerization. *Chem. Soc. Rev.* **2000**, *29* (5), 283–293.
- (273) Qazi, T. H.; Rai, R.; Boccaccini, A. R. Tissue Engineering of Electrically Responsive Tissues Using Polyaniline Based Polymers: A Review. *Biomaterials* **2014**, *35* (33), 9068–9086.

- (274) Foulds, N. C.; Lowe, C. R. Immobilization of Glucose Oxidase in Ferrocene-Modified Pyrrole Polymers. *Anal. Chem.* **2002**, *60* (22), 2473–2478.
- (275) Kim, J.; Kim, S. I.; Yoo, K. H. Polypyrrole Nanowire-Based Enzymatic Biofuel Cells. *Biosens. Bioelectron.* **2009**, *25* (2), 350–355.
- (276) Korkut, S.; Keskinler, B.; Erhan, E. An Amperometric Biosensor Based on Multiwalled Carbon Nanotube-Poly(Pyrrole)-Horseradish Peroxidase Nanobiocomposite Film for Determination of Phenol Derivatives. *Talanta* **2008**, *76* (5), 1147–1152.
- (277) Kizling, M.; Stolarczyk, K.; Tammela, P.; Wang, Z.; Nyholm, L.; Golimowski, J.; Bilewicz, R. Bioelectrodes Based on Pseudocapacitive Cellulose/Polypyrrole Composite Improve Performance of Biofuel Cell. *Bioelectrochemistry* **2016**, *112*, 184–190.
- (278) Çetin, M. Z.; Camurlu, P. An Amperometric Glucose Biosensor Based on PEDOT Nanofibers. *RSC Adv.* **2018**, *8* (35), 19724–19731.
- (279) Dubal, D. P.; Lee, S. H.; Kim, J. G.; Kim, W. B.; Lokhande, C. D. Porous Polypyrrole Clusters Prepared by Electropolymerization for a High Performance Supercapacitor. *J. Mater. Chem.* **2012**, *22* (7), 3044–3052.
- (280) Guo, B.; Zhao, Y.; Wu, W.; Meng, H.; Zou, H.; Chen, J.; Chu, G. Research on the Preparation Technology of Polyaniline Nanofiber Based on High Gravity Chemical Oxidative Polymerization. *Chem. Eng. Process. Process Intensif.* **2013**, *70*, 1–8.
- (281) Kim, H. J.; Piao, M. H.; Choi, S. H.; Shin, C. H.; Lee, Y. T. Development of Amperometric Hydrogen Peroxide Sensor Based on Horseradish Peroxidase-Immobilized Poly(Thiophene-Co-EpoxyThiophene). *Sensors* **2008**, *8* (7), 4110–4118.
- (282) Chen, X. X.; Shao, M. L.; Poller, S.; Guschin, D.; Pinyou, P.; Schuhmann, W. PQQ-SGDH Bioelectrodes Based on Os-Complex Modified Electrodeposition Polymers and Carbon Nanotubes. *J. Electrochem. Soc.* **2014**, *161* (13), H3058–H3063.
- (283) Pöller, S.; Koster, D.; Schuhmann, W.; Poller, S.; Koster, D.; Schuhmann, W. Stabilizing Redox Polymer Films by Electrochemically Induced Crosslinking. *Electrochem. commun.* **2013**, *34*, 327–330.
- (284) Wolowacz, S. E.; Yon Hin, B. F. Y.; Lowe, C. R. Covalent Electropolymerization of Glucose Oxidase in Polypyrrole. *Anal. Chem.* **2002**, *64* (14), 1541–1545.
- (285) Gray, K. M.; Liba, B. D.; Wang, Y. F.; Cheng, Y.; Rubloff, G. W.; Bentley, W. E.; Montembault, A.; Royaud, I.; David, L.; Payne, G. F. Electrodeposition of a Biopolymeric Hydrogel: Potential for One-Step Protein Electroaddressing. *Biomacromolecules* **2012**, *13* (4), 1181–1189.

- (286) Maerten, C.; Lopez, L.; Lupattelli, P.; Rydzek, G.; Pronkin, S.; Schaaf, P.; Jierry, L.; Boulmedais, F. Electrotriggered Confined Self-Assembly of Metal-Polyphenol Nanocoatings Using a Morphogenic Approach. *Chem. Mater.* **2017**, *29* (22), 9668–9679.
- (287) Rydzek, G.; Toulemon, D.; Garofalo, A.; Leuvrey, C.; Dayen, J. F.; Felder-Flesch, D.; Schaaf, P.; Jierry, L.; Begin-Colin, S.; Pichon, B. P.; Boulmedais, F. Selective Nanotrench Filling by One-Pot Electroclick Self-Constructed Nanoparticle Films. *Small* **2015**, *11* (36), 4638–4642.
- (288) Maerten, C. Bio-Inspired Self-Construction and Self-Assembly of Organic Films Triggered by Electrochemistry, under Supervision of Boulmedais F., Strasbourg University, Strasbourg, 2016.

Chapter 2

Material and Methods

Chapter 2 – Table of Contents

I. Material and sample Preparation	85
I.1 Polyphenols	85
I.1.1 Commercial catechol and gallol molecules.....	85
I.1.2 Chemical properties of polyphenols.....	86
I.1.3 Polyphenol/enzyme interaction	88
I.2 Enzymes	89
I.2.1 Glucose oxidase (GOx)	89
I.2.2 Horseradish peroxidase (HRP).....	90
I.3 Redox mediators.....	92
I.3.1 Ferrocene molecules.....	92
I.3.2 Others redox molecules	92
I.4 Nanoparticle synthesis.....	93
I.5 Polyurethane/graphene membrane preparation	94
II. Instrumentation	95
II.1 Electrochemical and quartz microbalance.....	95
II.1.1 The EC apparatus coupled with quartz crystal microbalance	95
II.1.2 The EC apparatus for gold interdigitated microelectrodes.....	97
II.1.3 The EC set-up for membrane testing.....	97
II.2 Spectroscopic apparatus	98
II.2.1 UV-Vis spectrophotometer	98
II.2.2 Dynamic light scattering	100
II.2.3 X-ray photoelectron spectroscopy.....	102
II.3 Electron Microscopy	102
II.3.1 Scanning electron microscopy.....	103
II.3.2 Transmission electron microscopy	105
III. Methods.....	106
III.1 Polyphenol and AuNPs Characterization.....	106
III.1.1 Gallol moieties quantification	106
III.1.2 Nanoparticles size	108

III.1.3	Nanoparticles concentration	109
III.2	Enzyme characterization	110
III.2.1	Enzyme and cofactor concentration	110
III.2.2	Enzyme size and glycosylation state	111
III.2.3	Enzyme activity with colorimetric test.....	111
III.2.4	Accessible lysine/cysteine residues.....	112
III.3	Enzyme/nanoparticles complexes	114
III.3.1	Estimation of the theoretical monolayer ratio	114
III.3.2	Aggregation/flocculation Test.....	115
III.3.3	Bradford test.....	115
III.3.4	Activity test	116
III.4	Electrodeposition and thin film characterizations	117
III.4.1	Preliminary electrochemical requirement	117
III.4.2	Estimation of the electroactive surface area.....	118
III.4.3	Preparation of electrodeposition solution.....	118
III.4.4	Deposit mass and electrodeposition efficiency	119
III.4.5	Morphology	120
III.4.6	XPS chemical analysis	120
III.5	Biosensor properties	120
III.5.1	Characterization of the biocatalytic current	120
III.5.2	Sensitivity, limit of detection, response time and interferents	121
III.5.3	Stability with time, tween-20 test and bending	122
III.5.4	Kinetics of michaelian enzymes.....	123
IV.	References	124

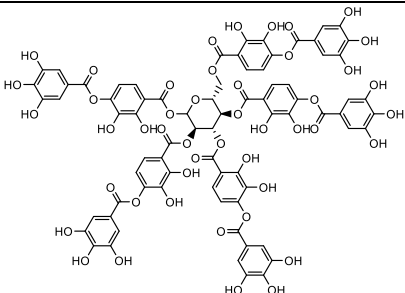
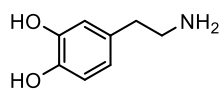
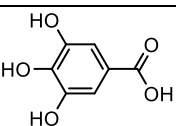
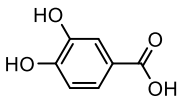
I. Material and sample Preparation

I.1 Polyphenols

I.1.1 Commercial catechol and gallol molecules

Polyphenol is defined as a structure containing at least two phenolic groups. Each aromatic ring in polyphenol can possess various number of hydroxyl groups which tune its reactivity.¹ In the following, catechol (1,2-dihydroxybenzene) and gallol (1,2,3-trihydroxybenzene) will be mainly discussed.

Table 2.1: Information on polyphenol compounds taken into consideration during this thesis. Solubility and pKa value were retrieved from Sci-finder database, asterisk () means that these values are not known experimentally but were computed.*

Name (Denoted as)	Structure	MW (g·mol ⁻¹)	Solubility in water (mM)	pKa*	Ref
Tannic Acid (TA)		1701.23	> 100	main pKa: ~6-7	[2,3]
Dopamine (DA)		153.18 (189.63 with HCl)	~100	OH~8.71* NH ₂ ~10.90*	[4]
Gallic Acid (GA)		170.12	76 ± 4	COOH ~ 4.5 OH ~10	[5]
Procatechuic Acid (PCA)		154.12	190 ± 7	COOH ~ 4.5 OH ~10	[5]

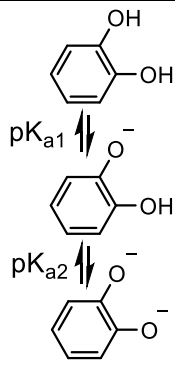
Several catechol and gallol molecules have been purchased either as a building block in thin film construction or as reference for the different tests (Table 2.1). Tannic acid (TA, Sigma-Aldrich, ref: 403040) and dopamine (Alfa Aesar, DA, ref: A11136) were purchased as multivalent molecules. Gallic acid and procatechuic acid as reference were purchased from

Sigma and Alfa Aesar respectively. Purity were higher than 95% in all case according to the supplier and were checked before use by a UV absorption and a Prussian Blue test (see Methods section III.1.1). Solution of fully dissolved polyphenols between 0.1 and 20 mM were obtained simply by adding the corresponding amount of polyphenol in degassed Milli-Q water or buffer.

1.1.2 Chemical properties of polyphenols

Tannic acid (TA) will be taken as the main example. It is one of the most studied tannin although its commercial source are not pure and are rather a blend of several polyphenols having between two and twelve phenolic moieties depending on the plant source.^{6,7} General properties and structure of TA are gathered in Table 2.1. It is a weak acid ($pK_a \sim 6$) that behave like a polyanion above its pK_a . It has to be noted that zeta potential of tannic acid remains negative at any pH and strongly decrease when the pH is raised.⁸ Tannic acid solution prepared in water has a pH between 2.8 and 5.5 depending on the concentration and a constant hydrodynamic size around 1.4-1.6 nm. When pH is manually adjusted above 6, hydrolysis of the ester bond begin and gallic acid is released.⁸ When pH is raised around 8-12, phenolic moieties of TA are turned into phenolate (Table 2.2) which has stronger nucleophilic properties.⁹ This explains why TA easily self-polymerize at high pH value (Figure 2.1.a-b).

Table 2.2: Comparison of the reactivity of gallol and catechol moieties. $E_{1/2}$ was retrieved from 0.1 mM PCA or GA solution in aqueous/methanol solution in acetate buffer (pH4).¹⁰ pK_a values were retrieved from density functional theory calculation and confirmed with experimental data.¹¹ Tannic acid potential (*) is not accurate as the reduction peak is not observed.

Name	pK_{a1}	pK_{a2}		Name	Half wave potential (V/AgCl), pH4
Pyrocatechol	9,4 ¹¹	13,7 ¹¹		Procatechuic Acid (PCA)	0.50 ¹⁰
Pyrogallol	9,05 ¹¹	11,2 ¹¹		Gallic Acid (GA)	0.33 ¹⁰
Tannic acid	$\sim 8,5^8$?		Tannic acid	0.3-0.4*

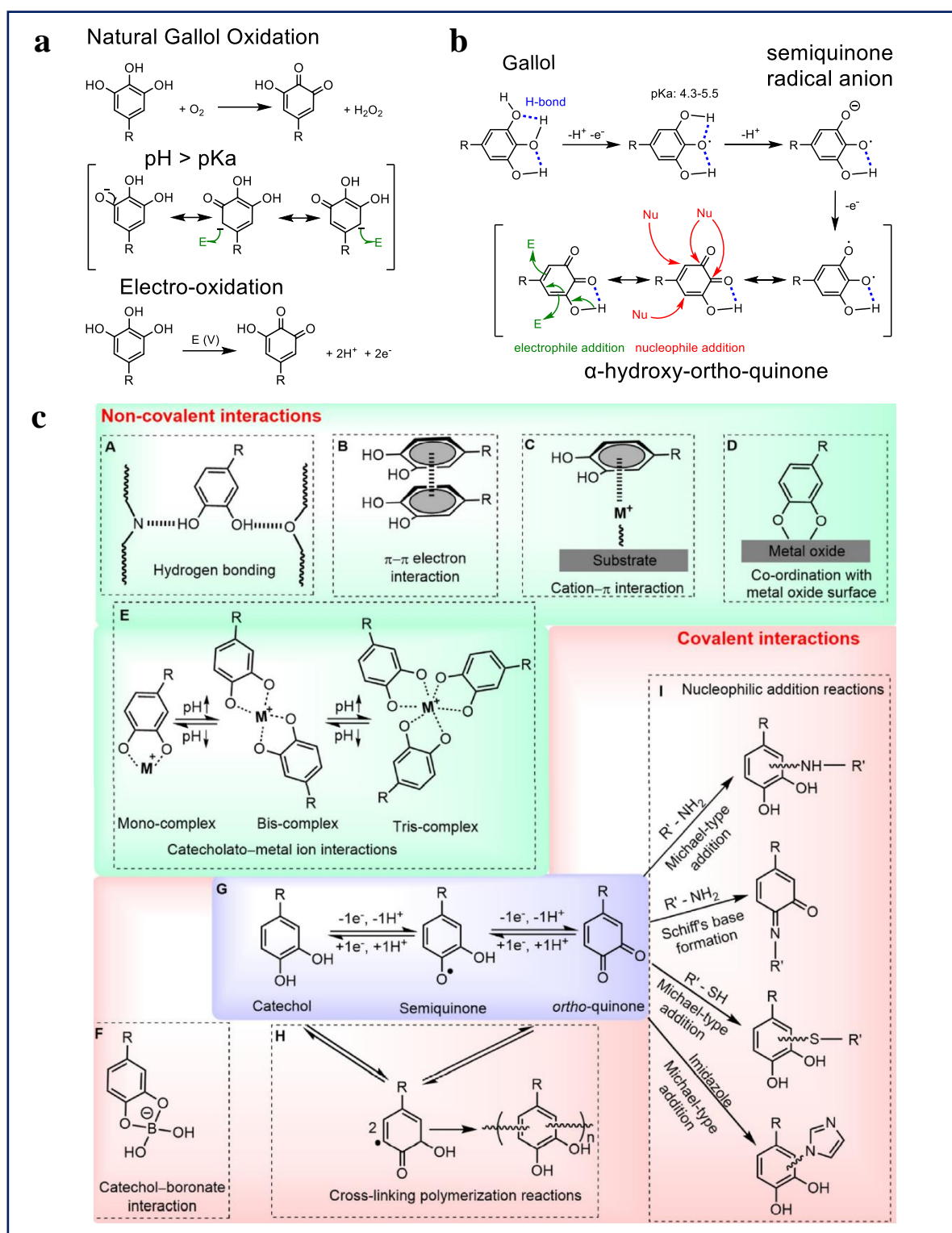


Figure 2.1: (a) Illustration of the gallol reactivity toward dissolved oxygen and the increased nucleophilic characters of gallol at $\text{pH} > \text{pKa}$ [9]. Electrooxidation mechanism is also illustrated. (b) Illustration of the electrophilic and nucleophilic character of gallol moieties through dehydrogenation according to [1]. (c) Illustration of the covalent and non-covalent versatility of catechol/quinone chemistry which is also applicable to gallol moieties according to [70].

Reactivity of gallol and catechol group is different. First, gallol moieties loose more easily a proton as its pKa is lower (Table 2.2). This results in easier semiquinone radical formation that can further react with nucleophiles and electrophiles⁹ (Figure 2.1.b). Also, the half wave potential is lower for GA as compared to PCA proving that gallol moieties can be more easily oxidized than catechol moieties (Table 2.2).

Even if gallol are more reactive than catechol moieties, both have the same chemistry. Their chemistry is very versatile as they can interact through many different pathways. Reviews generally distinguish covalent and non-covalent interactions⁹. Non covalent binding is mainly occurring from the reduced form and covalent binding from both forms (phenol or quinone state). Non covalent interactions are: hydrogen bonding, metal bonding and π - π stacking of the phenolic groups (Figure 2.1.c). Two main covalent bondings are often reported: catechol-boronate esterification and the nucleophilic attack of oxidized catechols – *i.e* quinone. As catechol and gallol can act as nucleophiles, they can attack activated quinone or semiquinone leading to the self-polymerization process with a not well defined polymer architecture (several sites for nucleophilic attack). Polyphenols can also undergo covalent bonding once they are oxidized with others nucleophiles such as primary amines and thiols via Michael adduct or Schiff base formation (Figure 2.1.c).

1.1.3 Polyphenol/enzyme interaction

Polyphenols are also known to strongly interact with proteins.¹² Similarly to polyphenol chemistry, interaction between polyphenols and enzymes is very complex. It depends on many intrinsic properties such as amino acid sequence and size of the enzyme. It is also dependent on the number of gallol moieties and molecular mass of the polyphenol. Many external parameters such as temperature, pH, salt concentration and the presence of others reagents like surfactants also affect this interaction. Hagerman *et al.* have published many works on these interactions that give a comprehensive overview of these complex systems.^{13–19} Hydrogen/hydrophobic interaction, electrostatic bonding and covalent bonding via Schiff Base or Michael adduct formation are often competing. It is also known that TA and more generally tannins can drastically change the catalytic activity of enzyme either by modification of their conformation or by substrate deprivation.^{12,20–23} Due to this potential inhibition, activity test of polyphenol/enzyme solution was systematically investigated.

I.2 Enzymes

I.2.1 Glucose oxidase (GOx)

Glucose Oxidase (GOx) is an oxido-reductase consisting of two identical subunits of 80 kDa bound together. It contains one tightly bound flavin adenin dinucleotide redox cofactor (FAD) and one iron in each subunit.²⁴ GOx type X-S from *Aspergillus Niger* (ref: G7141) was purchased from Sigma-Aldrich having an average activity of 168 U·mg⁻¹. All GOx samples presented in this thesis were made by dissolving GOx at concentrations from 0.01 to 50 mg·mL⁻¹ taking into account that 80% of the weighted mass is effectively enzyme according to preliminary test (see Methods section III.2.1). The remaining 20% are probably salts or stabilizing molecules added by the supplier.

Table 2.3: Information from supplier and literature about Glucose Oxidase from Aspergillus Niger.


Name	λ_{\max} (nm)	Ref	PDB Model (1CF3)
Molecular weight (kDa)	160 Range : 130-175	[24]	GOx dimer (FAD cofactor is represented in red) 
Carbohydrate	~ 18% Range : 16-25%	[24,25]	
Size (nm) from X-ray diffraction	6.0×5.2×7.7	[25,26]	
FAD per enzyme	2	—	
Cofactor half wave potential (V/AgCl)	-0.06 (pH5.3) -0.2 (pH9.3)	[27]	
pI	4.2	[24]	
ϵ_{280} (mM ⁻¹ ·cm ⁻¹)	263-267	[24,28,29]	
ϵ_{450} (mM ⁻¹ ·cm ⁻¹)	12-14	[24,29,30]	
Temperature stability	<50°C Optimum : 40-50°C	[31,32]	
pH stability	4-8 Opt : 5.5 pH7 : 80%	[24,31]	
KM (mM)	33-110	[24]	
Activity (U·mg ⁻¹)	~168	[24]	

Table 2.3 gathers all the available data for GOx from *Aspergillus Niger* such as size, glycosylation, absorbance, thermal and pH stability and activity properties. The mechanism of glucose catalytic oxidation is not well known but happens through conformational change with transfer of two protons and two electrons from glucose to FAD.³² One histidine residue is however believed to act as a catalytic base in the mechanism.³³

1.2.2 Horseradish peroxidase (HRP)

There are several isoenzymes in horseradish peroxidase commercial sources. Each has different properties but the most abundant, known as isoenzyme C, will be described here. Although HRP-C content is not known from our commercial source (ref: 31941, Serva), it generally vary between 50 and 90%. HRP solution was prepared taking into account that approximatively 90% of the weighted mass is effectively enzyme according to preliminary tests (see Methods section III.2.1).

HRP-C contains 308 amino acids, 4 disulfide bridges and nine potential N-glycosilation sites. The carbohydrate content is generally between 18 and 22%. It contains one iron(III) protoporphyrin IX cofactor usually referred as heme cofactor group.³⁴ Two calcium atoms are also present which are essential to stabilize the heme in its native state and their depletion or replacement by other divalent cations result in drastic activity loss.³⁵ Table 2.3 gathers all the available data for HRP such as size, glycosylation, absorbance, thermal and pH stability and activity properties.

HRP catalyzes the oxidation of H_2O_2 via a three-step cycle. First H_2O_2 is oxidized by HRP. During this step, an H_2O molecule is produced and one of the oxygen atom of H_2O_2 is fixed to the iron atom turning the cofactor into compound I (Figure 2.2). Then the cofactor is reduced back to the native step via a two-steps mechanism. This enzyme regeneration can be performed by several electron donor substrates. In our case, 2,2'-azino-bis(3-ethylbenzothiazoline-6-sulfonic acid (ABTS) was used as electron donor for colorimetric assay and ferrocenium in electrochemistry. The global reaction is detailed in Equation 2.1. HRP can also under specific condition act as a pseudo catalase but this mechanism will not be detailed here.³⁶

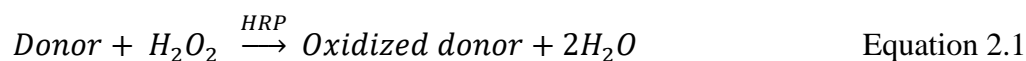
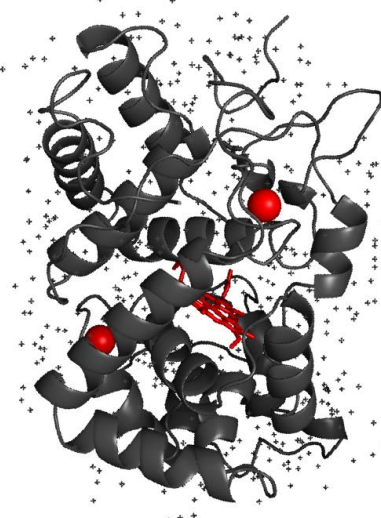


Table 2.4: Information from supplier and literature about Horseradish Peroxidase. Activity depend on the cosubstrate that is chosen.

Properties	Values	Ref	PDB Model (1HCH)
Molecular weight (kDa)	~ 44 kDa Range 40-44	[37,38]	<p>HRP model (Ca²⁺ and heme are represented in red)</p> 
Carbohydrate	18-22 %	[37,38]	
Size (nm) from X-ray diffraction	6.0×4.4×4.0	[39]	
Cofactor per enzyme	1 (≠ seller)	[31]	
Cofactor half wave potential (V/AgCl)	Nat(Fe ³⁺ /Fe ²⁺): -0.3V (pH7) Comp I/II/Nat.: 0.9 (pH7)	[27,40]	
pI	3 to 9 (≠ isoenzymes) HRP-C : 6.35	[37,38]	
ε ₂₈₀ (mM ⁻¹ ·cm ⁻¹)	28.86	[37]	
ε ₄₀₅ (mM ⁻¹ ·cm ⁻¹)	89.5 (76-105)	[41]	
Temperature stability	<50°C, Optimum: 45°C	[31]	
pH stability	5-10 ³¹ Optimum: 6-7 pH7.5: 84% activity	[37;38]	
K _M (μM)	2.5	[42]	
Activity 'U·mg ⁻¹)	~300 (pyrogallol)	[38,43]	

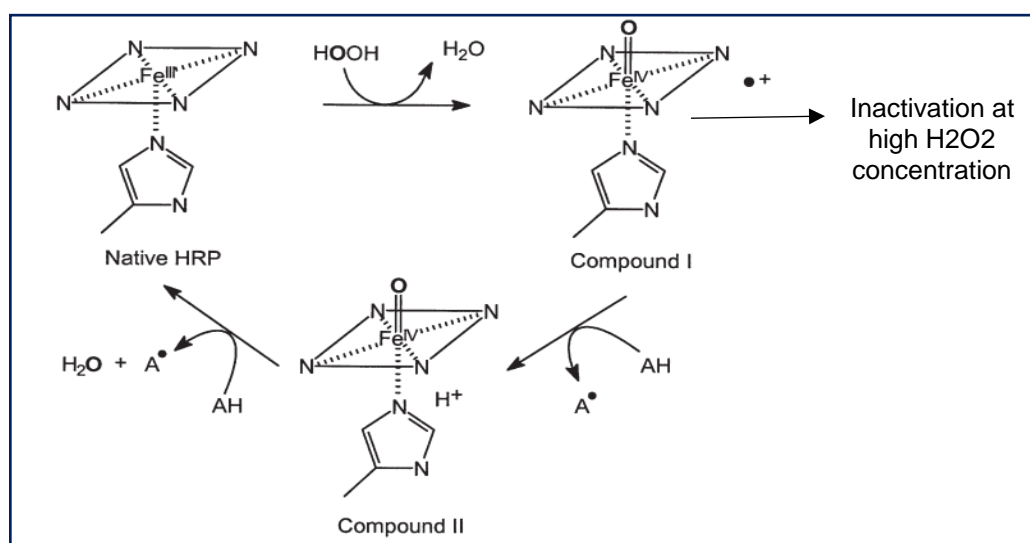


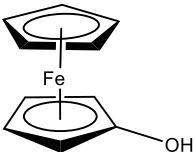
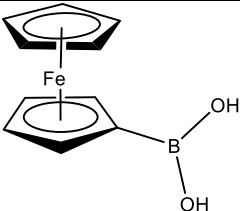
Figure 2.2: Illustration of the peroxidase catalytic site for HRP according to [71]

I.3 Redox mediators

I.3.1 Ferrocene molecules

Ferrocene methanol (FcOH) was used as a standard freely diffusing mediator at a concentration of 0.1 to 5mM and were purchased from Fluorochem. FcOH was solubilize in water/buffer solution using ultrasonic bath for 20 min to quicken the dissolution with a temperature kept below 40°C. After cooling at room temperature, the solution was filtered with a 0.2 µm regenerated cellulose syringe filter. Procedure was identical for Ferrocene Boronic Acid purchased from Sigma-Aldrich and denoted as FcBA. Purity was 95% for FcOH and 97% for FcBA according to the suppliers.

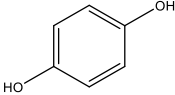
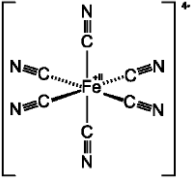
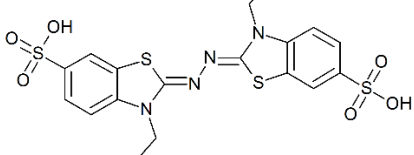
Table 2.5: Representation of redox mediators used in this thesis

Name (Denoted as)	Structure	Molecular Weight (g/mol)	Cofactor half wave potential (V/AgCl)	Ref
Ferrocene Methanol (FcOH)		216.06	0.21	[44]
Ferrocene Boronic Acid (FcBA)		229.85	—	—

I.3.2 Others redox molecules

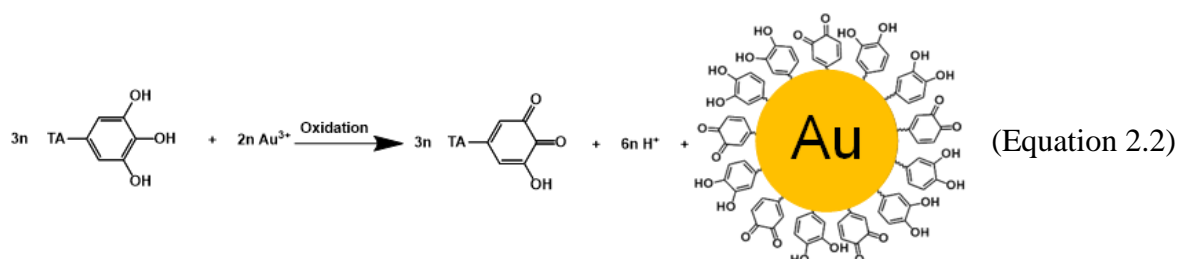
Para-hydroquinone redox mediator was purchased from Sigma-Aldrich and was found to be a good candidate for mediating reaction (low potential) as well as local acidification/basification due to the release/withdrawal of protons. Ferrocyanide $\text{Fe}^{\text{II}}(\text{CN})_6^{4-}$ was also tested as redox molecule for redox catalyzed electrochemical deposition (RCEC) as well as mediator for glucose sensing. $\text{Fe}^{\text{III}}(\text{CN})_6^{3-}/\text{Fe}^{\text{II}}(\text{CN})_6^{4-}$ were purchased from Merck. Last, ABTS was purchased from Alfa Aesar and was used in $\text{H}_2\text{O}_2/\text{HRP}$ activity test. It acts as an electron donor and its reduced form turn into green after reaction with HRP. Due to the high extinction coefficient of the reduced form ($36 \text{ mM}^{-1} \cdot \text{cm}^{-1}$ at 420 nm), ABTS was found to be convenient to follow HRP and GOx/HRP activity with colorimetric assay (see Methods section III.2.3).

Table 2.6: Representation of redox mediators used in this thesis

Name (Denoted as)	Structure	M.W (g/mol)	Half wave potential (V/AgCl), pH7	Ref
p-hydroquinone		110.11	0.521 - 0.059pH	[45]
Ferrocyanide [Fe ^{II} (CN) ₆] ⁴⁻		211.96	0.195	[46,47]
ABTS		514.62	ABTS ^{0/-} :0.89 ABTS ^{•-/2-} :0.50	[27]

I.4 Nanoparticle synthesis

Gold Chloride trihydrate was purchased from Alfa Aesar. The tannic acid capped gold nanoparticles synthesis (TA@AuNPs) was adapted from Sivaraman *et al.*⁴⁸ This synthesis uses gallol units as gold salt reductants and ligands for the further stabilization of the NPs (Equation 2.2). First, 2 mM HAuCl₄ and 0.3 mM TA solutions were prepared separately in Milli-Q water. TA solution was adjusted at pH 7 with 150 mM K₂CO₃. Both solutions were then filtered on 0.2 µm regenerated cellulose (RC) filters and flushed with argon for 5 min. 8 mL of HAuCl₄ solution were then slowly added into 12 mL of TA solution with a peristaltic pump (ISM596, Ismatec, Switzerland) at a constant flow rate of 500 µL·min⁻¹ under 750 rpm agitation. During the procedure, 20 µL of 150 mM K₂CO₃ was added every 2 min in order to compensate the acidification caused by the addition of HAuCl₄ solution as well as the oxidation of polyphenols. After 16 min of the addition step, a dark reddish solution was obtained with a final TA/Au ratio of 0.22.



The obtained TA capped gold nanoparticles were denoted as NP12 as their size was approximatively 12 nm. To obtain different diameters, the reactivity of the gold salt solution was adjusted by controlling the pH (addition of 150 mM K_2CO_3) before mixing the gold salt and acid tannic solution. With adjustment of $AuCl_4^-$ solution at pH7 and pH10 initial pH, NP25 and NP40 were respectively obtained. To decrease the NPs size, ferrocene boronate was added inside the tannic acid solution as a fast reducing agent.⁴⁹ The higher seed density in the early stage led to smaller NPs denoted as NP7. In all cases, NPs solutions were centrifuged at 13 500 rpm (12 200 g) with a VWR Microstar 12 centrifuge to remove all unbound polyphenols from the solution and redispersed in water or the GOx mixture solution. Required times for centrifugation were 15, 15, 60 and 120 min for NP40, NP25, NP12 and NP7 respectively.

1.5 Polyurethane/graphene membrane preparation

The polyurethane membranes coated with few layers graphene (PU-FLG) were prepared as follow by our collaborators from ICPEES (Institut de chimie et proceeds pour l'énergie, l'environnement et la santé, ICPEES – Strasbourg). I thank here Jean-Mario Nhut and Housseinou Ba for membrane electrospinning and graphene deposition respectively.

The polyurethane suspensions for electrospinning has been prepared following a recently published procedure.⁵⁰ First, 3.1% w/w of PEO ($M_w \sim 900 \text{ kg} \cdot \text{mol}^{-1}$ provided by Sigma-Aldrich) was dissolved in distilled water under magnetic stirring for 24 h. Subsequently, 50.7% w/w LUPHEN 700 (37% w/v% polyurethane content provided by BASF) was added to this PEO solutions and were kept under magnetic stirring for further 24 h. A home-made needleless emitter was used for membrane electrospinning with a stainless steel emitter. The emitter-collector distance was set at 20 cm with a total flow rate of $20 \text{ mL} \cdot \text{h}^{-1}$. A voltage of 40 kV was applied to the emitter and – 5 kV to the collector. The relative humidity was fixed at 30% and temperature was kept at 21 °C. Electrospinning was conducted during 60 min and the resulting membrane was dried at room temperature. Last, a final washing step to remove PEO was performed in distilled water while keeping the membrane attached to a Teflon frame for 24 h. Then, few layers of graphene were deposited from a graphene solution prepared by tip sonication (Blackleaf, Strasbourg).⁵¹ Membrane was spray-coated three times with a further drying at 40°C in an oven. The obtained membranes will be denoted as PU-FLG in the fifth chapter.

II. Instrumentation

II.1 Electrochemical and quartz microbalance

II.1.1 The EC apparatus coupled with quartz crystal microbalance

The electrochemistry coupled quartz crystal microbalance (EC-QCM) is a standard three electrodes set-up coupled to QCM configuration (Figure 2.3). Electrochemical characterization and electrodeposition optimization was based on the electrochemistry module QEM 401 (QSense AB®, Sweden)⁵² coupled to a CHI660E apparatus from CH instrument (Austin, Texas). Reference electrode was a 3.5 M Ag/AgCl electrode, counter electrode (CE) was a 1.2 cm² platinum plate and working electrode (WE) a gold coated quartz crystal from QuartzPro (Ref: QCM5140TiAu120-050-Q, ~80 nm Au). Internal volume of EC-QCM cell is 100 μ L and it was coupled to a peristaltic pump (ISM596, Ismatec, Switzerland) able to deliver flow rates ranging from 0.05 to 1.4 mL·min⁻¹. Distance between WE and CE was fixed at 0.8 mm and distance between WE and RE was 5 mm.⁵²

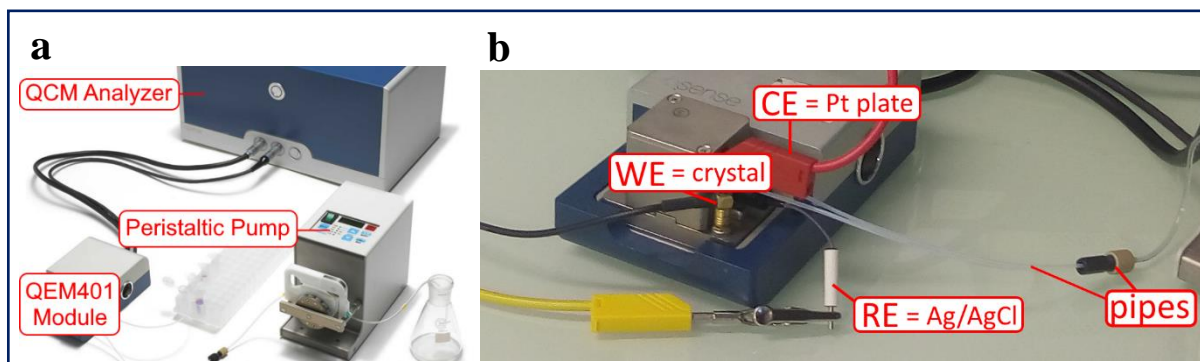


Figure 2.3: Illustration of (a) the EC-QCM Apparatus E-serie from QSense® and (b) zoom on the electrochemical cell QEM401

This EC set-up was coupled to quartz crystal microbalance E1 apparatus (QSense AB®, Sweden) enhancing to record the deposition of molecules from the solution onto the working electrode (Figure 2.4.a). By monitoring the changes in the resonance frequency f_v and the dissipation factor D_v of the oscillating gold coated quartz crystal excited at 5 MHz, viscoelastic nature and adsorbed mass of the deposit can be determined with the adequate mathematical model (Sauerbrey for rigid film⁵³, Voigt for viscoelastic film⁵⁴). When a rigid adhering layer is

deposited onto the crystal, the frequency shift according to equation 2.3. In case of small amount of deposited material, the harmonic oscillator frequency shift is proportional to the deposited mass (Figure 2.4.a). This formulae can be rearranged into the well-known Sauerbrey equation that predict a linear relation between frequency shift and deposited mass (Equation 2.4). Detection limit is in the order of $1 \text{ ng} \cdot \text{cm}^{-2}$. All the measurements in this thesis were performed at the fundamental 5 ($\nu = 1$) and 15 ($\nu = 3$), 25 ($\nu = 5$), 35 ($\nu = 7$) MHz overtones throughout the deposition process but only the third overtones is presented for simplicity's sake.

$$f \text{ (Hz)} = \frac{1}{2\pi} \sqrt{\frac{k}{m+M}} \approx \frac{1}{2\pi} \sqrt{\frac{k}{M}} \left(1 - \frac{m}{M}\right) \approx f_0 \left(1 - \frac{m}{M}\right) \text{ with } \begin{cases} k: \text{stiffness constant (N} \cdot \text{m}^{-1}) \\ m: \text{mass of the film (kg)} \\ M: \text{the AT-cut quartz mass (kg)} \\ f_0: \text{the initial resonance (Hz)} \end{cases} \quad (\text{Eq. 2.3})$$

$$\Delta m = -C \frac{\Delta f_N}{N} \text{ with } \begin{cases} C: \text{Sauerbrey constant} \\ \Delta f_N: \text{frequency change for harmonic N} \\ N: \text{harmonic rank (N=1 for the fundamental)} \end{cases} \quad (\text{Equation 2.4})$$

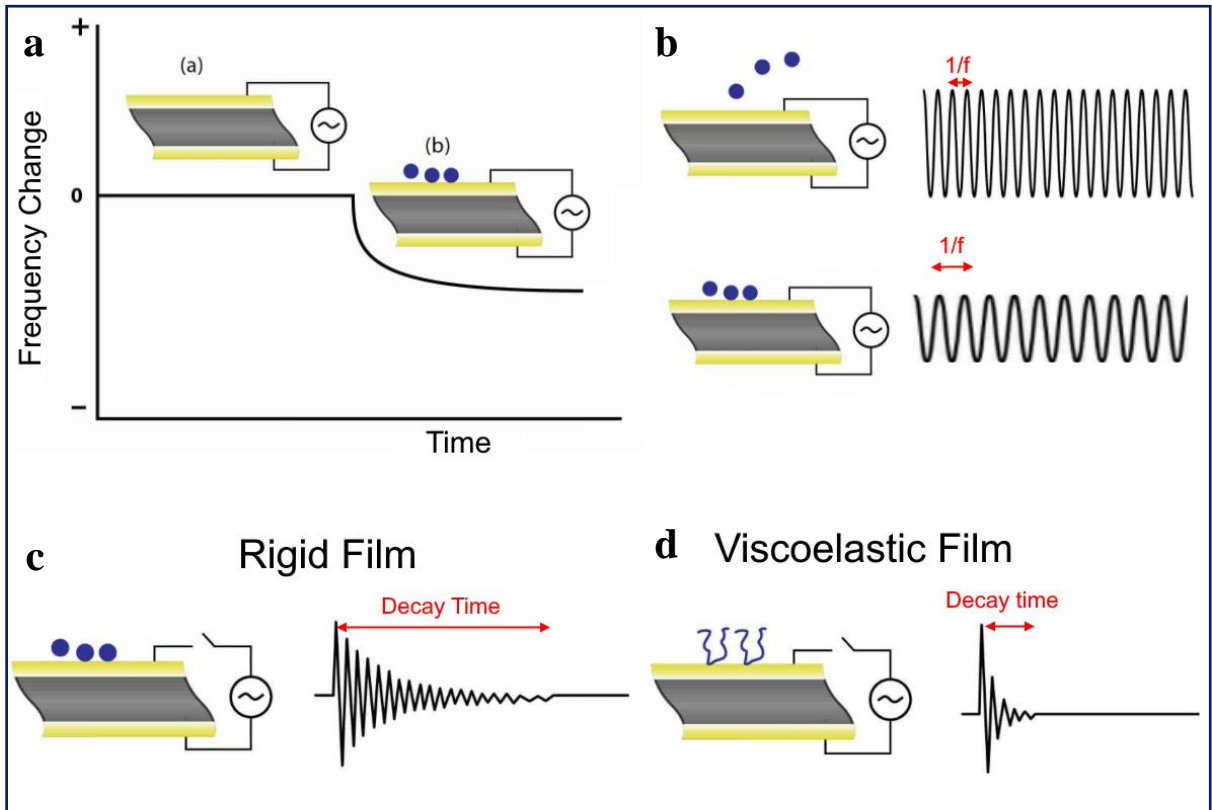


Figure 1.4: Illustration of QCM-D principle according to Biolin Scientific/ Q-Sense®. (a) frequency shift when a mass is deposited onto the oscillating crystal. (b) Illustration of the oscillating period ($1/f$) and amplitude change upon adsorption. (c,d) Illustration of the dissipation principle. When the oscillating perturbation is stopped, the typical oscillating decay time will be longer for (c) a rigid film compared to (d) a viscoelastic film.

Dissipation is also an interesting parameter in QCM experiment to statute on the nature of the adsorbed film. Indeed, when the oscillating perturbation is stopped, a rigid film will be highly coupled to the crystal so the decay time will be long (Figure 2.4.c). In comparison, a viscoelastic film such as adsorbed protein or low-reticulated polymer will have a shorter oscillating decay time (Figure 2.4.d).

II.1.2 The EC apparatus for gold interdigitated microelectrodes

Once the process has been optimized. Similar electrodepositions were performed with a second 3 electrodes set-up using a micro-sized working electrode (Figure 2.5). An interdigitated array (IDA ref: 012125, ALS Japan) with a gold thickness of 90 nm and two interdigitated gold tracks with a length of 2 mm, a width of 10 μm and a pair spacing of 5 μm was used in order to confirm the spatial deposition.

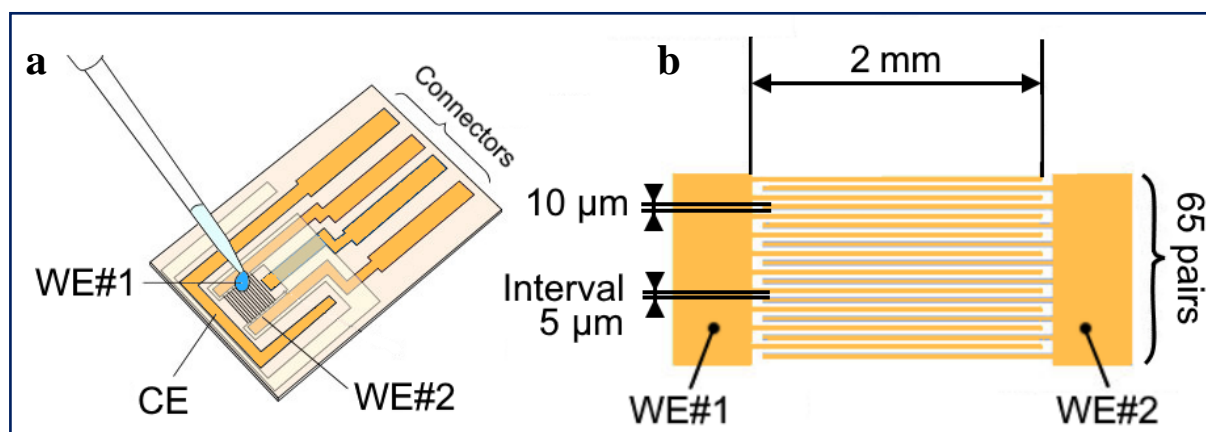


Figure 2.5: (a) Illustration of two interdigitated electrodes built on a glass support with lithographic techniques and (b) dimension of the interdigitated part adapted from ALS[®] documentation, Japan

II.1.3 The EC set-up for membrane testing

A slight different set-up was used in chapter 5 for membrane testing. A teflon cell containing a platinum wire as counter electron and a pseudo Ag/AgCl wire as reference electrode was used (Figure 2.6). The reference electrode was daily regenerated because the teflon cell is stored in dried state when not in use. Electrogeneration of AgCl on RE was performed by applying a bias of -2 V for 60 s and +1 V for 300 s on a two electrode system made by Ag/AgCl as WE and

platinum as CE.^{47,55} Electrolyte during this anodization process was made with 3.5M KCl and 0.01M HCl and enhance to get a reference potential with an accuracy of ± 0.05 V against a fresh Ag/AgCl electrode. The geometric surface of the membrane directly in contact with the solution was estimated to be 2 cm².

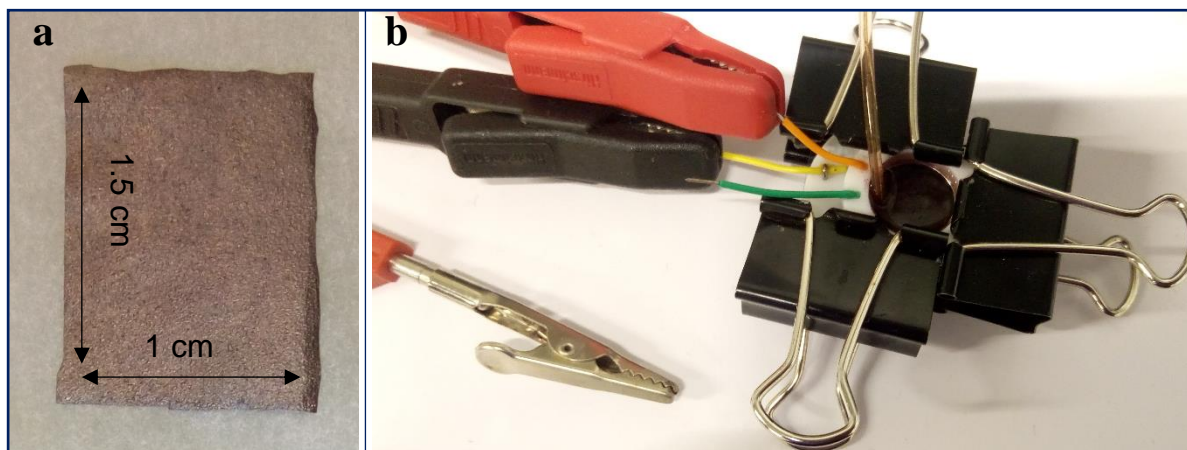


Figure 2.6: Illustration of (a) the polyurethane membrane with few layers graphene (PU-FLG) and (b) the three electrode set-up made from a Teflon hole embedding Pt and Ag/AgCl wires to test the membrane as working electrode

II.2 Spectroscopic apparatus

II.2.1 UV-Vis spectrophotometer

In spectrophotometry, the sample is illuminated with a beam having a precise intensity (Figure 2.7). This beam can be either reflected, adsorbed or transmitted. Neglecting the reflection and knowing the initial intensity (I_0) and the intensity after passing through the sample (I), the absorbance of the sample can be determined. Beer-Lambert's law correlate the amount of absorbed light with the concentration of absorbing species (Equation 2.5). Wavelength of the incident beam is controlled because each sample do not absorb equally each wavelength. Conversion of absorbance into concentration is possible only if the extinction coefficient at a given wavelength (ϵ_λ) and the optical length path (l) have been previously determined.

$$\log_{10} \frac{I_0}{I} = A = \epsilon_\lambda \times l \times c \text{ with } \begin{cases} \epsilon_\lambda: \text{extinction coefficient at } \lambda \text{ (mM} \cdot \text{cm}^{-1}) \\ l: \text{the optical path length (cm)} \\ c: \text{the concentration in attenuating species (mM)} \end{cases} \quad (\text{Equation 2.5})$$

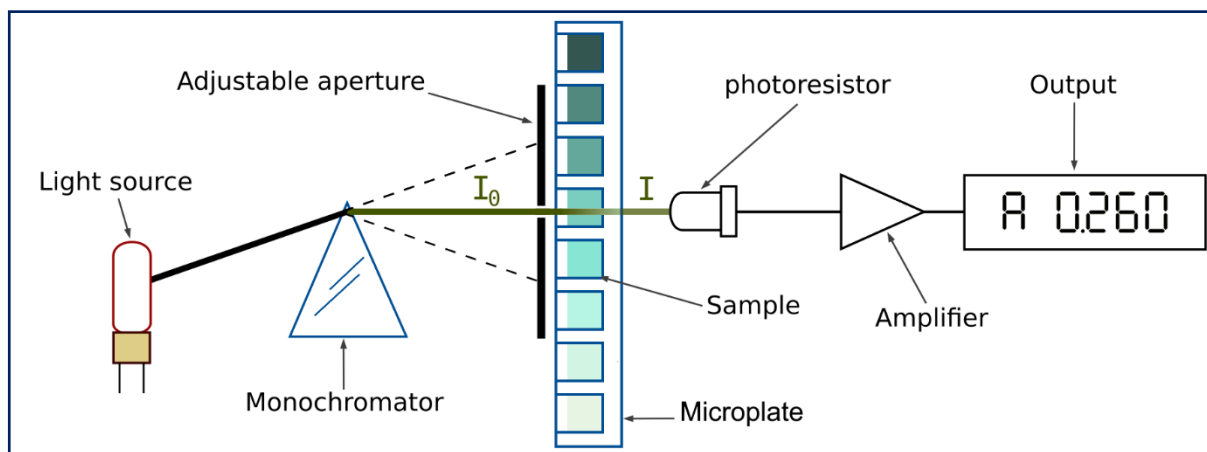


Figure 2.7: Illustration of the typical set-up used for absorption spectrometry equipped with a microplate reader. In practice two 45° mirrors are used in SAFAS Xenius (the microplate is horizontal and not vertical). Figure credits go to Yassine Mrabet.

A spectrophotometer SAFAS Xenius XC® (SAFAS, Monaco) equipped with microplates reader has been used for every absorbance experiment in the UV-Visible window. Spectral range started from 200 to 1000 nm with an excitation bandwidth of 5 nm.

Corning-type 96-wells UV-transparent microplates with a flat bottom were used within the 230-400 nm range and standard Corning® plate otherwise. Diameter of each well was 7.0 ± 0.1 mm which enhance to make the direct correlation between volume and light pathway inside the tested solution (Table 2.7). These geometric values were in good accordance with experimental observation of the optical lengthpath (Equation 2.6) according to Greiner Bio-one Application Note and Promega Technical Note.⁵⁶ Slight variations observed at low volume were due to capillarity forces (meniscus) as observed in Table 2.7. Experimentally, volume between 200 and 300 μL were systematically chosen for all assays.

$$l(\text{cm}) = \frac{(A_{977\text{nm}} - A_{900\text{nm}})_{\text{microplate}}}{(A_{977\text{nm}} - A_{900\text{nm}})_{1\text{cm-cuve}}} = \frac{(A_{977\text{nm}} - A_{900\text{nm}})_{\text{microplate}}}{0.18} \quad (\text{Equation 2.6})$$

Table 2.7: Determination of experimental pathway for UV/standard 96 wells-plate

Volume of assay	0 μL	100 μL	150 μL	200 μL	250 μL	300 μL
Geometric Light Pathway (cm) $\varnothing=7\text{mm}$	0.00	0.26	0.39	0.52	0.65	0.78
Experimental Light Path (cm)	-0.01	0.22	0.37	0.52	0.65	0.79

II.2.2 Dynamic light scattering

In dynamic light scattering technique, a monochromatic laser (633 nm) is used to illuminate a colloidal sample – *i.e* a liquid sample with particles in suspension. When the beam reaches a particle (enzyme or NPs), they will scatter the light in several directions and in a classic DLS set-up, the resulting scattered light will be collected at an angle of 173° in regard with the laser. At low concentration, particles can be seen as isolated and multiple scattering between two particles will be mostly limited. In that case the collected light will be an average of single scattered events and fluctuation of the light intensity will be observed due to the random Brownian motion of particles. Indeed by moving, particle will change their way to scatter and this will induce light fluctuation at the macroscale. Now the Brownian movement will also be size-dependent as smaller particle move quicker than larger one. Thus fast fluctuation in scattering is correlated to small particles and slow intensity fluctuation to large particles population (Figure 2.8.a). During DLS measurement, many snapshots on a short period range (10 seconds) will be collected and the intensity change will be compared to the previous snapshot (Figure 2.8.b). The faster the intensity pattern is lost, the faster the particle move and this change is recorded via an autocorrelation function (Figure 2.8.c and equation 2.7). This autocorrelation function is then fitted to retrieve the translational diffusion coefficient of particles D_T and this coefficient is directly proportional to the hydrodynamic diameter of the particle according to the Stokes-Einstein equation (equation 2.8).

$$G = \int_0^\infty I(t)I(t + \tau)dt = B + Ae^{-2q^2D_T\tau} \quad (\text{Equation 2.7})$$

$$d_H = \frac{kT}{3\pi\eta D_T} \text{ with } \begin{cases} k : \text{Boltzmann constant} \\ T : \text{Temperature (K)} \\ \eta : \text{Liquid viscosity (Pa s)} \\ D_T : \text{Translational diffusion coefficient (m}^2\cdot\text{s}^{-1}) \end{cases} \quad (\text{Equation 2.8})$$

It has to be noted that the Stokes-Einstein equation is only valid for spherical nanoparticles and that liquid viscosity and temperature has to be carefully settled in order to get an accurate size determination. Viscosity was determined by the solvent which is either Milli-Q water or saline phosphate buffer (PBS 10mM) in our case. Data about viscosity and refractive index of these solvent are gather in Table 2.8.

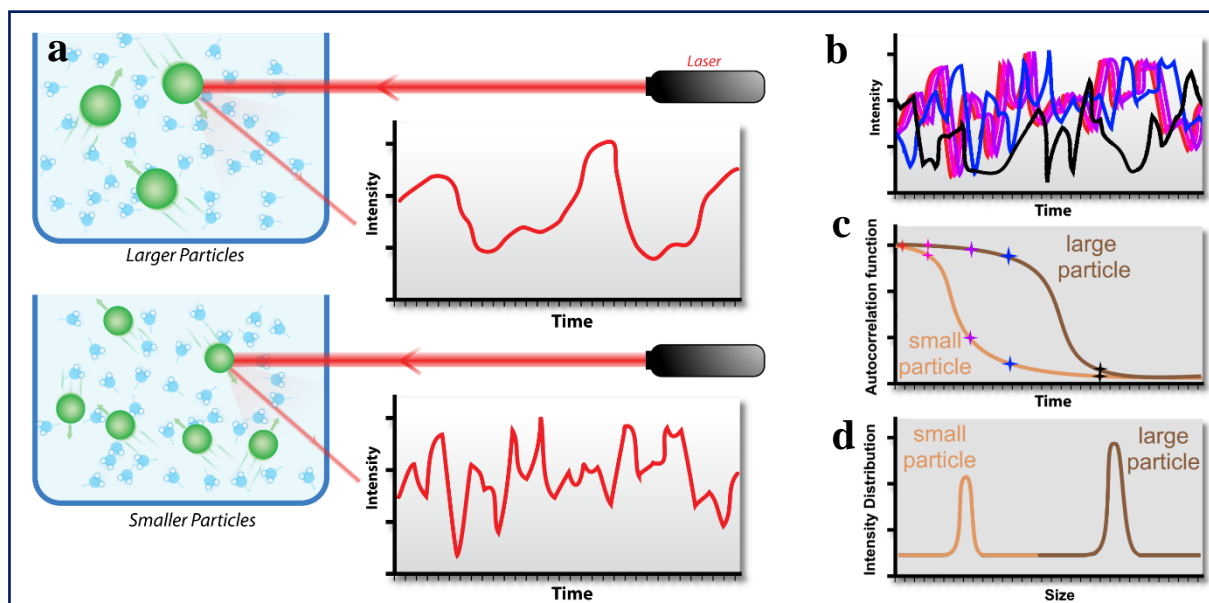


Figure 2.8: (a) Illustration of the dynamic light scattering measurement for two different particles size. Credit for the figure goes to Mike Jones with minors adaptations. (b) Illustration of the compilation of five intensity snapshot for large nanoparticles and (c) the resulting autocorrelation function. (d) Illustration of the final hydrodynamic size distribution using Stokes-Einstein equation.

Collected Measurement was following the DLS standard operating procedure (EUNCL-PCC-001) from the European Nanomedicine Characterization Laboratory. An optimized equilibrium time of five minutes before any measurement was settled and five measurements with twelve runs of ten seconds each were performed.

Table 2.8: Viscosity and refractive index of the solvent used in this thesis according to the EUNCL-PCC-001 procedure from the European Nanomedicine Characterization Laboratory

Dispersent	Viscosity (mPa.s)			Refractive Index
	20°C	25°C	37°C	
MQ water	1.002	0.89	0.692	1.332
NaCl10mM	1.003	0.891	0.693	1.332
PBS10mM	1.023	0.911	0.713	1.334

II.2.3 X-ray photoelectron spectroscopy

X-ray photoelectron spectroscopy (XPS) also known as Electron Spectroscopy for Chemical Analysis (ESCA) is an analytical technique for surface characterization (chemical analysis within the first 5-10 nm). When X-ray go toward a sample, it excites atoms' core electrons with a sufficient energy to break the photoelectron away from the nuclear attraction. These ejected photoelectrons have a characteristic energy that depends on the element, its initials orbitals and the chemical environment of the atom. Carbon or Oxygen 1s orbital will not be at the same binding energy (*i.e.* N 1s: 400 eV, C 1s: 285 eV, O 1s: 540 eV). Binding energy also depends on the oxydation state of the atom as illustrated with carbon on the figure 2.9.b. This binding energy (E_L) for the ejected electron is calculated with the photoelectric effect equation:

$$E_L = h\nu - T - \theta \text{ with } \begin{cases} h\nu: \text{energy of the Al-K}\alpha \text{ photons} \\ T: \text{the kinetic energy} \\ \theta: \text{work function (instrument correction)} \end{cases} \quad (\text{Equation 2.9})$$

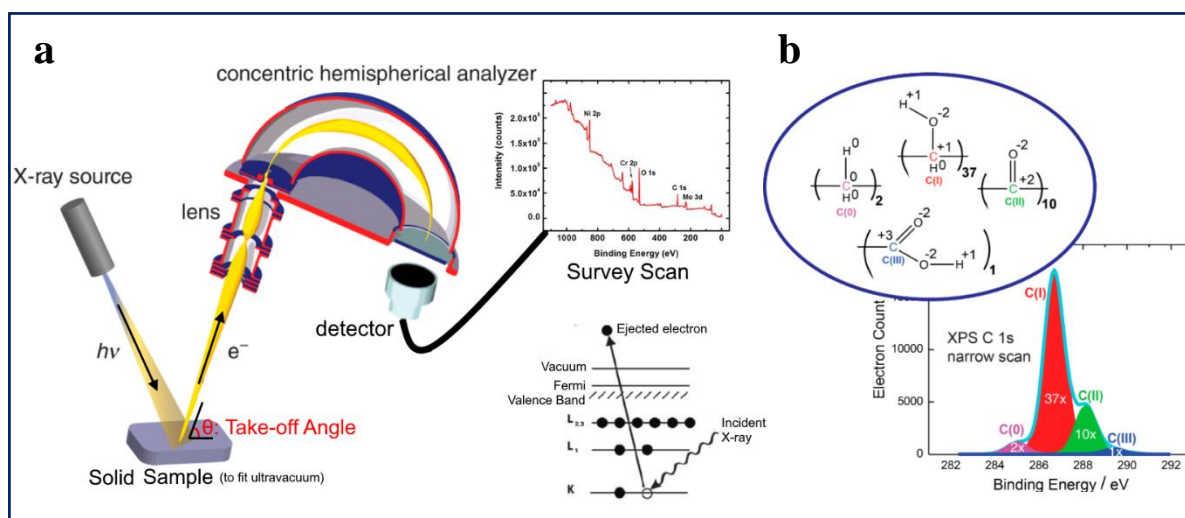


Figure 2.9: Illustration of the XPS Technique. (a) Instrumentation, illustration of the photoelectron extraction and the obtained survey when an energy range is sampled. (b) Illustration of the influence of carbon environment (oxidation state) on the binding energy with a narrow scan on the C1s band. Figure is adapted from [72]

II.3.1 Scanning electron microscopy

Scanning electron microscopy (SEM) is used to obtain images with high resolution from solid specimens. An electrons beam is focused on the surface of the sample through several electromagnetic lenses (Figure 2.10.a). Upon exposure, atoms on the electrons beam path will release X-ray, Auger electron but also back-scattered and secondary electron. Secondary electrons are electrons that are ejected from the valences shell of atoms. Back-scattered electrons are primary electrons (from the initial electron beam) that are elastically scattered (Figure 2.10.b). Both are used in SEM imaging. Secondary electron have generally low energy (50 eV) so only SE very close to the surface will be able to escape from the sample surface. One generally consider that SE electrons generally arise from the first 5 to 50 nm thus, they mainly contain information about sample topology. BSE electrons on the contrary have high energy (from 50 to the operating voltage). They can probe different thicknesses depending on the initial accelerating voltage (Figure 2.10.c) and the nature of the sample (heavy or light element). Also, heavy nucleus will scatter much more primary beam resulting in more BSE signal. For this reason BSE will contain information about sample composition and a Z-element contrast will be observed (brighter area contain heavy elements compared to dark areas). BSE or SE electrons escaping the sample are then collected with a detector that will be positioned at a given angle. This angle α will impact the nature of the collected signal. Electron focusing point will then be shifted along x and y-axis with beam deflection coils and the signal at the detector will be collected again. This operation will be repeated line by line to construct an image of the observed sample (Figure 2.10.a).

A Hitachi SU 8010 Ultra High Resolution Field Emission Scanning Electron Microscope was used to characterize the morphology of coatings in this thesis. Magnification of this device was from 100 \times to 800,000 \times which enhance a resolution around 1 nm. A cold cathode field emission was used as electron source and the accelerating voltage can be set from 0.5 kV to 30 kV. The microscope was equipped with two detectors. A top detector for high angle backscattered electron (HA-BSE) not used in this thesis and an upper detector used for mixed signal (SE+BSE). This upper detector can either collect SE or BSE signal. The contribution of each can be tuned depending on the voltage bias that is applied on a conversion electrode. (Figure 2.10.d). Thus with a single detector, one can either retrieve information on the topology (SE) or on the composition (BSE, Z-contrast).

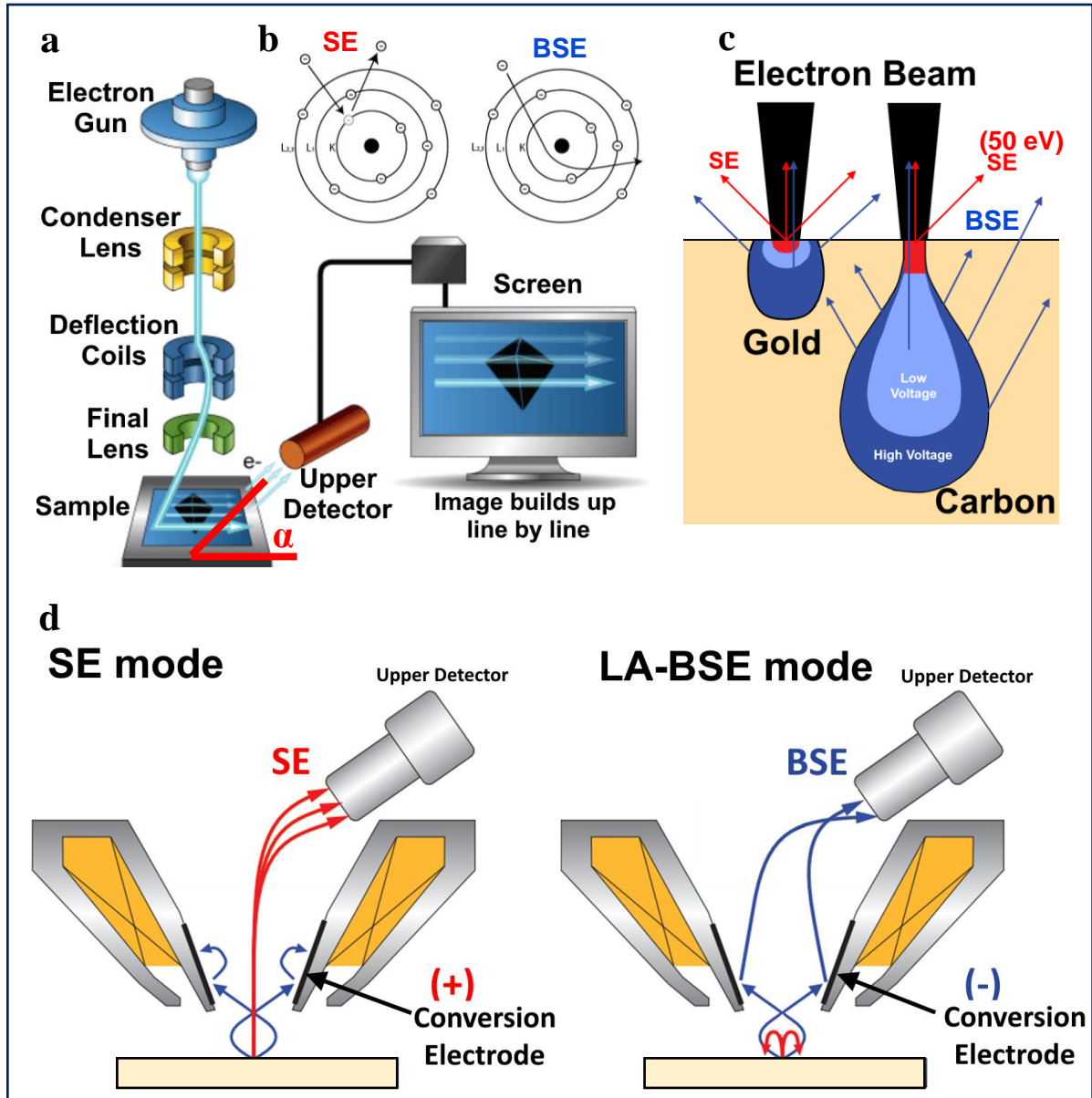


Figure 2.10: (a) Illustration of the scanning electron microscope principle with a line by line scanning of the sample with deflection coils according to [73]. (b) Zoom on the pear interaction onto heavy (gold) and light (carbon) element with the effect of voltage. (c) Illustration of the SE/BSE selection strategy based on a conversion electrode and the application of a voltage bias for SE/BSE discrimination [74].

II.3.2 Transmission electron microscopy

A Transmission Electron Microscope (TEM) was also used in this thesis. Principle is similar to SEM except that transmitted electron are collected (those that are not back-scattered). It requires more demanding sample preparation as the observed slice has to be sufficiently thin to enhance the electron beam to be transmitted to the detector located below the sample (Figure 2.11). Also the thinner the sample will be, the better the resolution could be as electron scattering area will be smaller.⁵⁷ A better spatial resolution than SEM can be obtained with TEM (< 0.1 nm) and information about the diffraction pattern by the sample can be obtained and give extra details about matter organization. When the detector is placed in the focal plane, the resulting contrast will be a function of sample density. Therefore, area where sample is thicker or where atoms are heavier will be dark and atoms with a low Z-value will be bright as it almost do not attenuate the beam. Compared to SEM, high tension are used (100-300 kV) and no deflection coils are required as the whole sample is analyzed at the same time. All the others constitutive elements of the TEM microscope are shared with SEM (Figure 2.11). For this thesis, a Technai G2 (FEI) with an Eagle 2k (FEI) ssCCD camera was used to image samples.

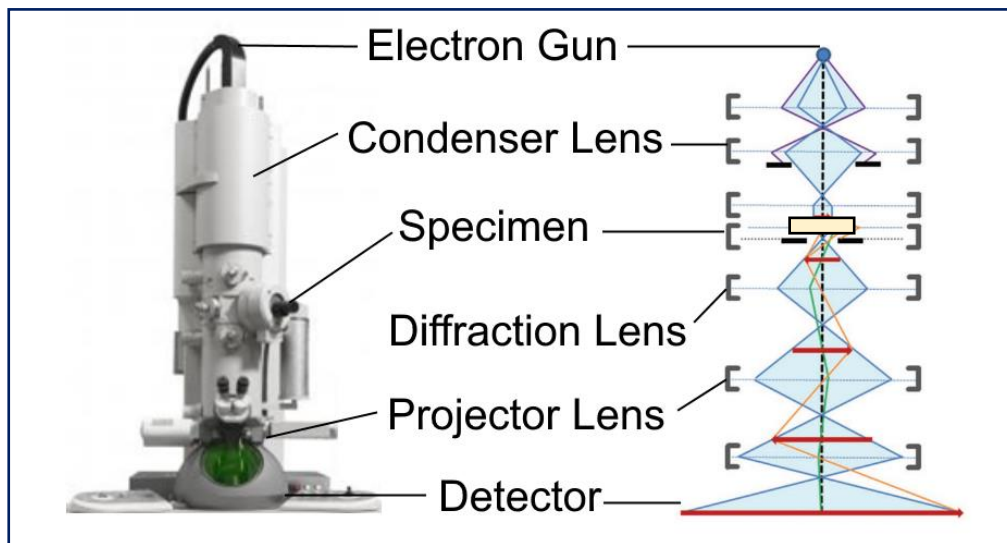


Figure 2.11: Illustration of a transmission electron microscope column according to [58].

III. Methods

III.1 Polyphenol and AuNPs Characterization

III.1.1 Gallol moieties quantification

As previously described, tannic acid was found to be a mixture much more complicated than the commonly accepted representation. The number of phenol groups per molecule may differ from the theoretical value of 10. Also their nature can be diverse such as catechol (1,2-dihydroxyquinone), gallol (1,2,3-trihydroxyquinone) or caffeic acid. Since the reactivity of tannic acid is the basis of this thesis from nanoparticle synthesis to film electrodeposition, it is crucial to correctly estimate the concentration of each function and its oxidation state. This estimation was performed in two stages, first phenol concentration was determined with UV-Vis absorption and then, reactivity was estimated from a Prussian blue assay.

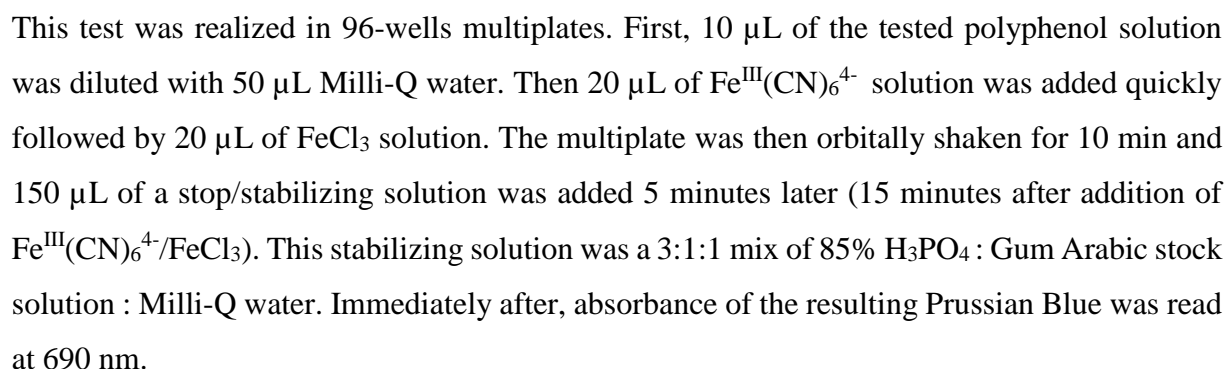
III.1.1.1 Using near UV absorption of phenolic groups

The estimation of each function was performed in special UV 96-wells multiplates with a volume of 200 μL . The tannic acid solution was prepared at 20 μM concentration and gallic acid (GA) and procatechuic acid (PCA) at 200 μM in order to stay below 1 unit of absorbance. Absorbance was recorded from 230 to 600nm with SAFAS Xenius device.

Table 2.9: UV and PB determination of gallol/catechol content in tannic acid

	Parameter		GA@260nm	PCA@250nm	TA@275nm
UV-Vis test	λ_{max} (nm)	Exp.	260	250	275
	Extinction Coefficient ($\text{mM}^{-1}\cdot\text{cm}$)	Exp.	8.8 ± 0.2	8.8 ± 0.2	76.5 ± 0.2
	UV-equivalent GA/molecule	Th.	1	1	10
		Exp.	–	1.0 ± 0.2	8.7 ± 0.2
Prussian Blue test	Slope ($\text{A}\cdot\text{mM}^{-1}$)	Exp.	3.2 ± 0.1	1.7 ± 0.1	15.2 ± 0.1
	PB-equivalent GA/molecule	Exp.	–	0.5 ± 0.1	4.8 ± 0.1

Reactivity of polyphenols was tested with a Prussian Blue assay adapted from A.E. Hagerman guidelines⁵⁹. Reaction is based on the reduction of $\text{Fe}^{\text{III}}(\text{CN})_6^{4-}$ to $\text{Fe}^{\text{II}}(\text{CN})_6^{4-}$ by hydroquinone moieties which then produce a strongly absorbent compound with Fe^{3+} from FeCl_3 named Prussian blue (Equation 2.10) :



A calibration curve was prepared with GA and PCA molecules with various concentrations from 0 to 100 μM and was used to present result in equivalent GA-reactivity or TA-reactivity (Table 2.9). It has been observed from this test that gallol and catechol moieties do not have the same redox activity. For a same concentration, GA transfer at least twice more electrons to

$\text{Fe}^{\text{III}}(\text{CN})_6^{3-}$ than PCA. Difference may arise from the kinetic and reactivity into a further oxidation of quinone/dimers.^{60,61} The Prussian blue test of tannic acid from Sigma-Aldrich gave a PB-equivalent GA/TA of 4.8 which is about half of the equivalent obtained from UV test. It is therefore probable that only the outer phenolic functions of tannic acid can react with $\text{Fe}^{\text{III}}(\text{CN})_6^{3-}$. Also, it can arise from the nature of the phenolic content, indeed catechol moieties react twice time less than GA (Table 2.9) and the higher maximum absorption of TA (275 nm) could also suggest the presence of others phenolic moieties in TA powder such as caffeic acid (320 nm absorption, unpublished data from own work).

The similar procedure was used to determine the number of GA per equivalent nm^2 of surface for each nanoparticles size (Table 2.10). Background subtraction was performed to remove the nanoparticle plasmonic band contribution at 690 nm. Equivalent GA was divided by the nanoparticle concentration and the surface of nanoparticles ($4\pi R_{\text{NP}}^2$) in order to be comparable. As observed in Table 2.10, significant differences in reactivity of NPs was observed depending of the NP size.

Table 2.10: PB determination of gallol/catechol content onto the nanoparticles

PB test Determination	NP10	NP20	NP30
Equivalent GA/ nm^2 of NP	11 ± 3	21 ± 3	33 ± 5

III.1.2 Nanoparticles size

Nanoparticle size was estimated from TEM micrographs (Hitachi SU-8000/FEI Tecnai G2, Japan) as well as DLS (Zetasizer Nano ZS from Malvern Panalytical, UK). TEM procedure consisted in deposition of 5 μL of washed NPs suspension onto a carbon covered grid that was then negatively stained with 5 microliters of uranyl acetate (2% in water) for 1 minute and finally dried using a filter paper. This staining was used to eventually observe the TA capping thickness onto nanoparticles. It was difficult to observe it and we stated that TA thickness was ≤ 1 nm meaning only a single monolayer of TA or GA is present as capping agent even after 2 month of storage. Size analysis was performed with Image J and distribution was made from 60 measurements along x and y axis on NPs (large NPs are quite oblongs).

Hydrodynamic size was recorded with a four time diluted NPs solution using DTS1070 cell (Malvern Panalytical, UK). An average of five measurements was collected and averaged using a temperature stabilization at 25°C. A Laplace inversion PSD analysis was used to fit the autocorrelation function assuming multiple diffusion coefficients may be presents in the sample. Last, size dispersion was presented using the particle intensity dispersion. Zeta potential was determined after size analysis using the procedure from the European Nanomedicine Characterization Laboratory (EUNCL-PCC-002).

III.1.3 Nanoparticles concentration

Two different methods were used to determine nanoparticle concentration. First the NPs concentration was determined with the assumption that all Au^{3+} ions have reacted and were dispersed equally between spherical nanoparticles. In our case, polyphenol were always in excess and we got narrow dispersion (except for NP40) so these assumptions were acceptable. Theoretically, this method gives the highest NPs concentration that we may get. In a nutshell, size on the population were taken from TEM/SEM micrographs and the following formula (Equation 2.11) was used:

$$c_{NPs}(\text{NPs/L}) = \frac{3 \cdot 10^{-3} [\text{HAuCl}_4] \times df \times Mw_{\text{Au}}}{4\pi \times (10^{-7} R_{NPs})^3 \times d_{\text{Au}}} \quad \left\{ \begin{array}{l} [\text{HAuCl}_4]: \text{concentration of the precursor solution (mM)} \\ df: \text{dilution factor which is } \frac{8}{20} \text{ in our case} \\ Mw_{\text{Au}}: \text{molar mass of gold atom (196.96 g}\cdot\text{mol}^{-1}) \\ R_{NPs}: \text{TEM radius of NPs (nm)} \\ d_{\text{Au}}: \text{volumic mass of gold (19.32 g}\cdot\text{cm}^{-3}) \end{array} \right. \quad (\text{Eq 2.11})$$

Second method was based on Beer-Lambert law using a molar extinction coefficient at the maximum wavelength that was retrieved from Liu *and al.* (Equation 2.12). The following relation was proven to be reliable on our size range (4-40 nm) and to be independent of the capping ligand.⁶²

$$\ln \varepsilon = 3.321 \ln(2R_{NPs}) + 10.805 \quad \text{with} \quad \left\{ \begin{array}{l} \varepsilon: \text{molar attenuation coefficient (M}^{-1}\cdot\text{cm}^{-1}) \\ R_{NPs}: \text{radius of PPhAuNPs (nm)} \end{array} \right. \quad (\text{Eq 2.12})$$

The maximum absorption at λ_{max} was determined with SAFAS Xenius in triplicate. The concentration of the washed NPs was also adjusted with dilution in MQ water to stay slightly below one unit of absorbance. The total volume assay was always set to 200 μL which correspond to 0.52 cm pathway length. The Beer-Lambert equation was then used to determine

the NPs concentration with this second method (Equation 2.13) using the extinction coefficient calculated from Equation 2.12. Both methods gave similar concentration with a standard deviation below $\pm 15\%$.

$$C_{PPhAuNPs} = \frac{A_{532nm} \times N_A}{0.21 \cdot \epsilon} \text{ (NPs/L) with } \begin{cases} \epsilon: \text{molar attenuation coefficient (M}^{-1} \cdot \text{cm}^{-1}) \\ N_A: \text{Avogadro Number (mol}^{-1}) \end{cases} \quad (\text{Eq 2.13})$$

III.2 Enzyme characterization

III.2.1 Enzyme and cofactor concentration

Concentration of enzymes was double checked via two different spectroscopic methods: the UV/Vis absorption at 280 nm and a Bradford assay.⁶³ UV absorption of enzymes at 280nm mainly arises from three amino acids: tyrosine, tryptophan and dimerized cysteine (cystine).⁶⁴ Extinction coefficient from the literature was taken but knowing the exact enzyme sequence (PDB database and ExpasyTools), it was also possible to confirm this molar extinction coefficient.⁶⁵ The enzymes were solubilized in MQ water at $1 \text{ mg} \cdot \text{mL}^{-1}$ and their absorption was determined for 200 μL volume assay in triplicate. FAD and Heme cofactor were also quantifiable at 452 nm²⁹ and 403 nm³⁷ respectively. Concentration was $10 \text{ mg} \cdot \text{mL}^{-1}$ and volume assay 200 μL . Ratio was used to determine the equivalent cofactor per enzyme that was conform with the theoretical values (Table 2.11).

Table 2.11: Enzyme concentration determination based on two spectroscopic methods (absorbance at 280 nm and a Bradford assay).

%mg of enzyme per weighted mg	Seller's specification	A280nm test	Bradford Assay	Retained value	Cofactor/enzyme
HRP-Serva	'Salt Free'	$91.1 \pm 0.3 \%$	$90 \pm 7 \%$	90%	~ 0.96
GOx-Sigma (batch 1)	78/81% Biuret	$79.6 \pm 0.3 \%$	$82 \pm 4 \%$	80%	~ 2.2
GOx-Sigma (batch 2)	78/81% Biuret	$76 \pm 4\%$	$74 \pm 2\%$	75%	—

Another standard staining test for protein concentration known as Bradford assay⁶³ was performed in complement. This test is based on the electrostatic interaction of Coomassie Brilliant Blue with some amino acids. In this test, interaction of the dye with amino acids

creating local acidic condition shift its absorbance from 465 to 595nm. 5 μL of enzyme at 1 $\text{mg}\cdot\text{mL}^{-1}$ in water was mixed with 250 μL of Bradford solution from Sigma (B6916). Solution absorbance at 595 nm was determined after 30 min. To retrieve enzyme concentration, a calibration curve against bovine serum albumin (BSA) was prepared between 0.1 and 1.4 $\text{mg}\cdot\text{mL}^{-1}$ according to Sigma guidelines. The resulting enzyme concentrations based on Bradford are gathered in Table 2.11. Deviations lower than 4% was obtained between UV test ($A_{280\text{nm}}$) and Bradford assay.

III.2.2 Enzyme size and glycosylation state

Enzyme size was determined from 2 $\text{mg}\cdot\text{mL}^{-1}$ concentration in water. DLS procedure was still following the standard (EUNCL-PCC-001) and measurements were replicated five times. Enzyme size from TEM was retrieved with an estimate of the “bright” spot obtained from uranyl acetate stained enzymes. An average on 30 measurements was performed with Image J (Table 2.12). Compared to DLS, enzymes did not appeared to be heavily glycosylated. For comparison a GOx batch from Apollo Scientific was previously used, having a DLS size around 8.2 nm.

Table 2.12: Enzymes size based on DLS and TEM measurement.

Enzyme Size	PBS X-ray model	DLS (nm)	TEM (nm)
HRP-Serva	1HCH ³⁹ : 6.0×4.4×4.0 nm ³	5.5 ± 0.5	4.3 ± 0.7
GOx-Sigma	1CF3 ²⁶ : 6.0×5.2×7.7 nm ³	6.9 ± 0.5	7.3 ± 0.7

III.2.3 Enzyme activity with colorimetric test

Activity tests were specific for each enzyme and are detailed below. The stability was tested with the repetition of the activity test over the time. Inhibition was tested by adding instead of the MQ-water fraction the corresponding amount of inhibitors (TA or NPs). For inhibition, a rest time of half an hour before addition of the substrate (ABTS/H₂O₂ or ABTS/Glucose) was set to let the enzyme/TA or enzyme/NPs interact until its final state. This resting time was chosen because it was the same used for electrodeposition of enzyme/NPs film.

Horseradish peroxidase (HRP) was tested with a chromogenic substrate: 2,2'-azino-bis(3-ethylbenzothiazoline-6-sulfonic acid) that will be further denoted as ABTS. The standard

procedure is detailed in table 2.13. This test is based on the reduction of H_2O_2 into water and the oxidation of ABTS into a colored radical cation ($\text{ABTS}^{\cdot+}$). Equation 2.15 is showing the reduced state ABTS^+ , but a further reduced state named ABTS^{2+} is also produced. Due to the potential inhibition of HRP by high H_2O_2 concentration, $\text{H}_2\text{O}_2/\text{ABTS}$ was set at 10 mM and it was found sufficient to saturate the enzyme response for twenty minutes at least depending on the enzyme concentration.

Glucose Oxidase (GOx) was also tested with a double enzymes assay.⁶⁶ The H_2O_2 produced by glucose oxidation (equation 2.14) is quantified with the previous HRP/ABTS system. In this case, HRP is added in the very late stage. HRP/ABTS were used in excess to avoid dual kinetic limitation. Details about volumes and concentrations are given Table 2.13.

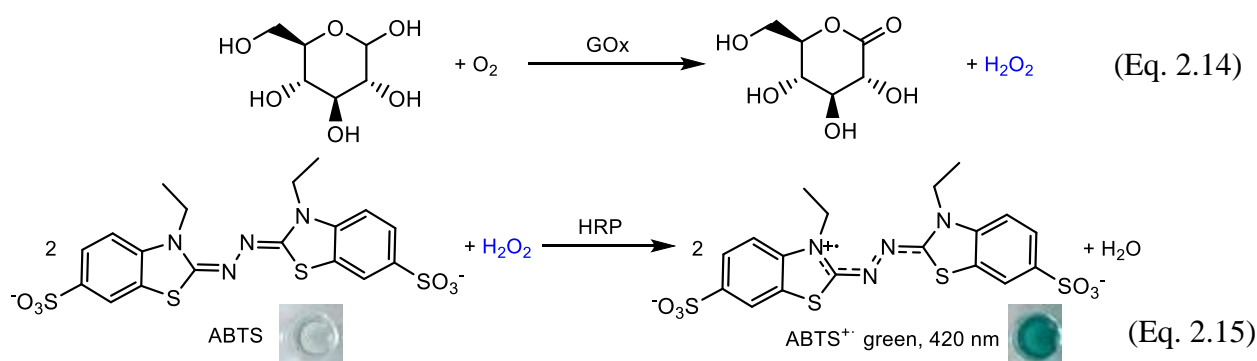


Table 2.13: Enzymatic colorimetric activity assay for HRP and GOx

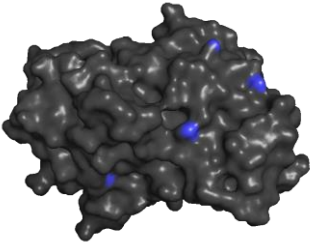
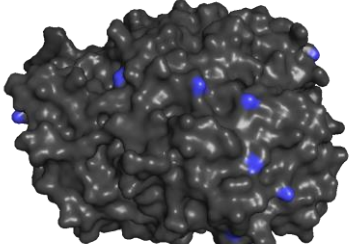
Colored Specie	HRP test	GOx test (dual enzyme test)
General Procedure	10 μL of HRP at $0.5 \mu\text{g}\cdot\text{mL}^{-1}$ in water 10 μL water 40 μL water of inhibitor Rest time 30min 140 μL 10 mM ABTS/10 mM H_2O_2 in PBS 10mM	10 μL GOx à $0.5 \mu\text{g}\cdot\text{mL}^{-1}$ in water 40 μL water of inhibitor Rest time 30min 10 μL of HRP at $1 \text{ mg}\cdot\text{mL}^{-1}$ ds MQ 140 μL 10 mM ABTS/10mM Glucose in PBS10 mM
Kinetic measurement	Measure à 420 nm every 15 s $\epsilon_{420\text{nm}}=36 \text{ mM}^{-1}\cdot\text{cm}^{-1}$	

III.2.4 Accessible lysine/cysteine residues

Available primary amine (lysine) and thiol (reduced cysteine) were estimated from the PDB model of enzyme (Table 2.14). Only functions present on the surface of the enzyme was taken into account using the following pymol code for determination (Table 2.14). Based on the X-

ray model, 30 lysines per GOx dimer and 5 lysines per HRP are available. It has to be noted that the PDB models do not take into consideration the N-glycosylation that may obviously reduce the number of accessible residues. According to the model, all cysteine bonds are reduced into cystine for HRP and GOx. Thus only amine are likely to react with quinone moieties.

Table 2.14: Information of lysine and cysteine residues of HRP and GOx

Enzyme Name	HRP-C	GOx-AN
PDB code	1HCH ³⁹	1CF3 ²⁶
Resolution (Å)	1.6	1.9
Released Date	2001	1999
Enzyme Model (GOx is the monomer)		
Accessible Lysine (-NH ₂)	5	15×2
Accessible Cysteine (-SH)	0	0
Pymol code	<pre> remove resn hoh # remove water h_add # add hydrogens as surface color grey30 # color the enzyme in grey select sulf_cys, (resn cys and (elem S)) # get the sulfur atom of cysteine color yellow, sulf_cys # color sulfur in yellow select disulfides, CYS/SG and bound_to CYS/SG color grey30, disulfides # remove coloration of disulfur bonds select amine_lys, (resn lys and name NZ) # get N from lysine color tv_blue, amine_lys # color free amines ("NZ" in PDB file) </pre>	

A ninhydrin (NHD) test has also been performed to confirm the presence of accessible amine. Briefly, solution were made from 50 µL of 20 mM NHD in EtOH and 150 µL of the adding enzyme in water (10 mg·mL⁻¹). Solution was then heated at 60°C in an oven for 30 min and the resulting colored complex named Ruhemann's purple was recorded at 570 nm. This test confirm the presence of amine however, heat denaturation and the reactivity of secondary amines to a lesser extent can led to an overestimate. Therefore, this test could not be accurately quantitative.

III.3 Enzyme/nanoparticles complexes

III.3.1 Estimation of the theoretical monolayer ratio

The theoretical molar ratio of enzyme/NPs to obtain an adsorbed monolayer (R_{th}) was defined as follow (Equation 2.16). The surface to cover was calculated at $R_{NP} + R_{ENZ}$ and divided by an estimate of the enzyme footprint S_e (Figure 2.12). It has to be noted that no compacity factor has been taken into account, thus, this calculated ratio is the upper theoretical value.

$$R_{th} = \frac{4 \times (R_{NP} + R_{ENZ})^2}{(R_{ENZ})^2} \quad (\text{Equation 2.16})$$

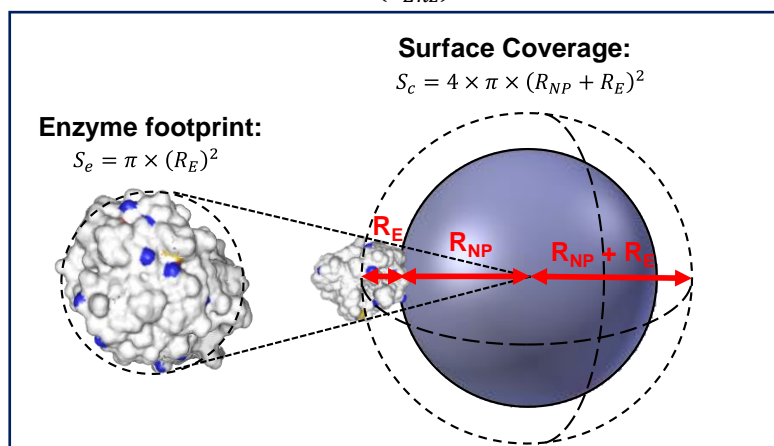


Figure 2.12: Illustration of enzyme footprint and the estimation of surface coverage at $R_{NP} + R_E$

Even if this simple calculation of R_{th} is imperfect (enzymes are assumed to be undeformable solid sphere and no compacity factor is taken into account), this ratio gives a good approximation for the considered enzyme and NP size range. We compute an incremental algorithm (known as the Thomson problem) and then verify that the distance between all points representing an enzyme is lower than $2 \times R_{ENZ}$ with Wolfram Mathematica. The solution found for GOx/NP10 with this algorithm is concordant with our simple estimation.

The calculation of the theoretical value is used in Chapter 3 and 4 for HRP, GOx, choline oxidase (ChOx) and urate oxidase (UOx). Values are gathered in Table 2.15.

Table 2.15: Calculated theoretical monolayer ratio as a function of enzyme and NP size

NP size (nm)	HRP (5.5nm, 44 kDa)	ChOx (6.0nm, 95 kDa)	GOx (6.9nm, 160 kDa)	UOx (7.4nm, 120 kDa)
6.8	20	18	16	15
10	36	32	27	25
30	148	128	102	92
40	298	256	201	178

III.3.2 Aggregation/flocculation Test

The aggregation test enhance to estimate the number of adsorbed enzymes. Indeed, our tannic acid coated nanoparticles alone are not stable above 50-100 mM NaCl (Figure 2.13.a). When increased amount of enzymes adsorb onto nanoparticles it will progressively create a protective corona that will prevent nanoparticles from aggregation (Figure 2.13.b). The aggregation can be followed by a change in size (DLS) or a change in the plasmonic band of nanoparticles that is shifted from the initial wavelength (526 nm for NP12) to higher values.

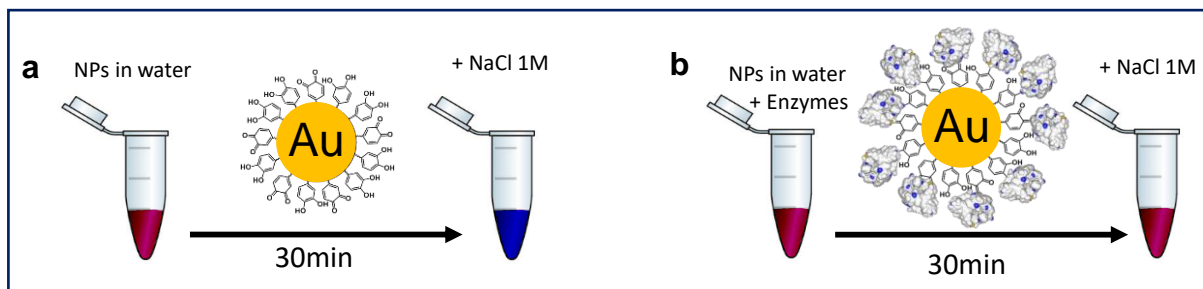


Figure 2.13: Illustration of NaCl 1M salt induced aggregation (a) in absence of enzymes and (b) in presence of a complete protective enzymes corona around nanoparticles.

For this test, 100 μL of enzyme solution at different concentration was mixed with 100 μL of undiluted NPs ($1 \cdot 10^{16}$ NPs $\cdot\text{L}^{-1}$ for NP12). Both were prepared in water at room temperature. Enzyme concentration was varied to get R/R_{th} ratios from 0 to 15. After a resting time of 30 min, the aggregation test was performed by addition of 50 μL NaCl solution at 5 M to the mixture to reach a final concentration of 1 M NaCl. The absorbance spectra of enzyme/NPs suspensions was then recorded with the spectrophotometer. The shift of λ_{max} allows to follow the aggregation of enzyme/NPs due to the color change. Also, the size of aggregates was determined by DLS measurement and used in addition to the change in plasmonic band to determine the enzymes/NPs ratio that prevent from aggregation.

III.3.3 Bradford test

The principle of the Bradford assay is similar to the test performed for enzyme quantification. The main difference is that here, nanoparticles/enzymes complexes were washed to only quantify adsorbed enzymes (Figure 2.14).

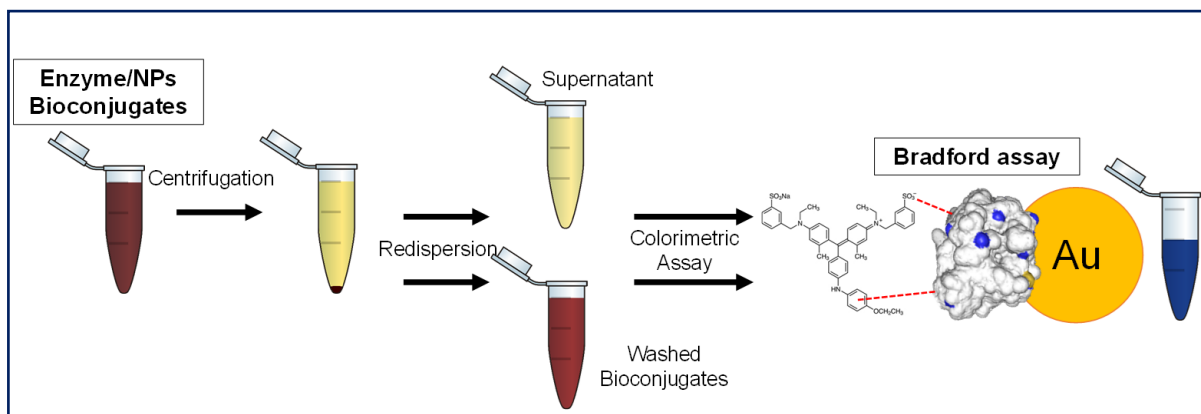


Figure 2.14: Illustration of the Bradford assay for adsorbed enzyme quantification

Enzyme and NPs were mixed at different ratio and after a resting time of 30 min, solution was centrifugated to remove any unbound enzymes using the same centrifugation time as for NPs alone. Sample preparation then consist in mixing 100 μL of washed bioconjugates with 200 μL of Bradford reagent for 30 min. Absorbance value was read at 595 nm. This test was strictly performed in the linear range of the assay meaning initial concentrations were adjusted to remain below 0.74 and 0.94 absorbance unit for HRP and GOx respectively. Background subtraction was performed using NPs as a blank since TA react with Coomassie blue to a lesser extent.

III.3.4 Activity test

The activity test of adsorbed enzymes was similar to the activity assay for enzymes only. The main difference is that here, nanoparticles/enzymes complexes were washed to only quantify adsorbed enzymes (Figure 2.15). The enzymes/NPs bioconjugates were prepared similarly to the Bradford assay and were also centrifugated after 30 minutes to remove unbound enzymes (Figure 2.15). In addition, tests were performed either at constant NPs or enzyme concentration. Supernatant was also tested to ensure that the uncertainty of $\sim 2\%_{\text{vol}}$ of the remaining supernatant was minimal compared to bound enzymes. The enzymatic test consisted in 10 μL of enzymes/NPs washed bioconjugates dispersed with 40 μL of water. 10 μL of a HRP solution at $\sim 50 \mu\text{g}\cdot\text{mL}^{-1}$ was added quickly followed by addition of 140 μL of 10 mM ABTS/10 mM glucose solution prepared in PBS 10 mM.

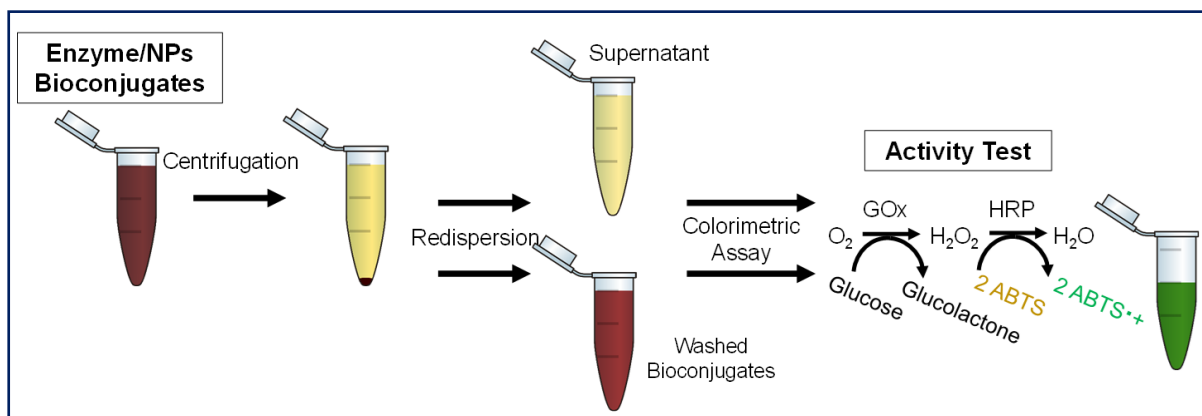


Figure 2.15: Illustration of the activity assay for adsorbed enzyme quantification

III.4 Electrodeposition and thin film characterizations

III.4.1 Preliminary electrochemical requirement

Before any experiments, the crystals were cleaned for 30 min using a UV/Ozone cleaner (ProCleaner, BioForce Nanoscience) in order to get a hydrophilic surface. This procedure was not used for PU-FLG membranes. Prior every electrochemical experiment, a RC impedimetric test, a capacitive and a faradic CV were performed.

For the AuQCM quartz crystal with the QEM401 cell, a resistance around $2 \pm 1 \, \Omega$ and a capacitance around $2 \pm 1 \, \mu\text{F}$ are expected with the RC impedimetric test. A capacitive cyclic voltammogram (CV) was also systematically performed in NaCl 50 mM to check the stability of the electrochemical set-up and the eventual presence of redox active contaminants. This test is supposed to give a squared CV signal of $\pm 10 \, \mu\text{A}$ for AuQCM on the water potential window (-0.1 to 0.7 V in presence of 50 mM NaCl). Last, the RE potential was carefully checked against $\text{Fc}^+\text{OH}/\text{FcOH}$. A 0.5 mM FcOH solution in 50 mM NaCl is expected to give two redox peaks at 0.19 V and 0.25 V vs Ag/AgCl respectively which is close to the expected Nernst value (59 mV). The standard potential $E_{1/2} = \frac{E_{\text{Ox}} + E_{\text{Red}}}{2} \approx E^0$ was found to be 0.21 V again close to the tabulated value.⁴⁴ At $50 \, \text{mV} \cdot \text{s}^{-1}$ scan rate, the faradaic current were found to be $|60| \pm 5 \, \mu\text{A}$ which is close to the predicted value by Randles–Ševčík equation that is $63 \, \mu\text{A}$ assuming a diffusing coefficient of $7.4 \cdot 10^{-6} \, \text{cm}^2 \cdot \text{s}^{-1}$. Similar preliminary test were performed on interdigitated electrode (IDA) with a geometric area of $0.013 \, \text{cm}^2$. For PU-FLG membranes, a higher variability of resistivity was observed for the $2 \, \text{cm}^2$ exposed geometric surface. The RC

test gave a resistivity between 20 and 200 Ω and a very high capacitance ($> 10,000 \mu\text{F}$) probably due to polyurethane properties. Not surprisingly, PU-FLG also gave higher surtension towards water electrolysis.

Prior any EC-QCM experiment, temperature of the cell was stabilized at 22°C in aqueous buffer solution. Amplitude of oscillation (A_{F3}) and dissipation (D_3) of the third overtone were checked. Values of 20.0 ± 0.5 and 180 ± 5 were expected for A_{F3} and D_3 respectively. These values are good indicators of a bubble-free set-up as long as one consider an AuQCM crystal in presence of liquid solution with a viscosity close to water.

III.4.2 Estimation of the electroactive surface area

To evaluate the electroactive surface area, the following test was performed before and after the deposition of enzymes/NPs coatings. Cyclic voltammogram were registered at various scan rate from 5 to 500 mV/s on the bare gold crystal (working electrode) in contact with 0.5 mM FcOH in 50 mM NaCl solution. After the electrodeposition, the coatings were rinsed with 50 mM NaCl for 10 min ($400 \mu\text{L} \cdot \text{min}^{-1}$) to remove all the free FcOH until only the capacitive signal is visible. The faradic CV cycles were then repeated for the electrodeposited coating and the Randles-Sevcik equation (Equation 2.17) was used to estimate the electroactive surface area (EASA).

$$i_p = 0.446nFAC^0 \left(\frac{nFvD_0}{RT} \right)^{1/2} \quad \left\{ \begin{array}{l} i_p: \text{current peak (A)} \\ n: \text{number of exchanged electron} \\ A: \text{electroactive surface (cm}^2\text{)} \\ v: \text{scan rate (V} \cdot \text{s}^{-1}\text{)} \\ D_0: \text{diffusion coefficient (cm}^2 \cdot \text{s}^{-1}\text{)} \\ C^0: \text{ferrocene concentration (mol} \cdot \text{cm}^{-3}\text{)} \end{array} \right. \quad (\text{Equation 2.17})$$

III.4.3 Preparation of electrodeposition solution

A 5 mM FcOH solution was prepared in water using an ultrasonic bath for 30 min to quicken its dissolution with a temperature kept below 40°C . After cooling at room temperature, the solution was filtered with a $0.2 \mu\text{m}$ RC syringe filter. The enzyme (GOx or HRP) was dissolved in the FcOH solution at the corresponding concentration by taking into account the enzyme commercial purity (80% for GOx and 90% for HRP). $300 \mu\text{L}$ of this solution was further added

to ten times pre-concentrated NPs solution (previously centrifugated and washed). After 30 min, 15 μL of 1 M NaCl solution was added to reach 50 mM NaCl in FcOH/GOx/NPs suspension. For electrodeposition of NPs only, similar procedure was followed and only FcOH solution was added to pre-concentrated NPs.

III.4.4 Deposit mass and electrodeposition efficiency

Sauerbrey equation was used to convert frequency shift into deposited mass using a C constant of $17.7 \text{ ng}\cdot\text{cm}^{-2}\cdot\text{Hz}^{-1}$ valid for 5 MHz AT-cut quartz crystal (Equation 2.18). C includes the constants inherent to the quartz crystal (Equation 2.19).

For deposition of nanoparticles only, the estimation of electrodeposition efficiency was calculated. Using a geometric surface of 0.8 cm^2 (roughness from supplier is $< 1 \text{ nm RMS}^{67}$) and knowing the mass of a single nanoparticle, the number of deposited nanoparticles n_d can be estimated (Equation 2.20). As the internal cell volume is around $100 \mu\text{L}^{67}$, overall number of nanoparticles between cathode and anode n_s can also be roughly estimated. Ratio of the two values enhance to estimate the electrodeposition efficiency of our nanoparticle electrodeposition process (Equation 2.21).

$$\Delta m = -C \times \frac{\Delta f_n}{n} \times A \quad \left\{ \begin{array}{l} C = 17.7 \text{ ng}\cdot\text{Hz}^{-1}\cdot\text{cm}^{-2} \text{ for a 5MHz quartz crystal} \\ \Delta f: \text{the drop of frequency during the deposition} \\ n = \text{overtone number} \\ A: \text{the crystal surface (cm}^2\text{)} \end{array} \right. \quad (\text{Equation 2.18})$$

$$C = \frac{\sqrt{\rho_q \times \mu_q}}{2f_0^2} \quad \left\{ \begin{array}{l} \rho_q: \text{quartz density (ng}\cdot\text{cm}^{-3}\text{)} \\ \mu_q: \text{shear modulus of quartz (g}\cdot\text{cm}^{-1}\cdot\text{s}^{-2}\text{)} \\ f_0: \text{resonant frequency of the fundamental mode (Hz)} \end{array} \right. \quad (\text{Equation 2.19})$$

$$n_d = \frac{\Delta m}{\frac{4}{3}\pi \times (10^{-7} \times R_{th})^3 \times M_{w,Au}} \quad \left\{ \begin{array}{l} \Delta m \text{ the deposited mass (g)} \\ R_{th} \text{ the radius of the nanoparticle} \\ M_{w,Au} = 19.32 \text{ g}\cdot\text{cm}^{-3} \end{array} \right. \quad (\text{Equation 2.20})$$

$$\text{electrodeposition efficient (\%)} = \frac{n_d}{n_s} \times 100 = \frac{n_d}{100 \times 10^{-6} \times C_{NPs}} \times 100 \quad (\text{Equation 2.21})$$

III.4.5 Morphology

A Hitachi SU 8010 Ultra High Resolution Field Emission Scanning Electron Microscope was used to characterize the morphology of coatings. Micrographs were retrieved with a working distance of 3 mm. An accelerating voltage of 1 kV and an emission current of 10 μ A were used for secondary electron (SE) micrographs. An accelerating voltage of 5 kV and an emission current of 10 μ A were used for low-angle backscattered electron (LA-BSE) micrographs.

III.4.6 XPS chemical analysis

A monochromatic Thermo Scientific Al-K-alpha+ line spectrometer was used as X-ray excitation (1486.6 eV) with pass energy of 50 eV to obtain high resolution spectra. The samples were analyzed using a microfocused, monochromated Al K α X-ray source (400 μ m spot size). XPS spectra were fit with one or more Voigt profiles (binding energy uncertainty: ± 0.2 eV) and Scofield sensitivity factors were applied for quantification.⁶⁸ All spectra were referenced to the C1s peak (C–C, C–H) at 285.0 eV binding energy controlled by means of the photoelectron peaks of metallic Cu, Ag, and Au, respectively. Carbon (C 1s) spectra were done at the beginning and after each resolution analysis, to check absence of any sample degradation under irradiation.

III.5 Biosensor properties

III.5.1 Characterization of the biocatalytic current

The biocatalytic properties of the coatings was determined either with cyclic voltammetry or chronoamperometry (Figure 2.16). Cyclic voltammetry principle has already been described in the chapter I section II. This technique has been used to ensure that signals in chronoamperometry arise from the enzymatic reaction and not the simple non enzymatic substrate oxidation. Also it has enhanced to study the kinetic rates of electron transfer via scan rate changes. All measurements were carried out in PBS (pH 7.4, 137 mM NaCl, 2.7 mM KCl, 10 mM phosphate buffer) to mimick the physiological solution. Cyclic Voltammetry measurements were performed by injecting 600 μ L of solutions of glucose solution at different concentrations in the absence (IMET biosensor) and in the presence of FcOH (MET biosensor). For MET biosensor, the ferrocene concentration was 0.5 mM for glucose solution and 0.1 mM

for H_2O_2 solutions. The ferrocene concentration has been optimized depending on the analyte range (Table 1.3 in chapter I). The reason why FcOH concentration has an impact on the biosensor linear range is briefly discussed in chapter 4.

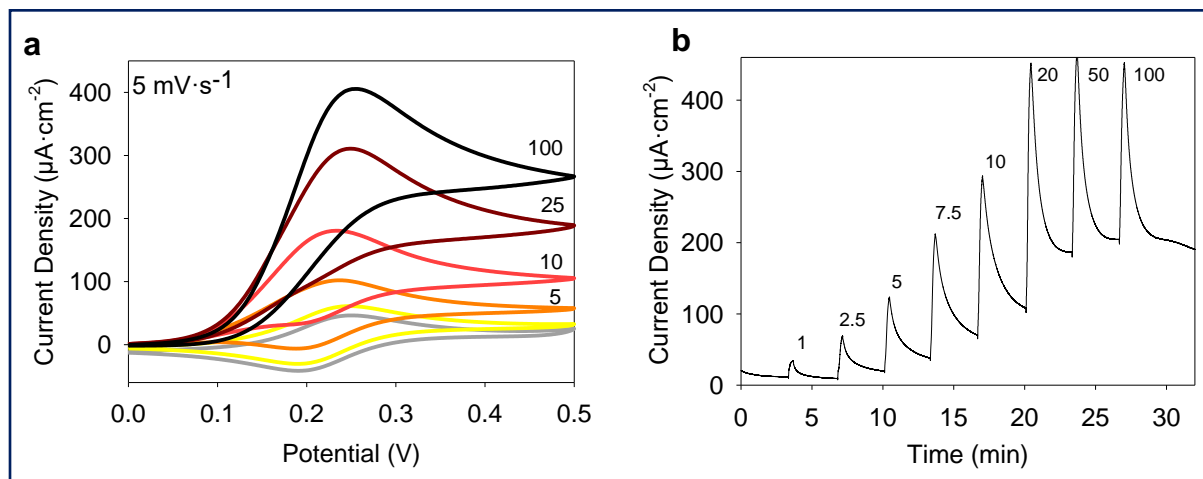


Figure 2.16: Illustration of the biocatalytic characterization of GOx/NPs coatings with (a) cyclic voltammetry and (b) chronoamperometry at 0.25V for different glucose concentration from 0 to 100 mM in presence of 0.5 mM FcOH.

III.5.2 Sensitivity, limit of detection, response time and interferences

Once the biocatalytic signal has been highlighted. The chronoamperometric curve were performed at a constant potential of 0.25 or 0.19 V vs Ag/AgCl for glucose and H_2O_2 biosensors respectively (Figure 2.16.b). These potential correspond to the redox peak potential of ferrocene methanol. A surface area of 0.8 cm^2 , corresponding to the exposed area of the gold QCM sensor, was used for current density calculations.⁶⁹

The sensitivity which is the slope within the linear range of the current density vs analyte concentration plot. It was calculated from the chronoamperometric curve using the current density value at steady state. The limit of detection (LOD) was determined from the sensitivity plot – i.e. current density ($\mu\text{A}\cdot\text{cm}^{-2}$) as a function of substrate concentration. LOD was calculated at three times the standard deviation of the intercept ($std_{intercept}$) using equation 2.18.

$$LOD \text{ (mM)} = \frac{3 \times \text{std}_{\text{intercept}}}{s} \begin{cases} \text{std}_{\text{intercept}}: \text{deviation at intercept } (\mu\text{A} \cdot \text{cm}^{-2}) \\ s: \text{the sensitivity } (\mu\text{A} \cdot \text{cm}^{-2} \cdot \text{mM}^{-1}) \end{cases} \quad (\text{Equation 2.18})$$

The upper limit of the linear range was estimated from the closest tested value that is fitting the linear range. The detection time of the biosensor was estimated from the injection point to time corresponding to 95% of the steady-state value. Last some common interferents from blood was tested such as natural redox molecules (ascorbic acid, uric acid) and some medications commonly found in the blood or the skin and having a redox behavior too. Salicylic acid (an aspirin byproduct and a product commonly used for skincare) and acetaminophen (paracetamol) was for instance tested. All of them were tested at their commonly encountered concentration in the serum according to Medscape.

III.5.3 Stability with time, tween-20 test and bending

Stability with time of the enzymatic coating was experienced via repetition of the chronoamperometric test. The sensitivity was monitored every two days to statute on the stability of the biosensor response over the time. The longest testing period was two weeks on two different glucose biosensors. The new sensitivity was divided by the initial sensitivity and multiplied by hundred to express the change in percentage sensitivity loss.

Tween-20 is a surfactant that is expected to remove any physically or electrostatically entrapped enzyme. Therefore coating were subjected to Tween-20 and the chronoamperometric test was repeated before and after addition of two successive injections of Tween-20 0.01% in PBS 10 mM and a rest time of ten minute before the washing steps. The result was expressed in percentage sensitivity loss.

The bending procedure only concern membrane biosensors. It consists in hundred times positive bending of the membrane and hundred time in the reverse way. The membrane sensitivity was retested afterwards via the chronoamperometric test. Again, the result was expressed in percentage sensitivity loss.

III.5.4 Kinetics of michaelian enzymes

Michaelian constants were determined electrochemically to retrieve the affinity of glucose toward GOx/TA@AuNPs films using the Lineweaver-Burk linearization (Figure 2.17) of Michaelis-Menten (Equation 2.17).

$$\frac{1}{i_{ss}} = \frac{K_M^{app}}{i_{max}} \times \frac{1}{[S]} + \frac{1}{i_{max}} \quad \left\{ \begin{array}{l} K_M^{app} \text{ the michaelis constant} \\ i_{ss} \text{ the steady state current} \\ [S]: \text{the corresponding glucose concentration (mM)} \\ i_{max} \text{ the current plateau for 100 mM glucose} \end{array} \right. \quad (\text{Equation 2.17})$$

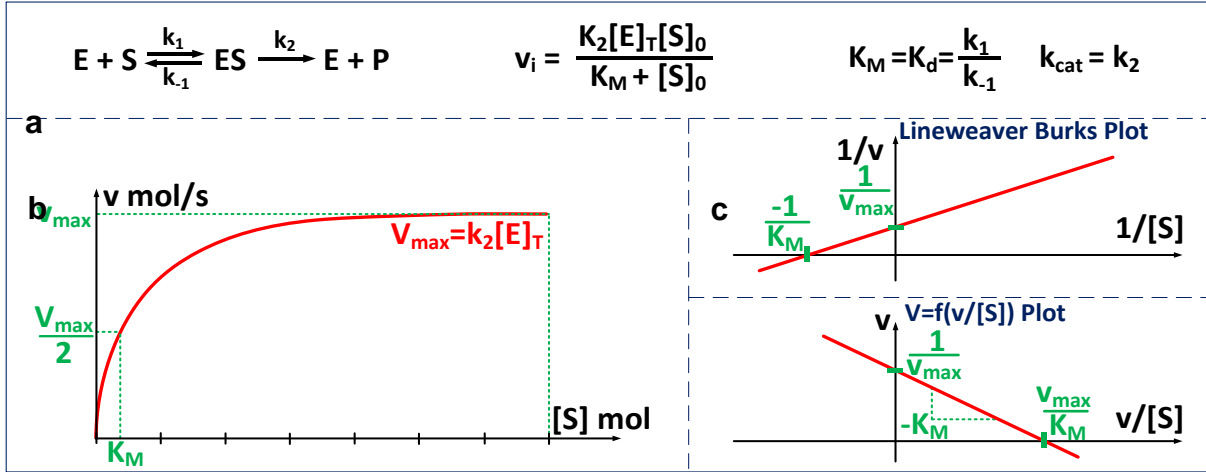


Figure 2.17: (a) Illustration of the Michaelis-Menten kinetics and (b) the corresponding typical Michaelis-Menten plot. v_i is the rate consumption of the enzymatic substrate and in the case where the enzymatic reaction is the limiting kinetics (i.e FcOH and substrate in excess), it is directly proportional to the catalytic current. (c) Two general linearization plot of the Michaelis-Menten kinetic to retrieve the $k_2 \sim k_{cat}$ and K_M parameters.

IV. References

- (1) Quideau, S.; Deffieux, D.; Douat-Casassus, C.; Pouysegu, L. Plant Polyphenols: Chemical Properties, Biological Activities, and Synthesis. *Angew. Chem., Int. Ed. Engl.* **2011**, 50 (3), 586–621.
- (2) Yan, W.; Shi, M.; Dong, C.; Liu, L.; Gao, C. Applications of Tannic Acid in Membrane Technologies: A Review. *Adv. Colloid Interface Sci.* **2020**, 284, 102267.
- (3) Ahmad, T. Reviewing the Tannic Acid Mediated Synthesis of Metal Nanoparticles. *J. Nanotechnol.* **2014**, 2014.
- (4) Carter, J. E.; Johnson, J. H.; Baaske, D. M. Dopamine Hydrochloride. *Anal. Profiles Drug Subst. Excipients* **1982**, 11 (C), 257–272.
- (5) Srinivas, K.; King, J. W.; Howard, L. R.; Monrad, J. K. Solubility of Gallic Acid, Catechin, and Protocatechuic Acid in Subcritical Water from (298.75 to 415.85) K. *J. Chem. Eng. Data* **2010**, 55 (9), 3101–3108.
- (6) Wilson, J. A. The Natural Organic Tannins (Nierenstein, M.). *J. Chem. Educ.* **1934**, 11 (12), 670.
- (7) Chatterjee, A.; Cole, A. R. H.; Grassmann, W.; Nozoe, T.; Pakrashi, S. C.; Price, R. J.; Schmidt, O. T.; Tamm, C.; Werner, G.; Wünsch, E. *Progress in the Chemistry of Organic Natural Products*; Zechmeister, L., Ed.; Springer Vienna, 1956; Vol. 13.
- (8) Oćwieja, M.; Adamczyk, Z.; Morga, M. Adsorption of Tannic Acid on Polyelectrolyte Monolayers Determined in Situ by Streaming Potential Measurements. *J. Colloid Interface Sci.* **2015**, 438, 249–258.
- (9) Krogsgaard, M.; Nue, V.; Birkedal, H. Mussel-Inspired Materials: Self-Healing through Coordination Chemistry. *Chem. - A Eur. J.* **2016**, 22 (3), 844–857.
- (10) Franck, T.; Mouithys-Mickalad, A.; Robert, T.; Ghitti, G.; Deby-Dupont, G.; Neven, P.; Serteyn, D. Differentiation between Stoichiometric and Anticatalytic Antioxidant Properties of Benzoic Acid Analogues: A Structure/Redox Potential Relationship Study. *Chem. Biol. Interact.* **2013**, 206 (2), 194–203.
- (11) Vedernikova, I.; Salahub, D.; Proynov, E. DFT Study of Hyperconjugation Effects on the Charge Distribution in Pyrogallol. *J. Mol. Struct. THEOCHEM* **2003**, 663 (1–3), 59–71.

-
- (12) Hagerman, A. E. Fifty Years of Polyphenol–Protein Complexes. *Recent Adv. Polyphen. Res.* **2012**, *3*, 71–97.
- (13) Czubinski, J.; Dwiecki, K. A Review of Methods Used for Investigation of Protein–Phenolic Compound Interactions. *Int. J. Food Sci. Technol.* **2017**, *52* (3), 573–585.
- (14) Hagerman, A. E. Fifty Years of Polyphenol-Protein Complexes. In *Recent Advances in Polyphenol Research*; 2012.
- (15) Wilson, T. C.; Hagerman, A. E. Quantitative Determination of Ellagic Acid. *J. Agric. Food Chem.* **1990**, *38* (8), 1678–1683.
- (16) Hagerman, A. E.; Butler, L. G. Choosing Appropriate Methods and Standards for Assaying Tannin. *J. Chem. Ecol.* **1989**, *15*, 1795–1810.
- (17) Makkar, H. P. S. Protein Precipitation Methods for Quantitation of Tannins: A Review. *J. Agric. Food Chem.* **1989**, *37* (4), 1197–1202.
- (18) Goldstein T., L. J. . S. The Inhibition of Enzymes by Tannins. *Phytochemistry* **1965**, *4*, 185–192.
- (19) Goldstein, J. L.; Swain, T. Methods for Determining the Degree of Polymerization of Flavans. *Nature* **1963**, *196*, 587–588.
- (20) Mole, S.; Waterman, P. G. Tannic Acid and Proteolytic Enzymes: Enzyme Inhibition or Substrate Deprivation? *Phytochemistry* **1986**, *26*, 99–102.
- (21) Mullins, J. T.; Lee, J. H. Interactions of Tannins with Enzymes: A Potential Role in the Reduced Rate of Ethanol Fermentation from High-Tannin Biomass. *Biomass and Bioenergy* **1991**, *1* (6), 355–361.
- (22) Yao, H. T.; Chang, Y. W.; Lan, S. J.; Yeh, T. K. The Inhibitory Effect of Tannic Acid on Cytochrome P450 Enzymes and NADPH-CYP Reductase in Rat and Human Liver Microsomes. *Food Chem. Toxicol.* **2008**, *46* (2), 645–653.
- (23) Hall, C. B. Inhibition of Tomato Pectinesterase by Tannic Acid. *Nat.* 1966 2125063 **1966**, *212* (5063), 717–718.
- (24) Description of G7141 product from Sigma Aldrich <https://www.sigmaaldrich.com/FR/fr/product/sigma/g7141> (accessed 2022 -01 -31).
- (25) Courjean, O.; Gao, F.; Mano, N. Deglycosylation of Glucose Oxidase for Direct and Efficient Glucose Electrooxidation on a Glassy Carbon Electrode. *Angew. Chemie* **2009**, *121* (32), 6011–6013.

- (26) Wang, Y.; Jonkute, R.; Lindmark, H.; Keighron, J. D.; Cans, A.-S. Molecular Crowding and a Minimal Footprint at a Gold Nanoparticle Support Stabilize Glucose Oxidase and Boost Its Activity. *Langmuir* **2019**, *36*, 37–46.
- (27) Kano, K. Redox Potentials of Proteins and Other Compounds of Bioelectrochemical Interest in Aqueous Solutions. *Rev. Polarogr.* **2002**, *48*, 29–46.
- (28) Fasman, G. D. *Handbook of Biochemistry and Molecular Biology*; Francis, T. &, Ed.; Abingdon-on-Thames (United Kingdom), 2019.
- (29) Courjean, O.; Flexer, V.; PrévotEAU, A.; Suraniti, E.; Mano, N. Effect of Degree of Glycosylation on Charge of Glucose Oxidase and Redox Hydrogel Catalytic Efficiency. *ChemPhysChem* **2010**, *11*, 2795–2797.
- (30) Swoboda, B. E.; Massey, V. Purification and Properties of the Glucose Oxidase from *Aspergillus*. *J. Biol. Chem.* **1965**, *240*, 2009–2215.
- (31) Description of enzymes from Toyobo Supplier
https://www.toyoboglobal.com/seihin/xr/enzyme/enzyme_list/ (accessed 2022 -02 -07).
- (32) Wilson, R.; Turner, A. P. F. Glucose Oxidase: An Ideal Enzyme. *Biosens. Bioelectron.* **1992**, *7* (3), 165–185.
- (33) Wohlfahrt, G.; Trivić, S.; Zeremski, J.; Peričin, D.; Leskovac, V. The Chemical Mechanism of Action of Glucose Oxidase from *Aspergillus Niger*. *Mol. Cell. Biochem.* **2004**, *260* (1–2), 69–83.
- (34) Veitch, N. C. Horseradish Peroxidase: A Modern View of a Classic Enzyme. *Phytochemistry* **2004**, *65* (3), 249–259.
- (35) Howes, B. D.; Feis, A.; Raimondi, L.; Indiani, C.; Smulevich, G. The Critical Role of the Proximal Calcium Ion in the Structural Properties of Horseradish Peroxidase. *J. Biol. Chem.* **2001**, *276* (44), 40704–40711.
- (36) Krainer, F. W.; Glieder, A. An Updated View on Horseradish Peroxidases: Recombinant Production and Biotechnological Applications. *Appl. Microbiol. Biotechnol.* **2015**, *99* (4), 1611.
- (37) Horseradish Peroxidase Interchim Datasheet <https://www.interchim.fr/ft/1/146500.pdf> (accessed 2021 -10 -08).
- (38) Description of P6782 product from Sigma Aldrich
<https://www.sigmaaldrich.com/FR/fr/product/sigma/p6782> (accessed 2022 -01 -31).

- (39) Cans, A. S.; Dean, S. L.; Reyes, F. E.; Keating, C. D. Synthesis and Characterization of Enzyme-Au Bioconjugates: HRP and Fluorescein-Labeled HRP. *NanoBiotechnology* 2007 31 **2007**, 3 (1), 12–22.
- (40) Harbury, H. A. Oxidation—Reduction Potentials of Horseradish Peroxidase. *J. Am. Chem. Soc.* **2002**, 75 (18), 4625.
- (41) Claiborne, A.; Fridovich, I. Chemical and Enzymatic Intermediates in the Peroxidation of O-Dianisidine by Horseradish Peroxidase. 2. Evidence for a Substrate Radical-Enzyme Complex and Its Reaction with Nucleophiles. *Biochemistry* **1979**, 18 (11), 2324–2329.
- (42) Zhang, Y.; Tsitkov, S.; Hess, H. Proximity Does Not Contribute to Activity Enhancement in the Glucose Oxidase–Horseradish Peroxidase Cascade. *Nat. Commun.* 2016 71 **2016**, 7 (1), 1–9.
- (43) Description of 31941 HRP Product from Serva
https://www.serva.de/enDE/ProductDetails/736_0_31941_Peroxidase_from_horseradish_min_1000_U_mg_lyophil_213_0.html (accessed 2022 -02 -12).
- (44) Savéant, J.; Costentin, C. *Elements of Molecular and Biomolecular Electrochemistry*, 2nd ed.; Wiley & Sons, Ed.; Hoboken (New Jersey), 2019.
- (45) Song, Y.; Xie, J.; Song, Y.; Shu, H.; Zhao, G.; Lv, X.; Xie, W. Calculation of Standard Electrode Potential of Half Reaction for Benzoquinone and Hydroquinone. *Spectrochim. Acta Part A Mol. Biomol. Spectrosc.* **2006**, 65 (2), 333–339.
- (46) O'Reilly, J. E. Oxidation-Reduction Potential of the Ferro-Ferricyanide System in Buffer Solutions. *Biochim. Biophys. Acta - Bioenerg.* **1973**, 292 (3), 509–515.
- (47) Bard, A. J.; Faulkner, L. R. *Electrochemical Methods: Fundamentals and Applications*, 2nd ed.; Wiley & Sons, Ed.; Hoboken (New Jersey), 2001.
- (48) Sivaraman, S. K.; Kumar, S.; Santhanam, V. Room-Temperature Synthesis of Gold Nanoparticles - Size-Control by Slow Addition. *Gold Bull.* **2010**, 43 (4), 275–286.
- (49) Ciganda, R.; Irigoyen, J.; Gregurec, D.; Hernández, R.; Moya, S.; Wang, C.; Ruiz, J.; Astruc, D. Liquid-Liquid Interfacial Electron Transfer from Ferrocene to Gold(III): An Ultrasimple and Ultrafast Gold Nanoparticle Synthesis in Water under Ambient Conditions. *Inorg. Chem.* **2016**, 55 (13), 6361–6363.
- (50) Dodero, A.; Castellano, M.; Vicini, S.; Hébraud, A.; Lobry, E.; Nhut, J.-M.; Schlatter, G. Eco-Friendly Needleless Electrospinning and Tannic Acid Functionalization of Polyurethane Nanofibers with Tunable Wettability and Mechanical Performances.

- Macromol. Mater. Eng.* **2022**, 2100823.
- (51) Ba, H.; Truong-Phuoc, L.; Romero, T.; Sutter, C.; Nhut, J. M.; Schlatter, G.; Giambastiani, G.; Pham-Huu, C. Lightweight, Few-Layer Graphene Composites with Improved Electro-Thermal Properties as Efficient Heating Devices for de-Icing Applications. *Carbon N. Y.* **2021**, 182, 655–668.
 - (52) *Q-Sense E1 Operator Manual Including the Acquisition Software QSoft 401*; Sweden, 2009.
 - (53) Sauerbrey, G. Verwendung von Schwingquarzen Zur Wägung Dünner Schichten Und Zur Mikrowägung. *Zeitschrift für Phys.* 1959 1552 **1959**, 155 (2), 206–222.
 - (54) Voinova, M. V; Rodahl, M.; Jonson, M.; Kasemo, B. Viscoelastic Acoustic Response of Layered Polymer Films at Fluid-Solid Interfaces: Continuum Mechanics Approach. *Phys. Scr.* **1999**, 59 (5), 391–396.
 - (55) Inamdar, S. N.; Bhat, M. A.; Haram, S. K. Construction of Ag/AgCl Reference Electrode from Used Felt-Tipped Pen Barrel for Undergraduate Laboratory. *J. Chem. Educ.* **2009**, 86 (3), 355–356.
 - (56) Calculation Nucleic Acid or Protein Concentration. *Promega Tech. Note* **2009**.
 - (57) Leonard, D. N.; Chandler, G. W.; Seraphin, S. Scanning Electron Microscopy. *Charact. Mater.* **2012**, 1–16.
 - (58) Franken, L. E.; Grünewald, K.; Boekema, E. J.; Stuart, M. C. A.; Franken, L. E.; Grünewald, K.; Boekema, E. J.; Stuart, M. C. A. A Technical Introduction to Transmission Electron Microscopy for Soft-Matter: Imaging, Possibilities, Choices, and Technical Developments. *Small* **2020**, 16 (14), 1906198.
 - (59) Hagerman, A. E. Modified Prussian Blue Assay for Total Phenols. *J. Agric. Food Chem.* **2002**, 805 (1992), 2002.
 - (60) Mathew, S.; Abraham, T. E.; Zakaria, Z. A. Reactivity of Phenolic Compounds towards Free Radicals under in Vitro Conditions. *J. Food Sci. Technol.* 2015 529 **2015**, 52 (9), 5790–5798.
 - (61) Kawabata, J.; Okamoto, Y.; Kodama, A.; Makimoto, T.; Kasai, T. Oxidative Dimers Produced from Protocatechuic and Gallic Esters in the DPPH Radical Scavenging Reaction. *J. Agric. Food Chem.* **2002**, 50 (19), 5468–5471.
 - (62) Liu, X.; Atwater, M.; Wang, J.; Huo, Q. Extinction Coefficient of Gold Nanoparticles with Different Sizes and Different Capping Ligands. *Colloids Surfaces B Biointerfaces* **2007**, 53, 3–7.

- (63) Bradford, M. M. A Rapid and Sensitive Method for the Quantitation of Microgram Quantities of Protein Utilizing the Principle of Protein-Dye Binding. *Anal. Biochem.* **1976**.
- (64) Mach, H.; Middaugh, C. R.; Lewis, R. V. Statistical Determination of the Average Values of the Extinction Coefficients of Tryptophan and Tyrosine in Native Proteins. *Anal. Biochem.* **1992**, 200 (1), 74–80.
- (65) Gill, S. C.; von Hippel, P. H. Calculation of Protein Extinction Coefficients from Amino Acid Sequence Data. *Anal. Biochem.* **1989**.
- (66) El-Maiss, J.; Cuccarese, M.; Lupattelli, P.; Chiumminto, L.; Funicello, M.; Schaaf, P.; Boulmedais, F. Mussel-Inspired Electro-Cross-Linking of Enzymes for the Development of Biosensors. *ACS Appl. Mater. Inter.* **2018**, 10 (22), 18574–18584.
- (67) Scientific, B. Specification Data from QSense QSX 301 and QEM401
<https://www.biolinscientific.com/qsense/>.
- (68) Scofield, J. H. Hartree-Slater Subshell Photoionization Cross-Sections at 1254 and 1487 EV. *J. Electron Spectros. Relat. Phenomena* **1976**, 8, 129–137.
- (69) Singh, K.; McArdle, T.; Sullivan, P. R.; Blanford, C. F. Sources of Activity Loss in the Fuel Cell Enzyme Bilirubin Oxidase. *Energy Environ. Sci.* **2013**, 6, 2460.
- (70) Patil, N.; Jérôme, C.; Detrembleur, C. Recent Advances in the Synthesis of Catechol-Derived (Bio)Polymers for Applications in Energy Storage and Environment. *Prog. Polym. Sci.* **2018**, 82, 34–91.
- (71) Azevedo, A. M.; Martins, V. C.; Prazeres, D. M. F.; Vojinović, V.; Cabral, J. M. S.; Fonseca, L. P. Horseradish Peroxidase: A Valuable Tool in Biotechnology. *Biotechnol. Annu. Rev.* **2003**, 9, 199–247.
- (72) Gupta, V.; Ganegoda, H.; Engelhard, M. H.; Terry, J.; Linford, M. R. Assigning Oxidation States to Organic Compounds via Predictions from X-Ray Photoelectron Spectroscopy: A Discussion of Approaches and Recommended Improvements. *J. Chem. Educ.* **2014**, 91 (2), 232–238.
- (73) Abbott, T. Selecting the right SEM for imaging your samples
<http://www.nuance.northwestern.edu/docs/tech-talks/techtalk-tirzah-presentation.pdf>.
- (74) *Ultra-High Resolution Scanning Electron Microscope - SU8000 Series*; Tokyo (Japan), 2022.

Chapter 3

Mussel-Inspired Electro-crosslinking of Tannic Acid Capped Gold Nanoparticles and Enzymes for Biosensing Applications

Chapter 3 – Table of Contents

Abstract	131
I. Introduction	131
II. TA@AuNPs synthesis and characterisation	134
III. GOx/TA@AuNPs complexes characterization	135
IV. Electrodeposition of GOx/TA@AuNPs coatings.	137
V. XPS analysis of GOx/TA@AuNPs coatings	140
VI. GOx/TA@AuNPs coating biosensing properties.....	144
VII. Versatility of the process.....	150
Conclusion.....	152
References	152

Abstract

Complementary tools to classical analytical methods, enzymatic biosensors are widely applied in medical diagnosis due to their high sensitivity, potential selectivity, and their possibility of miniaturization/automation. Among the different protocols of enzyme immobilization, the covalent binding and cross-linking of enzymes ensure a great stability of the developed biosensor. Obtained manually by drop casting using a specific cross-linker, this immobilization process is not suitable for specific functionalization of a single electrode out of a microelectrode array. Recently, we reported the first electro-crosslinking of enzyme process, based on mussel inspired chemistry, allowing the localized immobilization of glucose oxidase (GOx) on microelectrodes using a synthesized homobifunctionalized catechol cross-linker (El Maiss et al. *ACS Appl. Mater. and Inter.* 2018, 10, 18754). In the present work, we have extended the electro-crosslinking of enzyme process towards the use of a cheap natural molecule and metal nanoparticles to obtain an enzymatic biosensor with a high sensitivity and stability. After the synthesis of tannic acid capped gold nanoparticles (TA@AuNPs), GOx/TA@AuNPs coating was deposited by electro-crosslinked thanks to catechol chemistry through the application of an anodic potential to obtain a highly sensitive biosensor towards glucose. This electro-crosslinking process based on the use of TA@AuNPs (i) does not require the synthesis of a specific cross-linker (ii) is temporally and spatially controlled, (iii) keep a very stable sensitivity over two weeks at room temperature and (iv) is versatile, likely to work with any kind of redox enzymes.

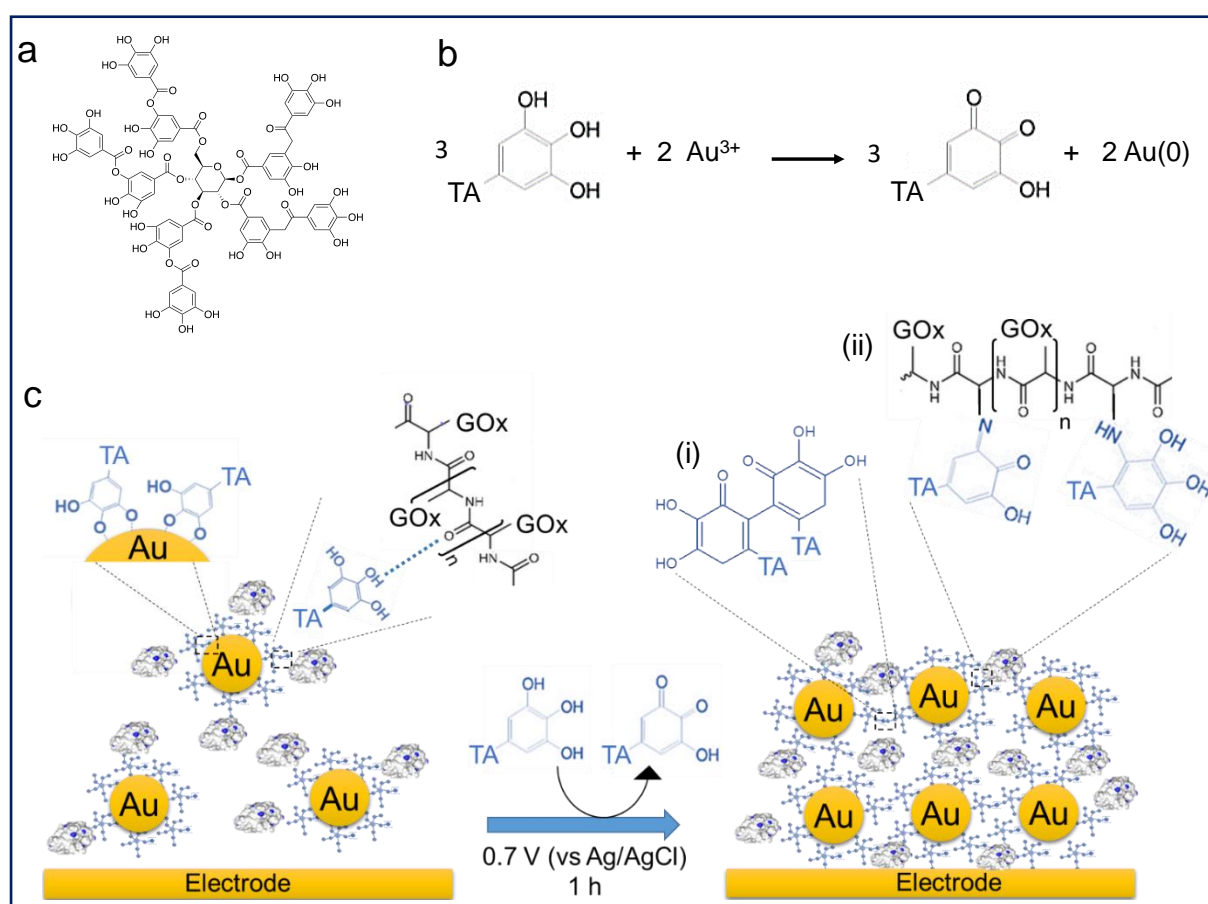
I. Introduction

In the fields of environmental monitoring, food industry or clinical analyses, the development of selective tools with rapid analysis time for biomolecule detection is more and more required. The interest in biosensors has grown exponentially in recent decades.¹ According to the definition of IUPAC, a biosensor is composed of (i) an immobilized biological element (protein, DNA) able to recognize and detect a specific analyte (organic (bio)molecule or ions) and (ii) a transducer that convert the (bio)chemical recognition into electrical, thermal or optical signals. They are complementary tools to classical analytical methods (e.g. high performance liquid chromatography) due to their inherent simplicity, rapid response and possibility of miniaturization. In particular, electrochemical enzymatic biosensor has shown great promise as a miniaturized real-time controller for human health (diabetes) and environment monitoring

(organopesticides pollution)^{2,3} with new opportunities discovered year after year.^{4,5} Enzyme immobilization on the working electrode is a key factor to develop mechanically robust biosensors which retain their selectivity, sensitivity and reproducibility over the time. Most of the protocols are almost restricted to dropcasting or electrodeposition routes based on adsorption, covalence, entrapment, cross-linking or affinity strategies. Each immobilization method presents advantages and drawbacks.⁶ Even if their activity is often decreased in comparison to its native form, covalent binding and cross-linking of enzymes ensure a great stability of the biosensor. Obtained manually by drop casting, these immobilization processes are not suitable for specific functionalization of a single electrode out of a microelectrode array.⁶ The electrodeposition of macromolecules is a simple and attractive bottom-up approach to finely control the immobilization of enzymes on electrode surfaces using an electrical stimulus. However, the enzymes are usually entrapped within a polymeric matrix or adsorbed on the electrode. Recently, we reported the first electro-crosslinking of enzymes process allowing the localized immobilization of glucose oxidase (GOx) on microelectrodes.⁷ In this mussel-inspired process, a synthesized homobifunctionalized catechol cross-linker was electro-oxidized to react with amine moieties of GOx by using ferrocene methanol (FcOH) as mediator. The cross-linked enzymatic film (i) was obtained in a one pot process using a native enzyme, (ii) was strongly linked to the metallic electrode surface thanks to catechol moieties and (iii) presented no leakage issues. The sensitivity of the biosensor was similar to the ones obtained by manual dropcasting of GOx and glutaraldehyde crosslinker. Nanomaterials, such as metal nanoparticles, have been widely used to improve the detection limits and sensitivity of enzymatic biosensors. Their large surface-to-volume ratio and good electron transfer ability allows to amplify the electrochemical signal and to improve the accuracy and lifetime of the glucose biosensors.⁸

In this work, we have extended the electro-crosslinking of enzyme process towards the use of natural and abundant molecule, *i.e.* tannic acid (TA), and metallic nanoparticles to obtain an enzymatic biosensor with high sensitivity. For this purpose, TA capped gold nanoparticles (TA@AuNPs) and GOx were electro-crosslinked by the application of an anodic potential (Scheme 3.1). TA is a polyphenol composed of five gallol moieties which have the same chemical properties as catechol. To avoid any use of synthesized crosslinker in the process, TA was used as both reducing of Au³⁺ ions and capping agent to synthesize TA@AuNPs. The presence of gallol moieties on the surface of TA@AuNPs allowed the adsorption of GOx around the NPs, through hydrogen bonds and hydrophobic interactions. When an anodic

potential is applied, gallol moieties are oxidized into quinones able to react covalently with amine moieties of GOx and gallol moieties of TA@AuNPs. An efficient immobilization of GOx/TA@AuNPs is obtained which allows the electrochemical detection of glucose using FcOH as free mediator in solution with a high sensitivity and selectivity. Finally, the film buildup, occurring exclusively from the surface, can be prepared on microelectrodes. This polyphenol based electro-crosslinking process (i) does not require the synthesis of a specific cross-linker (ii) is temporally and spatially controlled, (iii) keep a very stable sensitivity over two weeks at room temperature and (iv) is versatile, likely to work with any kind of redox enzymes.



Scheme 3.1: (a) Chemical formulae of tannic acid (TA), (b) mechanism of TA@AuNPs synthesis by reduction of Au^{3+} ions by TA in water. (c) Schematic representation of the electro-crosslinking of GOx/TA@AuNPs through electro-oxidation of gallol moieties of TA@AuNPs into quinone followed by the chemical reaction of quinone moieties with (i) gallol moieties of TA@AuNPs and (ii) free amino moieties of GOx through Michael addition and a Schiff's base condensation reaction.

II. TA@AuNPs synthesis and characterisation

Sivaraman et al⁹ protocol synthesis was adapted to produce TA@AuNPs by a simple and rapid process at room temperature. Thanks to its gallol moieties, TA was used as both reducing of Au³⁺ ions and stabilizing agent of Au metal (Scheme 3.1.a-b). TA@AuNPs synthesis was performed at pH 7 by slow addition of 2 mM HAuCl₄ solution into 0.3 mM TA solution. After 10 min of reaction, the suspension was centrifuged and redispersed in water. Negatively stained TEM images revealed regular and uniformly distributed metal species with a size of 12 ± 2 nm in diameter (Figure 3.1.a-b). The hydrodynamic diameter of the TA@AuNPs, measured by DLS in intensity, was of 24 ± 3 nm. The hydrodynamic radius is directly related to the diffusive motion of the particles and is usually higher than the inorganic core of the NPs.¹⁵ The concentration of the suspension was of $1.0 \pm 0.1 \cdot 10^{16}$ NPs·L⁻¹, i.e. 16 ± 2 nM, determined by UV-Visible spectroscopy ($\lambda_{\text{max}} = 526$ nm) and confirmed by the Turkevich and gravimetric methods. The size of the TA@AuNPs remained stable over a period of two storage months under argon, highlighting the high stability of the suspension (Figure 3.1.c-d).

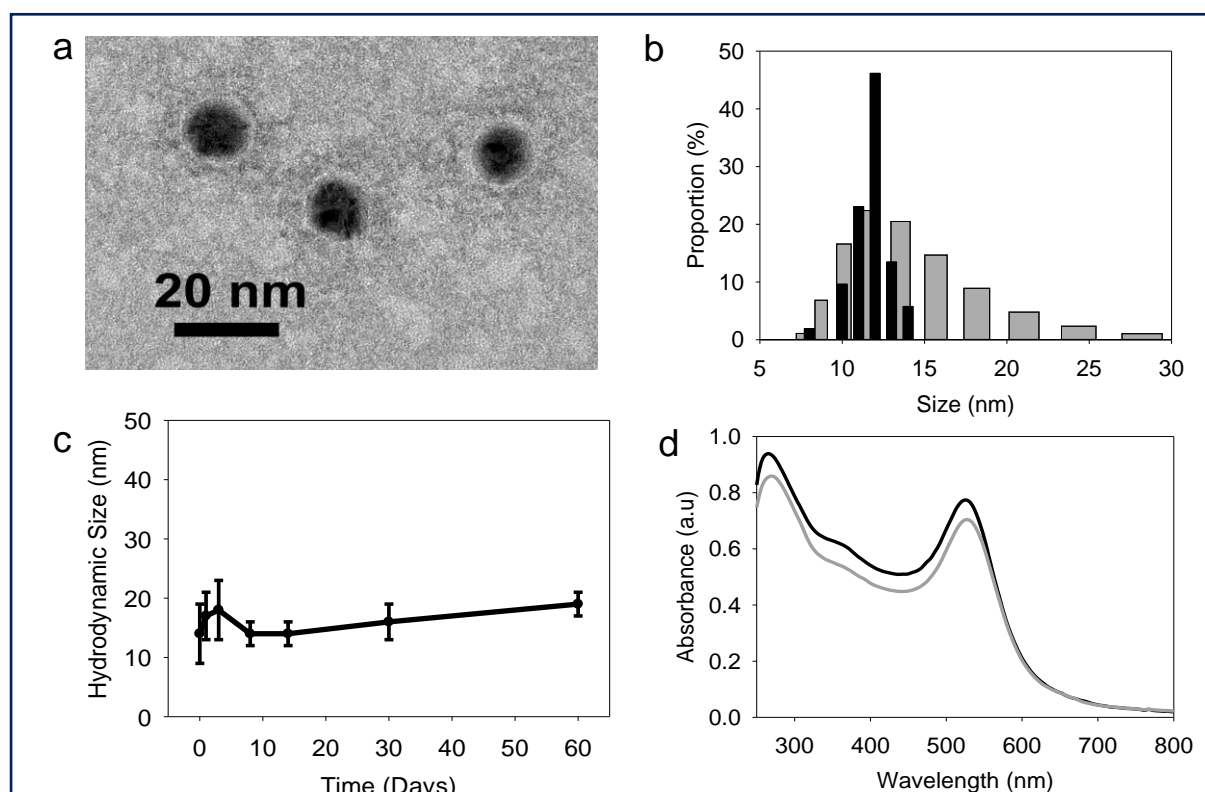


Figure 3.1. Characterization of TA@AuNPs: (a) TEM image, (b) size distribution of TA@AuNPs determined from TEM images (black) and DLS by number (grey). (c) DLS size over a period of two months of storage at 4°C under argon and (d) washed TA@AuNPs absorbance after one day (black) and after two month of storage (grey).

The reactivity of TA at the surface of the TA@AuNPs is a critical parameter for the mussel-inspired electro-crosslinking process. Indeed, this process is based on the reaction of electro-oxidized gallol moieties of TA with the amine moieties of the enzymes (Scheme 3.1.c).¹⁶ Thus, the content in gallol moieties, equivalent to gallic acid, was determined using a redox test based on the reduction of $\text{Fe}^{\text{III}}(\text{CN})_6^{3-}$ into $\text{Fe}^{\text{II}}(\text{CN})_6^{4-}$ and the further formation of Prussian Blue ($\text{Fe}^{\text{III}}_4[\text{Fe}^{\text{II}}(\text{CN})_6]_3$) in the presence of Fe^{3+} ions. Each TA@AuNPs presented $4.5 \pm 0.7 \cdot 10^3$ gallol moieties at their surface, corresponding to 10 moieties per nm^2 . With TA molecules equivalent to 4.73 gallol moieties, the NPs surface has approximatively 2 TA molecules per nm^2 . Knowing that TA has a hydrodynamic radius around 1.0 ± 0.3 nm, it is likely that TA is not in its native form when on the surface of NPs.

III. GOx/TA@AuNPs complexes characterization

After synthesis, the TA@AuNPs suspension was mixed with a GOx solution at 60 in GOx/NPs molar ratio and directly observed by TEM after uranyl acetate negative staining (Figure 3.2.a). The gold NPs present a light grey corona (red arrows) of ~8 nm due to the attachment of the protein to the NPs. In the background, some free enzyme molecules are visibles (black arrows) with a size of around 6 ± 2 nm (size of GOx deglycosylated dimer: $6.0 \times 5.2 \times 7.7$ nm³).¹⁷ The hydrodynamic size of GOx/TA@AuNPs, obtained by DLS in intensity, was measured at 35 ± 6 nm in agreement with the formation of a monolayer (Figure 3.2.c). It is known that full coverage of NPs by proteins prevents their aggregation in the presence of salt.¹⁸ To determine the optimal GOx/NPs molar ratio for full coverage of the NPs, a flocculation assay was performed at different molar ratios. With this aim, the maximum absorption wavelength (λ_{max}) and the hydrodynamic size of GOx/TA@AuNPs suspensions were measured after the addition of 1 M NaCl by UV-Visible spectroscopy and by DLS, respectively (Figure 3.2.c-d). At GOx/NPs molar ratio of 10, the addition of salt induced the shift of the λ_{max} from 528 to 548 nm and the formation of aggregates of 270 nm in size. Up to 33.5 in GOx/NPs molar ratio, the λ_{max} reached a plateau at 528 nm and the size of the aggregates decreased to the values of isolated GOx/TA@AuNPs in water (Figure 3.2.d). The flocculation of NPs is then prevented for GOx/NPs molar ratio ≥ 33.5 , in agreement with the theoretical value of 30 in GOx/NPs molar ratio corresponding to full coverage of the surface of the NPs (see Material and Methods III.3.1).

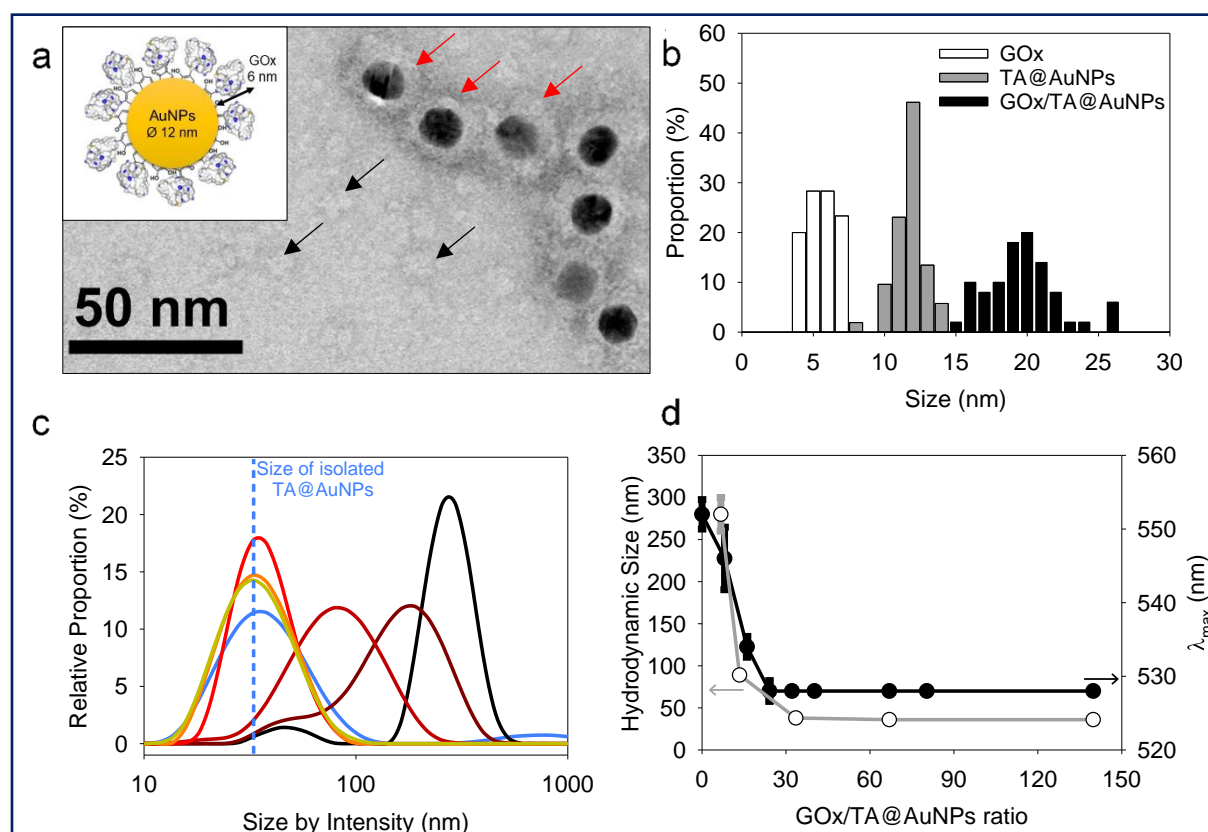


Figure 3.2. Characterization of GOx/TA@AuNPs complexes. (a) Typical TEM image, obtained after uranyl acetate staining at 2%. Red arrows show GOx/TA@AuNPs and black arrows some extra GOx in the supernatant. Inset is the illustration of GOx/TA@AuNPs complexes. (b) Size distribution of GOx, TA@AuNPs and GOx/TA@AuNPs determined from TEM images. (c) Hydrodynamic size in presence of NaCl 1M at GOx/TA@AuNPs molar ratio of 0 (black), 13.4 (dark red), 34 (red), 67 (orange), 140 (yellow) and in absence of NaCl (blue). (d) Flocculation test upon addition of 1 M NaCl in the GOx/TA@AuNPs suspension with the hydrodynamic size previously measured (white circle) and the maximum absorption wavelength of aggregates (black circle) as a function of GOx/NPs molar ratio.

TA strongly interacts with enzymes through hydrogen bonds, hydrophobic interactions, or covalent adduct formation.^{16,19} It is known that TA and more generally tannins inhibit the catalytic activity of enzymes either by modification of their conformation¹⁶ or by substrate deprivation.²⁰ Therefore, the enzymatic activity of GOx/TA@AuNPs was evaluated using a colorimetric assay and compared to GOx solution at the same enzyme concentration. Figure 3.3.a shows the percentage of inhibition of GOx at different GOx/NPs molar ratios. Above 0.5 GOx/NPs molar ratio, the GOx inhibition is less than 3% becoming completely negligible above

the value of 30, the theoretical ratio value for full coverage. Adsorbed GOx on the surface of TA@AuNPs remained fully active. After 24 h, the GOx/TA@AuNPs mixture suspension was centrifuged to determine the GOx activity of redispersed GOx/TA@AuNPs in water and the retrieved supernatant containing the enzyme in excess (Figure 3.3.b). The enzymatic activity of the rinsed GOx/TA@AuNPs increased with the quantity of GOx introduced which confirms the adsorption of active enzymes on TA@AuNPs. Beyond 33 in GOx/NPs molar ratio, the enzymatic activity of GOx/TA@AuNPs reached a plateau with an increase of the supernatant. Above this value, the amount of GOx added in the mixture is almost not adsorbed on the surface of the NPs and eliminated in the supernatant at the rinsing step. These results confirmed the adsorption of only one monolayer of active GOx on the surface of the TA@AuNPs.

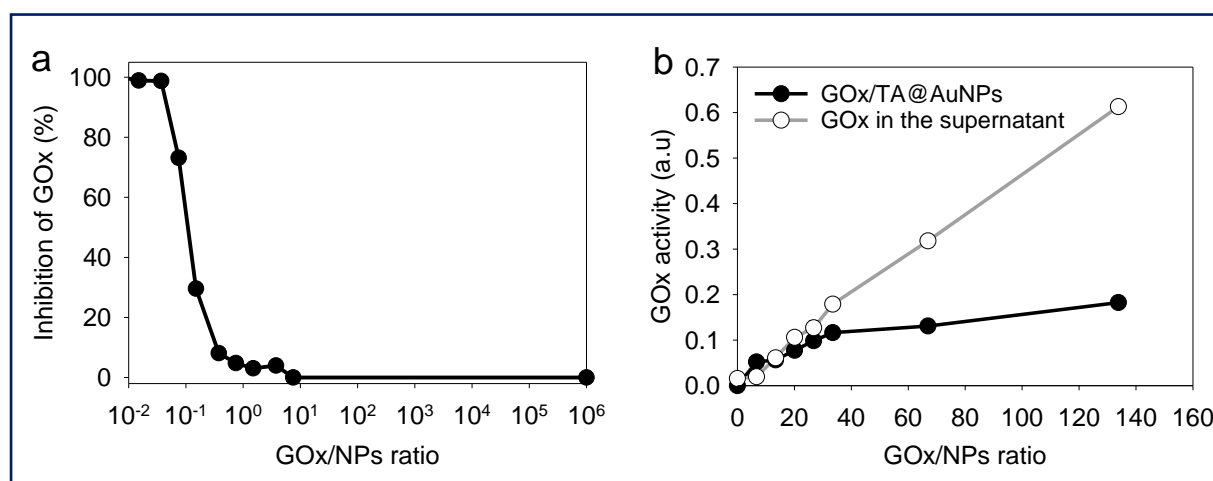


Figure 3.3: GOx/TA@AuNPs activity (a) percentage of enzymatic inhibition in the presence of TA@AuNPs as a function of GOx/NPs ratio, in comparison to the same concentration of GOx in solution (b) enzymatic activity of rinsed GOx/TA@AuNPs, i.e. after centrifugation and redispersion in water, and of the retrieved supernatant as a function of GOx/NPs ratio.

IV. Electrodeposition of GOx/TA@AuNPs coatings.

To electrodeposit GOx and TA@AuNPs on the surface of the working electrode, the electrodeposited solution FcOH/GOx/TA@AuNPs mixture was prepared in 5 mM FcOH/50 mM NaCl aqueous solution at GOx/NPs molar ratio of 30, close to the theoretical value of full coverage of NPs by GOx. The salt acts as a supporting electrolyte and FcOH as an electron mediator to oxidize the gallol moieties of TA within a diffusion layer in the vicinity of the

electrode. EC-QCM was used to monitor *in situ* during the applied voltage the evolution of the normalized frequency shifts. For clarity purposes, the evolution of the opposite value of the normalized frequency shift at 15 MHz is depicted which is proportional in a first approximation to the adsorbed mass (Figure 3.4.a). Thus, an increase of the signal is directly related to an increase in mass. After injection of the FcOH/GOx/TA@AuNPs mixture, an increase of the frequency shift of 60 Hz was observed which might originate from the physisorption of GOx/TA@AuNPs.

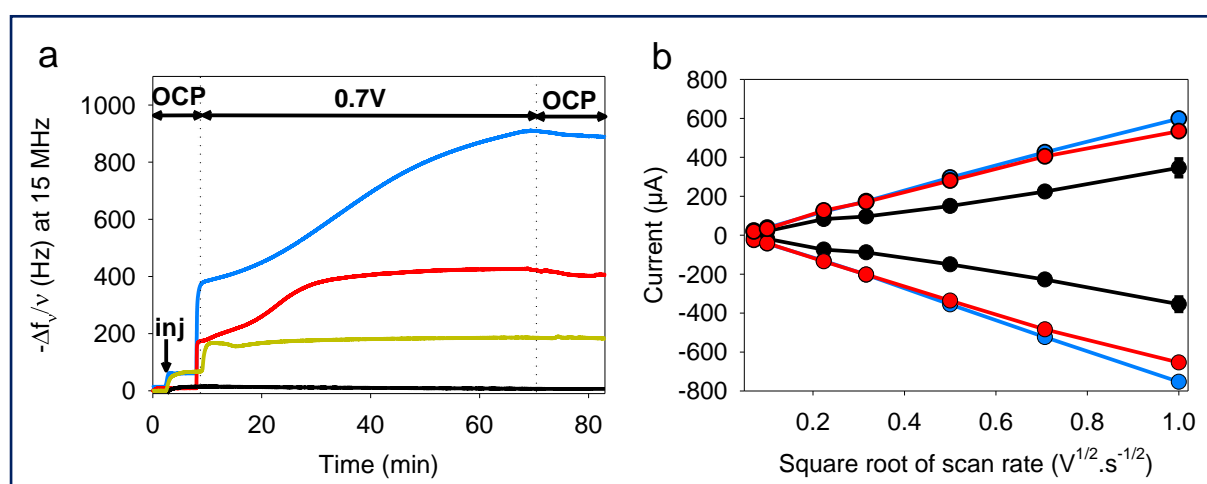


Figure 3.4: (a) Evolution of the normalized frequency shift, measured by EC-QCM-D, of FcOH/GOx/TA@AuNPs (blue curve), FcOH/TA@AuNPs (red curve), FcOH/GOx/TA (yellow curve), and GOx/TA@AuNPs (grey curve) mixture solution as a function of time during the application of 0.7 V. OCP means open circuit potential where no electrical stimulus is applied. The arrow Inj indicates the time of injection of the electrodeposited solution. (b) Redox peak intensities of FcOH (0.5 mM) as a function of the square root of scan rate measured in NaCl 50 mM in contact before electrodeposition (black curve) and after electrodeposition of GOx/TA@AuNPs (blue curve) and TA@AuNPs (red curve) coatings, obtained from FcOH/GOx/TA@AuNPs

After stabilization of the signal, the application of 0.7 V induced an instantaneous increase of the frequency shift towards 380 Hz followed by a slower phase reaching 910 Hz after 1 h (Figure 3.4.a). The following rinsing step decreased slightly the signal by 3%. When a GOx/TA@AuNPs mixture was used without the presence of FcOH, the EC-QCM signal remained stable when the electric potential was applied. The presence of the mediator is necessary to induce the buildup. In the case of the FcOH/TA@AuNPs mixture without GOx,

the frequency shift increased reaching a value at 400 Hz after 1 h. The electrodeposition could be explained by the cross-linking reaction between TA molecules adsorbed on AuNPs as reported elsewhere.²¹ In the case of the TA/GOx sample, a fast increase of the frequency shift to 180 Hz was reached – seven times lower than TA@AuNPs/GOx coatings. On the contrary to the polymer-complexing ferricyanides process²², the covalent cross-linking process is favored for more branched NPs than TA molecules. The electroactive surface area is a critical parameter for an electrochemical biosensor as it has an impact on the electrochemical reaction rate and thus its sensitivity. This parameter was measured for the obtained GOx/TA@AuNPs and TA@AuNPs coatings by applying cyclic voltammograms at different scan rates in the presence of 0.5 mM FcOH in NaCl 50 mM. Figure 3.4.b illustrates the peak reduction and oxidation currents of FcOH versus the square root of the scan rate. This linear relation is described by Randles-Ševčík (see Materials and Methods section III.4.1). The obtained linear behavior highlights that the faradaic process with FcOH is diffusion-controlled. An increase of the slope at the oxidation and reduction peaks of 150% and 180%, respectively, was observed for GOx/TA@AuNPs coatings as compared to the bare surface of the gold-coated QCM crystal (Figure 3.4.b). This change is likely to be explained by the increase of electroactive surface area highlighting the importance of NPs to virtually extend the electrode surface in three-dimension even when coated by enzymes and TA. In comparison, a similar result was observed for the TA@AuNPs coating with a 160% and 190% increase of the slope at the oxidation and reduction peaks, respectively. At the lower scan rate (lower square root scan rate), the measured currents were the same. No differences are visible before and after the electrodeposition of the coatings. Meanwhile, the TA/GOx coating has a similar electroactive surface to clean crystal for all over the tested scan rate range (data not shown).

After electrodeposition, the surface of the gold-coated QCM crystal became red due to the presence of TA@AuNPs (Figure 3.5.a inset). SEM observations of GOx/TA@AuNPs coatings clearly showed densely packed nanoparticles on the surface of the QCM crystal (Figure 3.5.a). The phenomenon of strong backscattering of electrons (BSE) on heavy elements was used to follow the distribution of AuNPs over the surface area of GOx/TA@AuNPs coatings. Heavier elements appear brighter due to the higher intensity of the secondary electrons backscattered from the surface. Isolated NPs significantly brighter than the rest of the surface were observed in BSE mode, which indicates the relatively high Au content with no aggregation phenomenon during the electrodeposition (Figure 3.5.b). Several TA@AuNPs layers were visible when the voltage was increased and the thickness was estimated to be around hundred nanometers thanks

to a crack caused by fast drying (data not shown here). Similar SEM images were obtained for TA@AuNPs coatings (Figure 3.5.c)

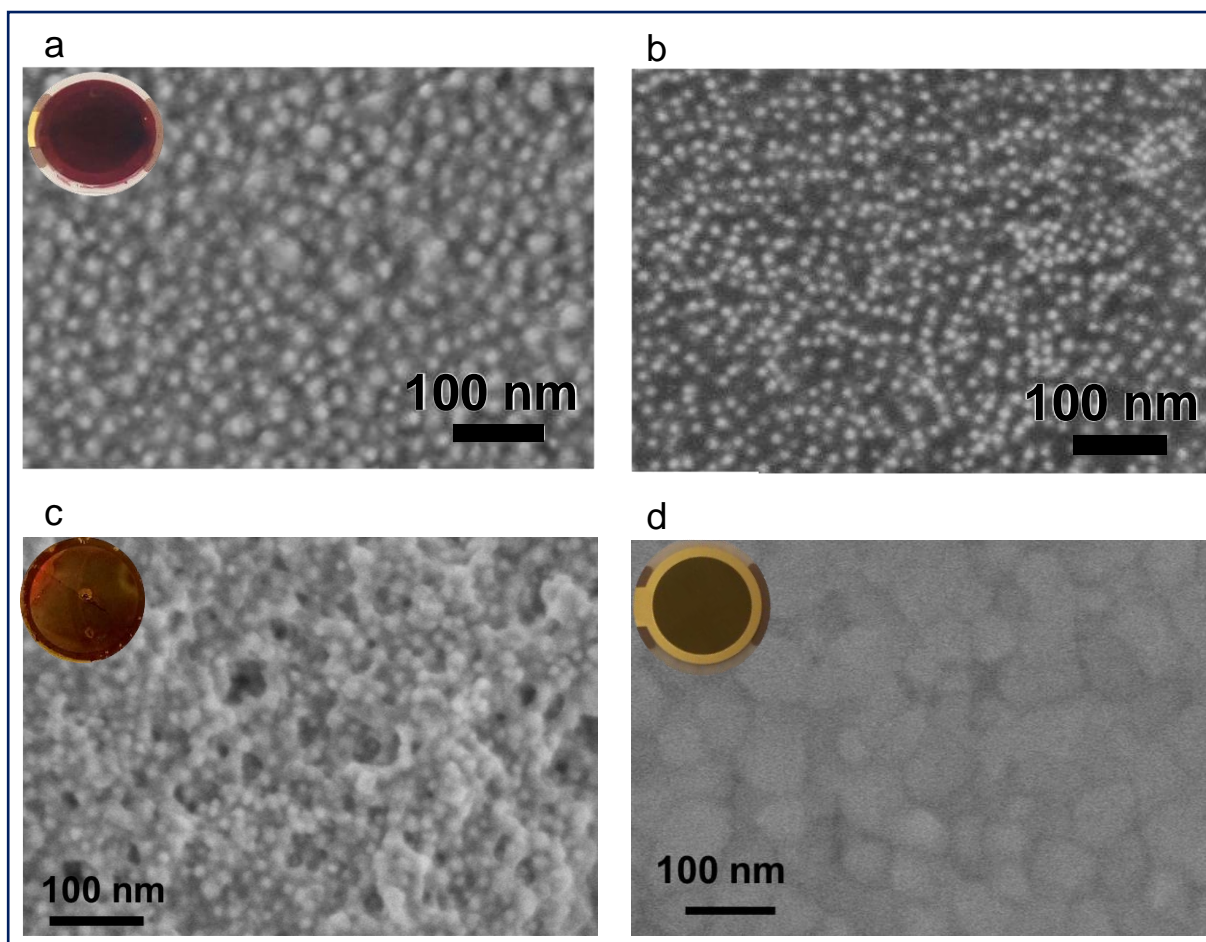


Figure 3.5: SEM micrographs of the electrodeposited GOx/TA@AuNPs coating, with (a) secondary electron and (b) backscattered electron detector. GOx/TA@AuNPs coating was obtained from the electrodeposition of FcOH/GOx/TA@AuNPs mixture. (c) SEM micrograph of electrodeposited TA@AuNPs coating obtained from FcOH/TA@AuNPs mixture and (d) of clean AuQCM crystal for comparison. Both are obtained with secondary electron detector. Inset are pictures of (a) GOx/TA@AuNPs coating (c) TA@AuNPs coating and (d) clean AuQCM for comparison.

V. XPS analysis of GOx/TA@AuNPs coatings

XPS analysis provides chemical information about the atomic and the chemical group composition of the surface coating. The TA@AuNPs coating was first compared to drop-casted

TA@AuNPs solution. Both survey XPS spectra revealed the presence of seven main elements including gold (Au 4f), carbon (C 1s), and oxygen (O 1s) (Figure 3.6.a). The presence of Au 4f peak could be due to the presence of AuNPs and/or the signal of the gold-coated QCM crystal used as a working electrode and as a substrate for the drop-casted solution. The spectrum of drop-casted TA@AuNPs suspension presented K 2s, Cl 2p, and Na 2p peaks coming from the synthesis medium. The presence of trace iron signal on the spectrum of the TA@AuNPs coating is due to the use of FcOH as a mediator during the electrodeposition process. The C 1s spectrum of both samples comprises one component located around 285 eV (yellow peak) characteristic of hydrocarbon environment (C-C/C-H) and two peaks centered at 286.5 (orange peak) and 289 eV (brown peak) corresponding to mono (C-OH) and bi oxygenated (O=C-O) carbon environments, respectively (Figure 3.6.b). The peak at around 291 eV (grey peak) is attributed to π - π^* shake-up, corresponding to the excitation of the π - π^* transition by the outgoing photoelectron from unsaturated carbon of C=C double bond.²³ The peaks at 293 and 296 eV present on the drop-casted TA@AuNPs suspension are from carbonates environment from potassium carbonates compound. With a closer look at the oxidized organic carbon signal (C_{ox}) gathering the peaks centered at 286.5, 287.5, 288.6, and 289.4 eV, we can notice that only the TA@AuNPs coating presents a peak around 287.5 eV corresponding to -C=O bond, representing 29% of the C_{ox} signal (Figure 3.6.c).

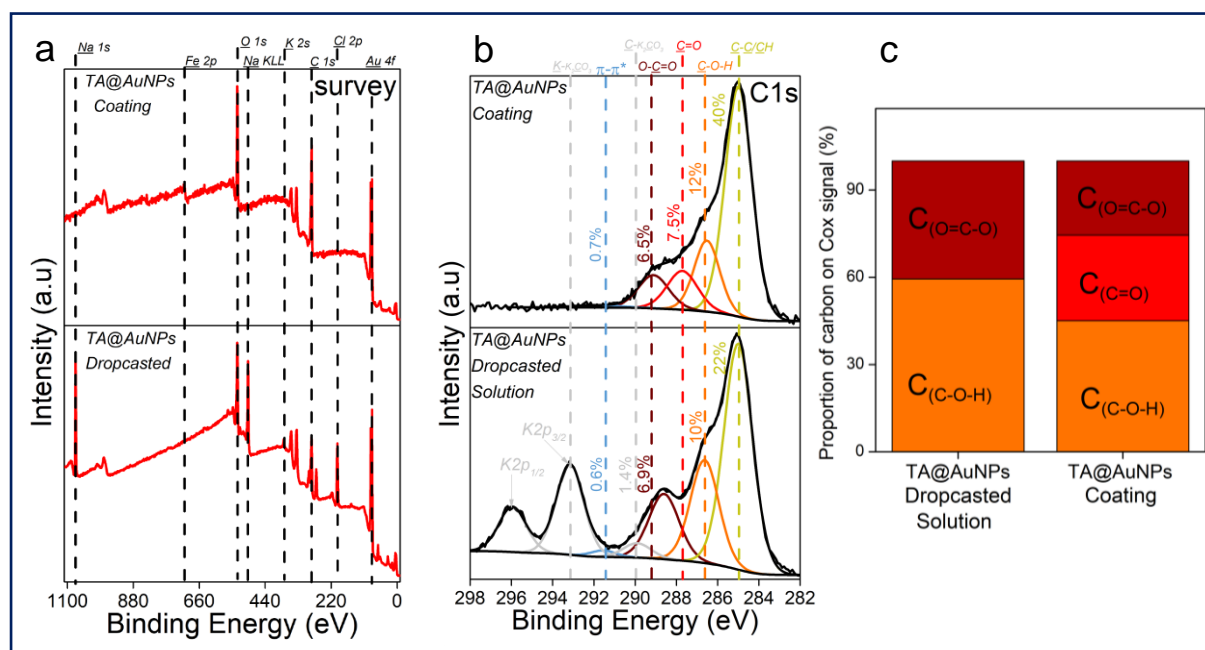


Figure 3.6: (a) Survey XPS spectra of TA@AuNPs coating, obtained by electrodeposition of FcOH/TA@AuNPs, and TA@AuNPs dropcasted solution (b) C 1s XPS spectra and (c) the

relative contribution of each component in the oxidized organic carbon (C_{ox}) signal of the TA@AuNPs coating.

This bond is linked to the formation of quinone from gallol moieties upon electro-oxidation and further reaction with non-oxidized gallol (Scheme 3.1.c). This presence confirmed the electro-crosslinking of TA@AuNPs upon application of the electric potential on FcOH/TA@AuNPs suspension. The GOx/TA@AuNPs coating was then characterized by XPS in comparison to drop-casted GOx and GOx/TA@AuNPs solutions. XPS survey spectra revealed the presence of gold (Au 4f), carbon (C 1s), oxygen (O 1s), and nitrogen (N 1s) (Figure 3.7.a). The N 1s peak, mainly composed of N-C=O environment, confirmed the presence of enzymes in the GOx/TA@AuNPs coating. C1s spectra gather signals coming from carbon species in five main environments. The three studied samples presented the yellow peak at 285 eV (C-C/C-H), the orange one at 286.7 eV (C-O-H), the red one at 288.1 eV, and the brown one at 289.4 eV (O-C=O). The red peak at 288.1 eV could correspond to the contribution of N-C=O amide from the enzyme and the C=O bond from oxidized TA (quinone).

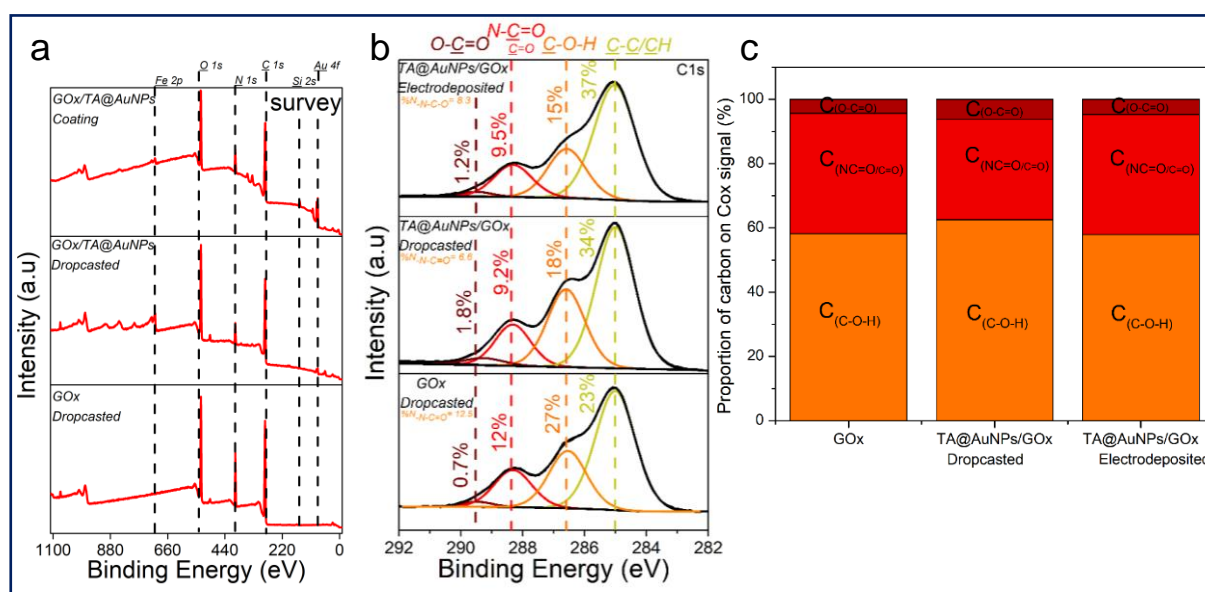


Figure 3.7: (a) Survey XPS spectra of GOx/TA@AuNPs coating, obtained by electrodeposition of FcOH/GOx/TA@AuNPs, FcOH/GOx/TA@AuNPs solution and GOx solution dropcasted (b) C 1s XPS spectra and (c) the relative contribution of each component in the oxidized organic carbon (C_{ox}) signal of the GOx/TA@AuNPs coating, the GOx/TA@AuNPs drop-casted and the GOx drop-casted solution.

As nitrogen is only present on GOx, the percentage of nitrogen detected should be similar to the percentage of carbon coming from the N-C=O environment (theoretical value of 1). This is the case for the GOx drop-casted solution where %N_{NCO}/ %C_{NCO} is equal to 1.06. In the case of the GOx/TA@AuNPs coating and the GOx/TA@AuNPs drop-casted electrodeposited solution, it can be seen that the percentage of carbon centered at 288.1 eV is higher than the amount of nitrogen from the N-C=O environment. This difference suggests that this peak included also the presence of the C=O environment in the GOx/TA@AuNPs coating and electrodeposited solution. The presence of the C=O environment confirmed the oxidation of gallol moieties of TA@AuNPs and their further crosslinking with non-oxidized catechol moieties of TA@AuNPs and with amine moieties of GOx. Before the application of the electric potential, it is likely that the oxygen of the air is already sufficient to oxidize gallol moieties of TA@AuNPs. It can be noticed also that C-OH relative proportion in C_{ox} is also decreasing with the anodic deposition. To get more information, we performed depth profiling with a MAGCIS ion gun which allows cluster argon bombardments on the different layers of the three samples (Figure 3.8). Cluster bombardment layer etching is mainly used on polymeric layers with the advantage of not destroying the structure of the analysed layers.

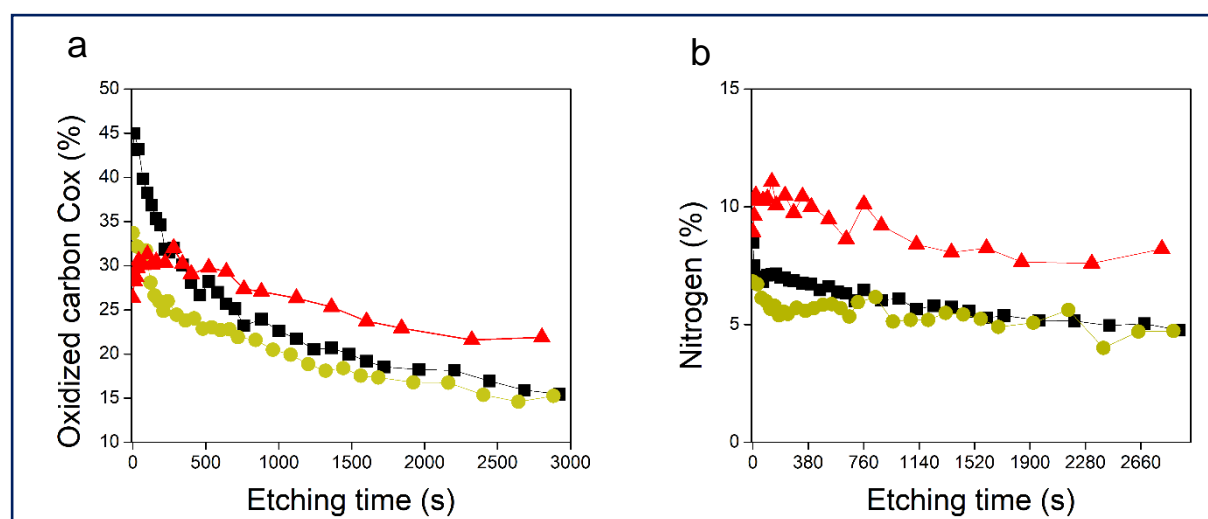


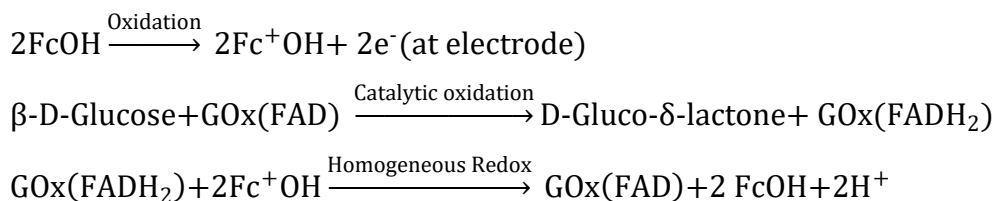
Figure 3.8. Depth profiling of (a) C_{ox} and (b) nitrogen contributions the GOx/TA@AuNPs coating (red triangle), the GOx/TA@AuNPs drop-casted electrodeposited solution (yellow circle), and the GOx drop-casted solution (black square). The evolution is plotted as a function of the etching time by cluster argon bombardments at 8 keV and 300 atoms

In the case of GOx and GOx/TA@AuNPs drop-casted solutions, a fast decrease of C_{ox} and nitrogen contributions was observed indicating weak stability of the deposition. On the

contrary, GOx/TA@AuNPs coatings present a relatively stable evolution of C_{ox} and nitrogen contributions, *i.e.* a stable signal until 1 000 s of etching followed by a small decrease. This suggests a homogeneous distribution of GOx all over the thickness of the coating and a strong interaction between GOx and TA@AuNPs, protecting the enzyme against argon cluster bombardment. In summary, the electrodeposition process induced the appearance of a C=O peak and allowed to obtain a stable coating towards etching with a strong interaction between the enzyme and the NPs. These observations are the indirect signature of the electro-crosslinking of GOx and TA@AuNPs.

VI. GOx/TA@AuNPs coating biosensing properties

The electrochemical biosensing capability of GOx/TA@AuNPs coating was evaluated using standard enzyme-catalyzed glucose oxidation in the presence of FcOH in physiological conditions (10 mM PBS pH 7.4). FcOH was used to enhance the electron transfer rate between GOx and the electrode because of the inaccessible enzymatic active site. The sensing mechanism of glucose is based on the following equations:



A potential is applied to the working electrode in order to oxidize FcOH into FcOH^+ . In the presence of glucose, GOx catalytically oxidizes glucose into gluconolactone and its cofactor (flavin adenine dinucleotide, FAD) is reduced into GOx-FADH₂. As already reported elsewhere,⁷ FcOH^+ is likely to retrieve electrons from the buried cofactor to the electrode through a spontaneous redox reaction. Indeed, $E_{\text{Fc}^+\text{OH}/\text{FcOH}}^0 = 0.21 \text{ V}^{24,25}$ is higher than the formal potential $E_{\text{FAD}/\text{FADH}_2}^0 = -0.4 \text{ V}^{26}$ vs Ag/AgCl. Figure 3.9.a shows the different cyclic voltammograms of GOx/TA@AuNPs coating in contact with 0.5 mM FcOH, prepared in PBS 10 mM pH 7.4 in the presence of different concentrations in glucose. The oxidation and reduction peaks of FcOH were observed at 0.25 V and 0.19 V. The introduction of glucose triggered an increase of the oxidation peak and a decrease of the reduction peak, due to the regeneration of FcOH and the depletion of FcOH^+ , respectively. A good bioelectrochemical

catalytic activity of the GOx/TA@AuNPs coating was obtained towards glucose. Indeed, complete disappearance of the reduction peak was observed for 10 mM glucose at $50 \text{ mV} \cdot \text{s}^{-1}$ (Figure 3.9.a) and $5 \text{ mV} \cdot \text{s}^{-1}$ (Figure 3.9.b). This indicates a complete consumption of FcOH^+ by the enzyme cofactor allowing the regeneration of GOx.

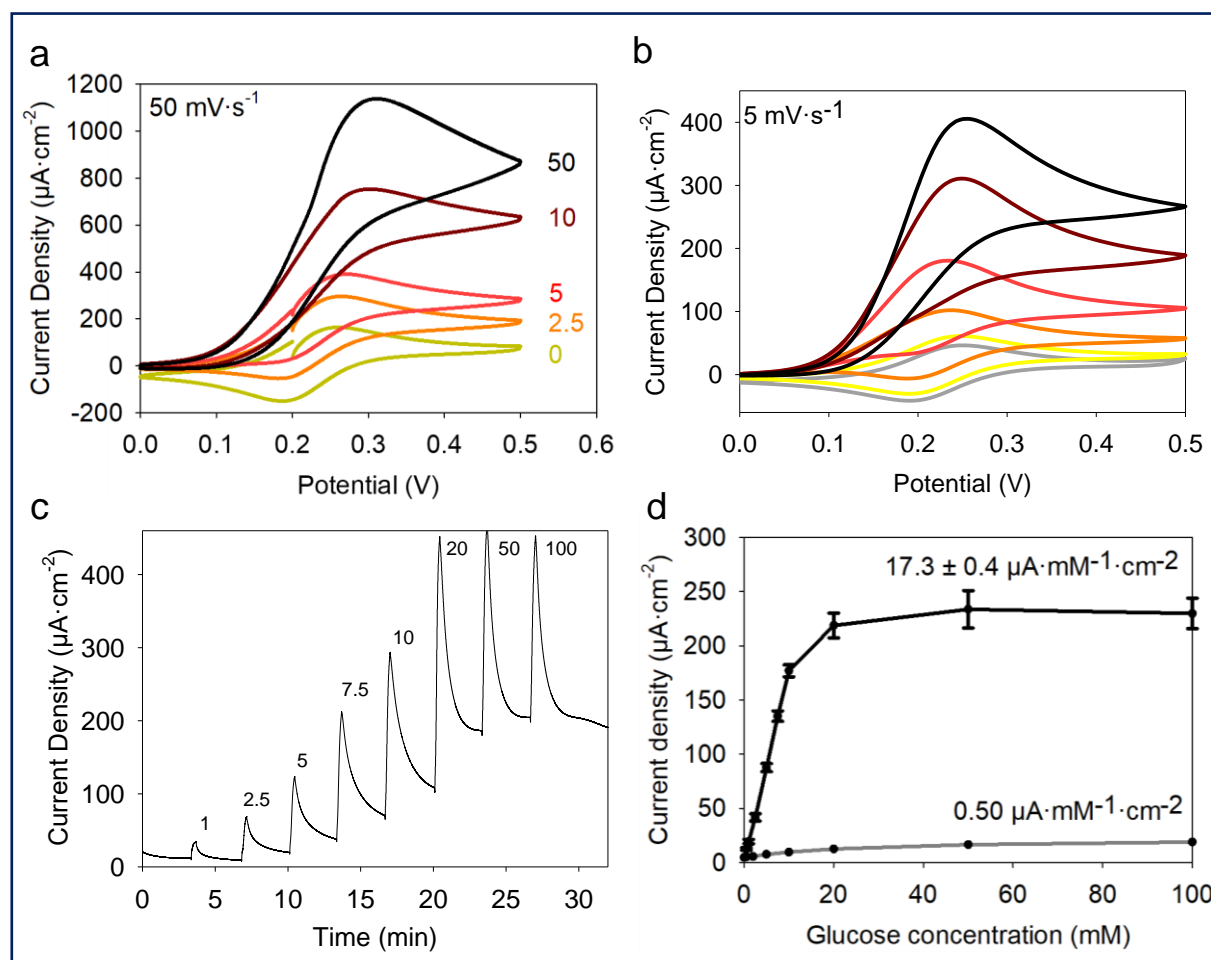


Figure 3.9: Cyclic voltammograms, performed at a scan rate of (a) $50 \text{ mV} \cdot \text{s}^{-1}$ and (b) $5 \text{ mV} \cdot \text{s}^{-1}$ of GOx/TA@AuNPs coating in contact with 0 to 100 mM of glucose solution prepared in 0.5 mM FcOH/10 mM PBS. (c) Chronoamperometric response at 0.25 V upon addition of different glucose concentration. (d) Average current density, measured at 0.25 V, as a function of the glucose concentration of GOx/TA@AuNPs (black curve) and GOx/TA (grey curve) coatings. The average and error bars of GOx/TA@AuNPs coatings were evaluated on six independent experiments.

The saturation plateau at 20 mM glucose arises from the typical hyperbolic Michaelian-Menten kinetic. At this concentration, GOx catalytic sites are saturated and the maximal glucose catalytic rate is reached. Thus, the amperometric response of the coating was measured at 0.25

V at different concentrations of glucose (Figure 3.9.c). Each fluid replacement led to an electrical current overshoot followed by a period of stabilization at a steady-state value after 200 s. The overshoot happened in the transient period because of a local rise of glucose and FcOH concentration at the injection step. The calibration curve, *i.e.* the current density measured after 200 s vs glucose concentration, showed a linear range that extends up to 10 mM with a typical saturation plateau of $220 \mu\text{A}\cdot\text{cm}^{-2}$ (Figure 3.9.d) caused by the saturation of the enzymes by the substrate. The average sensitivity, calculated from the slope of the calibration curve of 6 different samples, was $17.3 \pm 0.4 \mu\text{A}\cdot\text{mM}^{-1}\cdot\text{cm}^{-2}$ ($R^2 = 0.999$) with a limit of detection at 0.3 mM (LOD at a signal to noise ratio 3). These coatings would distinguish between healthy (3.8 and 6.5 mM) and hyperglycemic subjects (>7 mM). A great improvement of the sensitivity of electro-cross-linked enzymatic biosensor was reached thanks to the presence of NPs. Indeed, the sensitivity of TA/GOx ($0.5 \mu\text{A}\cdot\text{mM}^{-1}\cdot\text{cm}^{-2}$) and biscatechol/GOx⁷ ($0.66 \mu\text{A}\cdot\text{mM}^{-1}\cdot\text{cm}^{-2}$) coatings were found to be 34 and 28 times lower than GOx/TA@AuNPs coatings, respectively. Ramanavicius *and coll.* achieved higher sensitivity by electrochemical nucleation of dendritic AuNPs followed by drop-casting of GOx²⁷ or electropolymerization of a conducting polymer and covalent immobilization of GOx.²⁸

The covalent immobilization of GOx was proven by performing the chronoamperometry test before and after consecutive washes with 0.01% Tween-20 prepared in 10 mM PBS. These washes are expected to remove any physisorbed GOx.²⁹ No loss of mass was observed and the sensitivity remained stable after the Tween 20 treatment (Figure 3.10.a-b). Regarding durability, the biosensor can be stored up to 14 days in 10 mM PBS buffer at room temperature with a loss in sensitivity lower than 0.6% per day of storage (Figure 3.10.c) which is very competitive in regards to literature (Table 3.1). Others biosensors found in the literature were obtained manually by drop-casting using a specific cross-linker and are not suitable for specific functionalization of a single electrode out of a microelectrode array. The biological affinity of the immobilized GOx was determined by estimating the Michaelis-Menten constant. The Lineweaver-Burk equation³⁰ was used to fit the double reciprocal plot of current density vs concentration of glucose (Material and Methods section III.5). A low K_m^{app} indicates a high enzymatic activity of the immobilized GOx.³¹ We found a K_M^{app} value of 19 mM in good accordance with the literature value of 26 mM³² for glucose in solution. For comparison, the reported values of K_M^{app} are 10.36 mM for GOX/polyaniline³³ and 19 mM for GOX/ZnO³⁴ nanotubes biosensors obtained by drop-casting and reticulation with glutaraldehyde.

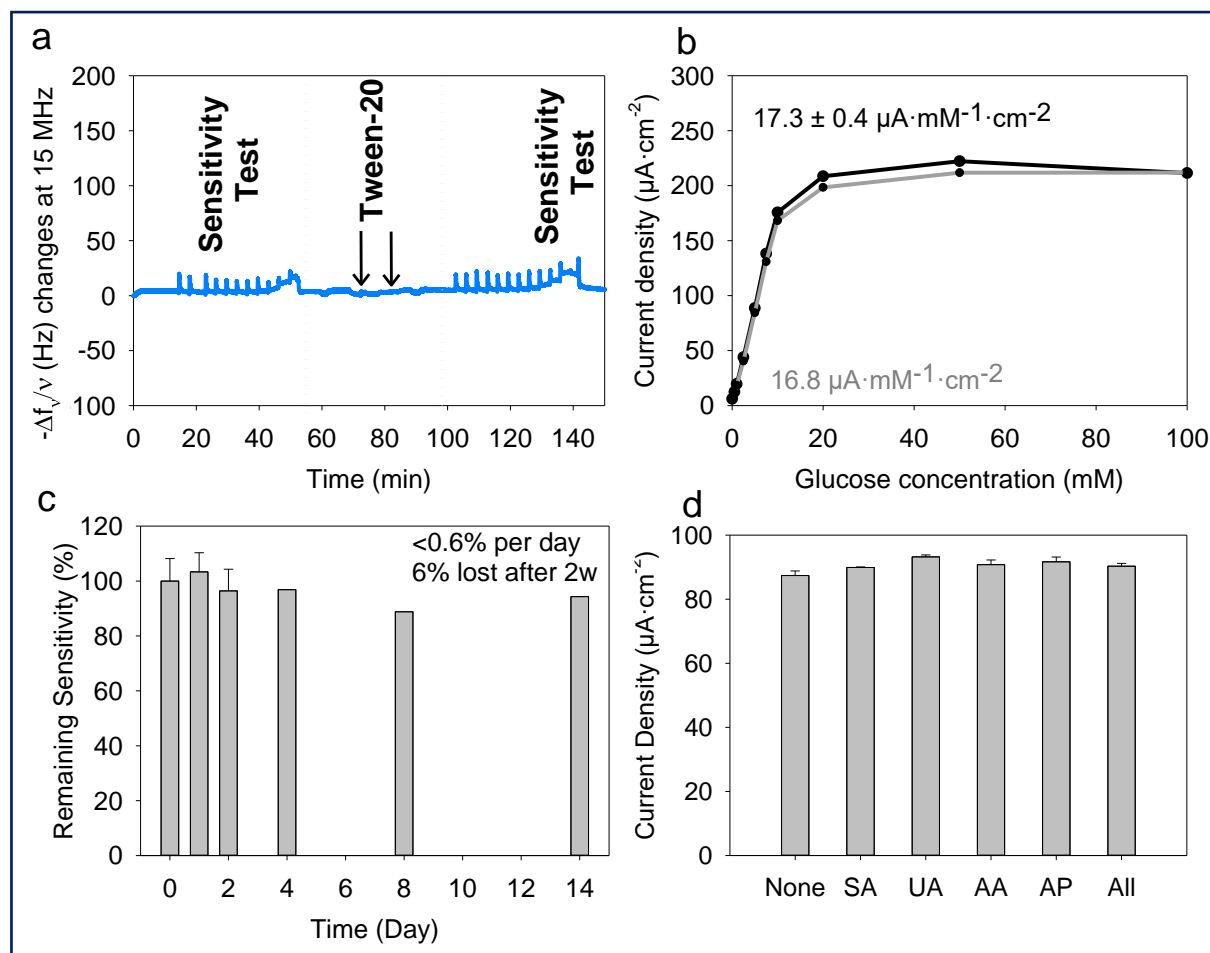


Figure 3.10: Tween-20 treatment of GOx/TA@AuNPs coating (a) Evolution of the normalized frequency shift, measured by QCM-D, as a function of time before and after addition of Tween-20 0.01% in PBS 10 mM (b) Current density, measured at 0.25 V in the presence of 0.5 mM FcOH in PBS 10 mM pH 7.4, as function of glucose concentration, before (black curve) and after (grey curve) Tween-20 treatment. (c) Stability of the biosensor sensitivity at different time periods keeping the sensor in the QCM cell in FcOH 0.5 mM PBS 10 mM at room temperature when not in use. (d) Current density, measured at +0.25 V in the presence of 0.5 mM FcOH, of GOx/TA@AuNPs coating in contact with 5 mM glucose solution in the absence (None) and in the presence of different interfering substances, salicylic acid (SA), uric acid (UA), ascorbic acid (AA) and acetaminophen (AP).

Table 3.1: Comparison of different biosensors, based on GOx and AuNPs coating deposited on gold electrode obtained by dropcasting and crosslinked by glutaraldehyde or thiol in comparison to this work. AuNPs were either dropcasted or electrodeposited from gold salt.

Process	Applied voltage V vs Ag/AgCl	Medium	Linear range (mM)	Sensitivity ($\mu\text{A} \cdot \text{mM}^{-1} \cdot \text{cm}^{-2}$)	Stability (day)	Ref
Electro-crosslinking Catechol	0.25	0.5mM FcOH 10 mM PBS pH7.4	0.3-10	17.4	14 days 93% at RT	This work
Dropcasting Thiol	0.34	0.1 mM FcOH 0.1 M PB (pH 7)	0.020-5.7	8.8	30 days 4°C	[35]
Dropcasting Cysteine & Glutaraldehyde	0.2	TTF In 0.05M PB pH7.4	0.01-10	14	28 day 4°C	[36]
Dropcasting Glutaraldehyde	0.29	0.25 mM FcOH 0.1M PBS pH 6.8	0.01-13	5.72	28 days 85% 4°C	[37]
Dropcasting Cystamine	0.3	0.1mM FcOH 0.1 M PB pH7	0.02-6	8.3	60 days	[38]
Ti patterned BSA Glutaraldehyde	1 direct H ₂ O ₂ oxidation	0.1M PBS	0.03-3.05	25.74 (CV)	–	[39]

The biosensor selectivity was tested towards common interferents at their maximum standard blood concentration with a standard glucose concentration of 5 mM (Figure 3.10.d). The variation of the response was between 0.2 and 1.6 % for salicylic acid (SA), uric acid (UA), ascorbic acid (AA), acetaminophen (AP), and all mixed 2% (Figure 10.d). In comparison, the standard deviation of the current density measured for glucose at 5 mM is 2% out of 6 samples. Therefore, no significant difference in the biosensor response was found with any interferents. Using rhodamine labelled GOx (GOx^{Rho}), a $\text{GOx}^{\text{Rho}}/\text{TA@AuNPs}$ film was built on interdigitated arrays (IDA) of electrodes by the application of 0.7 V on one of the two arrays for 15 min. The microelectrodes were imaged by optical microscopy in bright field and fluorescence to check the presence of GOx^{Rho} and to verify its spatial co-localization with TA@AuNPs (Figure 3.11.a-b). An excellent spatial-selectivity was obtained since a high fluorescence (GOx^{Rho}) was observed only on the addressed microelectrodes. The sensitivity of the obtained coating was $6.0 \mu\text{A} \cdot \text{mM}^{-1} \cdot \text{cm}^{-2}$ with a response time upon addition of 3.2 s at 0.4 mM glucose concentration change and 6.9 s at 7.5 mM addition (Figure 3.11.c). It should be noted that this electrodeposition was not optimized on the microelectrode and still give a good sensitivity.

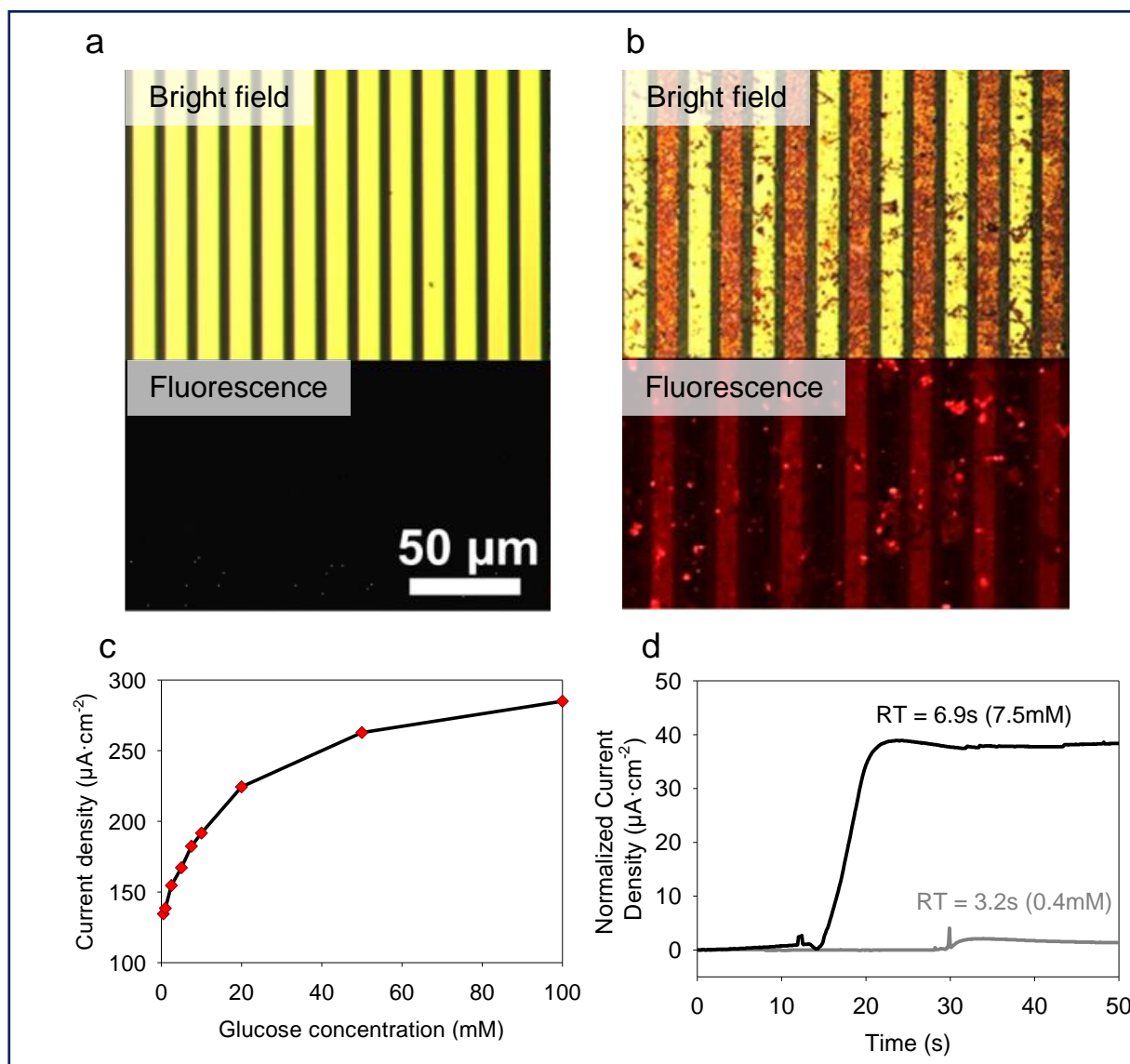
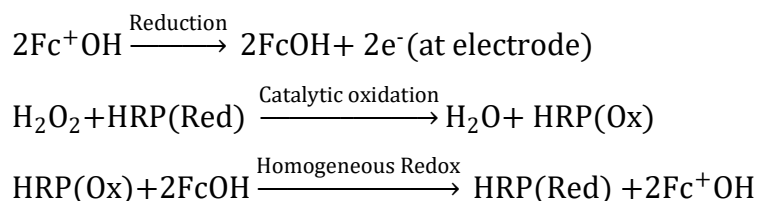


Figure 3.11: Optical microscope of 10 μm interdigitated electrode before (a) and after (b) electrodeposition of $\text{GOx}^{\text{Rho}}/\text{TA}@\text{AuNPs}$ coating. (c) Current density-glucose concentration curve obtained upon successive additions for $\text{GOx}/\text{TA}@\text{AuNPs}$ electrodeposited onto one interdigitated electrode and using the large bare Au as counter electrode. The current value is measured 20 seconds after addition. (d) Response time at 0.25V upon addition of 10 μL and 200 μL of Glucose 100mM/FcOH 0.5mM into 2.5mL FcOH 0.5mM in PBS10mM using $\text{GOx}/\text{TA}@\text{AuNPs}$ coating

VII. Versatility of the process

To illustrate the versatility of the process, we also designed a hydrogen peroxide (H_2O_2) biosensor by immobilizing horseradish peroxidase (HRP), a significantly smaller enzyme (44 kDa with a DLS size of 5.5 nm). H_2O_2 is a reactive oxygen species present in many biological processes including cell growth, apoptosis, inflammation, infection, or cancer.⁴⁰⁻⁴³ For instance, it is used at the early stage in wounds as an antibacterial and signaling danger agent. Indeed, H_2O_2 becomes detrimental at high concentrations slowing down the healing process. The electrodeposited solution was prepared by adjusting the HRP/TA@AuNPs molar ratio close to the full coverage of NPs by the enzyme which is 40. After the injection of the FcOH/HRP/TA@AuNPs electrodeposited solution, the application of 0.7 V for one hour led to an increase of the normalized frequency shift and a homogeneous distribution of HRP/TA@AuNPs on the electrode (Figure 3.12.a-b). The biosensing experiments were performed in 10 mM PBS at pH 7.4 using 0.1 mM FcOH as a mediator using chronoamperometry at 0.19 V. The reduction peak of the mediator was used because of the standard potential of the Heme of HRP which is at 0.95 V.²⁵ The sensing mechanism is based on the following reactions according to literature.^{44,45}



The presence of H_2O_2 induced an increase in the reduction peak signal of FcOH^+ at the electrode (Figure 3.12c). The current density measured as a function of H_2O_2 concentration showed a typical linear range from 10 to 250 μM with a LOD at 10 μM and a sensitivity of 220 $\mu\text{A} \cdot \text{mM}^{-1} \cdot \text{cm}^{-2}$ (Figure 3.12d). Without further optimization, the obtained HRP/TA@AuNPs coating showed a better sensitivity as a biosensor for H_2O_2 in comparison to the ones reported based on manual crosslinking of HRP with sensitivities of 0.5 and 30 $\mu\text{A} \cdot \text{mM}^{-1} \cdot \text{cm}^{-2}$ for HRP/cysteamine/glutaraldehyde⁴⁶ and HRP/cysteine bonds crosslinker,⁴⁷ respectively.

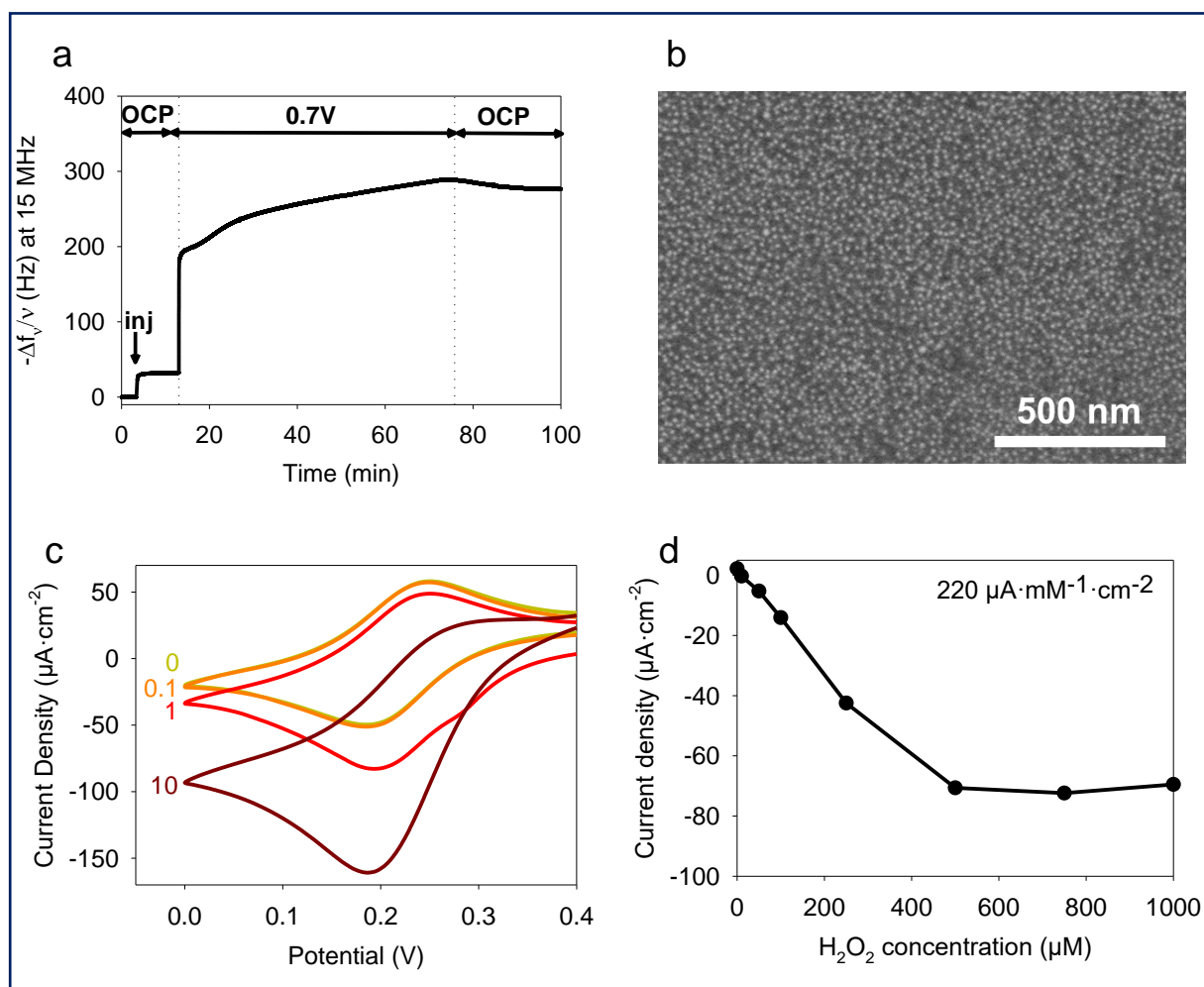


Figure 3.12: HRP/TA@AuNPs coating: (a) Buildup with the evolution of the normalized frequency shift of FcOH/HRP/TA@AuNPs solution as a function of time during the application of 0.7 V (b) BSE-SEM micrograph of the coating, (c) Electrocatalytic reduction current, measured at $50 \text{ mV} \cdot \text{s}^{-1}$, of 0 to 10 mM H_2O_2 prepared in 0.5 mM FcOH/10 mM PBS and (d) Current density, measured at 0.19 V, as a function of H_2O_2 concentration prepared in 0.1 mM FcOH/10 mM PBS

Conclusion

The electrochemical cross-linking of enzymes was generalized by the use of a natural and abundant polyphenol as a crosslinker and as a reductive agent to obtain gold nanoparticles. Thanks to gallol electro-oxidation at 0.7 V, the TA@AuNPs crosslinked and reacted chemically with amine moieties of enzymes. This process allowed (i) the design of enzymatic biosensor with competitive sensitivity and stability upon storage with regards to other well-implemented techniques and (ii) the functionalization of a single electrode out of a microelectrode array. Two systems had been developed to highlight the versatility of the process – namely a peroxide and a glucose biosensor. One of the further steps will be to obtain a third-generation biosensor by cross-linking simultaneously the mediator⁴⁷ or to incorporate a conductive polymer as supplementary components^{48,49}. Finally, both electrodes (GOX-based anode and HRP-based cathode) can also be used for the design of enzymatic biofuel cells.^{50,51}

References

- (1) P. Bhattarai, S. Hameed. Basics of Biosensors and Nanobiosensors, *Nanobiosensors Ed.*; Wiley, Weinheim 2020, pp 1–22.
- (2) L. C. Jr. Clark and C. Lyons. Electrode systems for continuous monitoring in cardiovascular surgery, *Ann. N. Y. Acad. Sci.* 1962, **102**, 29–45.
- (3) C. S. Pundir and N. Chauhan. Acetylcholinesterase inhibition-based biosensors for pesticide determination: A review, *Anal. Biochem.* 2012, **429**, 19–31.
- (4) M. Z. H. Khan, M. R. Hasan, S. I. Hossain, M. S. Ahommed and M. Daizy. Ultrasensitive detection of pathogenic viruses with electrochemical biosensor: State of the art, *Biosens. Bioelectron.* 2020, **166**, 112–431.
- (5) S. Szunerits, V. Mishyn, I. Grabowska and R. Boukherroub. Electrochemical cardiovascular platforms: Current state of the art and beyond, *Biosens. Bioelectron.* 2019, **131**, 287–298.
- (6) A. Sassolas, L. J. Blum and B. D. Leca-Bouvier. Immobilization strategies to develop enzymatic biosensors, *Biotechnol. Adv.* 2012, **30**, 489–511.
- (7) J. El-Maiss, M. Cuccarese, P. Lupattelli, L. Chiumminto, M. Funicello, P. Schaaf and F. Boulmedais. Mussel-Inspired Electro-Cross-Linking of Enzymes for the Development of Biosensors, *ACS Appl. Mater. Inter.* 2018, **10**, 18574–18584.

- (8) Y. Xie, T. Liu, Z. Chu and W.J. Jin. Recent advances in electrochemical enzymatic biosensors based on regular nanostructured materials, *Electroanal. Chem.* 2021, **893**, 115328.
- (9) S. K. Sivaraman, S. Kumar and V. Santhanam. Room-temperature synthesis of gold nanoparticles - Size-control by slow addition, *Gold Bull.* 2010, **43**, 275–286.
- (10) X. Liu, M. Atwater, J. Wang, and Q. Huo. Extinction coefficient of gold nanoparticles with different sizes and different capping ligands, *Colloids Surf., B* 2007, **53**, 3–7.
- (11) H. D. Graham. Stabilization of the Prussian blue color in the determination of polyphenols, *J. Agric. Food Chem.* 2002, **40**, 801–805.
- (12) O. Courjean, V. Flexer, A. PrévotEAU, E. Suraniti, N. Mano. Effect of degree of glycosylation on charge of glucose oxidase and redox hydrogel catalytic efficiency, *ChemPhysChem* 2010, **11**, 2795–2797.
- (13) J. H. Scofield. Hartree-Slater subshell photoionization cross-sections at 1254 and 1487 eV, *J. Electron Spectros. Relat. Phenomena* 1976, **8**, 129–137.
- (14) K. Singh, T. McArdle, P. R. Sullivan and C. F. Blanford. Sources of activity loss in the fuel cell enzyme bilirubin oxidase, *Energy Environ. Sci.* 2013, **6**, 2460-2464.
- (15) J. Lim, S. P. Yeap, H. X. Che and S. C. Low. Characterization of magnetic nanoparticle by dynamic light scattering, *Nanoscale Res. Lett.* 2013, **8**, 1–14.
- (16) A. E. Hagerman. Fifty Years of Polyphenol–Protein Complexes, *Recent Adv. Polyphen. Res.* 2012, **3**, 71–97.
- (17) H. J. Hecht, H. M. Kalisz, J. Hendle, R. D. Schmid and D. Schomburg. Crystal Structure of Glucose Oxidase from *Aspergillus niger* Refined at 2.3 Å Resolution, *J. Mol. Biol.* 1993, **229**, 153–172.
- (18) Y. Wang, R. Jonkute, H. Lindmark, J. D. Keighron and A.-S. Cans. Molecular Crowding and a Minimal Footprint at a Gold Nanoparticle Support Stabilize Glucose Oxidase and Boost Its Activity, *Langmuir* 2019, **36**, 37–46.
- (19) J. Yang, M. A. C., M. Stuart and M. Kamperman. Jack of all trades: Versatile catechol crosslinking mechanisms, *Chem. Soc. Rev.* 2014, **43**, 8271–8298.
- (20) S. Mole and P. G. Waterman. Tannic acid and proteolytic enzymes: Enzyme inhibition or substrate deprivation?, *Phytochemistry* 1986, **26**, 99–102.
- (21) A. Krywko-Cendrowska, L. Marot, D. Mathys and Boulmedais. Ion-Imprinted Nanofilms Based on Tannic Acid and Silver Nanoparticles for Sensing of Al(III), *ACS Appl. Nano Mater.* 2021, **4**, 5372–5382.

- (22) O Mergel, P. T. Küh., S. Schneider, U. Simon, and F. A. Plamper. Influence of Polymer Architecture on the Electrochemical Deposition of Polyelectrolytes, *Electrochim. Acta* 2017, **232**, 98-105
- (23) S. Tardio, M.-L. Abel, R. H. Carr, and J. F. Watts. Polystyrene-silicon bonding through π electrons: a combined XPS and DFT study, *Surf. Interface Anal.* 2016, **48**, 556–560.
- (24) J. Savéant, and C. Costentin, *Elements of Molecular and Biomolecular Electrochemistry*; Ed.; Wiley, Hoboken (USA) 2019.
- (25) K. Kano. Redox Potentials of Proteins and Other Compounds of Bioelectrochemical Interest in Aqueous Solutions, *Rev. Polarogr.* 2002, **48**, 29–46.
- (26) S. Liu, and H. Ju. Reagentless glucose biosensor based on direct electron transfer of glucose oxidase immobilized on colloidal gold modified carbon paste electrode, *Biosens. Bioelectron.* 2003, **19**, 177–183.
- (27) A. Ramanaviciene, N. German, A. Kausaite-Minkstiniene, and A. Ramanavicius. Glucose Biosensor Based on Dendritic Gold Nanostructures Electrodeposited on Graphite Electrode by Different Electrochemical Methods, *Chemosensors*, 2021, **9**, 188.
- (28) N. German, A. Ramanaviciene, and A. Ramanavicius. Dispersed Conducting Polymer Nanocomposites with Glucose Oxidase and Gold Nanoparticles for the Design of Enzymatic Glucose Biosensors, *Polymers*, 2021, **13**, 2173.
- (29) S.-K. Kim, C. Jeon, G.-H. Lee, J. Koo, S. Hwi Cho, S. Han, M.-H. Shin, J.-Y. Sim and S. K Hahn. Hyaluronate–Gold Nanoparticle/Glucose Oxidase Complex for Highly Sensitive Wireless Noninvasive Glucose Sensors, *ACS Appl. Mater. Interfaces* 2019, **11**, 37347–37356.
- (30) A. S. Campbell, M. F. Islam and A. J. Russell. Intramolecular Electron Transfer through Poly-Ferrocenyl Glucose Oxidase Conjugates to Carbon Electrodes: 2. Mechanistic Understanding of Long-Term Stability, *Electrochim. Acta* 2017, **246**, 294–302.
- (31) Y. Yonemori, E. Takahashi, H. Ren, T. Hayashi and H. Endo. Biosensor system for continuous glucose monitoring in fish, *Anal. Chim. Acta* 2009, **633**, 90–96.
- (32) S. Nakamura, S. Hayashi, and K. Koga. Effect of periodate oxidation on the structure and properties of glucose oxidase, *Biochim. Biophys. Acta - Enzymol.* 1976, **445**, 294–308.
- (33) M. Barsan, and C. A. Brett. A new modified conducting carbon composite electrode as sensor for ascorbate and biosensor for glucose, *Bioelectrochemistry* 2009, **76**, 135–140.

- (34) T. Kong, Y. Chen, Y. Ye, K. Zhang, Z. Wang, and X. Wang. An amperometric glucose biosensor based on the immobilization of glucose oxidase on the ZnO nanotubes, *Sensors Actuators, B Chem.* 2009, **138**, 344–350.
- (35) S. Zhang, N. Wang, H. Yu, Y. Niu, and C. Sun. Covalent attachment of glucose oxidase to an Au electrode modified with gold nanoparticles for use as glucose biosensor, *Bioelectrochemistry* 2005, **67**, 15–22.
- (36) M. L. Mena, P. Yáñez-Sedeño, and J. M. A Pingarrón. A comparison of different strategies for the construction of amperometric enzyme biosensors using gold nanoparticle-modified electrodes, *Anal. Biochem.* 2005, **336**, 20–27.
- (37) Y. Sun, F. Yan, W. Yang, and C. Sun. Multilayered construction of glucose oxidase and silica nanoparticles on Au electrodes based on layer-by-layer covalent attachment, *Biomaterials* 2006, **27**, 4042–4049.
- (38) S. Zhang, Y. Niu, and C. Sun. Immobilization of glucose oxidase on gold nanoparticles modified Au electrode for the construction of biosensor, *Sensors Actuators B Chem.* 2005, **109**, 367–374.
- (39) W. Lipińska, K. Siuzdak, J. Ryl, P. Barski, G. Śliwiński and K. Grochowska. The optimization of enzyme immobilization at Au-Ti nanotextured platform and its impact onto the response towards glucose in neutral media, *Mater. Res. Express* 2019, **6**, 1150e3.
- (40) C. C. Winterbourn. The Biological Chemistry of Hydrogen Peroxide, *Methods Enzymol.* 2013, **528**, 3–25.
- (41) S. Teramoto, T. Tomita, H. Matsui, E. Ohga, T. Matsuse and Y. Ouchi. Hydrogen peroxide-induced apoptosis and necrosis in human lung fibroblasts: protective roles of glutathione, *Jpn. J. Pharmacol.* 1999, **79**, 33–40.
- (42) R. Schreck, P. Rieberl and P. A. Baeuerle. Reactive oxygen intermediates as apparently widely used messengers in the activation of the NF- κ B transcription factor and HIV-1, *Embo J.* 1991, **10**, 2247–2258.
- (43) M. Mittal, M. Siddiqui, K. Tran, S. Reddy and A. Malik. Reactive oxygen species in inflammation and tissue injury, *Antioxid. Redox Signal.* 2014, **20**, 1126–1167.
- (44) A. Rondeau, N. Larsson, M. Boujtita, L. Gorton and N. El. Murr. The synergetic effect of redox mediators and peroxidase in a bienzymatic biosensor for glucose assays in FIA, *Analysis* 1999, **27**, 649–656.
- (45) H.-S. Wang, Q.-X. Pan and G.-X. Wang. A Biosensor Based on Immobilization of

- Horseradish Peroxidase in Chitosan Matrix Cross-linked with Glyoxal for Amperometric Determination of Hydrogen Peroxide, *Sensors* 2005, **5**, 266–276.
- (46) Y. Xiao, H. X. Ju, and H. Y. Chen. Hydrogen peroxide sensor based on horseradish peroxidase-labeled Au colloids immobilized on gold electrode surface by cysteamine monolayer, *Anal. Chim. Acta* 1999, **391**, 73–82.
- (47) S. Chen, R. Yuan, Y. Chai, L. Xu, N. Wang, X. Li and L. Zhang. Amperometric Hydrogen Peroxide Biosensor Based on the Immobilization of Horseradish Peroxidase (HRP) on the Layer-by-Layer Assembly Films of Gold Colloidal Nanoparticles and Toluidine Blue, *Electroanalysis* 2006, **18**, 471–477.
- (48) S. Ramanavicius, and A. Ramanavicius. Charge Transfer and Biocompatibility Aspects in Conducting Polymer-Based Enzymatic Biosensors and Biofuel Cells, *Nanomaterials*, 2021, **11**, 371.
- (49) N. German, A. Ramanaviciene, and A. Ramanavicius. Dispersed Conducting Polymer Nanocomposites with Glucose Oxidase and Gold Nanoparticles for the Design of Enzymatic Glucose Biosensors, *Polymers*, 2021, **13**, 2173.
- (50) A. Ramanavicius, A. K-Minkstimiene, I. M-Vilkonciene, P. Genys, R. Mikhailova, T. Semashko, J. Voronovic, A. Ramanaviciene. Biofuel cell based on glucose oxidase from *Penicillium funiculosum* 46.1 and horseradish peroxidase, *Chem. Eng. J* 2015, **264**, 165-173.
- (51) A. Ramanavicius, A. Kausaite, A. Ramanaviciene. Biofuel cell based on direct bioelectrocatalysis, *Biosens. Bioelectron.* 2005, **20**, 1962-1967

Chapter 4

Optimization of Electro-crosslinked Enzyme/Tannic Acid Nanoparticles as Nanohybrid Biosensors

Chapter 4 – Table of Contents

Abstract	158
Introduction	158
I. Nanoparticles Synthesis and characterization.....	160
II. Gold Nanoparticles Electrodeposited Coatings.....	162
III. Sensitivity optimization of enzyme/NPs coatings	164
IV. Enzyme/NPs bioconjugate characterization	169
Conclusion.....	173
References	174

Abstract

Enzymes/Nanoparticles (NPs) bioconjugates are massively used nowadays to develop thin films for optical and electrochemical biosensors. Nevertheless, their full characterization as a thin coating onto electrodes remains little discussed, in particular the influence of NPs size and enzyme/NPs ratio used in the electrodeposition solution. In this study, GOx (160 kDa) and HRP (44 kDa) were used in association with tannic acid capped gold NPs (a series with sizes from 7 to 40 nm) to electrodeposit biosensor coatings, sensitive towards glucose and H₂O₂ respectively. The electrodeposition process was based on a mussel-inspired electro-crosslinking between gallol moieties of tannic acid (at the surface of NPs) and amine moieties of the enzymes. On one hand, the sensitivity of the GOx/NPs coatings depends strongly on the NP size and the enzyme/NPs molar ratio of the electrodeposition solution. An optimal sensitivity was obtained by electrodeposition of 11 nm NPs at a GOx/NPs molar ratio close to the theoretical value of the enzyme monolayer. On the other hand, a modest influence of the NPs size was found on the sensitivity in the case of the electrodeposited HRP/NPs coatings, reaching a plateau at the HRP/NPs molar ratio close to the value of the theoretical enzyme monolayer. In both cases, the enzyme/NPs molar ratio played a role in the sensitivity. To fully understand the parameters driving the biosensor sensitivity, a comprehensive evaluation of the colloidal state of the bioconjugates is proposed here.

Introduction

Nanoparticle/enzyme bioconjugates have received great attention in the development of optical^{1,2} or electrochemical^{3,4} biosensors. The purpose is to combine the biological activity of the enzyme and its specificity towards an analyte with the unique properties of the nanoparticles (NPs) such as plasmonic band, surface-to-volume ratio, and/or conductivity to translate the biological signal of recognition into a quantifiable and processable one. Several studies showed that the curvature of NPs affects strongly the conformation of the adsorbed protein⁵⁻¹¹. However, contradictory trends were found regarding the activity of the adsorbed enzyme. For instance, Tadepalli *et al.* observed a significant decrease in the adsorbed horseradish peroxidase (HRP) activity with the increase of the gold NPs diameter from 10 to 40 nm¹¹, and Wu *et al.* the opposite trend with a similar size range (5-60 nm)⁹. Both studies used two different cosubstrates which can explain this inconsistency since the conformation change may affect

differently the cosubstrate/enzyme interaction. Another difference can be pointed out as in the first study the equivalent surface area of NPs was kept constant by adjusting the optical density value¹¹ whereas in the second one the NPs concentration (optical density) was kept constant⁹. Breger et al. studied the influence of the gold NP size (1.5 – 100 nm) using phosphotriesterase keeping constant the enzyme concentration and the surface density of NPs, varying the NPs concentration. In this case, the highest enzymatic activity was obtained with an optimum gold NPs size of 10 nm¹². Two antagonist effects are often competing: (i) large NPs adsorb more enzymes than small ones leading to higher activity per NPs^{13,14}, and (ii) small NPs seem to impact the activity of the adsorbed enzymes less than the large ones^{12,15,16}. Thus, an optimal NP size is eventually found at a given enzyme and NPs concentrations. Moreover, the protein size regarding NP size was recently found to be also crucial¹³. As a general trend, the activity of large enzymes (> 100 kDa) increases with the NPs size^{15–17} whereas the activity of small enzymes (< 50 kDa) decreases with the increase of NPs size^{11,18,19}. To the best of our knowledge, there is no exhaustive study on the effect of NPs size on the sensitivity of enzyme/NPs thin coatings. Most of the biosensors studies investigating enzymes/NPs coatings usually use small NPs to get a high electroactive surface with very concentrated enzyme aliquots (~20–200 μ M) to achieve the highest sensitivity²⁰. Until now, there is no evidence that the trends observed in solution will be similar in the case of thin films.

In this work, we studied the influence of the size of gold NPs and the enzyme/NPs molar ratio of the electrodeposition solution on the sensitivity of the nanohybrid biosensor. For this purpose, we used two glycosylated enzymes having two different sizes HRP (44 kDa, globular size 5.5 nm²¹) and glucose oxidase (GOx) (160 kDa, globular size 6.9 nm²²) and a series of tannic acid (TA) capped gold NPs ranging from 7 to 40 nm. The nanohybrid biosensors were obtained by a one-step mussel-inspired electro-cross-linking process (Figure 4.1a) using an electrodeposition solution of enzyme/NPs and ferrocene methanol (FcOH), acting as a mediator during the electrodeposition²³. The presence of gallol moieties on the surface of NPs allowed the adsorption of the enzyme, through hydrogen bonds and hydrophobic interactions. During the application of the anodic potential, FcOH molecules are electro-oxidized into ferrocenium, able to oxidize gallol moieties of TA into quinone. The immobilization of enzyme/NPs is thus obtained by a covalent reaction of quinone with amine moieties of the enzyme and gallol moieties of NPs (Figure 4.1b). The obtained nanohybrid coating can then be used for the electrochemical detection of the analyte (glucose or H₂O₂) using FcOH as a free mediator in

solution²³. This study aims to provide some general thoughts on the parameter driving the sensitivity of enzyme/NPs biosensors made by electrodeposition methods.

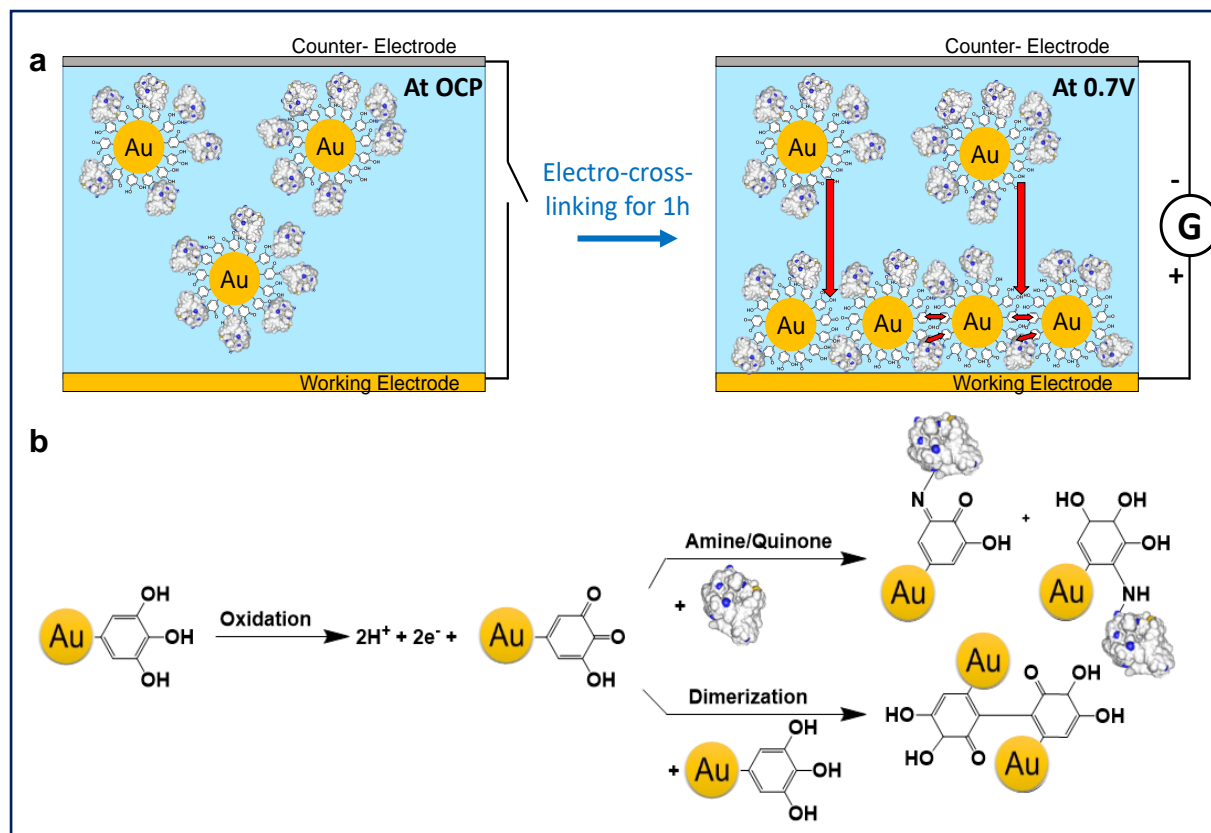


Figure 4.1. (a) Schematic representation of the electro-crosslinking of TA capped gold NPs and enzymes onto an electrode by application of an anodic potential. (b) Mechanism of the electro-cross-linking through electro-oxidation of gallol moieties of TA, present at the surface of NPs, into quinone. This oxidation is followed by the chemical reaction of quinone moieties with free amino moieties of the enzyme leading to imine and Michael adduct and with gallol moieties of TA (dimerization).

I. Nanoparticles Synthesis and characterization

NPs were prepared using an adapted protocol from Sivaraman et al.²⁴ based on the chemical reduction of gold salts by tannic acid (Figure 4.2a). The reaction proceeds in two stages: the production of “seeds” and their growth until the gold salt is consumed^{24,25}. To obtain different diameters, the reactivity of the gold salt solution was adjusted by controlling the pH with the addition of K_2CO_3 . The increase of the pH induces a change of the dominant species from $[AuCl_4]^-$ to $[AuCl_3(OH)]^-$, $[AuCl_2(OH)_2]^-$, $[AuCl(OH)_3]^-$ or $[Au(OH)_4]^-$ species.²⁶ By adjustment of the pH, NPs with a diameter of 11 ± 2 and 42 ± 6 nm were obtained and denoted NP11 and NP40, respectively.

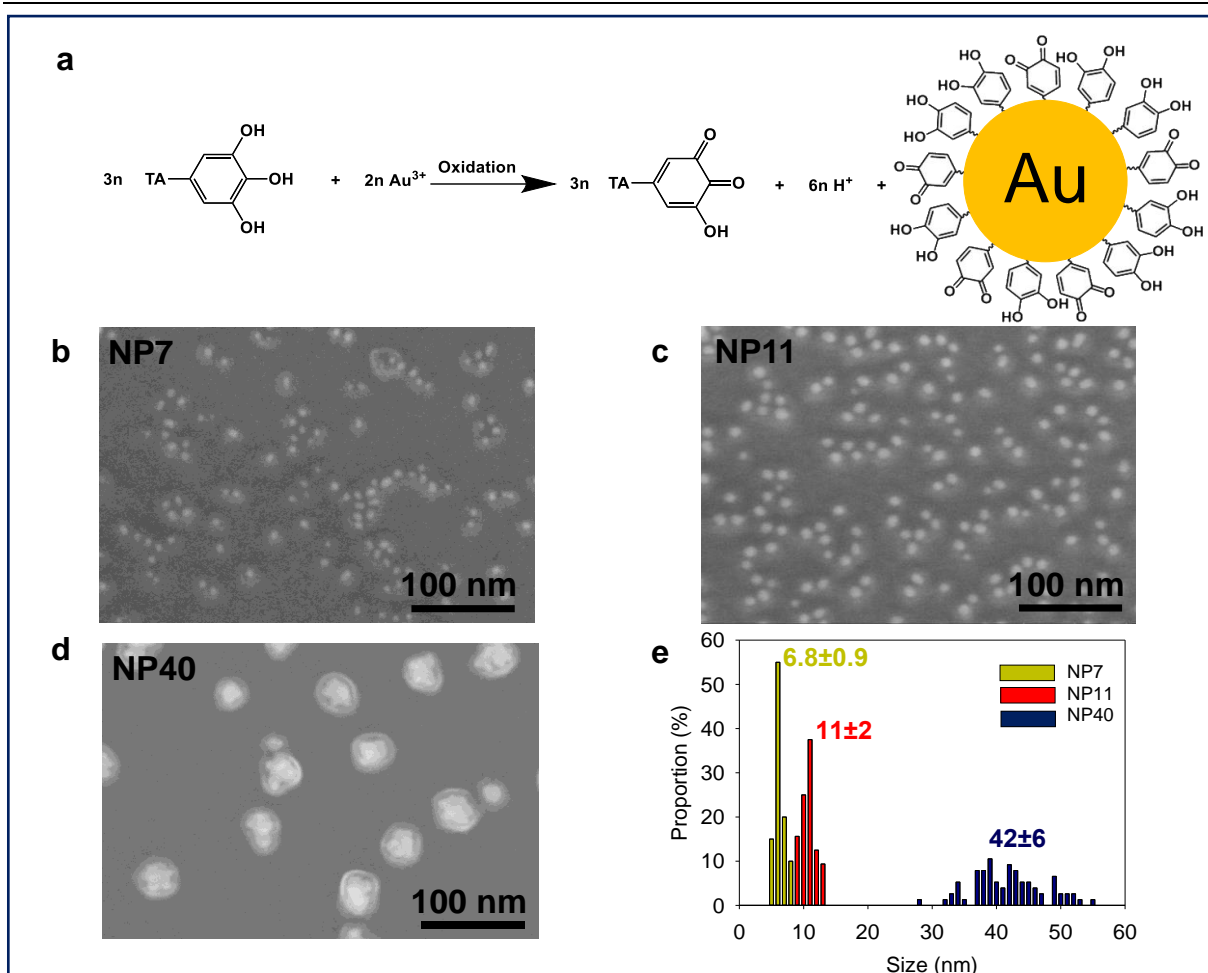


Figure 4.2: (a) Redox synthesis of tannic acid capped gold nanoparticles (NPs) based on TA and gold salt spontaneous reaction. SEM images of (b) NP7, (c) NP11, (d) NP40 and (e) their size (in nm) distribution retrieved from TEM size analysis.

To further decrease the NPs size, ferrocene boronate was added to the tannic acid solution as a fast reducing agent (higher seed density)²⁷, leading to NPs with a diameter of 6.8 ± 0.9 nm, named NP7. All NPs suspensions appeared in a non-aggregated form (Figure 4.2b-e). NP40 had a larger standard deviation as illustrated by its polydispersity. After their synthesis, the concentration of the NPs suspensions was determined (Table 4.1).

Table 4.1 : Centrifugation time and concentration of the NPs used in this study

Sample name	Size by TEM (nm)	Mean size by DLS (nm)	Centrifugation Time (min)	Concentration ($\times 10^{15}$ NPs·L ⁻¹)	Equivalent surface ($\times 10^{18}$ eq nm ² ·L ⁻¹)
NP7	7 ± 1	9 ± 2	120	45 ± 4	$\sim 7.1 \pm 0.9$
NP11	11 ± 2	12 ± 2	60	10 ± 1	$\sim 4.4 \pm 0.7$
NP40	42 ± 6	38 ± 7	15	0.2 ± 0.1	$\sim 1.5 \pm 0.4$

II. Gold Nanoparticles Electrodeposited Coatings

After the synthesis of the NPs, we first studied the electro-crosslinking of NPs based on the dimerization process (Figure 4.1b). A gold crystal was used as the working electrode and the electroactive surface area (EASA) was calculated depending on the NPs size, keeping the concentration in gold constant in the electrodeposition solution. To this aim, the NPs suspensions were centrifuged and concentrated ten times by addition of 5 mM FcOH/50 mM NaCl aqueous solution. The suspensions were stable in 50 mM NaCl with an average zeta potential of -60 ± 20 mV. The salt acts as a supporting electrolyte and FcOH as a catalytic mediator for tannic acid oxidation. Electrochemical quartz crystal microbalance (EC-QCM) was used to monitor *in situ* the evolution of the normalized frequency shift, proportional in a first approximation to the adsorbed mass. At the injection of the FcOH/NPs mixture, an increase in the normalized frequency shift was observed originating from the physisorption of NPs (Figure 4.3a). After stabilization of the signal, the application of 0.7 V induced an instantaneous increase of the frequency shift followed by a slower phase. After 1 h, the coating was rinsed with 50 mM NaCl solution leading to a small decrease in the signal. Since the deposited coating is rigid with $\left(\frac{\Delta D \times f_0}{\Delta f} < 1\right)$, the Sauerbrey equation was applied to calculate the deposited mass²⁸. The increase of the NPs size leads to the increase of the deposited mass (Figure 4.3b). The efficiency of the electrodeposition was then determined by the ratio between the number of NPs deposited and present in the electrodeposition solution in contact with the electrode (Fig 4.3b).

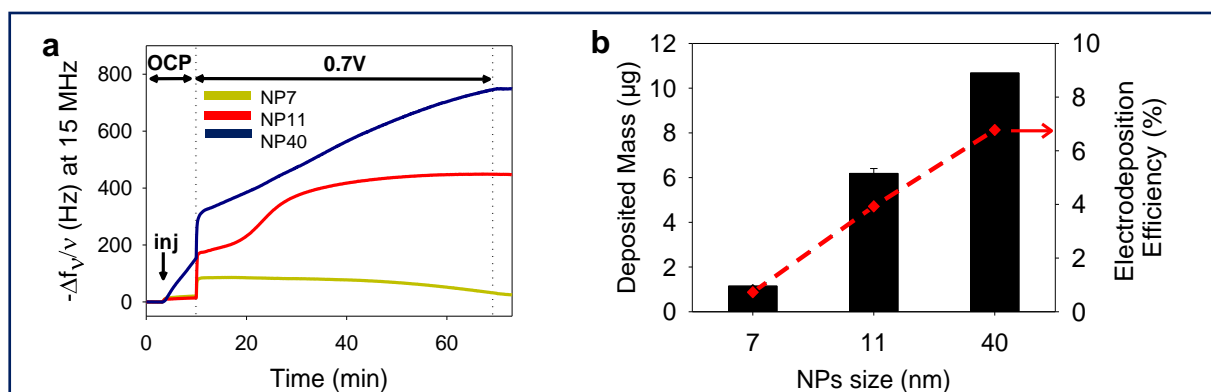


Figure 4.3: Electrodeposition of NPs with different sizes (a) Evolution of the normalized frequency shift of NPs/FcOH solutions, measured by EC-QCM, with NP7, NP11, and NP40, as a function of time during the application of 0.7 V. No electrical stimulus is applied during the OCP (open circuit potential). The arrow "inj" indicates the time of injection of the solution. (c) Deposited mass (μg), calculated from EC-QCM, using a geometric surface of 0.8 cm², and the corresponding electrodeposition efficiency (red diamond) for the different NP sizes.

The number of deposited NPs was estimated using the mass of a single NP, the deposited mass and the geometric surface of the electrode (0.8 cm^2 with a roughness $< 1 \text{ nm}$ ²⁹). The overall number of NPs of the electrodeposition solution in contact with the electrode (between the cathode and the anode) can also be roughly estimated by knowing the internal cell volume ($100 \text{ }\mu\text{L}$)²⁹. The efficiency of the electro-cross-linking was 0.7%, 3.9%, and 6.8% for NP7, NP11, and NP40, respectively. In comparison, an efficiency of $\sim 7\%$ is reached for the electrophoretic deposition of NP (size from 5 to 8 nm) in toluene at 100 V for 1 h³⁰. Using a similar size of NPs, the electro-cross-linking process is less efficient than EPD³¹ but with two main advantages: it is performed in mild conditions (aqueous NaCl 50 mM, pH 7, 0.7 V) and allows the formation of covalent bonds leading to more robust coatings.

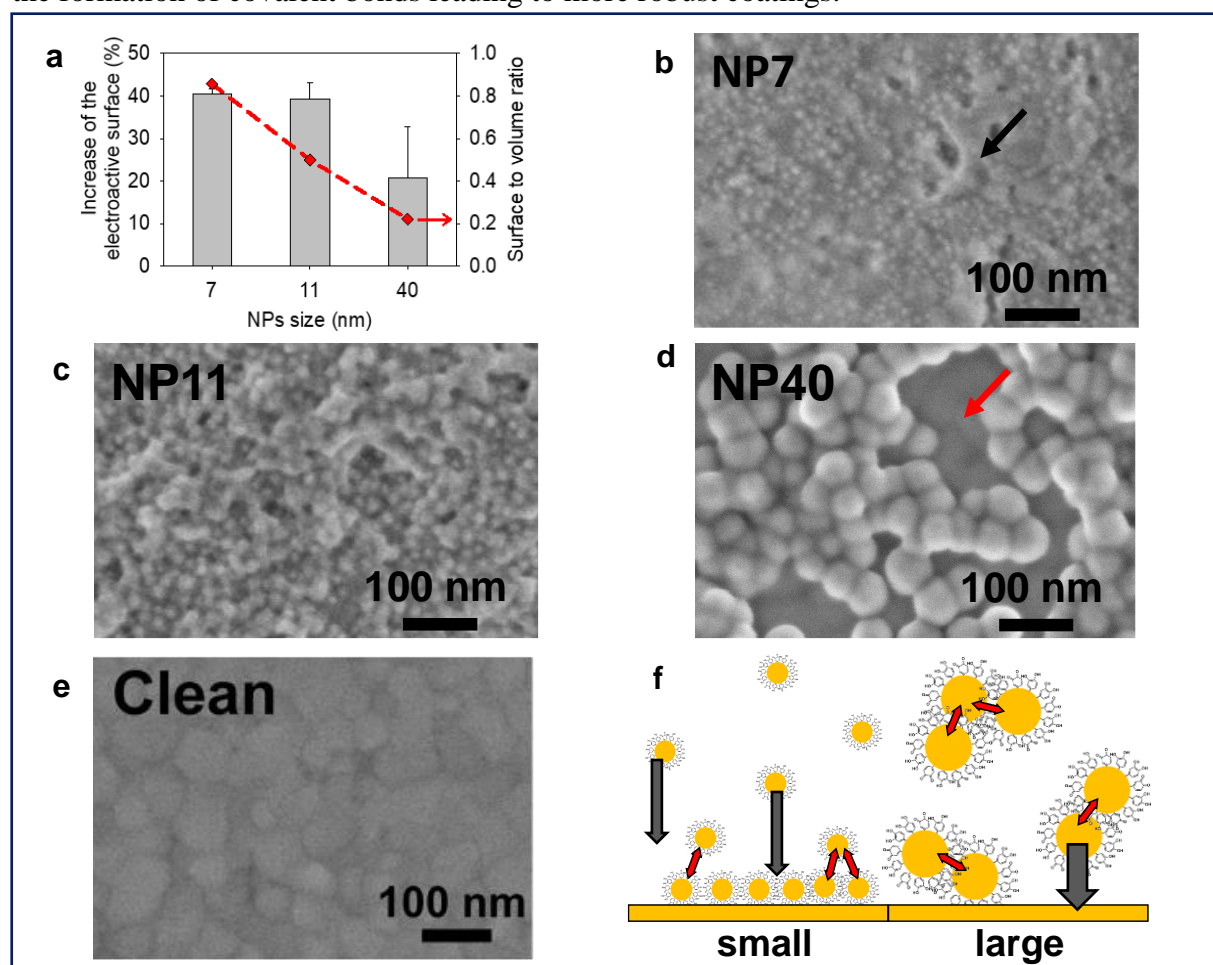


Figure 4.4: Electrodeposition of NPs with different sizes: (a) relative increase of the electroactive surface area (EASA) and surface to volume ratio of NPs (red diamond) as a function of NP size and (b) SEM micrographs of the obtained coatings using (b) NP7, (c) NP11 and (d) NP40. Red arrows indicate the presence of an uncoated area where the underlying electrode is visible and the black arrow the presence of an organic area. (e) Illustration of the sample surface for a clean coating and (f) the difference in the deposition of isolated or flocculated NPs.

The EASA of the electrode was determined before and after the electrodeposition of NPs as it is involved in the electron exchange of freely diffusing molecules (Figure 4.4a). In agreement with the surface to volume ratio of NPs, an increase of 40% of the EASA is obtained after the electrodeposition of NP7 and NP11 and only 20% with lower reproducibility with the electrodeposited NP40. SEM micrographs of the electrodeposited NPs coatings showed a full and homogeneous coverage of the electrode for NP7 and NP11 with few organic areas (Figure 4.4b-e). On the contrary, NP40 gave heterogeneous coatings with the presence of small aggregates, probably linked to their flocculation (Figure 4.4f).³² This could explain the low reproducibility of these coatings. For comparison, the SEM image of a bare gold QCM crystal, used as a working electrode, is shown in Figure 4.4e.

III. Sensitivity optimization of enzyme/NPs coatings

After the study of electrodeposited NPs coatings, the electrodeposition of enzyme/NPs was optimized in terms of sensitivity using two enzymes of different sizes, Horseradish peroxidase (HRP) and glucose oxidase (GOx). The biosensor sensitivity is one of the most important parameter. It corresponds to the proportionality coefficient between the output current value collected at the electrode and the initial substrate concentration in solution. The higher the sensitivity, the better the resolution of the biosensor (*i.e.* its ability to separate close concentrations). In this study, the sensitivities of GOx/NPs and HRP/NPs based coatings were measured by chronoamperometry with successive addition of their substrates (at 0.25 V with glucose and at 0.19 V with H₂O₂, respectively) in the presence of FcOH as mediator. This electrocatalytic signals of GOx/NPs towards glucose and HRP/NPs towards H₂O₂ were proven by cyclic voltammetry (Figure 4.5a-b). In the case of GOx/NPs, a total disappearance of the ferrocene reduction peak at 0.19 V and the overexpression of the oxidation peak at 0.25 V were observed by increasing the concentration in glucose. In the case of HRP/NPs, a total disappearance of the ferrocene oxidation peak at 0.25 V and the overexpression of the reduction peak at 0.19 V were observed increasing the concentration in H₂O₂.

The electrodeposition of enzyme/NPs was performed in the presence of 5 mM FcOH/50 mM NaCl for 1 h by applying a potential of 0.7 V (vs Ag/AgCl). The choice of electrodeposition time was made according to a preliminary study on the GOx/AuNPs system by EC-QCM (Figure 4.5c). The mass adsorbed and the sensitivity of GOx/AuNPs were smaller with shorter

electrodeposition times (30 min). At longer duration (2 h), the mass adsorbed increased but lower sensitivity was observed. The bioconjugates layers too far from the electrode can no longer communicate with the working electrode. These latter active layers rather tend to limit the diffusion of the mediator and the enzyme substrate in the film which lead to a decrease of the overall film sensitivity. The electro-cross-linking of GOx/NPs and HRP/NPs solutions were studied using the series of synthesized NPs, keeping the gold concentration constant, and varying the enzyme/NP molar ratio for each NPs size. To this aim, the NPs suspensions were centrifuged and concentrated ten times by addition of the adequate amount of enzyme (GOx or HRP) prepared in 5 mM FcOH/50 mM NaCl.

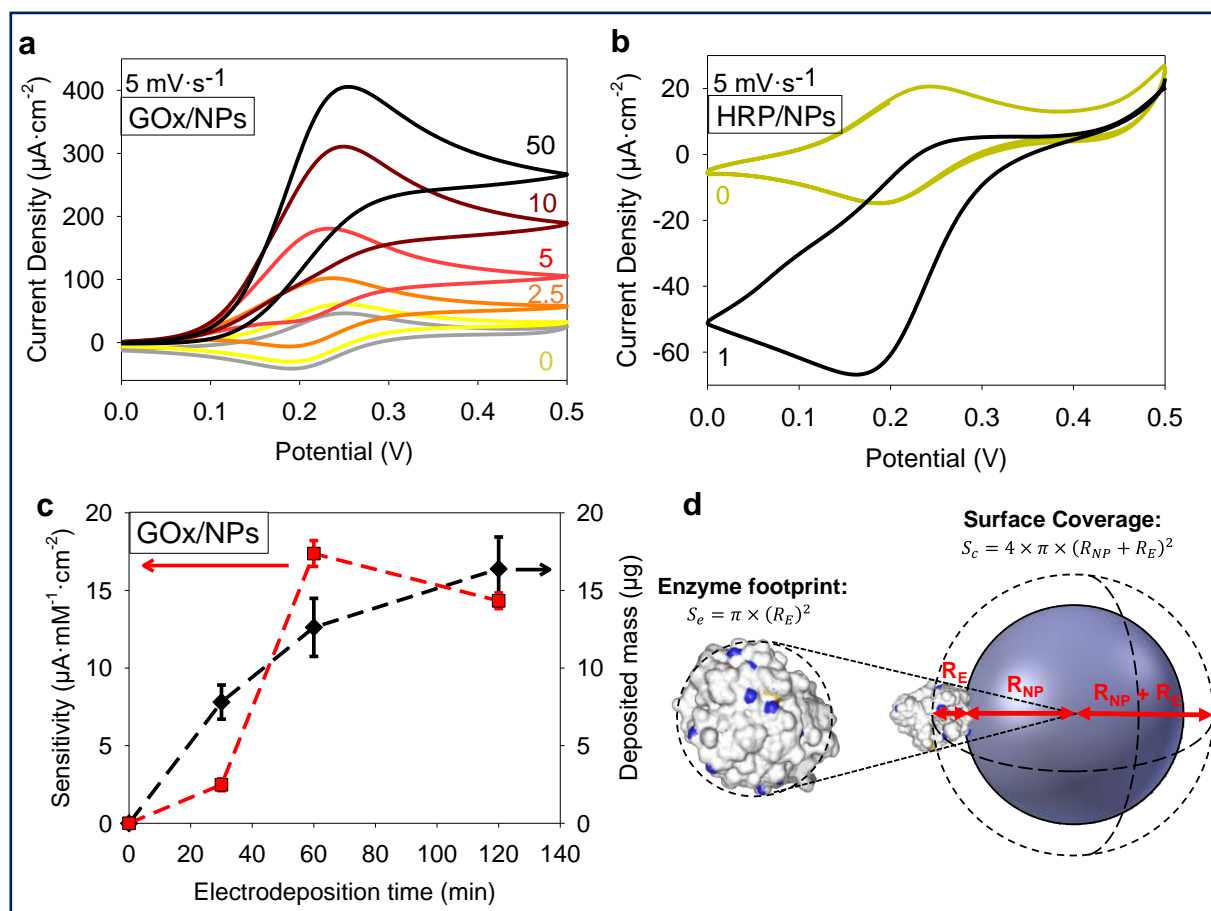


Figure 4.5: (a) Cyclic voltammogram at 5 mV·s⁻¹ of HRP/NP11 film built at $R/R_{th} = 1$ in the absence (yellow) and in the presence of 1 mM H₂O₂. H₂O₂ was dissolved in 100 μM FcOH / PBS 10 mM pH 7 solution. (b) Cyclic voltammogram at 5 mV·s⁻¹ of GOx/NP11 film built at $R/R_{th} = 1$ in the absence (yellow) and in the presence of different concentration of glucose from 1 to 50 mM. Glucose was dissolved in 500 μM FcOH / PBS 10 mM pH7 solution. (c) Evolution of the deposited mass (black symbol) and sensitivity (red symbol) of GOx@AuNPs with the electrodeposition time performed at +0.7 V. (d) Illustration of enzyme footprint and the estimation of the surface coverage.

To be able to compare the deposited mass and sensitivity of the different coatings, the mixture ratio R/R_{th} was introduced with R , the enzyme/NPs ratio of the electrodeposition solution, and R_{th} , the theoretical enzyme/NPs molar ratio required to obtain an enzyme monolayer at the surface of NPs. R_{th} was defined as the number of small non-deformable enzyme spheres that can be stacked around a single nanoparticle (Equation 4.1 and figure 4.5d).

$$R_{th} = \frac{4 \times (R_{NP} + R_{ENZ})^2}{(R_{ENZ})^2} \quad (\text{Equation 4.1})$$

Afterward, the sensitivity of the coatings was determined by chronoamperometry, *i.e.* by application of 0.25 V for GOx/NPs coatings and 0.19 V for HRP/NPs coatings, and measuring the current density, at different concentrations in glucose of H_2O_2 in the presence of FcOH. Ferrocene methanol is therefore not only used to initiate electroreticulation but also to enable the measurement of the electrocatalytic activity of the immobilized enzymes. Then, the coating sensitivity was plotted as a function of the ratio R/R_{th} (Figure 4.6a). For all tested NPs sizes, the optimal values in sensitivity were obtained at the mixture ratios R/R_{th} close to 1, where R , the value of the enzyme/NPs molar ratio, is close to the theoretical monolayer. The adsorbed mass followed the same behavior with optimal values at mixture ratios (data not shown). At low GOx/NPs molar ratio ($R < R_{th}$), uncoated and poorly coated NPs were electrodeposited leading to a low quantity of deposited enzyme and thus low enzymatic activity. The drastic decrease in sensitivity observed for a high GOx/NPs molar ratio ($R > R_{th}$) was concomitant to the decrease in mass adsorbed. The dense corona of enzymes onto the NPs prevents probably the electro-crosslinking process involving gallol moieties of TA. For a given mixture ratio, the sensitivity of the coatings present also an optimum value depending on the NP size with the following decreasing order $NP11 > NP7 > NP40$. The highest sensitivity, $17.5 \pm 0.4 \mu A \cdot mM^{-1} \cdot cm^{-2}$, is obtained for the GOx/NP11 coating at a mixture ratio of 27 ($R/R_{th} = 0.91$) and with an adsorbed mass of 10 μg obtained from the Sauerbrey equation.

A similar study was carried out for HRP/NPs coatings where the sensitivity toward H_2O_2 was evaluated by chronoamperometry at different concentrations in the presence of FcOH (Figure 4.6b). Different controls were carried out to validate that electrocatalytic signal observed in chronoamperometry at 0.19 V comes from the activity of HRP (Figure 4.6c-d). The sensitivity of NP11 film towards different H_2O_2 concentrations was studied and no electrocatalytic signal was obtained at 0.19V (Figure 4.6c). Indeed, the electro reduction of H_2O_2 at the electrode is observed at a lower potential such as -0.5 V. Also, a control with different initial concentration of HRP has proven the need of this enzyme to observe the electrocatalytic signal of H_2O_2 reduction (Figure 4.6d).

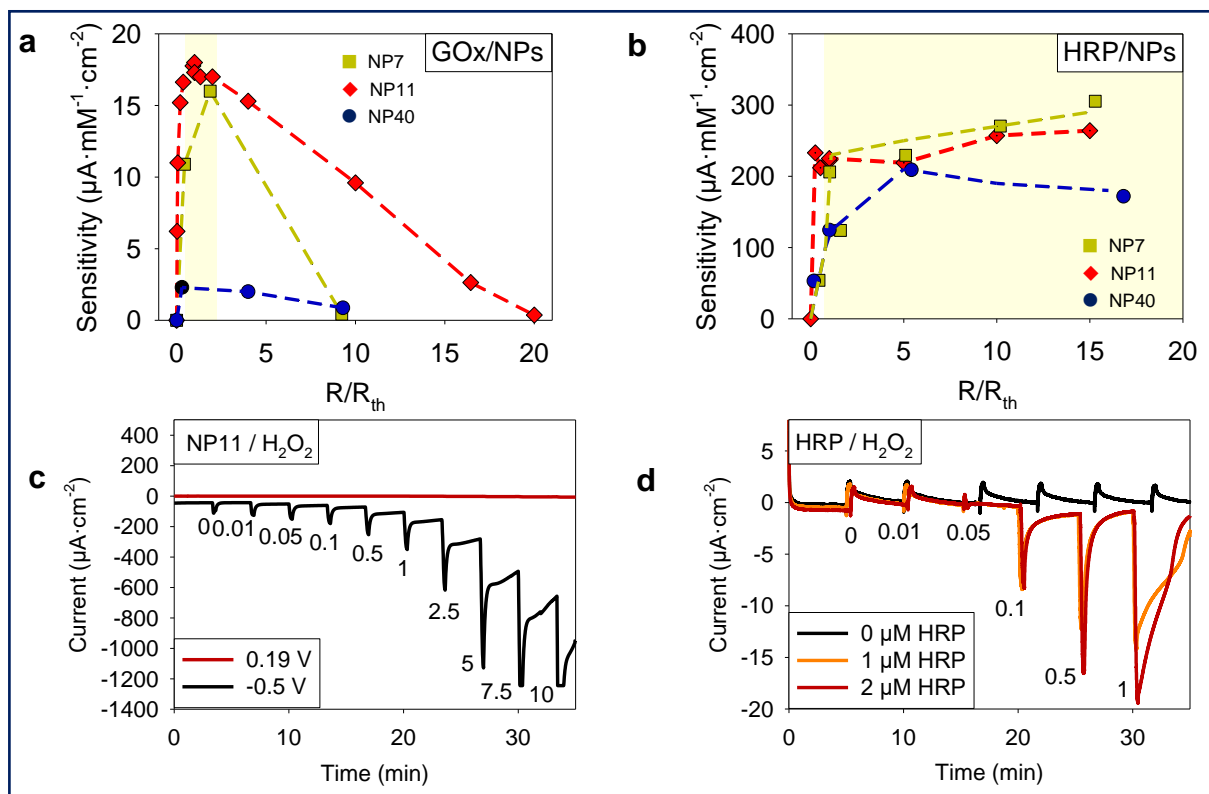


Figure 4.6: Characterization of GOx/NPs and HRP/NPs coatings. Evolution of the sensitivity of (a) GOx/NPs and (b) HRP/NPs coatings with NP7, NP11, and NP40 as a function of the mixture ratio, R/R_{th} , with R , the enzyme/NPs ratio of the electrodeposition solution and R_{th} , the theoretical enzyme/NPs molar ratio to obtain an enzyme monolayer at the surface of NPs (dashed line as a guide to the eye). (c) Chronoamperogram in the presence of H_2O_2 at 0.19 and -0.5 V on a NP11 film prepared from NP11/FcOH solution. (d) Chronoamperogram at 0.19 V in presence of H_2O_2 and HRP at various concentration on a clean gold crystal. H_2O_2 was dissolved in 100 μM FcOH / PBS 10 mM pH7 solution.

Contrary to the previous system, the sensitivity of HRP/NP films increased linearly with the R/R_{th} mixture ratio until a value close to 1 followed by a slower increase for small NPs (NP7 and NP11) or a slight decrease for NP40 (Figure 4.6b). The adsorbed mass follows the same trend reaching almost a plateau at the R/R_{th} value between 1 and 2 (data not shown). Thus keeping the NPs concentration constant (Table 4.1), the increase in HRP concentration in the electrodeposition solution did not impact the electro-crosslinking process as observed for GOx. Even in the presence of a large excess of HRP, gallol moieties sites on NPs seem to be accessible to react covalently, after oxidation, with others NPs or enzymes present in the solution. It is likely that for small NPs free HRP are also physically incorporated in the coating leading to the

small increase in sensitivity for high values of R/R_{th} (NP7 and NP11). Similar sensitivities were obtained independently of the NP size at the optimal ratio ($R/R_{th} \sim 1$). The highest sensitivity, $305 \mu\text{A} \cdot \text{mM}^{-1} \cdot \text{cm}^{-2}$, was obtained for HRP/NP7 coating at $R/R_{th} \sim 15$. Interestingly, an increase in the linear range was observed for HRP/NPs system when the R/R_{th} mixture ratio was increased shifting the highest detectable H_2O_2 concentration from $250 \mu\text{M}$ at $R/R_{th} \sim 0.2$ to $750 \mu\text{M}$ at $R/R_{th} \sim 10$ (Figure 4.7a). These results suggest a higher amount of active enzyme included in the HRP/NPs coating when the concentration in the enzyme is increased.

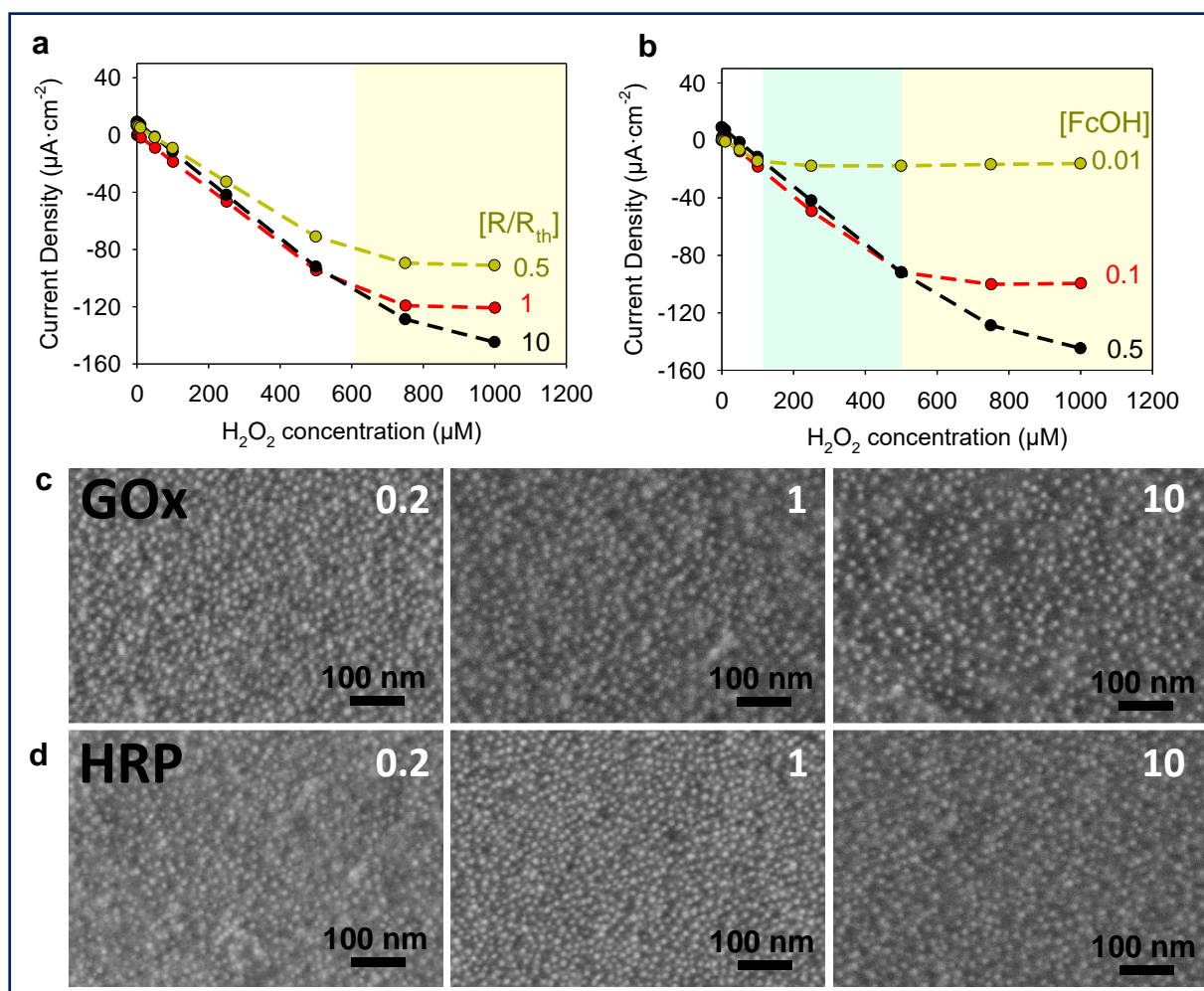


Figure 4.7: Current densities as function of H_2O_2 concentration measured for HRP/NP11 coatings: (a) built at different R/R_{th} mixture ratio (0.5, 1, and 10) using 0.5 mM FcOH as mediator and (b) built at $R/R_{th} = 10$ using 0.01, 0.1 and 0.5 mM FcOH as mediator. SEM micrographs, with secondary electrons detector of (c) GOx/NP11 and (d) HRP/NP11 coatings obtained at different enzyme/NP ratios, the number of each corresponds to the R/R_{th} value.

Moreover, the sensitivity plot at the highest tested ratio ($R/R_{th} \sim 10$) shows that FcOH concentration significantly modifies the linear range (Figure 4.7b). FcOH diffusion is probably the limiting kinetic of the overall system in the tested range for FcOH and H_2O_2 concentrations. It suggests that the HRP catalytic reaction kinetic is very fast compared to the FcOH mediated electron transfer. Figure 4.7c-d depicts the SEM micrographs of GOx/NP11 and HRP/NP11 coatings obtained with increasing the R/R_{th} mixture ratio showing an increase in organic materials content due to the enzymes. It can be concluded that fine-tuning both NPs size and enzyme/NP molar ratio is required to achieve an optimal sensitivity.

IV. Enzyme/NPs bioconjugate characterization

To get further insight into the differences found between GOx/NPs and HRP/NPs coatings, we studied the colloidal state of the enzyme/NPs bioconjugates using NP7, NP11, and NP40. It is known that full coverage of NPs by proteins prevents their aggregation in the presence of salt. To determine the optimal enzyme/NPs molar ratio for full coverage of the NPs, a flocculation assay was performed at different molar ratios with the addition of 1 M NaCl²². The aggregation of gold NPs leads to a color change from red/purple to blue of the suspension (Figure 4.8a). Thus after the addition of 1 M NaCl, the maximum absorption wavelength (λ_{max}) of enzyme/NPs suspensions was measured by UV-Visible spectroscopy depending on the mixture ratio, R/R_{th} . Figure 4.8b-c shows the change in λ_{max} (%), i.e. the relative shift in wavelength/ $\lambda_{max}(NP)$ at different mixture ratios. In the absence of enzymes ($R/R_{th} = 0$), NP7 and NP40 suspensions presented the higher shift in λ_{max} , with 30% and 40% change corresponding respectively to 160 and 200 nm shift. On the contrary, NP11 suspensions appeared to be more stable with only a λ_{max} shift of 5% (24 nm).

In the presence of GOx (160 kDa), the addition of salt to the NPs suspension induced a smaller shift of the λ_{max} with a threshold value R/R_{th} where no aggregation is observed for all studied NPs. In the case of NP7 and NP11, this threshold value is equal to 1 where a monolayer of GOx is formed on the surface of NPs. In comparison, the aggregation of NP40 is prevented for $R/R_{th} = 2$, suggesting the adsorption of more than one layer of the enzyme. A consequent change of GOx conformation could occur on large NPs leading to a larger footprint of the enzyme on a flat surface³³ than on small NPs, with a high curvature²². Upon adsorption, the enzymes could also unfold leading to the formation of two layers. In the presence of HRP (44 kDa), the NPs aggregation is fully prevented for larger values of R/R_{th} , i.e. 12 for NP7, and 9

for NP11. We can notice that partial prevention of the aggregation is observed for lower R/R_{th} values, indicating the effective adsorption of some HRP at the surface of NPs. In the case of NP40, the aggregation was observed for all the tested values of R/R_{th} . Finally, the enzyme/NPs bioconjugates were observed at $R/R_{th} = 10$ by TEM after uranyl acetate negative staining (Figure 4.8d). In comparison to NP11, GOx/NP11 bioconjugates presented a light grey corona of 5 nm due to the attachment of the protein to the NPs as previously reported²³. In the case of HRP/NP11, no light grey corona can be observed suggesting either a non-homogenous HRP coating or a thin unfolded HRP layer. Indeed, no close contact between the NPs was observed as for native NP11 (Figure 4.8d).

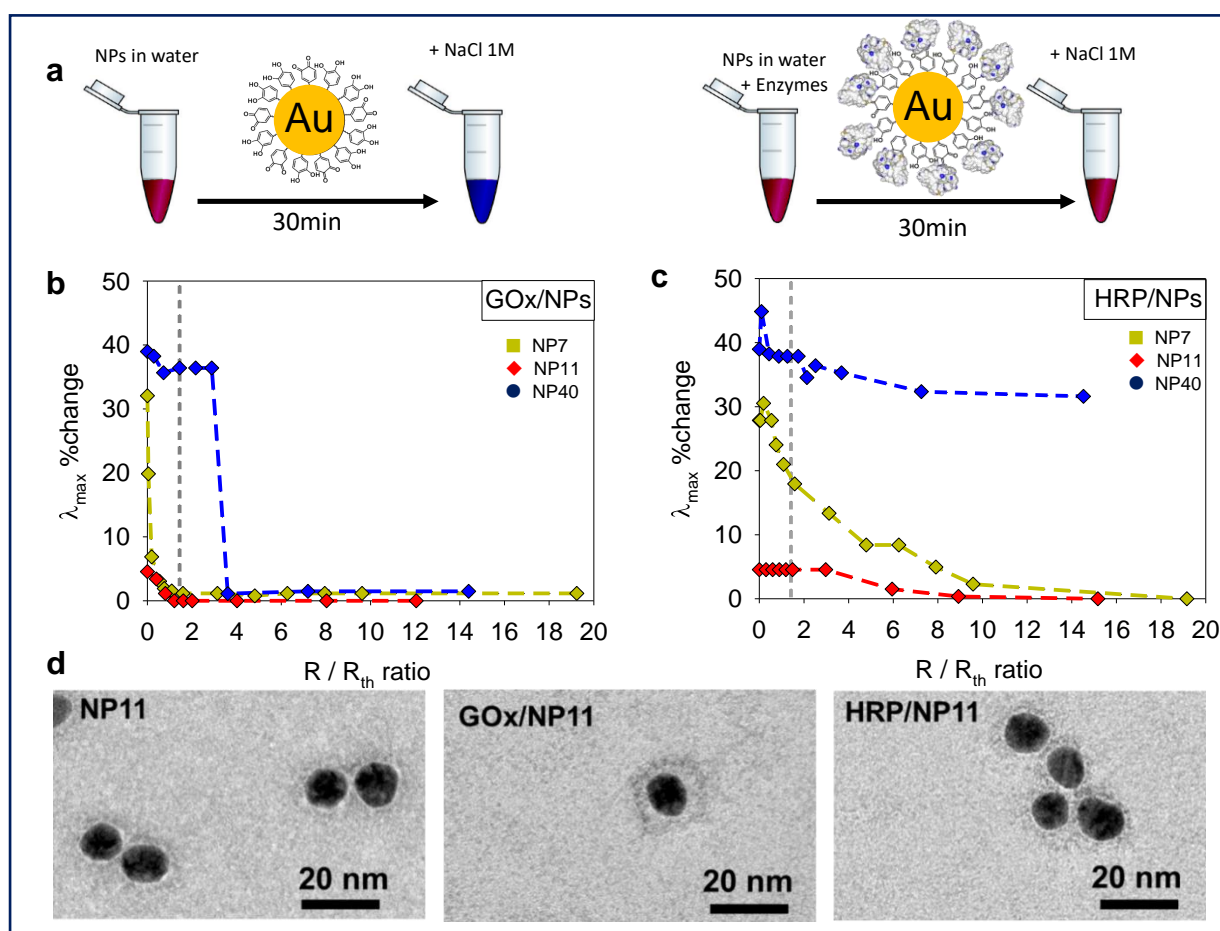


Figure 4.8: (a) Illustration of the gold NPs flocculation assay performed at 1 M NaCl in the absence and the presence of the enzyme. (b-c) Evolution of the relative change in λ_{max} (i.e. the shift in wavelength/ $\lambda_{max}(NP)$) as a function of the mixture ratio, R/R_{th} of (b) the GOx/NPs suspensions, and (c) the HRP/NPs suspensions with NP7, NP11, and NP40. (d) TEM images of NP11, GOx/NP11 and HRP/NP11 bioconjugates, both obtained at $R/R_{th} = 10$ after uranyl acetate negative staining.

Further studies were then performed to evaluate the number of enzymes per NPs and their activity in comparison to the enzyme solution. These assays were performed for GOx/NP11 and HRP/NP11 which gave the best sensitivities for the electrodeposited coating. After the addition of the enzymes solution to NP11 suspension at a given R (enzyme/NPs molar ratio) for 30 min, the mixture was centrifuged to separate the enzyme/NPs bioconjugates from the unbound enzymes (Figure 4.9a). The number of enzymes per NP was determined by the Bradford test and the enzymatic activity using a classical colorimetric test. Figure 4.9b-c shows the results obtained in number of enzymes per NP with the enzymatic activity in the equivalent of the enzyme activity in solution. For both enzymes, the number of enzymes per NPs increased with the enzyme/NPs (R/R_{th}) molar ratio reaching a plateau of around 20 enzymes per NPs for GOx at $R/R_{th} = 1$, close to the theoretical monolayer ratio value. Regarding the enzymatic activity, the equivalent number of GOx continuously increased until 10 up to $R/R_{th} = 10$. It is interesting to cross-check this information with the final sensitivity of the biosensor obtained at the high R/R_{th} ratio (Figure 4.6a). Indeed, the free bioconjugates in solution keep a constant enzymatic activity at high ratio ($R/R_{th}=10$), this corroborates the fact that at high ratio the sensitivity loss of the GOx/NPs coating does not come from the deposition of non-active enzymes but rather from the impossibility to electrodeposit these bioconjugates.

At a low mixture ratio ($R/R_{th} \leq 2$), mainly denaturated GOx adsorbed on the NP11 leading to a weak enzymatic activity (10% of adsorbed GOx are active). Upon adsorption, the enzymes are probably unfolded due to the strong interactions with TA, at the surface of NPs. Interacting strongly through hydrogen bonds and hydrophobic interactions, TA is known to inhibit the catalytic activity of enzymes by modification of their conformation or substrate deprivation^{34,35}. At higher mixture ratio $R/R_{th} = 10$, almost 50% of adsorbed GOx is enzymatically active. More enzymes interact with the surface leading to fewer interactions with each enzyme and less unfolding. Knowing that GOx has an ellipsoidal shape ($6.0 \times 5.2 \times 7.7 \text{ nm}^3$), the adsorption of the enzyme could shift from the long side to the short side with the increase in the enzyme/NPs ratio²².

In the case of HRP, the number of enzymes per NPs and the enzymatic activity increased with the mixture ratio, following the same behavior. The activity of HRP was comprised between 50 and 100%. The number of enzymes per NP reached a plateau at $R/R_{th} = 2$ with 100% of HRP active. The same trend was observed in the case of HRP/NPs coating (Figure 4.6b) with an increase of the enzymatic activity until $R/R_{th} \sim 1-2$ followed by a plateau. This confirms the adsorption of more than one layer of HRP on NP11.

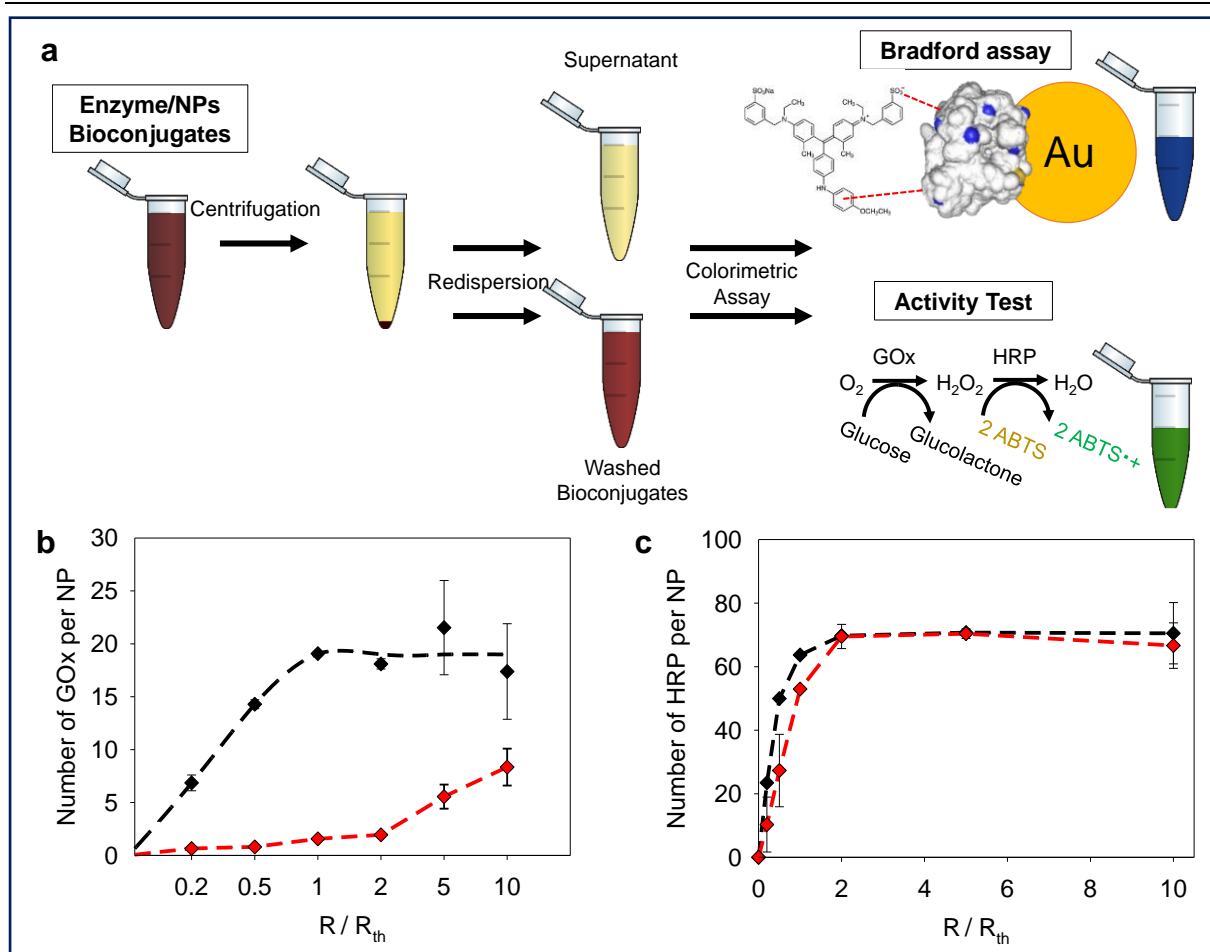


Figure 4.9: (a) Illustration of the Bradford and activity assays performed on enzyme/NP bioconjugates. Number of (b) GOx and (c) HRP per NP11 at different R/R_{th} mixture ratios, determined by Bradford (black curve) and activity assay (red curve), taking as a reference the activity of the enzyme-free in solution.

To assess the secondary structure of the enzymes adsorbed on NPs, FTIR spectra of the GOx/NPs and HRP/NPs bioconjugates were recorded in deuterium oxide and compared to GOx and HRP in solution, respectively (Figure 4.10). Upon adsorption on NPs, the secondary structure of GOx is strongly modified with a shift of the maximum peak from 1650 to 1646 cm^{-1} and a peakbroadening towards lower frequency. The loss in activity of GOx, through thermal denaturation, was shown to be linked to the loss of α -helix and increase in the unordered structure, *i.e.* a shift towards lower frequency³⁶. On the contrary, adsorbed HRP enzymes have similar secondary structure to HRP in solution. The maximum peaks are at the same value and a narrower shape. Structural studies of HRP showed that the amount of α -helix are important for the activity of the enzyme³⁷. Indeed, the inactivation of HRP is usually obtained by a strong decrease of alpha-helix structures³⁸. Upon adsorption, the tertiary structure of HRP is probably modified without affecting drastically the secondary structure and thus its activity.

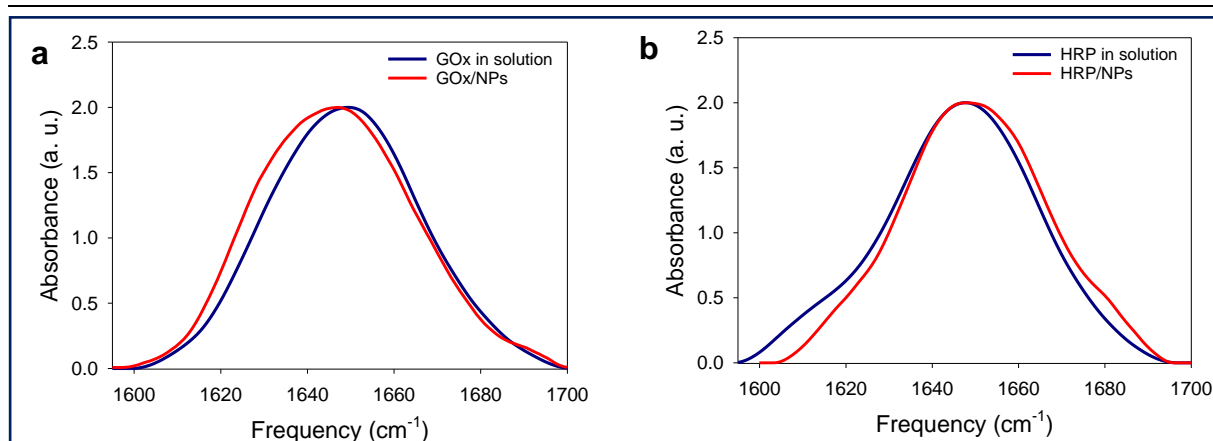


Figure 4.10: FTIR normalized spectra, amide I band region, (a) of GOx solution (10 mg/mL) and GOx/NPs suspension and (b) of HRP solution (10 mg/mL) and HRP/NPs suspension, prepared in D_2O .

To summarize independently of the NPs size, the electro-cross-linked GOx/NPs coatings present an optimal value of the sensitivity towards glucose when R , the enzyme/NPs molar ratio, is close to the theoretical R_{th} of a GOx monolayer ($R/R_{th} = 1$). Despite the loss of enzymatic activity caused by conformational changes, high sensitivity of the GOx/NPs coating was obtained when a monolayer of GOx was formed on NPs. At high values of R/R_{th} above 1, adsorbed GOx on NPs had a better enzymatic activity but form a very dense monolayer preventing efficient electrodeposition of the coating leading to a decrease of the sensitivity. The gallol moieties on the surface of NPs are probably not accessible to obtain the cross-linking with other coated NPs. In the case of HRP/NPs coatings, the sensitivity increased linearly with R/R_{th} until a value close to 1 - 2 followed by almost a plateau for all tested NPs sizes. Contrary to GOx, unfolded HRP can be adsorbed on NPs until the quantity of two layers keeping its enzymatic activity. HRP layers onto NPs could not be observed by TEM suggesting the formation of a thin layer of HRP. In this case, the electrodeposition of HRP/NPs bioconjugates is efficient even at a high R/R_{th} mixture ratio. The gallol moieties of NPs seem to be accessible to obtain the cross-linking.

Conclusion

The sensitivity of electro-crosslinked GOx/NPs and HRP/NPs biosensors was optimized by adjusting the NPs size and the enzyme/NP molar ratio of the electrodeposition solution. Contrary to HRP/NPs biosensors, the NPs size has a strong effect on the sensitivity of GOx/NPs with an optimal size of 11 nm. In both cases, the increase in enzyme/NPs molar ratio leads to an increase in the sensitivity until a threshold close to the theoretical value of an enzyme

monolayer. Above this threshold value, the sensitivity of the GOx/NPs coatings towards glucose decreased contrary to the HRP/NPs coatings that reached almost a plateau. A comprehensive evaluation of the colloidal state of the enzyme/NPs bioconjugates allows us to explain the main difference between the two enzymes. At high enzyme/NPs ratios, a too dense layer of GOx covers the surface of NPs preventing efficient electrodeposition of the coating leading to a decrease in its sensitivity. In the case of HRP, two layers of active enzymes can be adsorbed onto NPs. The HRP layer, not visible by TEM, seems to be thin and allowed access to gallol moieties ensuring efficient electrodeposition at a high enzyme/NPs ratio. This study opens the route toward the rational design of nanohybrid biosensors taking into account the NPs and the enzyme sizes.

References

- (1) Willner, I.; Basnar, B.; Willner, B. Nanoparticle–Enzyme Hybrid Systems for Nanobiotechnology. *FEBS J.* **2007**, *274* (2), 302–309.
- (2) Zhu, D.; Liu, B.; Wei, G. Two-Dimensional Material-Based Colorimetric Biosensors: A Review. *Biosens. 2021, Vol. 11, Page 259* **2021**, *11* (8), 259.
- (3) Yang, Z.; Zhang, C.; Zhang, J.; Huang, L. Development of Magnetic Single-Enzyme Nanoparticles as Electrochemical Sensor for Glucose Determination. *Electrochim. Acta* **2013**, *111*, 25–30.
- (4) Chen, J.; Jiang, Z.; Ackerman, J. D.; Yazdani, M.; Hou, S.; Nugen, S. R.; Rotello, V. M. Electrochemical Nanoparticle–Enzyme Sensors for Screening Bacterial Contamination in Drinking Water. *Analyst* **2015**, *140* (15), 4991–4996.
- (5) Lundqvist, M.; Sethson, I.; Jonsson, B. H. Protein Adsorption onto Silica Nanoparticles: Conformational Changes Depend on the Particles' Curvature and the Protein Stability. *Langmuir* **2004**, *20* (24), 10639–10647.
- (6) Gagner, J. E.; Lopez, M. D.; Dordick, J. S.; Siegel, R. W. Effect of Gold Nanoparticle Morphology on Adsorbed Protein Structure and Function. *Biomaterials* **2011**, *32* (29), 7241–7252.
- (7) Gagner, J. E.; Qian, X.; Lopez, M. M.; Dordick, J. S.; Siegel, R. W. Effect of Gold Nanoparticle Structure on the Conformation and Function of Adsorbed Proteins. *Biomaterials* **2012**, *33* (33), 8503–8516.
- (8) Tellechea, E.; Wilson, K. J.; Bravo, E.; Hamad-Schifferli, K. Engineering the Interface

- between Glucose Oxidase and Nanoparticles. *Langmuir* **2012**, 28 (11), 5190–5200.
- (9) Wu, H.; Liu, Y.; Li, M.; Chong, Y.; Zeng, M.; Lo, Y. M.; Yin, J. J. Size-Dependent Tuning of Horseradish Peroxidase Bioreactivity by Gold Nanoparticles. *Nanoscale* **2015**, 7 (10), 4505–4513.
 - (10) Aubin-Tam, M. E.; Zhou, H.; Hamad-Schifferli, K. Structure of Cytochrome c at the Interface with Magnetic CoFe₂O₄nanoparticles. *Soft Matter* **2008**, 4 (3), 554–559.
 - (11) Tadepalli, S.; Wang, Z.; Slocik, J.; Naik, R. R.; Singamaneni, S. Effect of Size and Curvature on the Enzyme Activity of Bionanoconjugates. *Nanoscale* **2017**, 9 (40), 15666–15672.
 - (12) Breger, J. C.; Oh, E.; Susumu, K.; Klein, W. P.; Walper, S. A.; Ancona, M. G.; Medintz, I. L. Nanoparticle Size Influences Localized Enzymatic Enhancement - A Case Study with Phosphotriesterase. *Bioconjug. Chem.* **2019**, 30 (7), 2060–2074.
 - (13) Marichal, L.; Degrouard, J.; Gatin, A.; Raffray, N.; Aude, J. C.; Boulard, Y.; Combet, S.; Cousin, F.; Hourdez, S.; Mary, J.; Renault, J. P.; Pin, S. From Protein Corona to Colloidal Self-Assembly: The Importance of Protein Size in Protein-Nanoparticle Interactions. *Langmuir* **2020**, 36 (28), 8218–8230.
 - (14) Roe, C. De; Courtoy, P. J.; Baudhuin, P. A Model of Protein-Colloidal Gold Interactions. *J. Histochem. & Cytochem.* **1987**, 35 (11), 1191–1198.
 - (15) Suzuki, M.; Murata, K.; Nakamura, N.; Ohno, H. The Effect of Particle Size on the Direct Electron Transfer Reactions of Metalloproteins Using Au Nanoparticle-Modified Electrodes. *Electrochemistry* **2012**, 80 (5), 337–339.
 - (16) Lata, J. P.; Gao, L.; Mukai, C.; Cohen, R.; Nelson, J. L.; Anguish, L.; Coonrod, S.; Travis, A. J. Effects of Nanoparticle Size on Multilayer Formation and Kinetics of Tethered Enzymes. *Bioconjug. Chem.* **2015**, 26 (9), 1931–1938.
 - (17) Park, H. J.; McConnell, J. T.; Boddohi, S.; Kipper, M. J.; Johnson, P. A. Synthesis and Characterization of Enzyme–Magnetic Nanoparticle Complexes: Effect of Size on Activity and Recovery. *Colloids Surfaces B Biointerfaces* **2011**, 83 (2), 198–203.
 - (18) Talbert, J. N.; Goddard, J. M. Influence of Nanoparticle Diameter on Conjugated Enzyme Activity. *Food Bioprod. Process.* **2013**, 91 (4), 693–699.
 - (19) Vertegel, A. A.; Siegel, R. W.; Dordick, J. S. Silica Nanoparticle Size Influences the Structure and Enzymatic Activity of Adsorbed Lysozyme. *Langmuir* **2004**, 20 (16), 6800–6807.
 - (20) German, N.; Ramanaviciene, A.; Voronovic, J.; Ramanavicius, A. Glucose Biosensor

- Based on Graphite Electrodes Modified with Glucose Oxidase and Colloidal Gold Nanoparticles. *Microchim. Acta* 2010 1683 **2010**, 168 (3), 221–229.
- (21) Cans, A. S.; Dean, S. L.; Reyes, F. E.; Keating, C. D. Synthesis and Characterization of Enzyme-Au Bioconjugates: HRP and Fluorescein-Labeled HRP. *NanoBiotechnology* 2007 31 **2007**, 3 (1), 12–22.
- (22) Wang, Y.; Jonkute, R.; Lindmark, H.; Keighron, J. D.; Cans, A.-S. Molecular Crowding and a Minimal Footprint at a Gold Nanoparticle Support Stabilize Glucose Oxidase and Boost Its Activity. *Langmuir* **2019**, 36, 37–46.
- (23) Savin, R.; Benzaamia, N.-O.; Njel, C.; Pronkin, S. N.; Blanck, C.; Schmutz, M.; Boulmedais, F. Nanohybrid Biosensor Based on Mussel-Inspired Electro-Cross-Linking of Tannic Acid Capped Gold Nanoparticles and Enzymes. *Mater. Adv.* **2022**, 3 (4), 2222.
- (24) Sivaraman, S. K.; Kumar, S.; Santhanam, V. Room-Temperature Synthesis of Gold Nanoparticles, Size-Control by Slow Addition. *Gold Bull.* 2010 434 **2010**, 43 (4), 275.
- (25) Wuithschick, M.; Birnbaum, A.; Witte, S.; Sztucki, M.; Vainio, U.; Pinna, N.; Rademann, K.; Emmerling, F.; Kraehnert, R.; Polte, J. Turkevich in New Robes: Key Questions Answered for the Most Common Gold Nanoparticle Synthesis. *ACS Nano* **2015**, 9 (7), 7052–7071.
- (26) Karasyova, O. N.; Ivanova, L. I.; Lakshtanov, L. Z.; Lövgren, L.; Sjöberg, S. Complexation of Gold(III)-Chloride at the Surface of Hematite. *Aquat. Geochemistry* 1998 42 **1998**, 4 (2), 215–231.
- (27) Ciganda, R.; Irigoyen, J.; Gregurec, D.; Hernández, R.; Moya, S.; Wang, C.; Ruiz, J.; Astruc, D. Liquid-Liquid Interfacial Electron Transfer from Ferrocene to Gold(III): An Ultrasimple and Ultrafast Gold Nanoparticle Synthesis in Water under Ambient Conditions. *Inorg. Chem.* **2016**, 55 (13), 6361–6363.
- (28) Sauerbrey, G. Verwendung von Schwingquarzen Zur Wägung Dünner Schichten Und Zur Mikrowägung. *Zeitschrift für Phys.* 1959 1552 **1959**, 155 (2), 206–222.
- (29) Scientific, B. Specification Data from QSense QSX 301 and QEM401 <https://www.biolinscientific.com/qsense/>.
- (30) Chandrasekharan, N.; Kamat, P. V. Assembling Gold Nanoparticles as Nanostructured Films Using an Electrophoretic Approach. *Nano Lett.* **2000**, 1 (2), 67–70.
- (31) Ammam, M. Electrochemical and Electrophoretic Deposition of Enzymes: Principles, Differences and Application in Miniaturized Biosensor and Biofuel Cell Electrodes. *Biosens. Bioelectron.* **2014**, 58, 121–131.

- (32) Cordelair, J.; Greil, P. Discrete Element Modeling of Solid Formation during Electrophoretic Deposition. *J. Mater. Sci.* **2004**, *39* (3), 1017–1021.
- (33) Bergman, J.; Wang, Y.; Wigström, J.; Cans, A. S. Counting the Number of Enzymes Immobilized onto a Nanoparticle-Coated Electrode. *Anal. Bioanal. Chem.* **2018**, *410* (6), 1775–1783.
- (34) Hagerman, A. E. Fifty Years of Polyphenol-Protein Complexes. In *Recent Advances in Polyphenol Research*; 2012.
- (35) Yang, J.; Stuart, M. A. C.; Kamperman, M. Jack of All Trades: Versatile Catechol Crosslinking Mechanisms. *Chem. Soc. Rev.* **2014**, *43*, 8271–8298.
- (36) Wang, Q.; Xu, W.; Wu, P.; Zhang, H.; Cai, C.; Zhao, B. New Insights into the Effects of Thermal Treatment on the Catalytic Activity and Conformational Structure of Glucose Oxidase Studied by Electrochemistry, IR Spectroscopy, and Theoretical Calculation. *J. Phys. Chem. B* **2010**, *114* (39), 12754–12764.
- (37) Chen, J.; Xu, Y.; Xia, C.; Li, S. Effect of Cyclodextrin on the Activity and Secondary Structure of Horseradish Peroxidase. *Protein Pept. Lett.* **2005**, *11* (6), 509–513.
- (38) Zhong, K.; Hu, X.; Zhao, G.; Chen, F.; Liao, X. Inactivation and Conformational Change of Horseradish Peroxidase Induced by Pulsed Electric Field. *Food Chem.* **2005**, *92* (3), 473–479.

Chapter 5

Toward smart wound dressings based on graphenized polyurethane membranes

Chapter 5 – Toward smart wound dressings based on graphenized polyurethane membranes

I.	Context of acute and chronic wounds	179
I.1	The wound healing process	179
I.2	Acute and chronic wounds	180
I.3	Simple biomarkers of the wound status	181
I.3.1	Hydrogen peroxide	181
I.3.2	pH value	182
I.3.3	Uric acid	183
I.3.4	Glucose	184
I.3.5	Summary on the studied biomarkers	184
II.	Development of a smart wound dressing	185
II.1	Characterization of PU-FLG membrane	185
II.2	Development of IMET glucose H ₂ O ₂ biosensors	188
II.3	Development of the pH sensor	192
Conclusions		194
References		195

I. Context of acute and chronic wounds

I.1 The wound healing process

In all wounds, the normal response occurs in three overlapping events: the inflammation, the proliferation (new tissue formation), and the remodeling stages (Figure 5.1). The inflammation stage occurs in the first 24 - 48h, the proliferative stage between 2 and 10 days, and the remodeling stage can take up to one year after the injury.¹

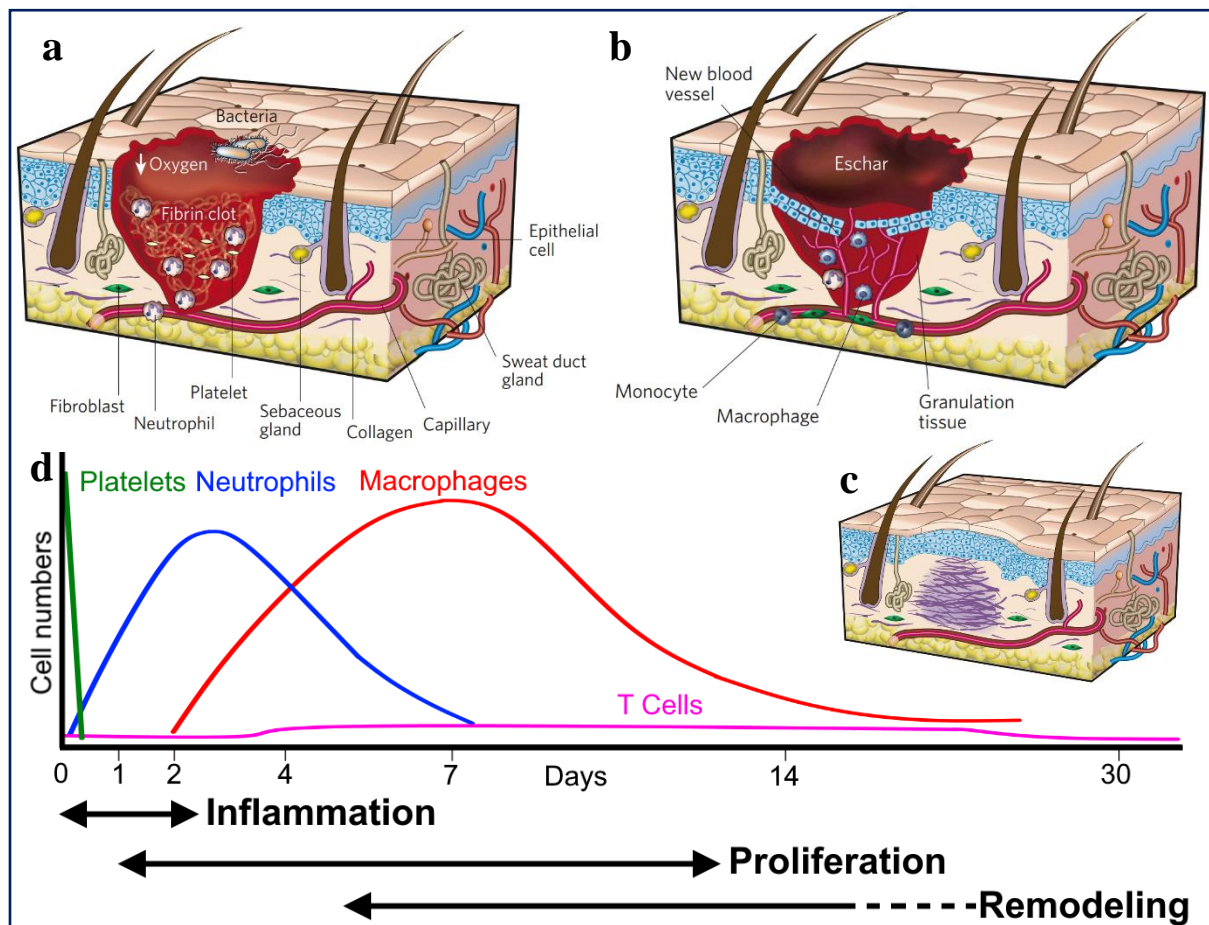


Figure 5.1: Illustration of the wound healing process occurring through three stages. (a) the inflammation, (b) the cell proliferation, and (c) the tissue remodeling. (d) Illustration of the macrophage stage following the neutrophil accumulation and succeeding the platelets coagulation. Memory T cells are also produced to protect the cell against reinfection. Figures are adapted from [1] and [2].

The inflammatory occurs directly after the damaging of the tissue and is the most critical stage in wound healing. This stage has to induce (1) coagulation to stop bleeding, (2) immune reaction to prevent the body from bacterial/virus infection, and (3) to initiate the removal of devitalized tissues. Mainly caused by the aggregation of platelets, the coagulation process will create a barrier against micro-organisms invasion (a scab) and enhance the migration of the first defensive cells. Immune cells, the neutrophils, migrate into the lesion and induce an antimicrobial environment by the production of reactive oxygen species (Figure 5.1.a).³ During the proliferation stage, keratinocytes and fibroblasts are recruited to repair the dermis and create new blood vessels (Figure 5.1.b).¹ In this stage, fibroblasts are differentiated into myofibroblasts cells that help in wound closure by bringing the edges closer together. Both cells produce collagen to regenerate the extracellular matrix. During this proliferation stage, monocytes are also differentiated into macrophages and help neutrophils with the elimination of pathogens and dead cells (Figure 5.1.d). The last stage consists of the departure of the latter cells and a slow remodeling of the collagen/protein matrix to obtain the properties of the tissue before injury (Figure 5.1.c).

I.2 Acute and chronic wounds

Two types of wounds require specific attention: acute and chronic wounds. Acute wounds are severe wounds, for example after surgery, which require a longer time to undergo the three normal stages, delaying the healing process. Chronic wounds are systematically blocked in one of the first two stages of the healing process. A wound is considered chronic when it cannot heal correctly after three months.⁴ These unhealed wounds are often called ulcers. 1 to 2% of the population will experience it during their lifetime. Mainly aged patients or people suffering from diabetes, obesity, vascular disorder are concerned with chronic wounds.⁵ Besides the associated medical costs, the unhealed wounds will cause pain and increase infection complications. To move from inflammation into an efficient proliferative stage, many growth factors, cytokines (small proteins), and proteases are required.⁶ Moreover, some small biomolecules (H_2O_2 , uric acid, etc...) are also known to undergo concentration changes all along the healing process. The measurement of their concentrations allows the monitoring of the wound status for the application of pertinent medical treatment. Few biomarkers will be discussed in the following.

I.3 Simple biomarkers of the wound status

I.3.1 Hydrogen peroxide

Hydrogen peroxide (H_2O_2) is commonly used to disinfect wounds (antiseptic agent). The wound closure is promoted at 10 - 50 mM H_2O_2 and concentrations >150 mM significantly delay the healing process on mice.^{7,8} A probable reason is that H_2O_2 is already used by the body to mediate several mechanisms of the healing process. For instance, H_2O_2 and other reactive oxygen species (ROS) are released at the inflammation stage by neutrophils and platelets to kill pathogens.⁹ They induce vasoconstriction following platelets exposure (coagulation process) and act as a signaling agent for rapid migration of neutrophils and others lymphocytes. In physiological conditions, 500 μM H_2O_2 was found to stimulate the inflammatory response¹⁰ and 0.5 - 50 μM H_2O_2 to be a good chemo-attractant for neutrophils.^{11,12} 10 μM of H_2O_2 is also found to promote cell division (*i.e* proliferation) of vascular endothelial cell, keratinocytes, fibroblasts and stimulate the collagen production.^{1,13,14}

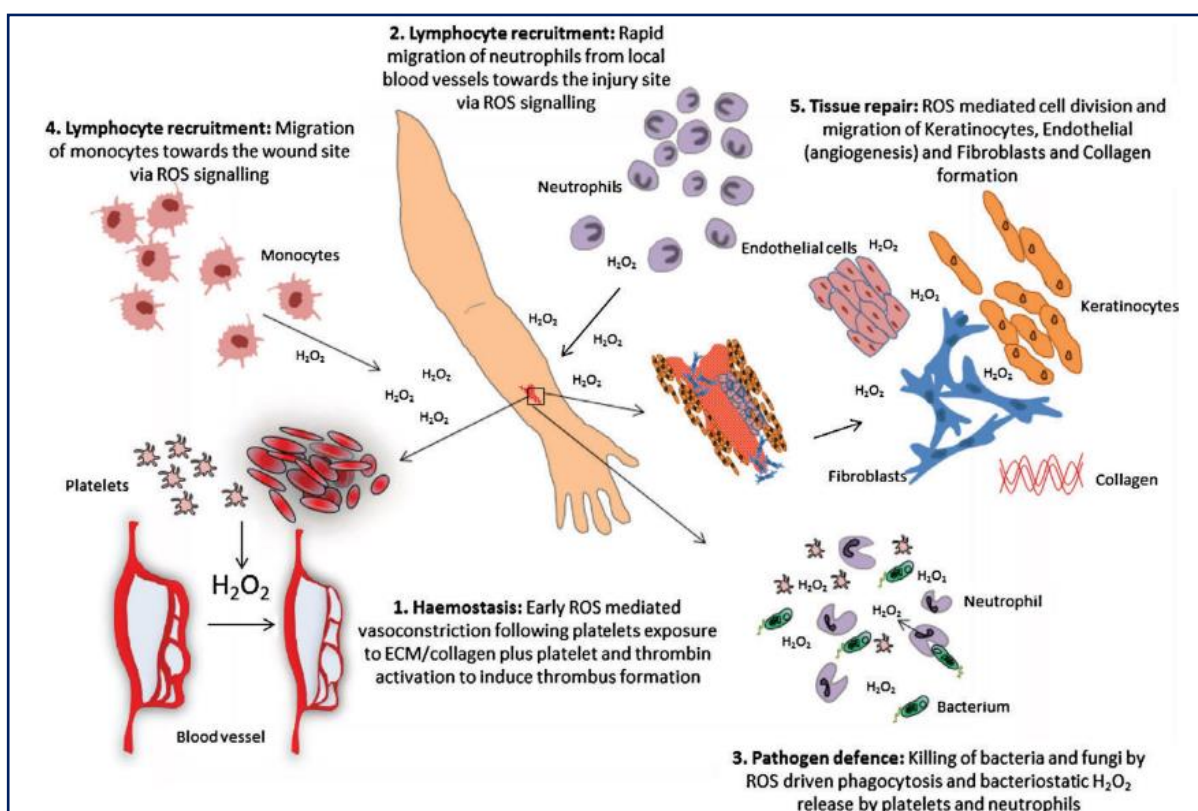


Figure 5.2: Illustration of the reactive oxygen species (ROS) role in the healing process according to [9]. Haemostasis through vasoconstriction, lymphocyte migration, pathogen killing, and cell tissue proliferation are all partly controlled by ROS signaling.

Although no precise profile of H_2O_2 concentration has been drawn in the literature for the different healing stages, a peroxide electrochemical biosensor could be an attractive strategy for a smart wound dressing given its crucial importance in all healing mechanisms. Based on the previous observations, a sensitivity from the micromolar to the millimolar range has to be achieved. Only a few optical sensor for H_2O_2 wound management have been reported and most of them are not enzymatic.^{15,16} There is no evident reason but H_2O_2 is one of the most underestimated biomarkers for wound monitoring.¹⁷ For instance, an electrospun membrane made from polyacrylonitrile nanofibers and Europium(III) coordination polymers has been experienced.¹⁶ This matrix was found to be sensitive to H_2O_2 in the range from 20 to 200 μM due to a significant fluorescence quenching. This fluorescent change was also used to detect a bacterial infection that lead to an inflammation response that partly involve H_2O_2 production from immune cells. Therefore, the quenching effect was present as long as the immune system was still fighting against bacteria. Another quenching biosensor based on the fluorescence of single-walled carbons nanotubes fluorescence has also been reported for H_2O_2 wound sensing in plants.¹⁵ This sensor was operating in the near-infrared with a logarithmic linear range between 1 μM and 1 mM H_2O_2 . Interestingly their biosensor has enhanced to see an interplay between H_2O_2 , Ca^{2+} , and electrical signaling in the plant defense mechanism. Therefore this biosensor allows not only to detect abnormal H_2O_2 concentration but also to go deeper in the comprehension of how cells communicate.

I.3.2 pH value

The normal pH of healthy skin is slightly acidic (around 6) to prevent bacterial proliferation.¹⁸ In a normal wound healing process, the inflammatory stage induces a drop of the pH at around 5 and the proliferative stage leads to an increase of the pH to alkaline values (Figure 5.3.a). This pH will then decrease back to its normal value around 6 for normal and acute wounds. In the case of chronic wounds, the pH value remains above pH 7.4 (Figure 5.3.b) and even more alkaline upon bacterial infection, due to the by-product of proliferative bacterial colonies.¹⁹ Thus, a pH sensor would indicate if a wound is healing or stuck in the inflammatory phase. Wound monitoring sensors have been recently developed using an agarose gel containing a fluorescent dye named 5(6)-carboxynaphthofluorescein for pH variations between 6 and 8.²⁰ An amperometric/potentiometric sensor based on a PEDOT:PSS film containing iridium cations showing an acid-base equilibrium has enhanced to monitor pH between 6 and 9.²¹

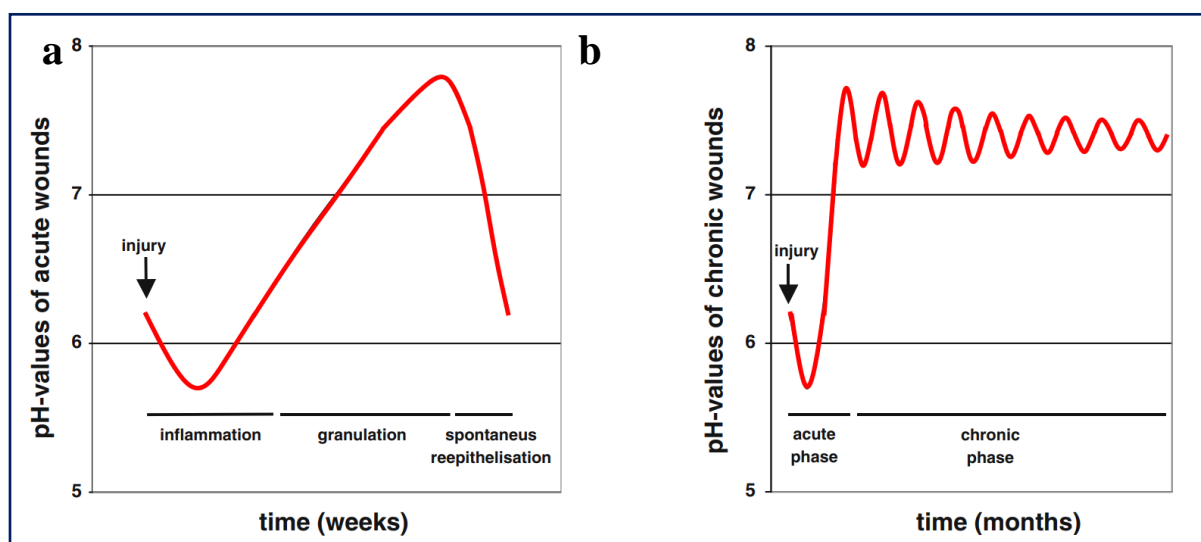


Figure 5.3: Illustration of the pH variation for (a) an acute wound healing and (b) a chronic wound. The granulation (wound filling) and the re-epithelialization correspond to the proliferative stage in the healing process. The figure is adapted from [22]

I.3.3 Uric acid

Uric acid is present in the blood at a concentration varying between 200 and 700 μM .²³ Trengove *et al.* found a median uric concentration of 410 μM for normal serum and 347 μM in wound fluid.²³ In the human body, the degradation of uric acid is obtained in the presence of high oxidants, such as reactive oxygen species (ROS).²⁴ Therefore, the determination of uric acid concentrations is a good estimation of oxidative stress and therefore an indirect way to quantify H_2O_2 concentration.²⁴ Moreover, bacteria can oxidize uric acid enzymatically. A decrease in uric acid concentration can therefore indicate the occurrence of bacterial infections.^{25,26} In summary, a low uric acid level is an indication of too high oxidative stress or bacterial infection leading to a healing process blocked in the inflammatory/proliferative stage even if the deviation between patients is very high (normal serum: 236-823 μM , wound fluid: 221-751 μM). According to Trengove *et al.*, the median change is still significant, so instead of using the uric acid concentration as an absolute value, the trend (increase or decrease) for a specific patient enhances to follow the healing progress. Several uric acid biosensors for wound monitoring have been developed.^{25,27} As an illustrative example, a urate oxidase/bovine serum albumin was crosslinked with glutaraldehyde onto a Prussian blue mediating layer. A sensitivity of $2.4 \mu\text{A} \cdot \text{mM}^{-1}$ was obtained and a linear range from 100 to 800 μM uric acid concentration.²⁵ An entrapped urate oxidase in a cationic poly(vinyl alcohol) derivative was also used to detect uric acid.²⁷ In this study, platinum nanoflakes and silver nanowires were found to be ineffective

to transduce the enzymatic process and only gold nanoparticles coupled to a freely diffusing mediator (ferrocene carboxylic acid) works. Their final sensitivity of $140 \mu\text{A} \cdot \text{mM}^{-1} \cdot \text{cm}^{-2}$ was obtained with a linear range from $14 \mu\text{M}$ to $500 \mu\text{M}$ using ferrocene as a freely diffusing mediator in the process.

I.3.4 Glucose

The concentration of glucose in the blood is usually between 4 and 8 mM and could raise above 10 mM for people suffering from diabetes (Medscape). It is also known that diabetes slows down wound healing, often resulting in chronic wounds. Chronic wounds have a median glucose value of around 1.2 mM compared to a wound fluid which is around 2 mM.²³ The glucose concentration appears to be distinct during the inflammatory stage (1.1 mM) and the proliferative stage (3.1 mM).²⁸ Although a wide variability has been observed among patients, the glucose concentration drops significantly in the early stage and further increases in the late stages of a normal healing process. Few wound biosensors based on glucose have been developed.^{20,29–31} As an example, a glucose oxidase/horseradish peroxidase bi-enzymatic system was immobilized covalently into an alginate/ Ca^{2+} gel. A fluorescent substrate of HRP was used to monitor the glucose concentration and a linear range up to 2.5 mM was obtained. This sensor was able to measure the concentration of glucose in chronic wound fluid but the saturation plateau would not enhance to record eventual healing towards normal values (> 4 mM).

I.3.5 Summary of the studied biomarkers

The following table gathers all information about the expected analyte concentration changes in wound fluid through the successive healing stages. As noticed previously, uric acid level is rather tricky to follow so absolute changes are rather recorded.

Table 5.1: Main information about biomarkers in wound fluid. Asterisk (*) are putative values

Biomarker	Inflammation	Proliferation	Healed	Bacterial infection
H_2O_2	High ($>100 \mu\text{M}$)*	Medium ($10\text{-}100 \mu\text{M}$)*	Low ($<10 \mu\text{M}$)*	High ($>100 \mu\text{M}$)*
Uric Acid	Wound Fluid ∇ : $\sim 347 \mu\text{M}$		$\sim 410 \mu\text{M}$	Low ($< 400 \mu\text{M}$)
Glucose	1.1 mM	3.1 mM	4-8 mM	–
	Chronic: 1.2 mM			
pH	~ 5	8	6	–
	Chronic: 7-8			

II. Development of a smart wound dressing

After having developed and optimized nanohybrid enzymatic biosensors in chapters 3 and 4, the following results will describe the preliminary results obtained on the design of a smart wound dressing (Figure 5.4). In the framework of a collaborative project with Anne Hébraud, Jean-Mario Nhut (ICPEES), and Housseinou Ba (Blackleaf), electrospun polyurethane membranes coated with few layers of graphene (PU-FLG) were used as working electrodes to electrodeposit three sensors. After the electrochemical characterization of the membranes, GOx/TA@AuNPs and HRP/TA@AuNPs nanohybrids coatings were electrodeposited and evaluated as biosensors towards H_2O_2 and glucose, respectively. A pH sensor was also obtained by electrodeposition of a polydopamine coating, using a method reported by Amiri *et al.*³²

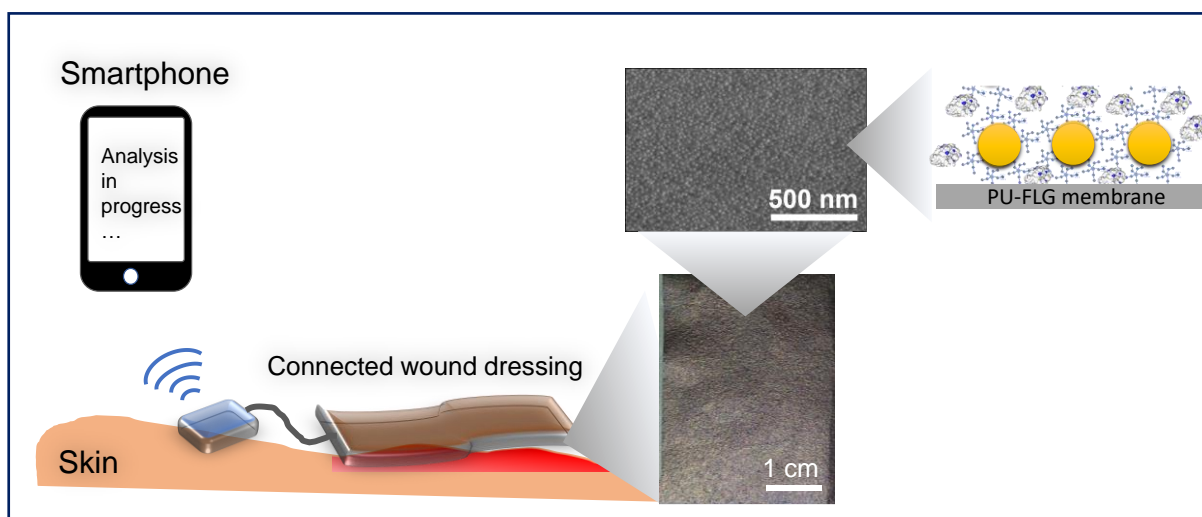


Figure 5.4: Representation of the connected smart wound dressing envisioned with the PU-FLG membrane in contact with the wound and coated by the nanohybrid biosensor.

II.1 Characterization of PU-FLG membrane

The fabrication of the PU-FLG membrane was done by our collaborator and is described in the Material and Methods (chapter 2). The elastic PU-FLG membranes have a silver color due to the adsorbed graphene (Figure 5.5.a) and are around 30 μm in thickness (Figure 5.5.b). The graphene coating is composed of 1 μm large FLG stacked on a less than 1 μm in thickness (Figure 5.5.b). Estimated with a classical multimeter in a dry state, the resistivity of the membranes was around $1.0 \pm 0.3 \Omega \cdot \text{m}$. This electrical resistivity is consistent and slightly higher than others reported values for graphene sheets ($\sim 0.28 \Omega \cdot \text{m}$).^{33,34}

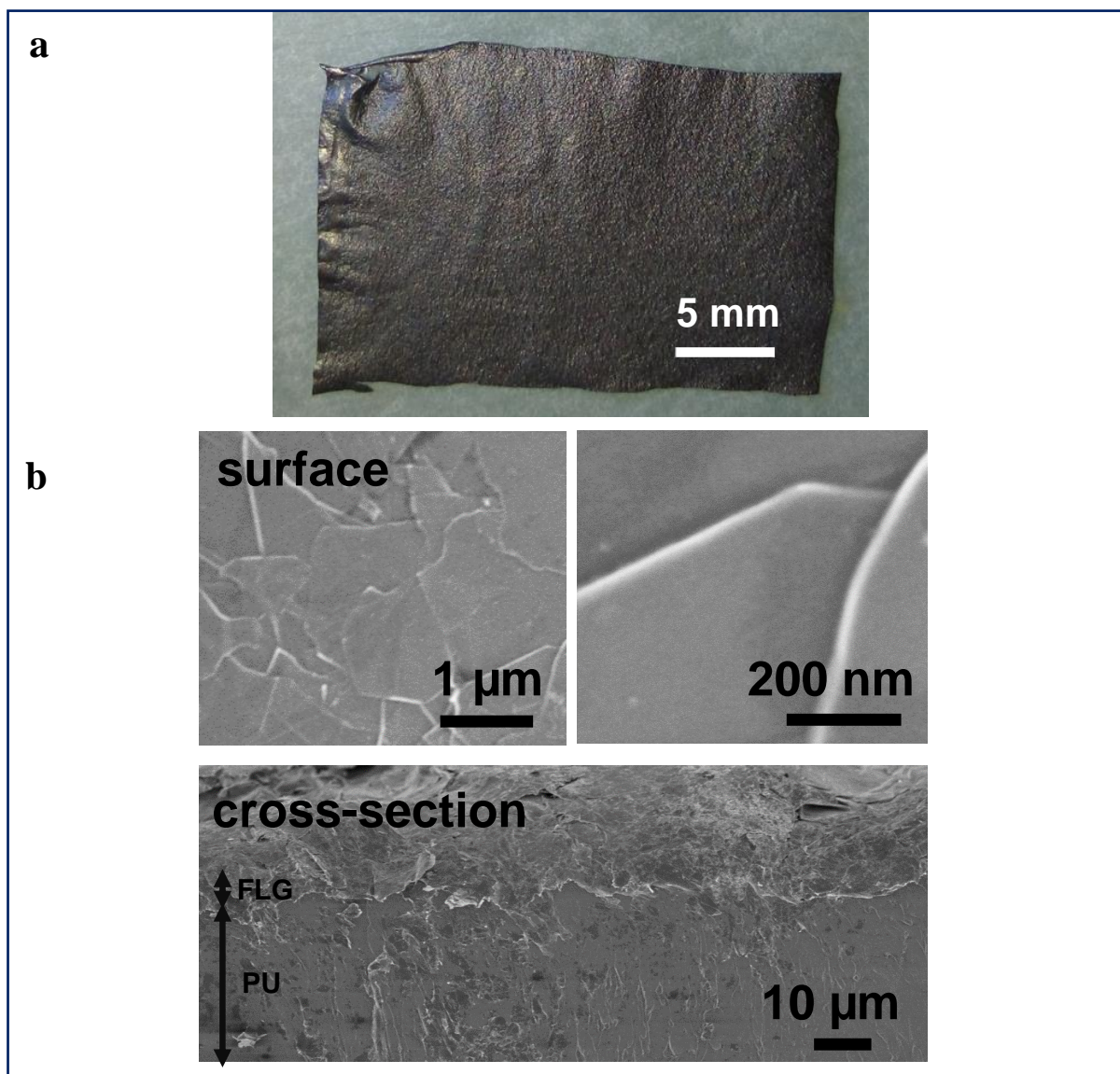


Figure 5.5: (a) photograph of PU-FLG membrane and (b) SEM micrographs, obtained at 1 kV and 10 μ A, of its surface membrane at different magnification as well as its cross-section.

The characterization of the membrane was then performed soaked in phosphate buffer saline solution (10 mM PBS) buffer. The RC impedimetric measurement gave a value of $40 \pm 20 \Omega$ with a high capacitance (characteristic time $\tau > 10000 \mu$ s) probably due to the PU. The Randles–Ševčík equation allowed us to determine the electroactive surface of the PU-FLG membrane. For this aim, cyclic voltammograms were monitored in the presence of 0.5 mM FcOH (diffusion coefficient of $7.4 \cdot 10^{-6} \text{ cm}^2 \cdot \text{s}^{-1}$) at a scan rate of $5 \text{ mV} \cdot \text{s}^{-1}$. The electroactive surface was evaluated at 0.50 cm^2 and 2.05 cm^2 for geometric surfaces of 0.5 and 2 cm^2 , respectively. The electroactive surface was therefore very similar to the geometric surface with a deviation below 3%.

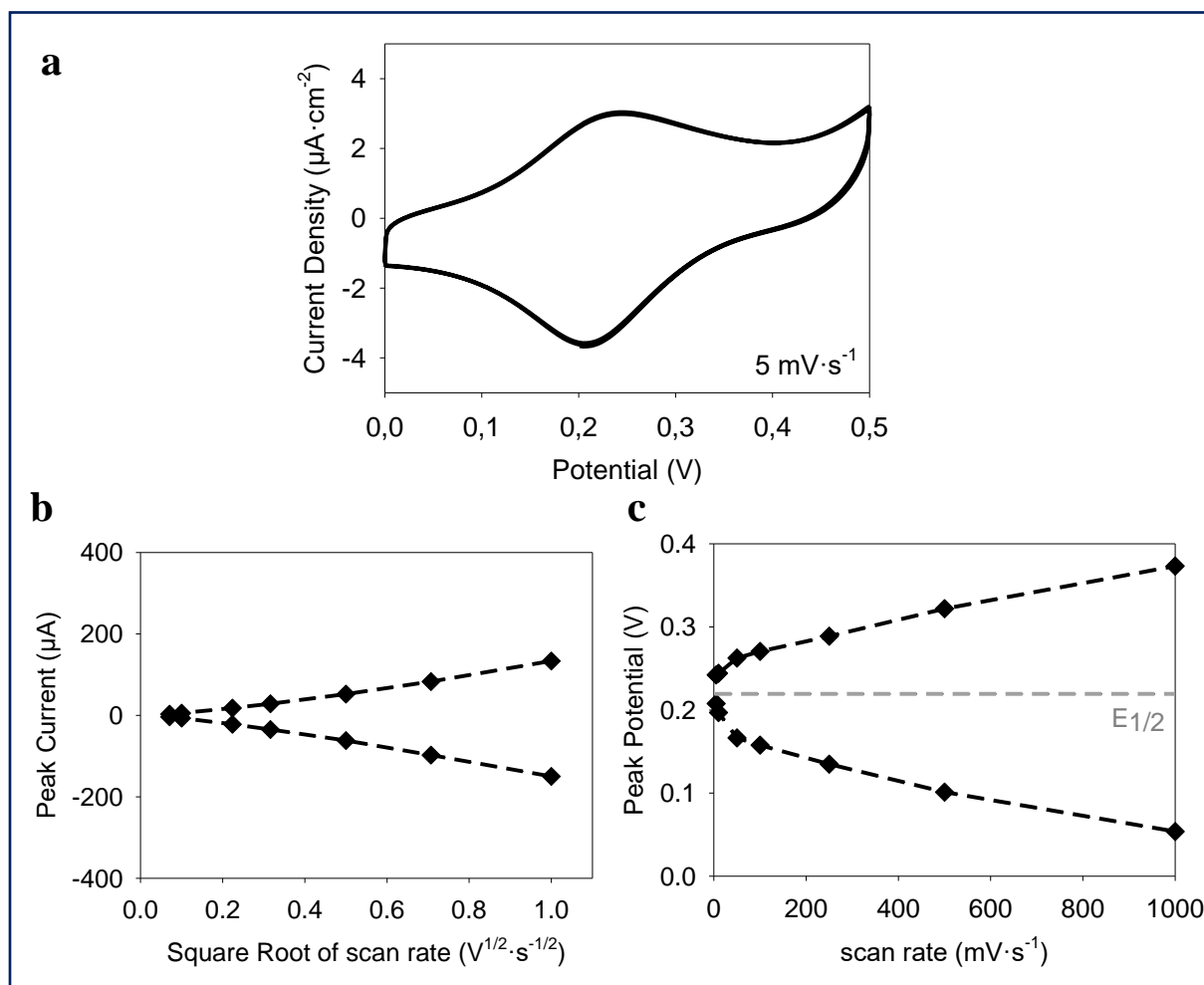


Figure 5.6: (a) Cyclic voltammogram of entrapped FcOH, performed at $5\text{ mV}\cdot\text{s}^{-1}$ in 10 mM PBS, on a 0.5 cm^2 membrane at low scan rate. After contact with the FcOH solution, 10 mL of 10 mM PBS was used at the washing step. Evolution of (b) the peak currents as a function of the square root of the scan rate. (c) the peak potentials (E_{ox} and E_{red}) as a function of the scan rate.

After several washing steps with 10 mM PBS, the redox peak of FcOH was still present with a small decrease of the peak currents. The resulting cyclic voltammogram is represented in figure 5.6.a. The peak currents were found to be linear with the square root of scan rate as predicted for freely diffusing molecules (Figures 5.6.b). However, in this case, the peak separation should not vary with the scan rate as seen in Figure 5.6.c. The peak separation was evaluated at 18 mV at $5\text{ mV}\cdot\text{s}^{-1}$ which is between the adsorbed case (0 mV) and the diffusion value (57 mV at 25°C).³⁵ This deviation may suggest that electron transfer from the remaining ferrocene and the electrode is slow and only reversible at a low scan rate. If we assume that the ferrocene is adsorbed on the graphene, a surface density of $1.4 \pm 0.2 \cdot 10^{-9}\text{ mol}\cdot\text{cm}^{-2}$ is found using equation

1.2 in Chapter 1 for adsorbed species.^{35,36} This value is slightly higher than the concentration of adsorbed FcOH on graphene found in another study ($1.1 \cdot 10^{-11} \text{ mol} \cdot \text{cm}^{-2}$, 2% of a monolayer coverage).³⁷ Using the calculation of this study with a FcOH size of 0.45 nm, surface coverage of $340 \pm 40\%$ is found. This value appears reasonable and indicates that the retained FcOH is only adsorbed onto graphene via $\pi - \pi$ stacking acting as a diffusing reservoir. The reason why the electron transfer is slow between FcOH and the electrode remains however unclear.

II.2 Development of IMET glucose H_2O_2 biosensors

GOx/NP12 and HRP/NP12 coatings were electrodeposited onto PU-FLG using the procedure developed in chapters 3 and 4. The mixture solution, composed of 10 μM GOx or 13.3 μM HRP, 166 μM of NP12, 5 mM FcOH and 50 mM NaCl, was electrodeposited on the PU-FLG membrane for one hour at 0.7 V using a home-made cell. After two 1 mL rinsing steps using 50 mM NaCl, 1.5% w/v gum Arabic (GA), prepared in 50 mM NaCl, was drop casted for 10 min to obtain an impermeable coating to avoid FcOH release. Figure 5.7 shows the SEM images of the electrodeposited HRP/NP12@PU-FLG/GA coating. Densely packed NPs are observed on the rough surface of the PU-FLG membrane (Figure 5.7).

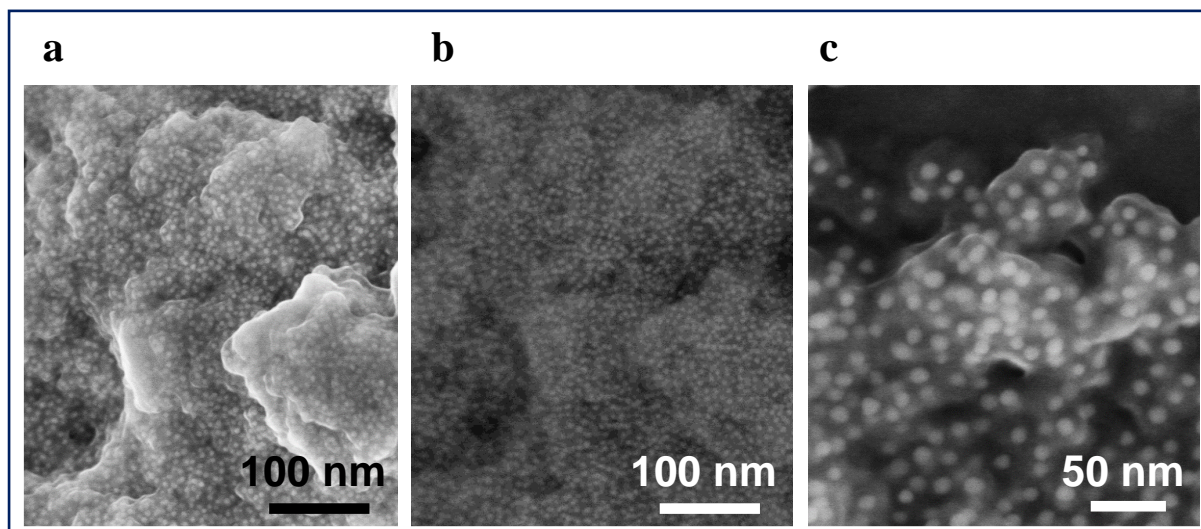


Figure 5.7: SEM micrographs of a typical HRP/NP12/GA coating on PU-FLG, obtained at a working distance of 3 mm using an electron beam of 5 kV and 10 μA , with the secondary electrons at different magnification (a,c) and the same area was then observed with back-scattered electron (b).

The sensitivity of GOx/NP12/GA functionalized membranes were then evaluated towards glucose. First of all, similarly to the bare membrane, the signal of FcOH was still observed after the washing step using 10 mL of PBS (Figure 5.8.a).

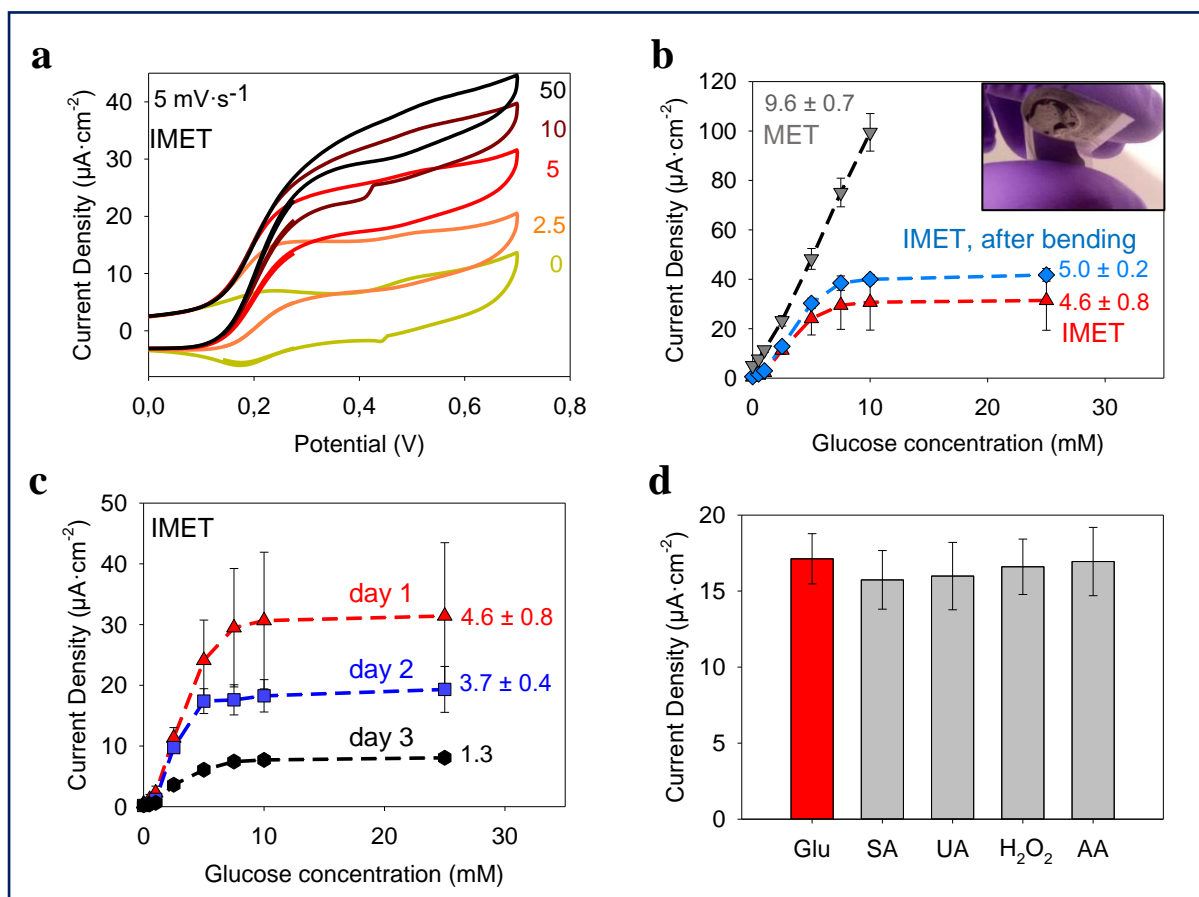


Figure 5.8: GOx/NP12@PU-FLG membrane glucose sensor based on IMET. (a) CV of IMET catalytic current arising from glucose oxidation with concentration ranging from 0 to 50 mM. (b) chronoamperometric IMET response of the sensor at 0.25V just after sample preparation (red) and after a hundred bending repetitions (blue) for different glucose concentrations in 10 mM PBS and in the presence of 0.5 mM FcOH in the medium (grey). Inset is the illustration of the bending process. (c) IMET response of the biosensor on the first day (red), the 2nd day (blue) and the 3rd day (black) after the electrodeposition. (d) Influence of common interferents on the membrane response at their expected concentration in wound fluid: 0.75 mM salicylic acid (SA), 0.5 mM uric acid (UA), 1 mM H_2O_2 and 0.15 mM ascorbic acid (AA) along with 5 mM glucose in 10 mM PBS.

The current density value at the oxidative peak was close to the one measured on the bare PU-FLG (3.3 against $3\text{ }\mu\text{A}\cdot\text{cm}^{-2}$). This suggests that a similar amount of FcOH is retained within the functionalized membrane. In the presence of glucose, the catalytic current can be highlighted on the oxidation branch of adsorbed FcOH (Figure 5.8.a). Indeed, FcOH is continuously produced by the enzymatic reaction and on the contrary, ferrocenium is depleted

due to the continuous reaction with the GOx cofactor. This change resulted in higher FcOH oxidation current density. Evaluated by chronoamperometry at 0.25 V without the addition of FcOH in the medium, the sensitivity of the biosensor was $4.6 \pm 0.8 \mu\text{A} \cdot \text{mM}^{-1} \cdot \text{cm}^{-2}$ (Figure 5.8.b). The upper limit of linearity was 5 mM with a LOD of 0.6 mM in glucose. By comparison, if 0.5 mM FcOH is present in the medium, the sensitivity increased to $9.6 \pm 0.7 \mu\text{A} \cdot \text{mM}^{-1} \cdot \text{cm}^{-2}$ with a linear range up to 10 mM and a LOD of 0.7 mM in glucose. The sensitivity and the linear range obtained by MET were improved by a factor of 2 compared to IMET (adsorbed FcOH). A lower value was indeed expected as the available concentration of FcOH can rapidly be the limiting factor in such systems. In comparison with the devices developed in Chapter 3 on a gold electrode, the sensitivity is almost 4 times lower. However based on the common concentration range in the wound fluid (1 - 5 mM), the GOx/NP12@PU-FLG membrane could be an efficient glucose sensor in the IMET version. It could also work for glucose sensing in urine and tears according to the targeted range (Chapter I, section II.6). In the context of its use as a smart wound dressing, the stability of the response was evaluated towards the bending and upon storage. The membrane was bent in a positive and reverse manner a hundred times each (Figure 5.8.b). Slightly higher current values were measured after the bending test with a similar sensitivity within the standard deviation. The biosensor is stable towards mechanical deformations of the bending. Upon storage in 10 mM PBS at room temperature, the biosensor kept 80% and 28% of its sensitivity 2 and 3 days after the electrodeposition (Figure 5.8.c). By the addition of FcOH followed by the washing step, the sensitivity was restored. This sensitivity loss was due to the progressive desorption of the FcOH upon storage. Therefore, this could be improved by grafting of ferrocene or the use of biphenylferrocene³⁸, known to adsorb strongly on graphene. The repeatability of the biosensor was also tested with 5 mM glucose. The standard deviation (2σ) was 4% (Red bar, Figure 5.8.d). The possible interferences from redox-active molecules, often present in serum, were tested with deviations of 8% for salicylic acid, 6% for uric acid, 3% for H_2O_2 , and 1% for ascorbic acid. Except for salicylic acid, the deviation values were comparable to the deviation for glucose only.

The same study was performed on HRP/NP12 functionalized PU-FLG membranes using adsorbed FcOH for the sensitivity (Figure 5.9). After the building and a successive washing of unbound FcOH, a catalytic current proportional to H_2O_2 concentration was observed at 0.19 V with a sensitivity of $29 \pm 3 \mu\text{A} \cdot \text{mM}^{-1} \cdot \text{cm}^{-2}$, a linear range up to 250 μM and a LOD of 6 μM . This sensitivity was seven times lower than the MET H_2O_2 sensor built on the gold electrode

(Chapter 3). Still, the obtained biosensor is a good candidate to monitor the healing state during the inflammatory and proliferation stages as the H_2O_2 concentration in a wound fluid is expected to be between 10 and 500 μM . After the bending of the membranes 200 times, the sensitivity of the coating was preserved with a significantly lower upper limit for H_2O_2 (100 μM vs 250 μM) (Figure 5.9.b). This change can be due to a modification either of the active enzyme concentration or the available mediator (loss of some adsorbed mediators).

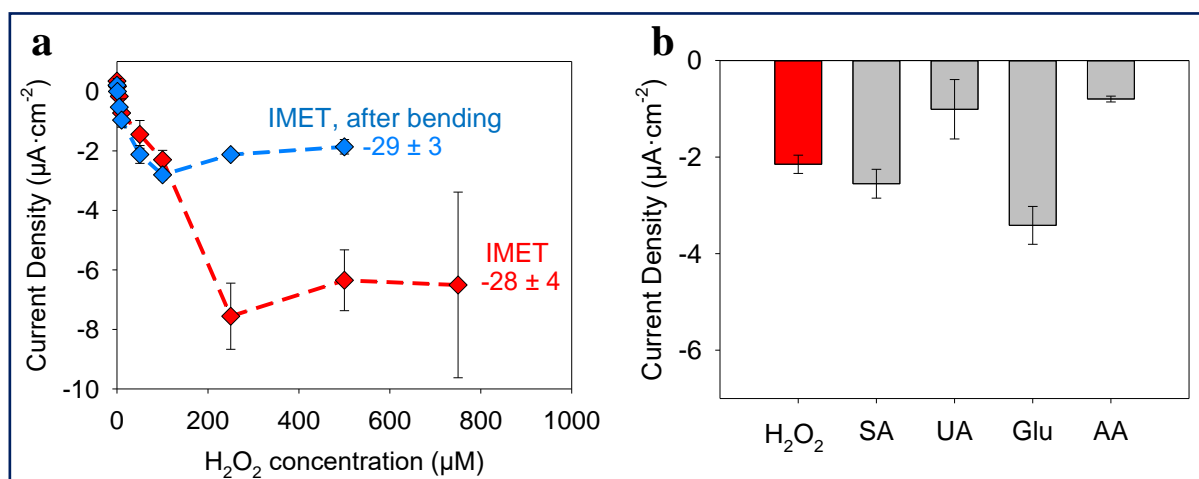


Figure 5.9: HRP/NP12@PU-FLG membrane H_2O_2 biosensor based on IMET electron transfer. (a) Sensitivity plots, retrieved from chronoamperometric curves at 0.19 V in 10 mM PBS before (red) and after (blue) the bending procedure. The bending consists in 100 positive bending and 100 reverse bendings (b) Influence of common interferents on the membrane response at their expected concentration in wound fluid: 0.75 mM salicylic acid (SA), 0.5 mM uric acid (UA), 1 mM H_2O_2 and 0.15 mM ascorbic acid (AA) along with 100 μM H_2O_2 in 10 mM PBS.

The repeatability of the measurement and the interferences molecules were tested (Figure 5.9.b). The standard deviation for three consecutive determinations of 100 μM H_2O_2 was 8% which is pretty high for a mid-range value. In the presence of interferences molecules, the deviation values were 18% for salicylic acid, -52% for uric acid, 58% for H_2O_2 and -62% for ascorbic acid. These analytes interfere significantly at their common concentration. A solution could be to deposit a selective membrane permeable to H_2O_2 and impermeable to ascorbic acid and uric acid such as poly(o-toluidine).³⁹

II.3 Development of the pH sensor

As highlighted in the introduction, the development of pH sensors implemented inside a wound dressing would be of great interest to detect the healing progress. Also, the previous biosensors for glucose and H_2O_2 have a tuned sensitivity with pH because the enzymatic activity is pH-sensitive.^{40,41} Therefore, enzymatic biosensors are generally coupled to a pH electrode when they operate in a media with variable pH. We choose to develop a polyphenol-based pH sensor, rather than polypyrrole or polyaniline conductive coatings.^{19,42,43} Dopamine electropolymerization (PDA) was considered here instead of tannic acid because the primary amine of dopamine undergoes intra-michael addition blocking the possible interference of nucleophiles such as thiol on the coating response.³²

The electrodeposition of polydopamine (PDA) was done using a method published by Amiri *et al.*³² In contact with a solution of 5 mM dopamine in acetate buffer (0.1 M, pH 5), 10 cycles of CV between -0.4 and +1.5 V were applied at $50 \text{ mV}\cdot\text{s}^{-1}$ in scan rate. The resulting film was washed ten times with acetate buffer and CVs in different pH were then recorded (Figure 5.10.a). At $\text{pH} < 6$, two clear redox peaks were observed, and above this pH only the oxidation peak was visible suggesting an irreversible electron-proton coupled transfer at high pH. Fortunately, this does not seem to have an impact on the repeatability of the pH sensing at pH 7.4 with a repeatability of 1.3% (Figure 5.8.c, blue peak). The stability of the response upon bending of the membrane gave a standard deviation of 2% (Figure 5.10.b). The sensitivity of the sensor was $-41 \pm 2 \text{ mV}\cdot\text{pH}^{-1}$ ($R^2=0.996$) with an intercept at 292 mV. This value is quite different from the Nernst's expectation ($59.1/n$ at 25°C) and also lower than other flexible or PDA-based pH electrodes (Table 5.2). It has to be noted that this sensor was made without further optimizations. The electrodeposition potential could be optimized to improve the sensitivity of the sensor. The standard deviation in the presence of glucose, salicylic acid, uric acid, hydrogen peroxide and ascorbic acid were respectively 3%, 7%, 2%, 55% and 180% (Figure 5.10.c). H_2O_2 and ascorbic acid were therefore found to strongly interfere with the pH measurement, probably because they modify the state of polydopamine by a redox reaction. Further improvements of the pH electrode may consist in the development of H^+ selective coatings or the use of current probing instead of open circuit potential that appear less impacted by interferences.²¹

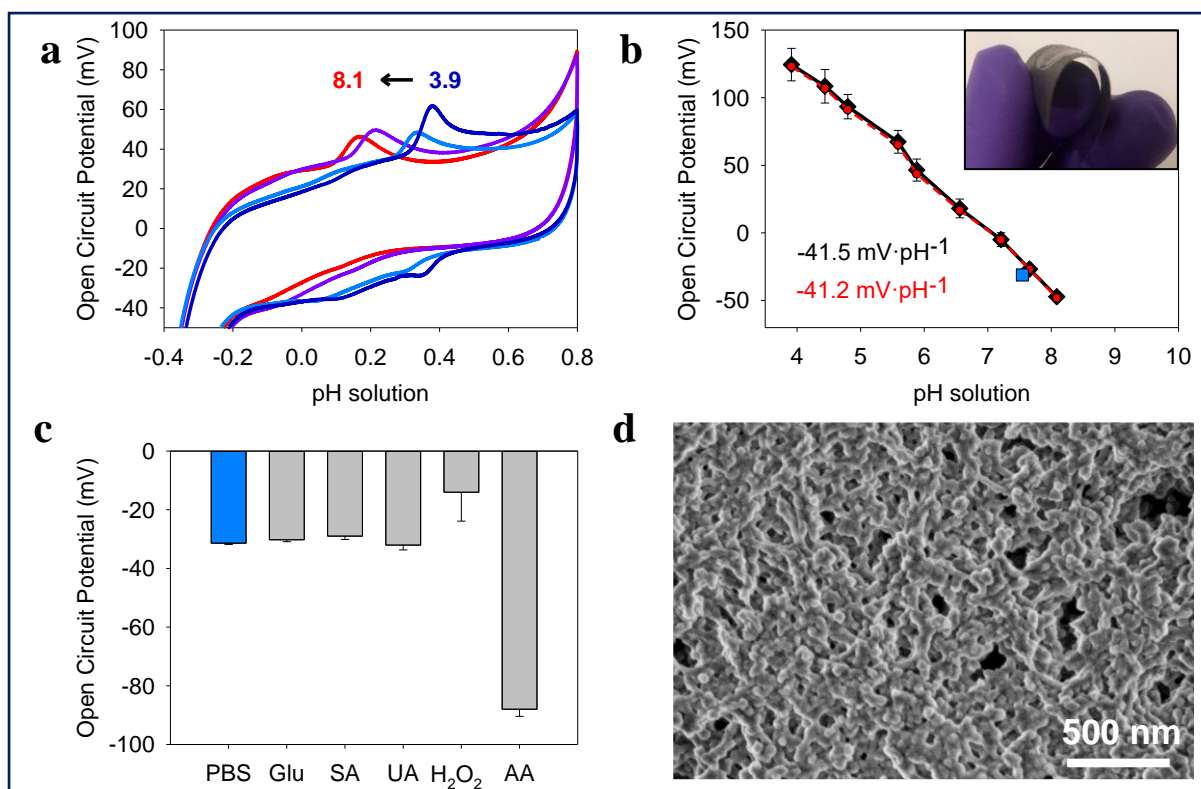


Figure 5.10: PDA@PU-FLG membrane pH sensor (a) CV, performed in 10 mM PBS, at pH 3.9 (dark blue), 7.2 (cyan), 4.8 (purple) and 3.9 (red) with potentials measured against 3.5 M Ag/AgCl reference electrode (b) Dependence of the open circuit potential (OCP), measured after 200 s, as a function of the pH before (black diamond) and after (red diamond) after 100 positive and reverse bendings and in 10 mM PBS (blue square) and (c) Influence of the different interferents on the OCP response of the sensor: Glucose (Glu), salicylic acid (SA), uric acid (UA), H_2O_2 and ascorbic acid (AA) at 1 mM in 10 mM PBS (d) Micrograph of PDA@PU-FLG membrane.

Table 5.2: Comparison of the pH sensitivity of various pH electrodes either designed with polydopamine or onto the flexible electrode

Nature of the coating	Slope ($\text{mV} \cdot \text{pH}^{-1}$)	Flexibility	pH tested range	Ref
PPy on interdigitated electrode	51	No	2-11	[42]
PDA/ multilayered fullerenes on GCE	51.2	No	2-10	[44]
PDA on carbon electrode	58.2	No	1-12	[32]
PANI/Polyimide membrane	58.6	Yes	5.4-8.6	[43]
PANI/carbon electrode	50	Yes	4-10	[19]
PDA on PU-FLG	41.5	Yes	3-8	This work

Conclusions

A flexible conductive membrane was used as a working electrode for wound dressing with embedded point-of-care sensors for wound monitoring. In collaboration with Anne Hébraud, Jean-Mario Nhut (ICPEES) and Housseinou Ba (Blackleaf), we have investigated the use of electrospun polyurethane membranes coated with few layers of graphene (PU-FLG), which is highly conductive and flexible. The use of freely diffusing redox mediator (FcOH) strongly limits *in-situ* application. It was found that the mediator was retained onto the graphene layer of PU-FLG with a stable signal for up to two days. The electrodeposition of HRP/NPs and GOx/NPs coatings lead to good sensitivities in the absence of free diffusing mediators. The response was stable for two days but drastically decrease for longer times due to a loss in adsorbed FcOH. Moreover, the bending of the resulting membranes does not significantly change the sensitivities. For HRP/NPs coatings, interferences were however important. A flexible pH-sensor was also developed by electrodeposition of polydopamine. A reproducible potentiometric response was obtained towards pH changes with no influence of the membrane bending. These results suggest that PU-FLG is a very promising platform for multi-biomarkers analysis in wound fluids to record the healing progress. We can highlight that: (i) H_2O_2 , glucose, and pH were easily quantifiable with our architecture, (ii) the linear ranges achieved were perfectly fitting the common range of these biomarkers in wound fluids, (iii) no free diffusing mediators were used and a true immobilized electron transfer electrocatalysis was highlighted and (iv) the response of these coatings was found to be independent on the bending.

References

- (1) Gurtner, G. C.; Werner, S.; Barrandon, Y.; Longaker, M. T. Wound Repair and Regeneration. *Nat.* 2008 4537193 **2008**, 453 (7193), 314–321.
- (2) Cañedo-Dorantes, L.; Cañedo-Ayala, M. Skin Acute Wound Healing: A Comprehensive Review. *Int. J. Inflam.* **2019**, 1 (1), 1–15.
- (3) Gonzalez, A. C. D. O.; Andrade, Z. D. A.; Costa, T. F.; Medrado, A. R. A. P. Wound Healing - A Literature Review. *An. Bras. Dermatol.* **2016**, 91 (5), 614.
- (4) Martin, P.; Nunan, R. Cellular and Molecular Mechanisms of Repair in Acute and Chronic Wound Healing. *Br. J. Dermatol.* **2015**, 173 (2), 370–378.
- (5) Järbrink, K.; Ni, G.; Sönnerngren, H.; Schmidtchen, A.; Pang, C.; Bajpai, R.; Car, J. Prevalence and Incidence of Chronic Wounds and Related Complications: A Protocol for a Systematic Review. *Syst. Rev.* **2016**, 5 (1), 1–6.
- (6) Tarnuzzer, R. W.; Schultz, G. S. Biochemical Analysis of Acute and Chronic Wound Environments. *Wound Repair Regen.* **1996**, 4 (3), 321–325.
- (7) Roy, S.; Khanna, S.; Nallu, K.; Hunt, T. K.; Sen, C. K. Dermal Wound Healing Is Subject to Redox Control. *Mol. Ther.* **2006**, 13 (1), 211–220.
- (8) Loo, A. E. K.; Wong, Y. T.; Ho, R.; Wasser, M.; Du, T.; Ng, W. T.; Halliwell, B. Effects of Hydrogen Peroxide on Wound Healing in Mice in Relation to Oxidative Damage. *PLoS One* **2012**, 7 (11), e49215.
- (9) Dunnill, C.; Patton, T.; Brennan, J.; Barrett, J.; Dryden, M.; Cooke, J.; Leaper, D.; Georgopoulos, N. T. Reactive Oxygen Species (ROS) and Wound Healing: The Functional Role of ROS and Emerging ROS-Modulating Technologies for Augmentation of the Healing Process. *Int. Wound J.* **2017**, 14 (1), 89–96.
- (10) Shi, M. M.; Godleski, J. J.; Paulauskis, J. D. Regulation of Macrophage Inflammatory Protein-1 α mRNA by Oxidative Stress (*). *J. Biol. Chem.* **1996**, 271 (10), 5878–5883.
- (11) Klyubin, I. V.; Kirpichnikova, K. .; Gamaley, I. . Hydrogen Peroxide-Induced Chemotaxis of Mouse Peritoneal Neutrophils. *Eur J Cell Biol.* **1996**, 70 (4), 347–351.
- (12) Niethammer, P.; Grabher, C.; Look, A. T.; Mitchison, T. J. A Tissue-Scale Gradient of Hydrogen Peroxide Mediates Rapid Wound Detection in Zebrafish. *Nat.* 2009 4597249 **2009**, 459 (7249), 996–999.
- (13) Stone, J. R.; Collins, T. The Role of Hydrogen Peroxide in Endothelial Proliferative Responses. <http://dx.doi.org/10.1080/10623320214733> **2009**, 9 (4), 231–238.

- (14) Murrell, G. A. C.; Francis, M. J. O.; Bromley, L. Modulation of Fibroblast Proliferation by Oxygen Free Radicals. *Biochem. J.* **1990**, 265 (3), 665.
- (15) Lew, T. T. S.; Koman, V. B.; Silmore, K. S.; Seo, J. S.; Gordiichuk, P.; Kwak, S. Y.; Park, M.; Ang, M. C. Y.; Khong, D. T.; Lee, M. A.; Chan-Park, M. B.; Chua, N. H.; Strano, M. S. Real-Time Detection of Wound-Induced H₂O₂ Signalling Waves in Plants with Optical Nanosensors. *Nat. Plants* 2020 64 **2020**, 6 (4), 404–415.
- (16) Wu, K.; Wu, X.; Chen, M.; Wu, H.; Jiao, Y.; Zhou, C. H₂O₂-Responsive Smart Dressing for Visible H₂O₂ Monitoring and Accelerating Wound Healing. *Chem. Eng. J.* **2020**, 387, 124127.
- (17) Pusta, A.; Tertiş, M.; Cristea, C.; Mirel, S. Wearable Sensors for the Detection of Biomarkers for Wound Infection. *Biosens. 2022, Vol. 12, Page 1* **2021**, 12 (1), 1.
- (18) Percival, S. L.; McCarty, S.; Hunt, J. A.; Woods, E. J. The Effects of PH on Wound Healing, Biofilms, and Antimicrobial Efficacy. *Wound Repair Regen.* **2014**, 22 (2), 174–186.
- (19) Rahimi, R.; Ochoa, M.; Parupudi, T.; Zhao, X.; Yazdi, I. K.; Dokmeci, M. R.; Tamayol, A.; Khademhosseini, A.; Ziaie, B. A Low-Cost Flexible PH Sensor Array for Wound Assessment. *Sensors Actuators B Chem.* **2016**, 229, 609–617.
- (20) Jankowska, D. A.; Bannwarth, M. B.; Schulenburg, C.; Faccio, G.; Maniura-Weber, K.; Rossi, R. M.; Scherer, L.; Richter, M.; Boesel, L. F. Simultaneous Detection of PH Value and Glucose Concentrations for Wound Monitoring Applications. *Biosens. Bioelectron.* **2017**, 87, 312–319.
- (21) Mariani, F.; Serafini, M.; Gualandi, I.; Arcangeli, D.; Decataldo, F.; Possanzini, L.; Tessarolo, M.; Tonelli, D.; Fraboni, B.; Scavetta, E. Advanced Wound Dressing for Real-Time PH Monitoring. *ACS Sensors* **2021**, 6 (6), 2366–2377.
- (22) Schneider, L. A.; Korber, A.; Grabbe, S.; Dissemond, J. Influence of PH on Wound-Healing: A New Perspective for Wound-Therapy? *Arch. Dermatol. Res.* **2007**, 298 (9), 413–420.
- (23) Trengove, N. J.; Langton, S. R.; Stacey, M. C. Biochemical Analysis of Wound Fluid from Nonhealing and Healing Chronic Leg Ulcers. *Wound Repair Regen.* **1996**, 4 (2), 234–239.
- (24) James, T. J.; Hughes, M. A.; Cherry, G. W.; Taylor, R. P. Evidence of Oxidative Stress in Chronic Venous Ulcers. *Wound Repair Regen.* **2003**, 11 (3), 172–176.

- (25) Kassal, P.; Kim, J.; Kumar, R.; De Araujo, W. R.; Steinberg, I. M.; Steinberg, M. D.; Wang, J. Smart Bandage with Wireless Connectivity for Uric Acid Biosensing as an Indicator of Wound Status. *Electrochem. commun.* **2015**, *56*, 6–10.
- (26) Sharp, D.; Davis, J. Integrated Urate Sensors for Detecting Wound Infection. *Electrochem. commun.* **2008**, *10* (5), 709–713.
- (27) RoyChoudhury, S.; Umasankar, Y.; Bhansali, S. A Wearable Electrochemical Sensor to Monitor Progression of Wound Healing. *ECS Trans.* **2017**, *80* (10), 1345–1353.
- (28) Iizaka, S.; Sanada, H.; Minematsu, T.; Oba, M.; Nakagami, G.; Koyanagi, H.; Nagase, T.; Konya, C.; Sugama, J. Do Nutritional Markers in Wound Fluid Reflect Pressure Ulcer Status? *Wound Repair Regen.* **2010**, *18* (1), 31–37.
- (29) Zhu, Y.; Zhang, J.; Song, J.; Yang, J.; Du, Z.; Zhao, W.; Guo, H.; Wen, C.; Li, Q.; Sui, X.; Zhang, L. A Multifunctional Pro-Healing Zwitterionic Hydrogel for Simultaneous Optical Monitoring of PH and Glucose in Diabetic Wound Treatment. *Adv. Funct. Mater.* **2020**, *30* (6), 1905493.
- (30) Krismastuti, F. S. H.; Brooks, W. L. A.; Sweetman, M. J.; Sumerlin, B. S.; Voelcker, N. H. A Photonic Glucose Biosensor for Chronic Wound Prognostics. *J. Mater. Chem. B* **2014**, *2* (25), 3972–3983.
- (31) Kafi, M. A.; Paul, A.; Vilouras, A.; Hosseini, E. S.; Dahiya, R. S. Chitosan-Graphene Oxide-Based Ultra-Thin and Flexible Sensor for Diabetic Wound Monitoring. *IEEE Sens. J.* **2020**, *20* (13), 6794–6801.
- (32) Amiri, M.; Amali, E.; Nematollahzadeh, A.; Salehniya, H. Poly-Dopamine Films: Voltammetric Sensor for PH Monitoring. *Sensors Actuators B Chem.* **2016**, *228*, 53–58.
- (33) Chen, C. M.; Huang, J. Q.; Zhang, Q.; Gong, W. Z.; Yang, Q. H.; Wang, M. Z.; Yang, Y. G. Annealing a Graphene Oxide Film to Produce a Free Standing High Conductive Graphene Film. *Carbon N. Y.* **2012**, *50* (2), 659–667.
- (34) Pei, S.; Zhao, J.; Du, J.; Ren, W.; Cheng, H. M. Direct Reduction of Graphene Oxide Films into Highly Conductive and Flexible Graphene Films by Hydrohalic Acids. *Carbon N. Y.* **2010**, *48* (15), 4466–4474.
- (35) Savéant, J.; Costentin, C. *Elements of Molecular and Biomolecular Electrochemistry*, 2nd ed.; Wiley & Sons, Ed.; Hoboken (New Jersey), 2019.
- (36) Bard, A. J.; Faulkner, L. R. *Electrochemical Methods: Fundamentals and Applications*, 2nd ed.; Wiley & Sons, Ed.; Hoboken (New Jersey), 2001.

- (37) Li, W.; Tan, C.; Lowe, M. A.; Abruña, H. D.; Ralph, D. C. Electrochemistry of Individual Monolayer Graphene Sheets. *ACS Nano* **2011**, 5 (3), 2264–2270.
- (38) Yang, M.; Batchelor-Mcauley, C.; MoreiraGonçalves, L.; Lima, C. F. R. A. C.; Vyskočil, V.; Tschulik, K.; Compton, R. G. Ferrocene Aryl Derivatives for the Redox Tagging of Graphene Nanoplatelets. *Electroanalysis* **2016**, 28 (1), 197–202.
- (39) Erdogdu, G.; Ekinici, E.; Karagozler, A. E. Preparation and Electrochemical Behavior of Dopamine-Selective Polymeric Membrane. *Polym. Bull. 2000 442* **2000**, 44 (2), 195–201.
- (40) Description of enzymes from Toyobo Supplier https://www.toyobo-global.com/seihin/xr/enzyme/enzyme_list/ (accessed 2022 -02 -07).
- (41) Description of G7141 product from Sigma Aldrich <https://www.sigmaaldrich.com/FR/fr/product/sigma/g7141> (accessed 2022 -01 -31).
- (42) Lakard, B.; Segut, O.; Lakard, S.; Herlem, G.; Gharbi, T. Potentiometric Miniaturized PH Sensors Based on Polypyrrole Films. *Sensors Actuators B Chem.* **2007**, 122 (1), 101–108.
- (43) Li, Y.; Mao, Y.; Xiao, C.; Xu, X.; Li, X. Flexible PH Sensor Based on a Conductive PANI Membrane for PH Monitoring. *RSC Adv.* **2019**, 10 (1), 21–28.
- (44) Zuaznabar-Gardona, J. C.; Fragosó, A. A Wide-Range Solid State Potentiometric PH Sensor Based on Poly-Dopamine Coated Carbon Nano-Onion Electrodes. *Sensors Actuators B Chem.* **2018**, 273, 664–671.

Conclusion and Outlooks

The electro-triggered deposition is a powerful tool to grow thin films exclusively near a surface. The manufacturing of bioelectrodes, and especially biosensors, based on the electro-crosslinking of enzymes has started in 2015 with the pioneering work made by our team, using poly(allylamine) as a model.¹ The strategy was based on mussel-inspired chemistry using a bifunctional catechol cross-linker allowing the covalent reaction between amine moieties and electro-oxidized catechol moieties, and the strong adhesion of the obtained coating onto the working electrode. In 2018, a proof-of-concept was made in the manufacturing of glucose biosensors using the same strategy.² The obtained coatings had a sensitivity of $0.66 \mu\text{A} \cdot \text{mM}^{-1} \cdot \text{cm}^{-2}$ and a linear range from 1 to 12.5 mM in glucose, competitive with the biosensors obtained by drop-casting using glutaraldehyde. This biosensor was able to discriminate hypo and hyper-glycemia at the common blood concentration. However, the concentration of glucose is often smaller in the other biological fluids (wound fluid, ocular fluid, sweat...). To generalize the process to other biomarkers (neurotransmitters, H_2O_2 , uric acid), the enzymatic coating should be able to sense in the micro-molar range. The bioelectrode nanoarchitectures have to be redesigned to achieve higher sensitivities. Moreover, the use of a synthesized bifunctional catechol molecule limits the application of this process.

To tackle the sensitivity issue and to generalize the process to commercially available molecules, tannic acid-capped gold nanoparticles (TA@AuNPs) were prepared and used as a cross-linker, thanks to available gallol moieties, in the presence of the enzyme (GOx and HRP). Metallic nanoparticles are known to boost the electroactive surface of the electrodes and eventually tune the intrinsic catalytic rate of enzymes. Gold is probably the most biocompatible metal and its use in the nanoparticle state strongly limits the cost (~20 μg , less than one euro cent per sensor). The synthesis of TA@AuNPs was optimized using a simple room-temperature procedure to obtain several NP sizes.

GOx/NPs and HRP/NPs coatings were obtained using the electro-crosslinking process in the presence of FcOH, acting as a mediator, to oxidize gallol moieties of TA and thus trigger the covalent reaction with gallol moieties of TA and amine moieties of enzymes. Even though TA is known to strongly interact with proteins leading to their denaturation, we proved that (i) adsorbed GOx and HRP enzymes were active onto TA@AuNPs, (ii) their electro-cross-linking deposition was enhanced similarly to catechol/GOx alone, (iii) the enzyme/NPs deposition was reproducible with a homogeneous distribution of enzyme/NPs onto the electrode, (iv) and

spatially controlled onto 10 μm interdigitated electrodes, and (v) the enzymes were firmly attached on the electrode. The sensitivity of the nanohybrid biosensor was greatly increased compared to the biosensors containing no NPs. Competitive with the ones obtained by drop-casting methods, the electro-crosslinked GOx/NPs biosensors had a sensitivity of $17.4 \mu\text{A} \cdot \text{mM}^{-1} \cdot \text{cm}^{-2}$ towards glucose, ~ 30 times better than the GOx/catechol system.² A linear range from 0.3 to 10 mM in glucose was achieved allowing the potential use of the biosensor to test wound fluids or urine (Chapter 1 Table 1.3). For HRP/NPs coatings, a sensitivity of $220 \mu\text{A} \cdot \text{mM}^{-1} \cdot \text{cm}^{-2}$ towards H_2O_2 was obtained with a linear range from 10 to 500 μM . The biosensor is competitive in terms of sensitivity and can be used to test ocular fluid, urine, and eventually wound fluid (Chapter 1 Table 1.4).

A complete study with both enzymatic coatings was carried out on the influence of enzyme/NPs ratio and NP size (7, 11, and 40 nm in diameter). The GOx/NPs biosensor sensitivity was found to be strongly affected by the NPs size with an optimum using 11 nm diameter NPs. An optimal sensitivity was also observed at the theoretical GOx/NPs monolayer ratio with a drastic decrease when the ratio was higher or lower. The low enzymatic loading on NPs, along with a loss of their activity, explained the low sensitivity at small ratios. At high ratios, a large GOx corona onto NPs hide gallol moieties of TA preventing the electro-crosslinking process. For HRP/NPs coatings, the results were pretty different. First, no activity loss was found for adsorbed HRP on the NPs as compared to HRP in solution and the sensitivity of the biosensor film was found to be independent of the NPs size. Also, the maximum value of the sensitivity was achieved at two times the theoretical HRP/NPs monolayer ratio, reaching almost a plateau. Indeed, the higher ratios lead to similar sensitivities and mass deposited due to the saturation of NPs by HRP. No corona of enzymes were observed by TEM on NPs. HRP enzymes were likely adsorbed as a thin film on NPs and did not prevent the electro-crosslinking process.

Finally, a flexible conductive membrane was used as working electrode to be close to an application, a point-of-care sensor for wound monitoring. In collaboration with Anne Hébraud, Jean-Mario Nhut (ICPEES) and Housseinou Ba (Blackleaf), we have investigated the use of electrospun polyurethane membranes coated with few layers of graphene (PU-FLG), which is highly conductive and flexible. The use of free diffusing redox mediator (FcOH) strongly limits *in-situ* application. It was found that the mediator was retained onto the graphene layer with a stable signal up to two days. The electrodeposition of HRP/NPs and GOx/NPs coatings lead to good sensitivities in the absence of free diffusing mediators. The response was stable for two days but drastically decrease for longer times. Moreover, the bending of the resulting

membranes does not significantly change the sensitivities. For HRP/NPs coatings, interferences were however important. A flexible pH-sensor was also developed by electrodeposition of polydopamine. A reproducible potentiometric response was obtained towards pH changes and robust on the membrane bending. These results suggest that PU-FLG is a very promising platform for multi-biomarkers analysis in wound fluids to record the healing progress. We can highlight that: (i) H_2O_2 , glucose, and pH were easily quantifiable with our architecture, (ii) the linear ranges achieved were perfectly fitting the common range of these biomarkers in wound fluids, (iii) no free diffusing mediators were used and a true immobilized electron transfer electrocatalysis was highlighted and (iv) the response of these coatings was found to be independent on the bending.

As outlook of this thesis, a stronger way to retain the mediator, ferrocene, onto graphene still requires to be developed to achieve great 2.5th generation biosensors onto flexible membranes. Several covalent immobilization techniques of ferrocene onto graphene or stronger π - π^* stacking have already been successfully developed in the literature and deserve to be experienced here.³⁻⁵ Regarding the HRP/NPs biosensor, an adequate permeability-selective coating towards H_2O_2 and acting as a barrier for uric acid and ascorbic acid could be deposited above the biosensor.⁶ Another interesting outlook would be the development of a sense-act-treat smart membrane. To this aim at the very late stage of this thesis, few progress was obtained on the electro-release of bovine serum albumin (BSA) and rhodamine B (RhodB) as model drugs using TA/Fe(III) films (Figure 6.1.a). Either in the presence of BSA or RhodB, the electrodeposition of TA/Fe(III) coating was performed using the method introduced by our team.⁷ Briefly, TA/Fe(III) coating was electro-self-assembled at 0.4 V for 30 min on a PU-FLG membrane. An anodic potential was applied to a mixture of TA/Fe(II) solution to oxidize Fe(II) into Fe(III) leading to the electro-self-assembly of TA/Fe(III) coating. After the buildup of TA/Fe(III)/BSA and TA/Fe(III)/RhodB coatings, the application of a cathodic potential (-2 V) allowed to electro-release BSA and RhodB, respectively as illustrated with Rhodamine on figure 6.1.c. Even if this system was found to be interesting, the use of high overpotential (- 2 V) for the release would not be suitable for the point-of-care application.

We could envision a smart wound dressing able to analyze the wound fluid via multi-analytes and to favor the healing process by electro-release of a controlled amount of antibacterial or growth factors agents. The drug administration has to be accurate as a reverse effect (slowing down the healing process or leading to non-organized tissue) could be obtained if the delivered

amount is too high. Another electro-release strategy could be the use of electro-cleavable bonds such as cystine and boronate-catechol complexes,⁸ that could be obtained with TA and a boronate-functionalized or cysteine-functionalized drug.

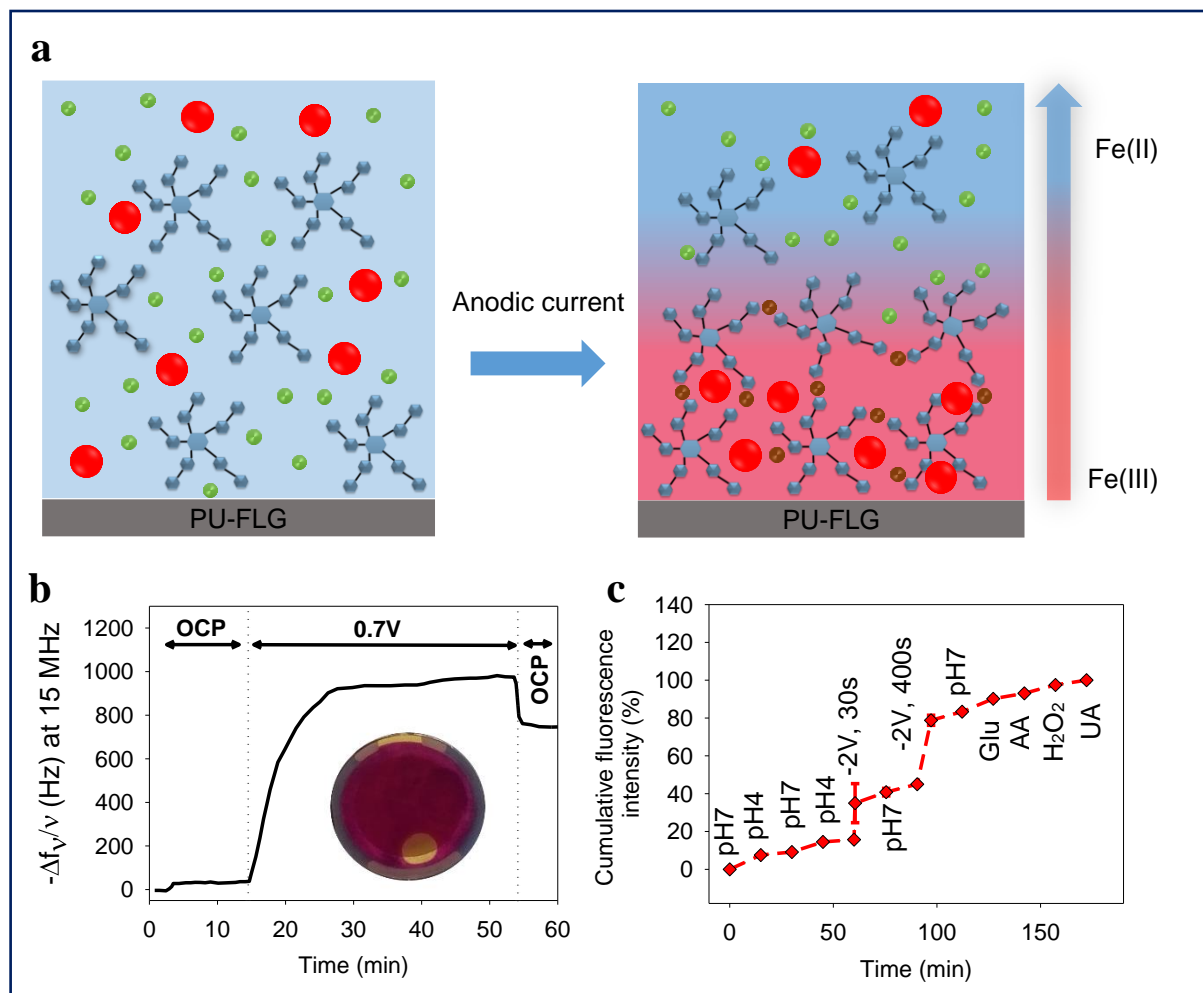


Figure 6.1: (a) Principle of the electro-triggered construction of TA/Fe(III) via the oxidation of Fe(II) into Fe(III) and the concomitant rhodamineB (red spheres) entrapment. (b) QCM frequency shift during the electrodeposition of TA/Fe(III) coating at 0.4 V for 30 min using a mixture made from 6 mM TA, 15 mM Fe(II) and 1 mM Rhodamine B in 10 mM PBS with 10% EtOH. Inset correspond to the resulting film. (b) Rhodamine B electro-release from TA/Fe(III)/RhoB film built onto PU-FLG followed by fluorescence using excitation and emission wavelength of 554 and 576 nm respectively. Both peak correspond to -2 V potential (30s and 400s). Influence of pH onto uncontrolled release was experienced in citrate/phosphate buffer in the typical range of wound fluid. Interferents (Uric Acid, Glucose, Ascorbic Acid, H₂O₂) were tested at 1 mM in PBS 10 mM.

References

- (1) Maerten, C.; Garnier, T.; Lupattelli, P.; Chau, N. T. T.; Schaaf, P.; Jierry, L.; Boulmedais, F.; Trang, N.; Chau, T.; Schaaf, P.; Boulmedais, F.; Maerten, C.; Garnier, T.; Lupattelli, P.; Chau, N. T. T.; Schaaf, P.; Jierry, L.; Boulmedais, F. Morphogen Electrochemically Triggered Self-Construction of Polymeric Films Based on Mussel-Inspired Chemistry. *Langmuir* **2015**, *31* (49), 13385–13393.
- (2) El-Maiss, J.; Cuccarese, M.; Lupattelli, P.; Chiummiento, L.; Funicello, M.; Schaaf, P.; Boulmedais, F. Mussel-Inspired Electro-Cross-Linking of Enzymes for the Development of Biosensors. *ACS Appl. Mater. Inter.* **2018**, *10* (22), 18574–18584.
- (3) Elanchezian, M.; Manoj, D.; Saravanakumar, D.; Thenmozhi, K.; Senthilkumar, S. Amperometric Sensing of Catechol Using a Glassy Carbon Electrode Modified with Ferrocene Covalently Immobilized on Graphene Oxide. *Microchim. Acta* **2017**, *184* (8), 2925–2932.
- (4) Trindade, E. K. G.; Silva, B. V. M.; Dutra, R. F. A Probeless and Label-Free Electrochemical Immunosensor for Cystatin C Detection Based on Ferrocene Functionalized-Graphene Platform. *Biosens. Bioelectron.* **2019**, *138*, 111311.
- (5) Liu, M.; Wang, L.; Deng, J.; Chen, Q.; Li, Y.; Zhang, Y.; Li, H.; Yao, S. Highly Sensitive and Selective Dopamine Biosensor Based on a Phenylethynyl Ferrocene/Graphene Nanocomposite Modified Electrode. *Analyst* **2012**, *137* (19), 4577–4583.
- (6) Erdogdu, G.; Ekinici, E.; Karagozler, A. E. Preparation and Electrochemical Behavior of Dopamine-Selective Polymeric Membrane. *Polym. Bull.* **2000**, *44* (2), 195–201.
- (7) Maerten, C.; Lopez, L.; Lupattelli, P.; Rydzek, G.; Pronkin, S.; Schaaf, P.; Jierry, L.; Boulmedais, F. Electrotriggered Confined Self-Assembly of Metal-Polyphenol Nanocoatings Using a Morphogenic Approach. *Chem. Mater.* **2017**, *29* (22), 9668–9679.
- (8) Cheng, X.; Li, M.; Wang, H.; Cheng, Y. All-Small-Molecule Dynamic Covalent Gels with Antibacterial Activity by Boronate-Tannic Acid Gelation. *Chinese Chem. Lett.* **2020**, *31* (3), 869–874.

La chimie des catéchols pour le développement de biocapteurs : Synthèse et électro-réticulation de nanoparticules d'or fonctionnalisées par des enzymes

Résumé en français

L'intérêt pour les bioélectrodes croît exponentiellement depuis plusieurs dizaines d'années. En particulier, les biocapteurs et les biopiles enzymatiques ont montré des performances intéressantes pour la surveillance in-situ de biomarqueurs d'intérêts ou pour l'alimentation électrique de dispositifs miniaturisés bio-implantés. Malgré la multitude d'applications envisagées, ces dispositifs peinent encore à se généraliser sur le marché à cause de plusieurs limitations majeures. Le coût, la facilité de fabrication, la sensibilité et surtout la stabilité dans le temps sont des paramètres encore à améliorer. Etant des limitations intrinsèques au choix et à l'organisation des matériaux constituant la couche sensible, nous avons proposé par ce travail une nouvelle voie de fabrication des bioélectrodes. Nous avons utilisé un mélange de polyphénol, sel d'or, médiateur électrochimique et enzyme (relative au biomarqueur d'intérêt) qui a ensuite été électro-réticulés en complexes enzymes/nanoparticules organisés. Enfin, nous avons généralisé ce concept sur membrane souple avec co-immobilisation du médiateur ce qui constitue une approche originale dans le développement de pansements intelligents pour le suivi des plaies chroniques.

English summary

Interest in biosensors has grown exponentially in recent decades. In particular, enzymatic biosensors and biofuel cells have shown great promises as in-situ monitoring of interesting biomarkers or as miniaturized bio-implanted powering devices. Despite the multitude of applications, these devices are struggling to widespread on the market due to several limitations. Cost, ease of fabrication, sensitivity and stability over time are parameters that still deserve to be improved. The choice and spatial organization of the materials within the sensitive layer need to be reconsidered in order to propose new strategies for bioelectrodes manufacturing. In this work, a simple mixture of polyphenol, gold salt, electrochemical mediator and enzyme (related to the biomarker) were electro-crosslinked into an organized enzymes/nanoparticles film. Finally, this concept was transferred onto flexible membrane with co-immobilization of the mediator. This original approach has enhanced to develop smart chronic wound dressings.